Bonding Mechanisms and Strength of Hooked-end Steel Fibre Reinforced Cementitious Composites

By

Sadoon Mushrif Abdallah

Department of Mechanical, Aerospace and Civil Engineering

College of Engineering, Design and Physical Sciences

A thesis submitted for the degree of Doctor of Philosophy

May 2017

Abstract

Concrete is a strong material as to its compressive strength. However, it is a material with a low tensile and shear strength, and brittleness at failure. Concrete has to be reinforced with appropriate materials. Steel fibre is one of the most common materials currently being used to develop reinforced concrete, which may replace partially or completely conventional steel reinforcement. Successful reinforcement of concrete composite is closely related to the bond characteristics between the reinforcing fibre and matrix.

The effective utilisation of steel fibre reinforced concrete (SFRC) requires in-depth and detailed understanding of bonding mechanisms governing the tensile behaviour. In response to this demand, this study embraced two main areas: understanding the reinforcing mechanisms of fibres in SFRC and material's post-cracking behaviour. Comprehensive experimental and theoretical programmes have therefore been developed: the experimental work is subdivided into three parts. The first part was to investigate the effect of various physical parameters, such as fibre characteristics (i.e. geometry, inclination angle, embedded length, diameter and tensile strength) and matrix strength which controls the pull-out behaviour of steel fibres. The second part is concerned with the assessment of the bond mechanisms of straight and hooked end fibres after exposure to elevated temperatures and varying matrix strength. The third part is devoted to gain further insight on the bond mechanisms governing the post-cracking behaviour through uniaxial and bending tests. It was found that the varying hook geometry and matrix strength each had a major influence on the pull-out response of hooked end fibres. As the number of the hook's bends increased, the mechanical anchorage provided by fibre resulted in significant improvement of mechanical properties of SFRC. The reduction in bond strength at elevated temperatures is found to be strongly related to the degradation in properties of the constituent materials, i.e. the fibre and concrete. The most effective combination of matrix strength and fibre geometry was found to be as follows: 3DH (single bend) fibre with normal-medium strength matrix, 4DH (double bend) fibre with high strength matrix and 5DH (triple bend) fibre with ultra-high performance matrix.

Two analytical models to predict the pull-out behaviour of hooked end fibres were developed. Both models were able to predict the pull-out response of SFRC made from a variety of fibre and matrix characteristics at ambient temperature.

This work has established a comprehensive database to illustrate the bonding mechanisms of SFRC and anchorage strengthening of various hooked end fibres, and this should contribute towards an increasing interest and growing number of structural applications of SFRC in construction.

Acknowledgements

I owe my deepest gratitude to my supervisor Professor Mizi Fan. Without his continuous optimism encouragement, enthusiasm and support concerning this research, this project would hardly have been completed. I also express my sincere gratitude to my second supervisor Dr. Xiangming Zhou for all his support and expert advice throughout this research project.

I am also deeply grateful to Dr David Rees. His guidance into the analytical analysis and laboratory supervision has been essential during this work.

I would also like to express my appreciation to Dr. Katherine Cashell for her support and invaluable advice for some parts of my research.

The Ministry of Higher Education and Scientific Research of Iraqi Government and University of Anbar are acknowledged for their financial support for this PhD research.

I want to express my gratitude to the technicians in the engineering labs, including, Mr Paul Szadorski, Mr Simon Le Geyt, Mr Neil Macfadyen, and Mr Gerald Edwardson for their support and help throughout the experimental work in the lab.

I would like to thank my friends for accepting nothing less than excellence from me.

Last but not the least, I would like to thank my family: my parents, my wife and to my brothers and sister for supporting me spiritually from the very beginning of the PhD project.

Declaration

The work in this thesis is based on research carried out at Brunel University London, United Kingdom. I hereby declare that the research presented in this thesis is my own work except where otherwise stated, and has not been submitted for any other degree.

Table of Contents

List of Figures

List of Tables

List of Abbreviations

BS EN	British Standard European Norm
C.G.A	Crushed granite aggregates
CMOD	Crack mouth opening displacement
CRC	Conventional reinforced concrete
DH	Dramix hooked end fibre
HSC	High strength concrete
ITZ	interfacial transition zone
L/D	Aspect ratio
LVDT	linear variable differential transformer
MSC	Medium strength concrete
NSC	Normal strength concrete
PH	Plastic hinge
RC	Reinforced concrete
RH	Relative humidity
SEM	Scanning electron microscope
SFD	Slump-flow diameter
SFRC	Steel fibre-reinforced concrete
SFRCCs	Steel fibre-reinforced cementitious composites
SFR-SCC	Steel fibre reinforced-self compacting concrete
T500	Time to reach 500mm spread
UHPC	Ultra-high performance concrete
UHP-FRC	Ultra-high performance fibre reinforced concrete

UTS	Ultimate tensile strength
Vw	Virtual work
W/B	Water-to-binder ratio

List of Symbols

R	Reaction forces at the pulley centres
N	Normal force
N_s	Normal reaction
A	Cross-sectional area of a fibre
τ	Interface shear stress
Δ	Relative slip of the fibre after full debonding
P_f	Critical pull out force
P	Pull-out force
F_{PH}	Rotational friction component
Δ_0	Relative slip of the fibre at end of full debonding
n	The normal force/unit length of fibre
τ_{max}	Bond strength of interface between fibre-matrix
R	Reaction forces at the pulley centres
τ_e	Elastic shear stress
q_e	Elastic shear flow
μ	Friction coefficient
F_{PH}	Rotational friction component
τ_{fd}	Frictional shear stress
μ_d	Dynamic friction coefficient
τ_{ult}	The bond's ultimate shear strength
q	Shear flow
q_f	Frictional shear flow

τ_f	Frictional bond stress at the fibre-matrix interface
ψ	Circumference of a fibre
l	Embedded length of a fibre
τ_f	Frictional shear stress
T	Chord tension in the pulley
Δ_f	Relative slip of the fibre
μ_s	Static friction coefficient
u^v	The virtual displacement
δ_f	Local displacements in the fibre
δ_m	Local displacements in the matrix
ε_f	Axial strains in the fibre
ε_m	Axial strains in the matrix
θ^v	The virtual rotation
σ_f	Transverse failure stress
σ_t	Tensile stress
A_f	Fibre cross-sectional area
A_m	Matrix cross-sectional area
d_f	Fibre diameter
E_f	Modulus of elasticity of fibre
E_m	Modulus of elasticity of matrix
k	Interfacial bond modulus
ε_f	Axial strains in the fibre
ε_m	Axial strains in the matrix

θ^{v}	The virtual rotation
σ_f	Transverse failure stress
σ_t	Tensile stress
A_f	Fibre cross-sectional area
A_m	Matrix cross-sectional area
d_f	Fibre diameter
E_f	Modulus of elasticity of fibre
l	Embedded length of fibre
L	Hook length
M_P	Plastic moment
η	Factor reflective of steepness of descending branch of pull-out curve
r_f	Fibre radius
u	Debonded length of fibre
V_f	Fibre volume friction
θ_1,θ_2,β	Hook angles
μ	Friction coefficient of the fibre-matrix interface
ν_f	Poisson's ratio for fibre
ν_m	Poisson's ratio for matrix
ξ	Damage coefficient
σ_{u}	Fibre ultimate strength
σ_y	Fibre yield strength
ψ	Fibre perimeter
$\mathrm{P}_{\mathrm{max}}$	Maximum pull-out load

$\sigma_{\max}$	Maximum fibre stress
W_{total}	Total pull-out work
P_{peak}	Peak load
τ_{av}	Average bond strength
τ_{eq}	Equivalent bond strength
S_{peak}	Slip at peak load
M_{loss}	Mass loss
f_c'	Compressive strength at room temperature
f_{cT}'	Compressive strength at elevated temperatures

Chapter 1 Introduction

1.1 Overview

The development of steel fibre reinforced concrete (SFRC) marks a huge step forwards in building materials and construction technology, which is indispensable in the modern structural applications. It is well known that cementitious materials such as concrete and mortar are characterized by weakness in resisting tensile stresses and fail in a brittle manner [1,2]. The idea of adding short randomized reinforcing steel fibres to cementitious materials is to improve their tensile behaviour by resisting the cracking propagations [3-5]. To what extent the tensile response of SFRCCs could be improved depends on several parameters. Fibre characteristics, fibre shape, fibre content, fibre distribution and orientation with respect to load direction, the quality of the cementitious matrix surrounding the fibre and bond characteristics all affect the tensile response together. Of these, the interfacial bond characteristics between fibre and matrix play a crucial role in controlling the overall behaviour of the composite. Therefore, understanding and predicting suitably the bond mechanisms between fibre and matrix is of primary importance in order to produce reliable and economical fibre reinforced concrete composites.

Since the 1960s with development of steel fibre, there has been a rapid growth in research and innovation in the field of fibre reinforced concretes [6]. Advances in this field, e.g. steel fibre reinforced self-compacting concrete (SFR-SCC), high performance fibre reinforced cementitious composites (HPFRCC), slurry infiltrated fibre concrete (SIFCON) and engineered cement composites (ECC) have attracted considerable attention among researchers and civil engineers. These composites are characterized by multiple cracks and hardening tensile behaviour due to the high crack-bridging capacity provided by fibres. This leads to increased load-carrying capacity of fibres and post-cracking strength of SFRC significantly. Consequently, minimum cover requirements are no longer needed for SFRC elements and cover thickness can be significantly reduced. Therefore, conventional reinforcing (mesh or rebars) can be partially or totally replaced with short steel fibres reinforcement. As is the case with conventional reinforced concrete (CRC), steel fibre reinforced concrete (SFRC) makes up for the weakness of the cementitious matrix under tension as well as static or dynamic loading conditions. However, the basic difference between CRC and SFRC lies in the fact that the failure of conventional reinforcement is of a yielding nature, while steel fibres pull-out as they yield.

Over the past a few years, SFRC has been used extensively for a wide variety of new applications. Of these, shotcrete and tunnel liner industries represent the majority of SFRC applications in most countries [7]. Although the material cost of the rebar is less than for steel fibres, there are significant savings to be made by the elimination of manufacturing, handling and storage of reinforcement cages. In addition to the economic benefits, technical advantages are obtained by the use of steel fibres. One of the major advantages of SFRC, when compared to conventional reinforced concrete, is its excellent durability. SFRC, unlike structural reinforced concrete, will not support the classic galvanic corrosion cells. The fibres, being non-continuous and discrete, provide no mechanisms for propagation of corrosion activity. Moreover, the risk of the concrete spalling is totally excluded as the increase in volume due to the corroded fibres is not sufficient to split the concrete [8]. Another important advantage of SFRC is its homogenous reinforcement. The steel fibres randomly distributed in the concrete and present close to the surface, ensure an excellent reinforcement at the joints of the structure elements. When reinforced with rebar, damage at the edges and corners very often occurs.

Despite these significant advances in the field of SFRC that have been attained recently, there are still some specific limitations hindering its widespread use. Characterization and quality control of SFRC’s material properties in its hardened state must be improved to comply with the industry demand for increased structural applications. Thereby, comprehensive understanding of bonding mechanisms governing the tensile response of SFRC is of paramount importance for optimising the overall properties and providing the basis for more economical SFRC applications.

The lack of comprehensive and detailed international standards on the fundamental properties of SFRC is the main reason behind the underutilisation in engineering practice so far. Recently, some international building codes and national guidelines for the structural design of SFRC, such as *fib* Model Code 2010 have been developed in response to this limitation. However, even though these relevant advances have recently been drawn up, some basic aspects still open questions and feed doubts on the uniaxial tensile constitutive relationships proposed by various international standards and guidelines. Further studies are still needed to provide in-depth and comprehensive knowledge on the tensile behaviour of SFRC and serve as the basis possible for better design and future codes.

1.2 The challenges to be addressed

This research project is set to tackle the issues associated with the lack of comprehensive and detailed knowledge on bonding mechanisms governing the tensile behaviour of SFRC. Since the bond mechanisms directly influence the tensile behaviour of the composite, and since the tensile response directly controls both the compressive and the bending response, it is evident that the bonding mechanism is the single most important parameter for understanding and hence utilising SFRC with optimized properties. Consequently, several studies [4,9-11] to understand and characterize the bond between reinforcing steel fibre and cementitious matrix have been carried out over the last four decades. Whereas the bond characteristics of straight fibres were the subject of early and intensive investigations, bond mechanisms associated with the pull-out behaviour of the deformed fibres, such as hooked end of single bend (i.e. 3D), are not completely understood, although several experimental studies have been carried out in the past 15 years to investigate the influence of factors, such as fibre embedded length, fibre shape and the quality of the matrix on the pull-out behaviour of deformed steel fibres. Some [12-14] attempts to model the effect of fibre geometry on the pull-out response have also been made in recent years, however, these models are restricted to a set of material properties and experimental boundary conditions. Their ability to provide an effective understanding of the bonding mechanisms is limited due to involving a large number of parameters. Therefore, an accurate prediction of the pull-out behaviour of the deformed fibres is of paramount importance for the structural design of SFRC elements. Yet, suitable and reliable predictions of the pull-out behaviour of hooked end steel fibres are still needed.

Recently, the hooked end steel fibres of improved geometrical and tensile properties, namely, Dramix® 4D and 5D were introduced in the market, which are in fact the most widely used in variety of construction applications [15]. These fibres are designed to increase the anchorage capacity of a concrete structure to bear complex loading including tension, compression and shear. However, despite the wide range of new applications, some principal concerns remain, giving rise to the skepticism towards their uses. Like other construction materials, the SFRC structural member is prone to exposure to various loading and environmental conditions, such as those during a fire. The mechanical and physical properties of reinforcing steel fibre and cementitious matrix as well as the bond characteristics between them may become progressively worse with temperature. Current understanding of the bonding mechanisms of these reinforcing steel fibres is incomplete; hence further investigation is required before an accurate assessment of the overall behaviour of these fibres may be made. Therefore, there is an urgent need to establish a new perspective to better understanding the bonding mechanisms that controls the tensile behaviour of these newly developed fibres.

This research has been carried out to better understand bonding mechanisms, particularly those associated with the pull-out behaviour of newly developed hooked end fibres. A comprehensive characterisation of every single parameter and detailed descriptions of reinforcing mechanisms of steel fibres in the SFRC have been achieved. The outcomes of this research would provide a better understanding of the bond mechanisms of SFRC and serve as a basis for better design and application of steel fibres.

1.3 Objectives of the project

This PhD research project aims at developing a comprehensive and in-depth understanding of bonding mechanisms governing the tensile behaviour of SFRC. Specific objectives are:

- To study the main bond components encountered in SFRC;
- To determine the influence of physical parameters, such as matrix strength, fibre geometry, fibre tensile strength, fibre orientation and fibre embedded length on pull-out behaviour;
- To investigate the effect of elevated temperatures on the bonding mechanisms of straight and hooked end steel fibres;
- To develop rationale and comprehensive analytical models to predict the pull-out behaviour of various hooked end fibres embedded in different matrix strength;
- To investigate the post-cracking behaviour of SFRC elements through uniaxial tensile and three-point bending tests.

Figure 1.1 illustrates the connections between sub-objectives. Each sub-objective is to be concluded and then serves as a foundation of the next consecutive sub-objective. The success of the project relies on the complete coordination of these sub-objectives links.

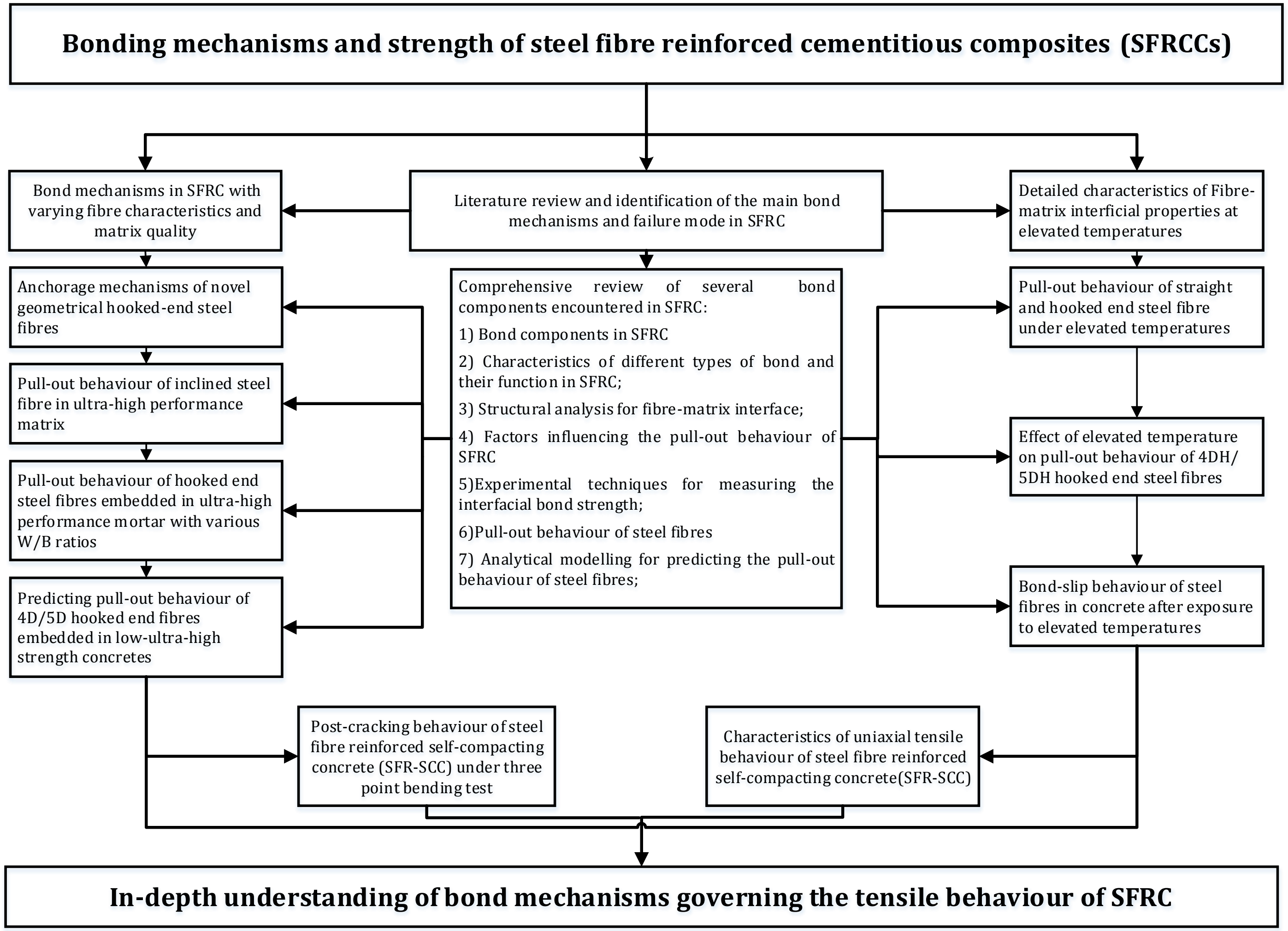

Figure 1.1 Schematic objective chart of this project

1.4 Research strategy

In order to fulfil the major goals of this PhD project, an efficient strategy was developed as follows:

Firstly, an extensive review of literature was performed to determine critical information regarding the bond mechanisms governing the tensile behaviour of SFRC, and identify research needs in order to explore the full potential of steel fibres and their SFRC in smart utilisation and stimulate the advancement of SFRC in structural applications .

Secondly, a comprehensive experimental programme was developed to investigate bonding mechanisms and failure modes of SFRC through evaluating the influence of processing and material parameters, such as matrix strength, fibre geometry, fibre tensile strength, fibre inclination and fibre embedded length on pull-out behaviour.

Thirdly, based on the experimental results of pull-out tests, analytical models were developed to predict the pull-out behaviour of various hooked end fibres. To ascertain the reliability and applicability of the proposed model with varying matrix strength, a comparison between model predictions and those experimental results was performed.

Fourthly, an investigation was made of interfacial bonding mechanisms after exposure to elevated temperatures (20-800°C). The influence of temperature on the bond between the steel fibre and concrete matrix, and constituent materials themselves were examined.

Finally, the post-cracking tensile response of SFRC composite was experimentally investigated by two different tests: Three point bending tests on large SFRC beam were performed to characterize the post-cracking response and the tensile behaviour of SFRC was characterized through a uniaxial tensile test on notched cylinders. To understand the characteristics of post-cracking behaviour, the comprehensive investigation and interpretation of different parameters were carried out.

1.5 Outline of the thesis

This thesis consists of nine chapters. The structure and the brief overview of the chapters are outlined below:

Chapter 1 Introduction

This chapter introduces the basic facts on the development and utilization of steel fibre reinforced concrete and identifies the problems and challenges to be addressed. The motivations for this PhD research project along with the strategies to achieve the goals are also pointed out.

Chapter 2 Literature review

This chapter presents the state of the art of the subjects addressed in this research. A literature review of bond characteristics between reinforcing steel fibre and cementitious matrix is provided. Comprehensive analyses of bonding mechanisms and failure mode governing the tensile behaviour of SFRC is explained. This chapter also reviews pervious works regarding experimental pull-out tests as well as modelling of pull-out behaviour of hooked end fibres.

Chapter 3 Materials and methodologies

This chapter provides a general description of the materials used in the research, as well as a detailed description of the sample preparations and testing procedures. Details of testing equipment and standard for each test are also provided.

Chapter 4 Pull-out behaviour of straight and hooked-end steel fibres

This chapter presents the experimental results of pull out tests on the hooked end fibres embedded in various cementitious matrices. A comprehensive and in-depth analysis is accomplished in this chapter, focusing on the effect of fibre geometry on pull-out behaviour with varying matrix strength. This chapter also investigates the effect of fibre orientation on the pull-out behaviour of straight and hooked end fibres. For that purpose, both fibres are selected to be embedded in ultra-high performance concrete matrix under different inclination angles. In this chapter, the influence of parameters such as fibre embedded length, fibre diameter, water/binder ratio on pull-out response of hooked end fibres are also studied.

Chapter 5 Predicting pull-out behaviour of hooked-end steel fibres embedded in various concretes

This chapter advances an analytical model to predict the pull-out behaviour of hooked end fibres embedded in normal, medium, high and ultra-high performance concrete matrices. In this chapter, the model predictions are validated against experimental pull-out test results reported in Chapter 4.

Chapter 6 Pull-out behaviour of straight and hooked-end fibres after exposure to elevated temperatures

This chapter presents the results of an experimental investigation into the effect of elevated temperature on the bond characteristics of straight and hooked end fibres. The initial and residual thermal and mechanical properties of the concrete are also investigated in this chapter.

Chapter 7 Flexural behaviour of steel fibre reinforced self-compacting concrete (SFR-SCC)

This chapter utilises the outcomes of all the experimental investigations reported in Chapter 4 to study the bonding mechanisms of hooked end fibres and their link to post-cracking strength of the composite. To investigate the post-cracking behaviour in a SFRC composite the concrete matrix with the best rheological and workability properties are selected and tested in bending. This chapter also presents the experimental investigation of flexural tests which are aimed at evaluating the influence of fibre shape and fibre content on the stress-crack width response. Specifically, it focuses on the fibre distribution and orientation in the direction of applied load which are the key factors to control the post-cracking response.

Chapter 8 Characteristics of uniaxial tensile behaviour of steel fibre reinforced self-compacting concrete (SFR-SCC)

In this chapter, the post-cracking behaviour of SFRC is assessed through uniaxial tensile tests. The same combination i.e. concrete matrix and fibre content designed in Chapter 7 is used to assess the crack-bridging effect on the tensile response of SFRC throughout the uniaxial tensile test.

Chapter 9 Conclusions and future perspectives

This chapter is the final appraisal of the project. The conclusive statements and concise summary are established, and on this platform, the recommendations and future prospective are given. Particular emphasis is given to the bond characteristics of hooked end fibres.

1.6 Outcomes of this PhD project

The following original research articles and presentations have been produced to disseminate the findings of the research results:

Journal articles:

1) **S. Abdallah**, M. Fan, D.W.A. Rees, Effect of elevated temperature on pull-out behaviour of 4DH/5DH hooked end steel fibres, *Composite Structures*. 165 (2017) 180-191. http://dx.doi.org/10.1016/j.compstruct.2017.01.005.
2) **S. Abdallah**, M Fan, KA Cashell, Pull-Out behaviour of straight and hooked-end steel fibres under elevated temperatures, *Cement and Concrete Research* (2017) 95: 132-140. http://dx.doi.org/10.1016/j.cemconres.2017.02.010.

3) **S. Abdallah**, M Fan, KA Cashell, Bond-slip behaviour of steel fibres in concrete after exposure to elevated temperatures, *Construction and Building Materials* (2017) 140: 542-551. http://dx.doi.org/10.1016/j.conbuildmat.2017.02.148.

4) **S. Abdallah**, M. Fan, Anchorage Mechanisms of Novel Geometrical Hooked-End Steel Fibres." *Materials and Structures* 140 (2017) 542-551. http://doi: 10.1617/s11527-016-0991-5

5) **S. Abdallah**, M. Fan, D.W.A. Rees, Analysis and modelling of mechanical anchorage of 4D/5D hooked end steel fibres, *Materials and design*. 112 (2016) 539-552. http://dx.doi.org/10.1016/j.matdes.2016.09.107

6) **S. Abdallah**, M. Fan, X. Zhou, S. Geyt, Anchorage Effects of Various Steel Fibre Architectures for Concrete Reinforcement, *International Journal of Concrete Structures and Materials*. 10(2016) 325-335. http://doi:10.1007/s40069-016-0148-5

7) **S. Abdallah**, M. Fan, X. Zhou, Pull-Out Behaviour of Hooked End Steel Fibres Embedded in Ultra-high Performance Concrete with Various W/B Ratios, *International Journal of Concrete Structures and Materials*. 17(2017) 193-198. http://doi: 10.1007/s40069-017-0193-8

8) **S. Abdallah**, M. Fan, X. Zhou, Effect of Hooked-End Steel Fibres Geometry on Pull-Out Behaviour of Ultra-High Performance Concrete, World Academy of Science, Engineering and Technology, *International Journal of Civil, Environmental, Structural, Construction and Architectural Engineering*. 10 (2016) 1530-1535.

9) **S. Abdallah**, M. Fan, D.W.A. Rees, Predicting pull-out behaviour of 4D/5D hooked end fibres embedded in low-high strength concretes, *Computers and Structures*. (under review).

10) **S. Abdallah**, M. Fan, D.W.A. Rees, Bonding mechanisms and strength of steel fibre reinforced cementitious composites: An overview, *Journal of Materials in Civil Engineering*. (accepted).

International conferences:

1) **Abdallah, S.**, Fan, M., & Zhou, X. (2016). Anchorage Effect Of Various Steel Fibres On Pull-Out Behaviour Of Ultra-High Performance Concrete. In Proceedings of the 9th Rilem International Symposium on Fiber Reinforced Concrete Befib2016.

Poster and oral presentations at conferences :

1) ResCON14 'Bonding mechanisms and strength of fibre reinforced cementitious composites (FRCCs)': 23-16 June 2014, Brunel University, London, UK.
2) Workshop/conference on Future emerging materials for green buildings: 30th of October 2015. European Centre of Excellence, London, UK.

Chapter 2 Literature Review

2.1 Introduction

Cementitious materials such as concrete and mortar are well-known for their low ability in resisting tensile stresses [16-18]. The use of steel fibres is one of the most promising solutions to overcome the brittleness of cementitious materials [19-21]. The principal benefit of incorporating discontinuous fibres into cementitious materials is to resist and delay cracking propagation [22-24]. It is generally believed that the addition of fibres improves the pre-cracking resistance of concrete by increasing its critical cracking strength [25,26]. The fibre contribution appears as concrete cracking initiates and often enhances the post-cracking behaviour due to improved stress transfer provided by the fibres bridging the cracked sections [27,28]. In the post-cracking stage, the efficiency of fibres in transferring applied stresses is strongly dependent on interfacial bond properties between fibre and matrix [29-31].

The bond refers to the medium through which shear forces are transmitted between the steel fibres and the surrounding cement matrix. A part of these forces is resisted by the cementitious matrix, whilst the remainder is resisted by the fibres [4]. The tensile strength of steel fibre-reinforced concrete (SFRC) can be quite variable, depending on the fibre-matrix interfacial bonding strength. Where the fibres have a weak bond with the matrix, the pull-out is likely to occur at low loads and thus, the fibre does not contribute much to resisting the propagation of cracks. Conversely, if the bond is too strong, fibre rupture may occur before it can contribute fully to the post-cracking strength. Therefore, an investigation of bond failure mechanisms is necessary for understanding the tensile behaviour of SFRC.

There are two main mechanisms through which bonds develop between the matrix and fibres, namely physiochemical bond (i.e. adhesion and friction) and mechanical bond (i.e. interlock) [5]. The former, is determined predominantly by the properties of the interfacial transition zone (ITZ) as well as the fibre surface properties [32]. This type of bond is the first mechanism to be activated in the pull-out process and mainly controls the pull-out resistance of straight fibres. For perfectly straight fibres, i.e. with no bend or pre-deformations, only the physicochemical bond exists. The second type of bond, mechanical interlock, is determined by the geometric deformation in the length of the fibre and the transversal tensile stress resistance of the concrete [9,33].

Research projects concerning the bond characteristics of deformed fibres have received more attention over the past few years due to the significant increase in their applications [34-37]. Currently, nearly all fibres available for reinforcement are mechanically pre-deformed [38]. Hooked end fibres are now more widely used in cementitious composites than any other type of steel fibre [13,37]. Thus, there is an urgent need to understand the main mechanisms governing the bond of pre-deformed fibres. This review is aimed at understanding this particular bond mechanism more thoroughly, thereby providing fundamental information for effective applications and further research development. Of particular of interest is the efficiency of these fibres showing variations in their physical and geometrical parameters.

2.2 Bond characteristics of SFRC

The success and effectiveness of any reinforced composite depends largely on the bond characteristics between the reinforcing bar or fibre and the matrix [39]. Similar to the normal reinforcing bar for concrete (RC), the behaviour of steel fibre reinforced concrete (SFRC) is dictated fundamentally by the interface conditions [40]. In fact, the transmission of stress from the matrix to the fibre and vice-versa is achieved through the interfacial bond. Another essential similarity between RC and SFRC is that their steel reinforcement makes up for weakness in concrete under tension. However, there is a substantial difference in the fact that reinforcing fibres, unlike a reinforcing bar, are not continuous. An additional major difference is that plastic hinge collapse is predominant in the case of RC, while the steel fibres are usually pulled-out before hinges can form [40].

The nature of bonding mechanisms in SFRC is multiple and complex [26]. This is mainly due to the presence and combined action of several bond components. It will be seen that these include physical and chemical adhesions between fibre and matrix, friction, fibre-to-fibre interlock and mechanical components within geometric deformations in hooked end, crimped and twisted fibres [41]. Consequently, for the past several years, investigations have been made to understand each one of these mechanisms. Successful attempts to improve bond-slip resistance through mechanical deformations of fibres have been reported in [13,35,38]. However, there have been only a few studies which investigate the effect of fibre hook geometry on the bond-slip characteristics of SFRC [12,42].

Interfacial bonding of SFRC between the fibres and cement matrix plays a different role after cracking takes place [40]. In the case of un-cracked composite, the stress is transmitted from the matrix to the longitudinal axis of the fibre primarily through the frictional bond at the interface. When cracking of the matrix occurs, the load is transmitted to the fibres bridging the crack. An efficient mechanical bond enables the stress to be transferred back into the uncracked parts of the matrix. This bond will also resist the pull-out of the fibres from the matrix. The bond quality is therefore one of the main factors influencing the mechanism and mode of failure of a composite.

2.3 Types of bond

Bond in SFRC can be characterized according to the type of stress transferred across the interface. If a direct tensile stress P/A_f is less than its ultimate value (A_f = section area of a high strength fibre), the bond will resist both shear and tension at the interface from the transfer of direct tensile stress in the fibre in the following ways.

2.3.1 Shear bond

Consider a hooked end fibre embedded in a concrete matrix subjected to an axial tensile load as shown in Figure 2.1a. The applied 'pull-out' force P is reacted by an interfacial elastic shear stress τ_e in Figure 2.1b .

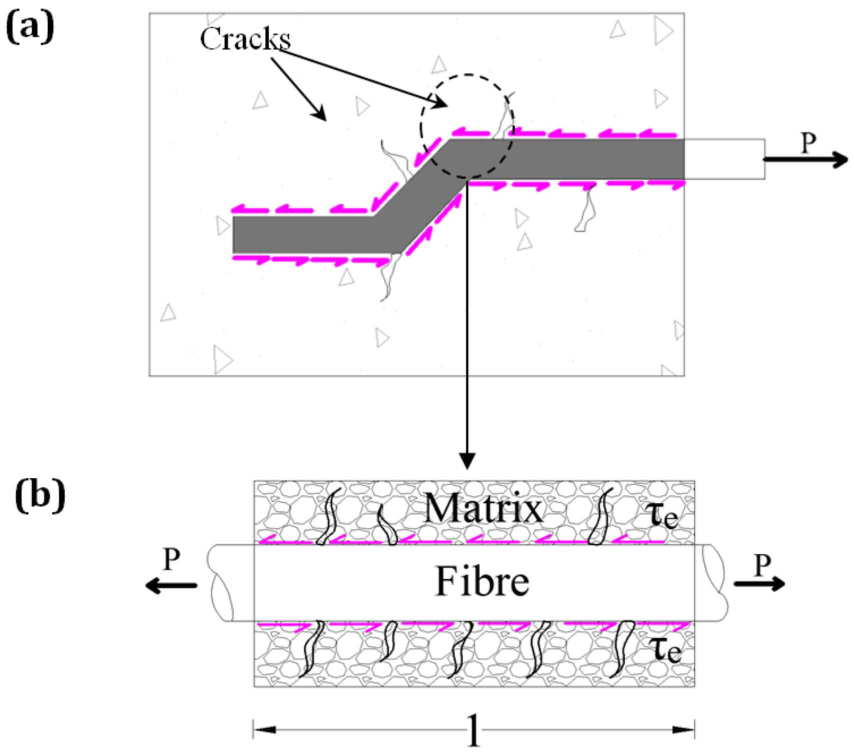

Figure 2.1 Interfacial shear under axial force

This shear stress τ may be referred to the outer surface area A for a length l of fibre as shown in Figure 2.2a.

$$\tau_e = \frac{P}{A} = \frac{P}{\psi \times l} \quad \left(\frac{N}{mm^2}\right) \tag{2.1}$$

where $\psi = \pi d$, is the circumference of a wire diameter d. A constant shear flow q is referred to a unit length of fibre (see Figure 2.2b).

$$q = \frac{P}{l} = \tau_e \times \psi \ \left(\frac{N}{mm}\right) \tag{2.2}$$

in which τ_e and ψ may vary with length, but maintain a constant q as their product, i.e. q appears as a tangential shear force per unit length of the fibre. When τ_e is exceeded the bond's ultimate shear strength τ_{ult} governs the safe and unsafe design conditions as explained in either Figures 2.2a or b for the full and unit lengths respectively.

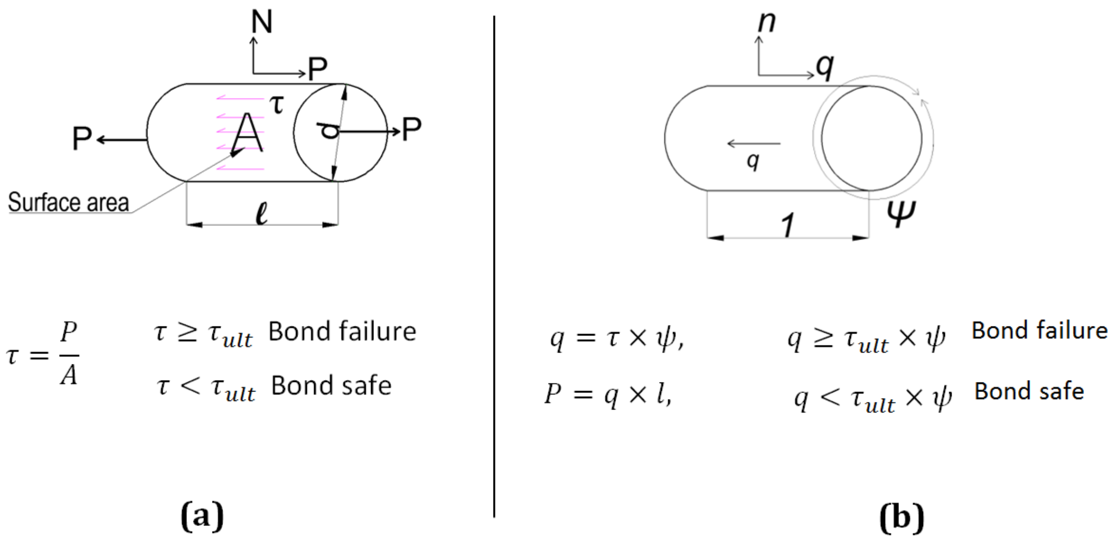

Figure 2.2 (a) Interface shear stress τ and (b) shear flow q

Elastic shear Bond:

The safe elastic bond exists when $\tau = \tau_e$ is less than the interfacial shear stress τ_f, which is required for frictional slip to occur, that is, $\tau_e < \tau_f$, or, in terms of the limiting shear flow for an elastic bond:

$$q_e < q_f = \frac{P_f}{l} \tag{2.3}$$

where P_f is a critical pull out force for a relative displacement, Δ_f, to occur at the interface between the wire fibre and the concrete matrix (see Figure 2.3).

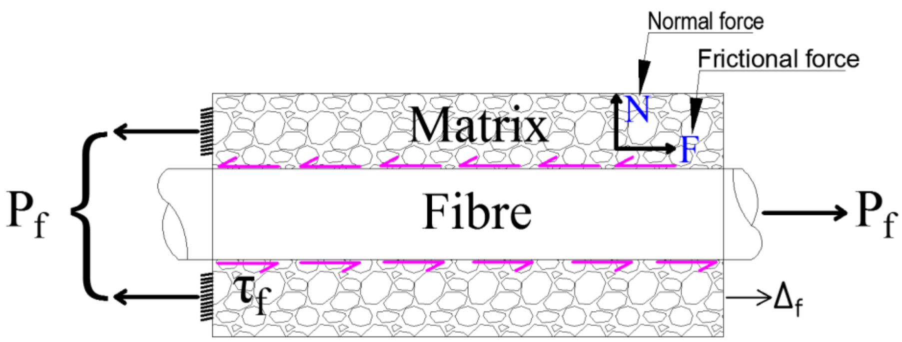

Figure 2.3 Interfacial slip with failure of shear bond

When, $\tau_e < \tau_f$, the elastic bond is characterised by the compatibility condition which prevails at the interface. That is, an equality prevails between the axial and circumferential strains in the wire and the concrete to ensure an absence of relative slip between them.

Frictional shear Bond:

Under the pull out force P_f , the limiting frictional bond shear stress τ_f is reached in which compatibility is violated allowing a relative slip to occur. The bond forces shown in Figure 2.3 remain in quasistatic equilibrium under P_f , as pull out proceeds with increasing frictional slip Δ_f. This involves a failure of the elastic shear bond but without further damage to the concrete matrix from not having attained its ultimate shear strength. That is:

$$\tau_e < \tau_f < \tau_{ult} \tag{2.4}$$

By definition the frictional coefficient μ is the ratio between the frictional force and a normal reaction upon the interface. Referred to a unit length in Figure 2.2b:

$$\mu = \frac{q}{n} \tag{2.5}$$

where, n is the normal force/unit length of fibre. Provided both q and n are uniformly spread along the length the coefficient μ is independent of the area in contact, Eq.(2.5) and Figure 2.2a show:

$$\mu = \frac{P}{N} < 1 \tag{2.6}$$

There are two values of μ: a static value $\mu_s \approx 0.5$ which prevails initially for an elastic bond and a kinematic value $\mu_d < \mu_s$ which applies to the frictional slip motion at the bond interface when $P = P_f$ in Eq.(2.6).

2.3.2 Tensile bond

An unbroken interfacial elastic bond constrains the lateral contraction of the fibre. A normal force N is induced such that the fibre pulls laterally upon the matrix along the interface as shown in Figure 2.4. Eq.(2.6) shows that $N > P$ and therefore N must be considered for the possibility of a tensile failure in each of the three modes shown in Figures 2.5a-c.

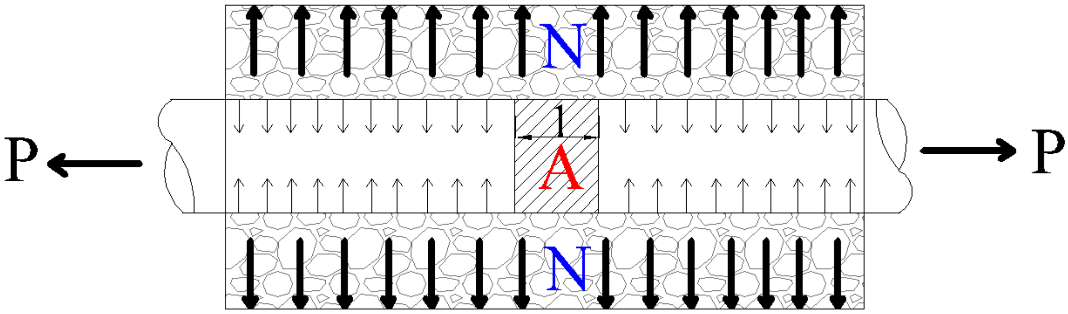

Figure 2.4 Normal reactional N under pull-out force P

Thus, in Figure 2.5a, N has separated the fibre from the matrix and with τ_f having been attained, this allows frictional slip to occur. Initially a normal reaction $N_s = \frac{P}{\mu_s}$ applies which drops to $N_d = \frac{P}{\mu_d}$ with continuous slip. In Figure 2.5b an interface tensile failure of the matrix is shown for a greater N value ($N > N_s$). The tensile stress at which this occurs is given as:

$$\sigma_t = \frac{N}{A} \qquad (2.7a)$$

where A is the peripheral contact area for a length l of fibre and σ_t equates to either the ultimate tensile strength of the concrete or the bond depending upon which is weaker. When Eq.(2.7) is referred to the unit length of fibre at the interface in Figure 2.4, then $N = nl$ giving:

$$\sigma_t = \frac{nl}{A} = \frac{n}{\psi} \qquad (2.7b)$$

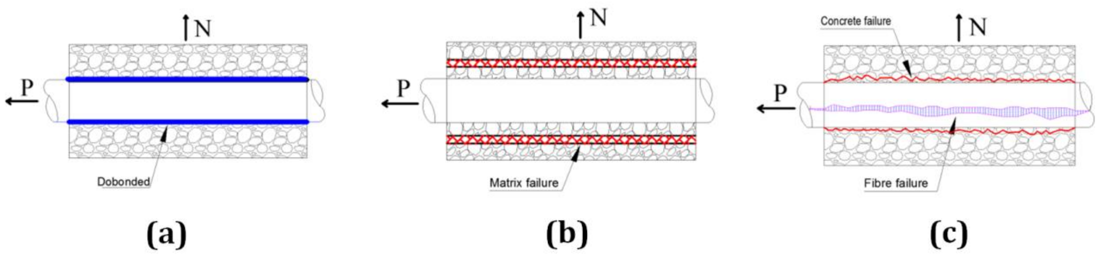

Figure 2.5 Tensile failure modes under normal force N

Figure 2.5c shows an unlikely tensile failure in which fibre splitting occurs. Here N must be sufficient to promote splitting where correspondingly, the transverse failure stress σ_f may refer to the full central axial section area $d \times l$ or to a unit length (Figure 2.6) equally as:

$$\sigma_f = \frac{N}{dl} = \frac{n}{d} \tag{2.8a}$$

in which σ_f must have attained the fibre's transverse UTS. Here, provided the bond remains secure, there is also a greater possibility of tensile failure within the adjacent matrix particularly for a section of narrow width w as shown in Figure 2.6.

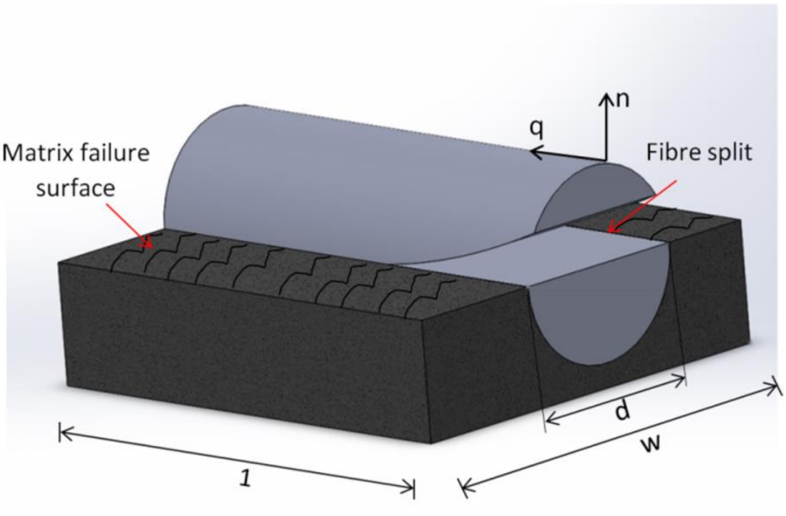

Figure 2.6 Fibre splitting/matrix failure under normal loading upon a unit length

In this case the UTS for concrete is attained when

$$\sigma_t = \frac{N}{(w-d)l} = \frac{n}{w-d} \tag{2.8b}$$

The relative magnitude of σ_f and σ_t in Eqs (2.8a) and (2.8b) will determine which failure mode between Figures 2.5 and 2.6 applies. Normally each failure mode may be discounted for a large matrix volume containing many fibres distributed with random orientations. However, a supporting column with restricted section area may be prone to a transverse tensile failure. Additionally, the tensile failure mode is important to be considered globally. Figure 2.7a shows a random array of fibres in which it is possible for a brittle tensile failure under P to follow a mainly perpendicular path between fibres. Here an arrangement of fibres lying parallel to P would be preferable to those aligned with N. It follows that a unidirectional reinforcement (Figure 2.7b) with fibres lying parallel to P is the best arrangement to offset tensile failure from P, but is ineffective in resisting tensile failure between fibres under N as shown. Because both P and N co-exist during pull-out, the random orientation is the proper choice where some internal fibres lie in their optimum orientations to resist N and P, i.e. orientations (i) and (ii), respectively as indicated in Figure 2.7a.

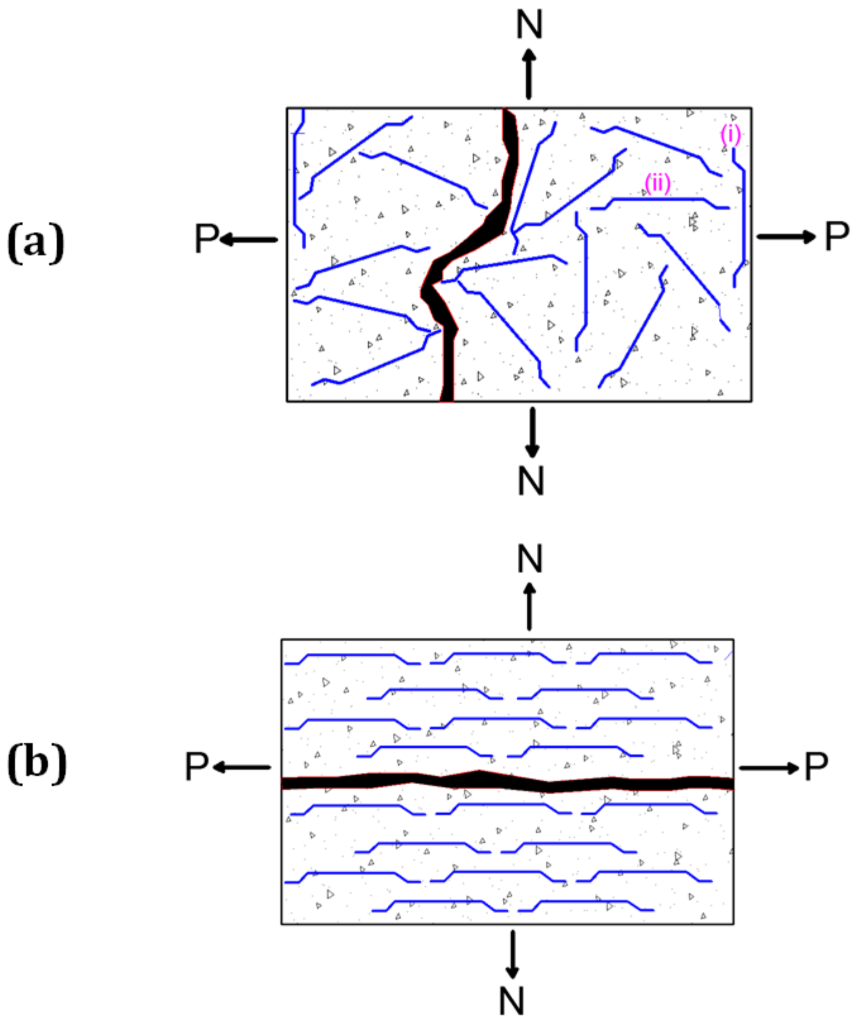

Figure 2.7 Fibre arrangements: (a) Random 3D fibre distribution with optimum orientations (i) and (ii), and (b) unidirectional distribution

2.4 Fibre/matrix interface

For all reinforced composites, the adhesive/chemical bond establishes a mutual interface between the reinforcement and the surrounding matrix [32,43]. For a fibre reinforced cementitious composite, the transmission of stress between fibre and surrounding matrix is achieved when the bond acts as an interfacial transition zone (ITZ) [44]. The efficiency of fibres in transferring the applied stress is strongly dependent upon the interfacial properties between fibre and matrix [45]. Thus, the strength of the bond within an ITZ plays a significant role in the tensile response of the composite [46,47].

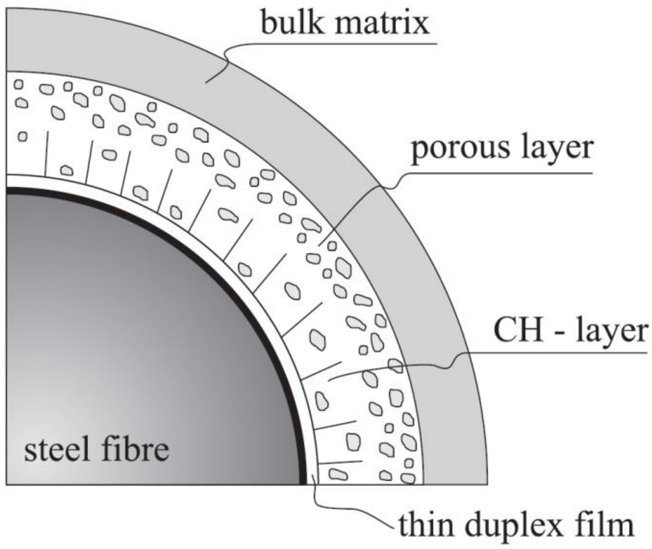

Figure 2.8 Transverse cross-section of the ITZ between fibre and matrix [32]

Owing to the porous nature of the ITZ in a cementitious composite, the transition zone between fibres and matrix is the weakest feature among the constituents governing composite properties [45]. The microstructure of the ITZ between fibre and matrix to a large extent is similar to that observed in the cement paste-aggregate bond, which are both characterized by high porosity and a large amount of calcium-hydroxide (CH) (Figure 2.8) [43]. CH contributes to a wall effect where local bleeding around fibres results in a less dense dispersion of particle packing around the fibre in the fresh state [32,45]. As a consequence of inefficient packing of cement particles, the empty spaces become partially filled with hydration products [43]. It is generally agreed that in a cementitious composite, with aggregate and fibre inclusion, the matrix in the vicinity of an inclusion can be different in its microstructure from the bulk cement matrix [44]. Hence, the matrix in the annular region around the fibre has higher porosity than the bulk cement paste matrix. Therefore, the stiffness and strength of ITZ are significantly lower than those of the bulk cement paste. It has been found from micro X-ray computed tomography (μXCT) images that there are over 12,300 pores with size ranging from 25 to 1400 μm, among which 97.7% are smaller than 600 μm[48]. The radial depth of the transition zone is generally determined through a microhardness test [44]. For steel fibres, the microhardness of the ITZ is much lower (around 30-50%) than the bulk cement matrix for a maximum depth of approximately 75 μm [49]. Based on SE Microscope observations, Bentur and Mindess [50,51] found that the width of the ITZ can range from 20-50 μm, while Li and Stang [52] estimated the width to be between 40-70 μm.

Among the various attempts made to increase the hardness of the transition zone, the most effective is densification of the ITZ [53,54]. This can be achieved through a decrease of water/binder ratio or by using micro-fillers (e.g. silica fume) [45]. The densification of the ITZ is an important parameter but is not completely effective in improving the interfacial bond strength. Here the contrast between the aggregate porosity and the absence of porosity in a steel fibre surface places a limit on the increase in the hardness of the ITZ [32].

2.5 Major factors affecting bond behaviour

The pull-out force versus slip behaviour of steel fibres depends upon a variety of parameters [55,56] including the following:

2.5.1 Fibre geometry

The many types of steel fibres used in cementitious composites are classified according to their shape into deformed and un-deformed fibres (Figure 2.9). The latter type (i.e. a straight fibre) is rarely used in practice and almost all commercially available fibres today have a mechanically pre-deformed geometry [38]. The primary reason for the addition of mechanical deformation to fibres is to introduce a mechanical anchorage i.e. contribution to bond within the cementitious matrix [57-59]. Deformation can be applied either at fibre ends, such as hooks, paddles, and buttons or along the fibre length, such as indented, crimped and polygonal twisted fibres (Figure 2.9). While the pull-out behaviour of straight steel fibres is predominantly controlled by the bond's frictional component, that of a deformed fibre is mainly dependent upon the mechanical anchorage component [9,60]. Due to variations in geometry, there is a significant variation in the mechanical anchorage contribution among different types of deformed fibres. These differences have a great influence on the pull-out force for a fibre and thus upon the tensile response of SFRC. To understand the influence of fibre geometry on the pull-out behaviour of deformed fibres extensive pull-out tests have been conducted [12,34,35]. Despite this, it appears that the bond mechanisms associated with the pull-out behaviour of deformed fibres are still not yet completely understood [42,61].

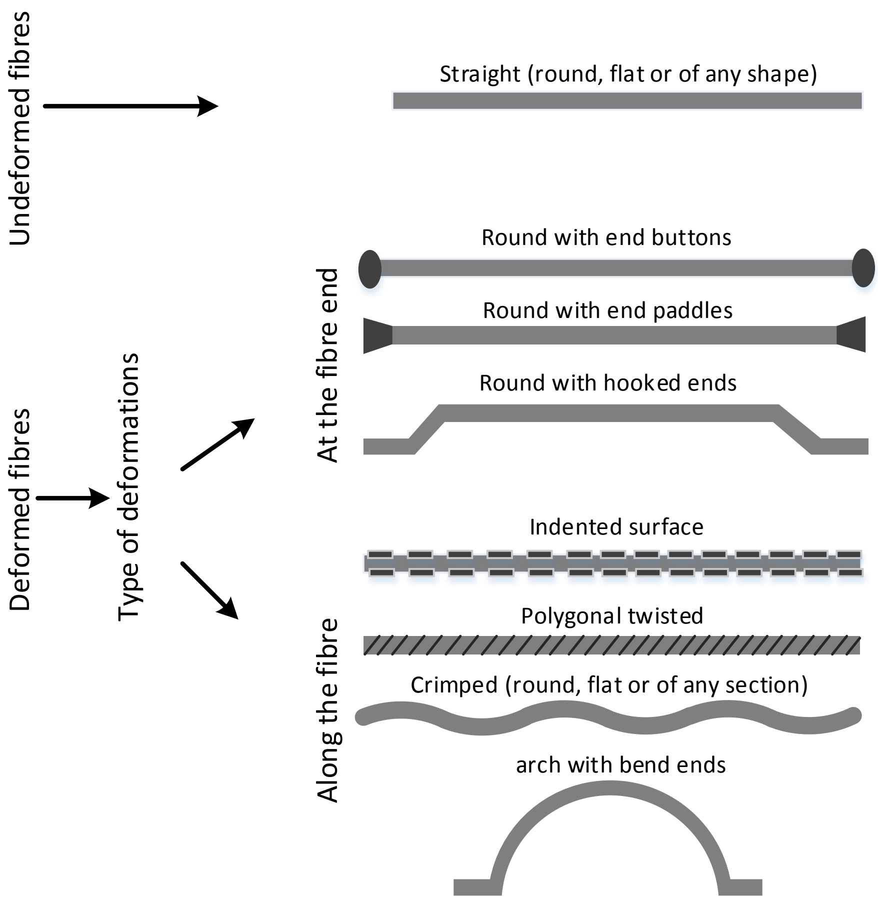

Figure 2.9 Different types of steel fibres categorized according to their geometric shape[33]

2.5.2 Fibre inclination

In fibre reinforced cementitious composites, the fibres are randomly distributed and oriented in different directions, and therefore, not all fibres would lie in the same directions as the applied loads [62-64]. In comparison to a simple tensile pull-out load for an aligned fibre, a complex stress state applies to a fibre inclined to the loading direction, as is the found in practice [38,65].

Bond mechanisms governing the pull-out force versus slip response of inclined fibres are different from those verified experimentally for aligned fibres [42]. In addition to a common de-bonding and friction along the fibre-matrix interface, the inclined fibre introduces fibre bending and local friction effects at the exit points [61]. Consequently, the pull-out resistance of some inclined fibres can be raised significantly. It has been shown by several researchers [43,57,61,66] that the pull-out strength of inclined fibres tend to be higher than aligned fibres for which an optimum inclination lies between 0° and 20° (Figure 2.10). However, for inclination angles greater than 30° fibre rupture and matrix spalling are very likely due to the bending effect and a concentration of frictional stress at the fibre's exit point. An additional related reason appears to be due to the strength differential i.e. when a low strength matrix is combined with a high tensile strength fibre or vice versa [42].

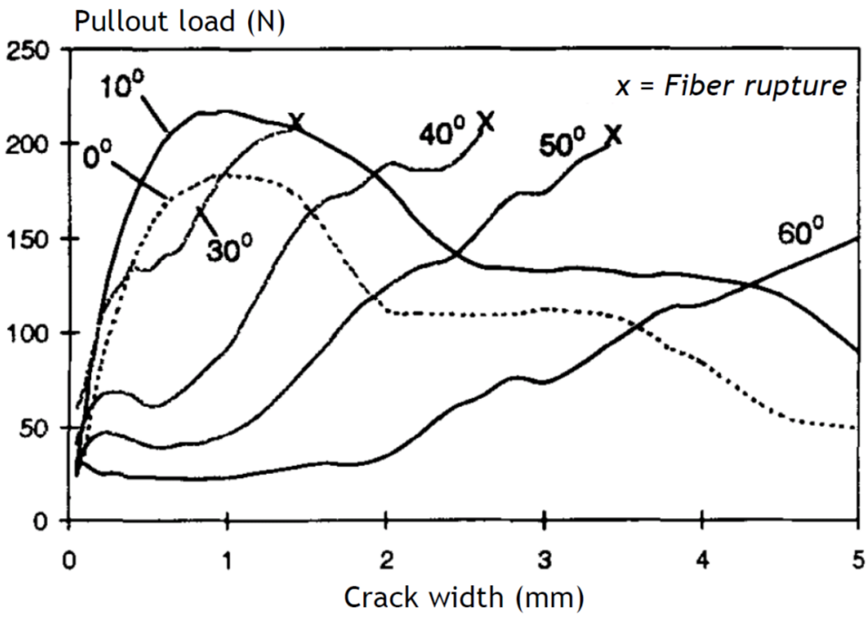

Figure 2.10 Pull-out behaviour of hooked end steel fibres at different inclination angles [42]

2.5.3 Fibre embedded length

It is generally accepted that the increase of embedded length may enhance the pull-out resistance [32]. While this assumption seems to be reasonable for straight fibres due to the fact that fibre with a larger embedded length leads to a larger area of the fibre in contact with the cementitious matrix, it usually does not apply for deformed (e.g. hooked end) fibres [43]. For similar hook end geometry, a higher pull-out load for a shorter embedded length can apply [43]. This behaviour is explained by the fact that the pull-out resistance, represented by the plastic deformation of the fibre hook is greater than that provided by a frictional bond along the embedded length. On the other hand, in the case of a test with an embedded length shorter than the hook length, full plastic deformation and straightening of the hook is unlikely. Therefore, the embedded length should be larger than the length of the hook to guarantee a test with full utilization of mechanical anchorage component [27].

2.5.4 Matrix strength

The mechanical properties of a matrix determined by the compression test play a major role on the pull-out response [11,67-69]. High tensile strength fibres combined with a matrix of low compressive strength, tend to be pulled out at relatively low loads [66]. Consequently, the mechanical anchorage may not fully develop and thus pull-out resistance is rather poor [70]. On the other hand, fibres with low tensile strength combined with a high strength matrix tend to rupture at the early stage of the pull-out [42]. It is important therefore to have a balanced combination of fibre and matrix strengths in order to guarantee the full mechanical anchorage contribution to pull-out resistance.

Several methods have been reported in the literature to improve the bond strength by improving the quality of the matrix. These include: i) reducing the water/cement ratio [55,67], ii) the addition of micro-fillers (e.g. silica fume, fly ash, metakaoline, and polymer additions) [45,54,71] and iii) using high strength cement and low-grade aggregates [32,43]. It has been observed by Van Gysel [72] that the maximum pull-out load can be increased by 30-40% when the water/ binder ratio (W/B) was reduced from 0.45 to 0.29. Robins et al [61] reported that an addition of silica fume (10% vol.) enhanced the maximum pull-out load and pull-out work up to 50%. With a further increase in dosage up to 30%, the pull-out work increased twofold. However, as the bond strength only increased by 14% an optimum content was found to be in the range of 20-30% [73]. They attributed the considerable increase in pull-out work to the high amount of cementitious material adhering to fibre surface, thus contributing to the frictional resistance during pull-out. Guererro and Naaman [74] found an addition of fly ash (20% vol.) led to an increase in the maximum pull-out load of hooked end fibre of approximately 50%. The addition of metakaoline (10% vol.) resulted in fibre rupture due to the full utilization of the tensile capacity of the fibre. Cunha [32] reported that the presence of coarse aggregate generally decreased the bond strength. This occurred because de-bonding and crack growth took place within the weakest 'link' in the fibre-matrix composite, where the coarse aggregate lay adjacent to the interfacial zone.

2.6 Experimental research on the bond characteristics of SFRC

Many experimental research investigations have been conducted on bond characteristics of SFRC during the past a few decades, for both deformed and un-deformed fibres [75]. Several test techniques have been proposed to measure, directly or indirectly, the shear strength of the interfacial bond between fibre and cementitious matrix [76]. One of the direct methods to characterize the interfacial properties between fibre and matrix is through the pull-out test. This is an ideal test to simulate the realistic case of crack bridging by fibres, from which a pull-out load versus slip relationship is obtained [33]. The results obtained from this relationship can be used to develop a bond stress versus slip relation which provides basic information on the interfacial bond properties and could be considered as a constitutive relation to evaluate the bond of SFRC [77]. In an indirect test, measurements of the mechanical properties of SFRC are commonly made to determine the bond strength, as with the microhardness test. Although, numerous experimental tests have been conducted, there is yet no standard method to investigate bond characteristics in SFRC [42]. Consequently, due to variations between the test methods, there is a remarkable variation between the corresponding data available in the literature.

Traditionally pull-out tests have been a popular approach to investigate the bond strength at the fibre-matrix interface [9,33,41]. These tests can be categorized either according to the method of applying the tensile force in single-sided and double-sided tests or by the number of fibres embedded varying from single to multiple, as shown in Table 2.1. This review of the literature indicates that one-sided pull-out tests have been performed mostly upon single-fibre due to the simplicity and configuration of this test [29,76]. It presents three main advantages in placating composite behaviour in service where: 1) the geometry and configuration of the test specimen are quite similar to those of single fibre pull-out from a crack opening, 2) the residual stresses induced in the specimen, owing to curing of the matrix are apply, and 3) interfacial bonding behaviour is represented. However, when deciding which test technique is the most appropriate to characterize the interfacial bond of SFRC, there are ten criteria to be considered (see Table 2.2).

Table 2.1 Experimental techniques of pull-out test setup

Specimen shape	Test configuration	Matrix	Fibre type	Criteria										Ref.
				1	2	3	4	5	6	7	8	9	10	
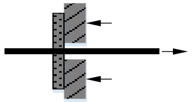	Single fibre-single sided	NSC	undeformed	P	P	N	N	Y	N	N	N	N	N	[78]
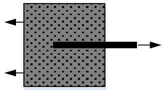		NSC, HSC,UHPC	deformed and undeformed	Y	P	Y	Y	Y	P	P	Y	Y	P	[12,32,66,67,70,79]
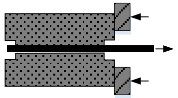		NSC	undeformed	Y	P	N	P	P	N	Y	N	N	P	[80]
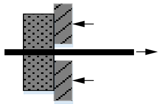		NSC	deformed	N	P	N	N	N	P	N	N	P	N	[81]
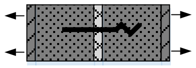		NSC,HSC	deformed and undeformed	Y	P	N	P	P	N	P	P	N	P	[61,82]
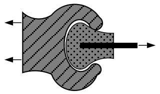		NSC, HSC, UHPC	deformed and undeformed	N	P	P	P	P	N	Y	N	P	P	[33,54,83,84]
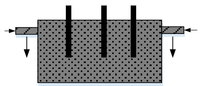		NSC,VHSC	deformed and undeformed	N	N	N	P	N	Y	Y	N	Y	Y	[11,85]
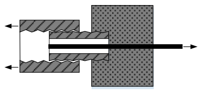		NSC	undeformed	P	P	N	Y	Y	Y	P	P	P	N	[86-88]
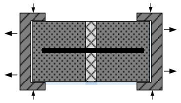	Single fibre-double sided	NSC	deformed	Y	Y	N	P	P	N	P	Y	N	Y	[89]

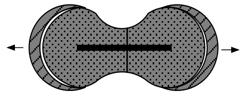		NSC, MSC	Straight steel fibre	N	P	N	N	N	N	P	N	P	N	[90]
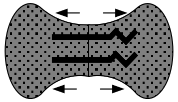	Multiple fibre-single sided	NSC, UHPC	deformed and undeformed	P	Y	P	P	N	N	N	N	N	N	[29,91,92]
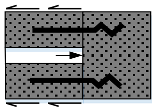		NSC	deformed	Y	P	N	N	N	N	N	N	N	N	[93]
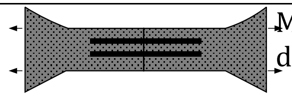	Multiple fibre-double sided	NSC	undeformed	P	P	P	N	Y	P	N	N	P	N	[85]
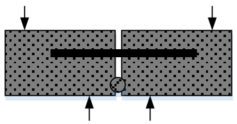		NSC, MSC	undeformed	Y	P	P	N	P	P	P	N	P	P	[94]

Y: Criteria is completely satisfied
P: Criteria is partially satisfied
N: Criteria is not satisfied

NSC: Normal strength concrete
MSC: Medium strength concrete
HSC: High strength concrete
UHPC: Ultra-high performance concrete

Table 2.2 Ten criteria for evaluation of pull out test technique [76,95,96]

	Criteria
1)	The specimen shape should replace an element of a real composite.
2)	The embedded length should be determined and measured accurately. The free end of the fibre should be very short.
3)	The specimens should be easy to manufacture because an appropriate statistical evaluation requires an enormous number of specimens in order to secure reliability of the results.
4)	The configuration of the specimens should facilitate the pull-out of fibre up to 90° orientation with respect to the direction applied load.
5)	Test configuration should allow a direct observation and investigation of the fibre-matrix interface.
6)	During the manufacture of specimens, the fibres should be aligned accurately and secured by the matrix.
7)	The specimen should be manufactured to handle with a minimum danger of damage.
8)	The specimens should be manufactured to cure in large numbers under different conditions.
9)	The specimens should be manufactured to allow the application of secondary loads to the matrix (e.g. radial and axial compression).
10	The specimen shape should be designed to minimise the concentration of the stress and shrinkage of the matrix.

2.7 Pull-out behaviour of steel fibres

2.7.1 Straight fibre

It is known that the pull-out behaviour of straight fibre involves a combination of two different mechanisms: de-bonding and frictional pull-out [97]. Here, the de-bonding arising from cracking within and along the ITZ is followed by fibre pull-out under frictional resistance only (Figure 2.11i)[32].

The pull-out response of straight fibres is characterized by a rapid increase in pull-out load (a-b) followed an equally rapid drop at (b), indicating that the fibre de-bonds suddenly from the concrete [33] (Figure 2.11iii). Experimental observations on steel fibres with embedded lengths of 30 mm and 0.70 mm diameter show that these lengths are fully de-bonded for fibre slip up to 0.08 mm [72]. Thereafter, the pull-out load from (b-c) continues to fall with increasing slip. Hence, the straight fibres bond is made up only of chemical adhesion and friction with no mechanical interlock. So, once these mechanisms are overcome, the fibre slips with the low pull-out force necessary to overcome kinetic friction (Figure 2.11iii).

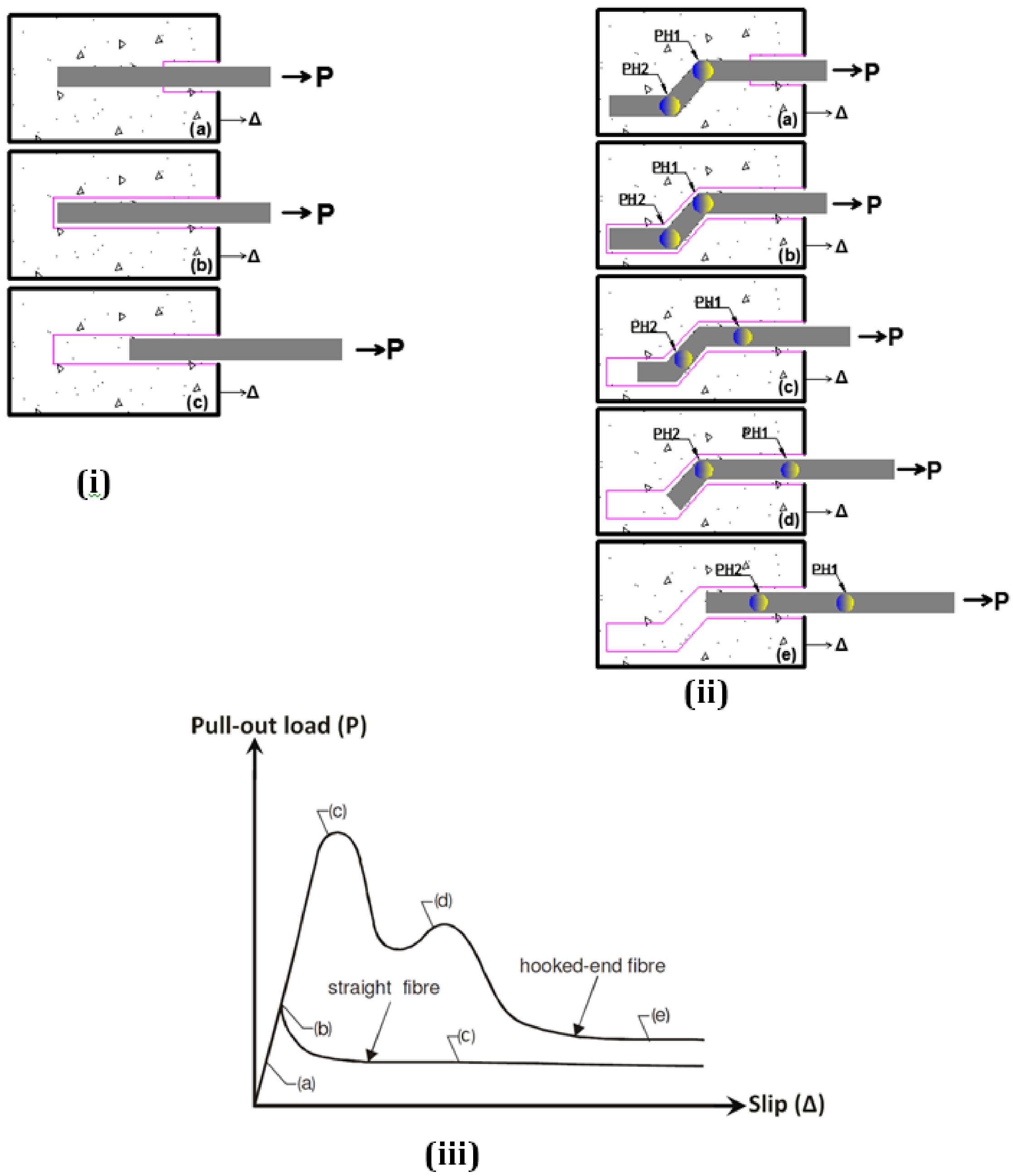

Figure 2.11 Pull-out behaviour: (i) straight fibre (a-c), (ii) hooked end fibre (a-e) and (iii) typical pull-out -slip response of straight and hooked end fibres [43].

2.7.2 Hooked end fibre

Initial mechanisms governing the pull-out behaviour of hooked end fibres are similar to those measured for straight fibres (i.e. de-bonding, followed by frictional pull-out) [43]. In addition to de-bonding and friction along the interface, mechanical anchorage is introduced by the plastic deformation of the fibre hooks [98]. In contrast to a straight fibre, the mechanical anchorage contribution provided by a hooked fibre increases the pull-out load after de-bonding significantly.

The pull-out process of hooked-end fibre can be divided into five different stages (Figure 2.11ii). These include the first two phases of the straight fibre pull-out i.e. partial and full de-bonding stages (a) and (b) in Figure 2.11ii. Here, however, the frictional pull-out (stage e) is preceded by mechanical interlocking stages c and d. To release (c) and (d) both curvatures must straighten within plastic hinges (PH1 and PH2). Thus the fibre hook must undergo considerable plastic deformation, resulting in a substantial increase and maximum pull-out load at c (Figure 2.11iii). It has been reported that the larger is the fibre diameter, the more energy is involved in unlocking, due to the increased bending stiffness of the fibre [42]. Other related factors, such as the initial interfacial bond properties, matrix strength, and the hook geometry influence contribute to the total energy needed to deform the hook [32].

Beyond its maximum, the pull-out load starts to decrease due to the progressive mobilization and entrance of PH1 into the straight part of the channel. When PH1 has straightened, the wire moves into the straight part of the channel. Then moving and straightening of PH2 results in a slight increase in pull-out load (stage d). Once both PH1 and PH2 are completely deformed and straightened, the pull-out load need only overcome kinetic frictional resistance as for a straight fibre (stage e). This phase prevails until the whole fibre is completely removed from the matrix.

Despite the fact that no further plastic deformation of the fibre hook can occur, a residual load increase at the last stage of the pull-out has been observed. This behaviour is most likely due to an elastic springback resistance from the free length of fibre upon the matrix whole boundary. It arises from a partial strengthened hook whose slip has been assisted by matrix crushing [32,70].

2.8 Analytical models of the bond between fibre and matrix

In the last four decades, numerous analytical models have been developed to investigate the bond mechanism between fibre and cementitious matrix. The first strength-based analytical model to clarify the transmission of the tensile stress between fibre and matrix was advanced by Cox [99]. In this model, it was assumed that the tensile and shear stresses in the matrix are negligible compared to those in the fibre. Furthermore, the shear stress in the fibre is small compared to that in the matrix. Based on the Cox model assumptions, Greszczuk [100] proposed an interfacial de-bonding criterion from the shear-lag theory. Later [100] he postulated that at the instant when the shear strength of the interface is first attained, catastrophic de-bonding would occur over the entire length of the embedded fibre. In reality, however, with irregularities in geometry and bond quality, de-bonding is limited to the zone in which the elastic shear stress exceeds the adhesional shear bond strength. Here the process of load transfer involves the frictional shear transfer at the de-bonded zone and elastic shear transfer over the remaining length of the fibre. The limitation of Greszczuk's model is that it does not account for a frictional bond. Moreover, this solution does not consider the stabilization of the de-bonding process when there remains a kinetic frictional shear bond along the de-bonded interface. Lawrence [101] extended Greszczuk's theory by considering a progressive de-bonding of the fibre-matrix interface. This model includes the influence of both the interfacial elastic and frictional shear stresses to recognize the conditions for either a gradual, or an instantaneous de-bonding of the interface. The frictional shear stresses were assumed to remain constant along the de-bonded zone.

In later work Gopalratnam and Shah [102], Gopalaratnam and Cheng [103], Nammur et al. [104], Stang et al. [105] proposed models based on the Lawrence [101] model to simulate the fibre pull-out mechanisms. These models showed how both the elastic and frictional shear stress, which develop parallel to the fibre-matrix interface control the fibre to matrix stress transfer. In addition, Figure 2.4 shows how stress and strain will develop normal to the fibre-matrix interface as a consequence of a constrained Poisson's lateral strain, multiaxial loading and volume change. Each will influence the resistance of frictional slip, which is sensitive to normal stress. Therefore, a comprehensive approach to the stress-transfer problem is required to consider all aforementioned effects, including de-bonding, elastic shear transfer, frictional slip and the Poisson's effect. To overcome such limitations, Takaku and Arridge [106] and Hsueh [107-109] proposed a more conceptual approach than the previous models, which take into account the effect of fibre contraction on the pull-out load. However, their approach is somewhat limited since this aspect was considered after interfacial de-bonding was completed i.e. the instantaneous recovery of the constrained contraction during progressive de-bonding was ignored, which proved to be a major limitation of most earlier models. Recovery of Poisson's contraction was considered by [107] throughout progressive de-bonding. This analysis did not provide a closed form solution but is adaptable to a numerical iteration.

Nammur and Naaman [40] developed an analytical model of bond interface shear between steel fibre and cementitious matrix based on the bond stress-slip relationship. Although this model is able to predict the distribution of the shear and normal tensile stresses along the fibre-matrix interface, its applicability is limited because it only deals with the bond stress at the interface. The pull-out behaviour was not taken into account. Subsequently, an analytical solution based on the relationship between the bond behaviour and the shear stress-slip curves at the interface was advanced by Naaman et al. [41]. This model also adopted the frictional stress values of the post de-bonding stage from experimental results instead of the constant value assumed by Nammur and Naaman [40]. On the other hand, the pull-out model introduced by Nammur et al. [104] assumes a cohesive interface. The latter takes the relative displacement between the fibre and the matrix to activate the transmission of stress at the interface. In addition, in this model the interfacial traction is described as a function of the displacement discontinuity. Hence, it is not required to distinguish between the bonded and de-bonded interfaces. This implies that slip resistance due to chemical adhesion is negligible. An additional limitation of this approach is the constant value of interfacial shear stress assumed at the de-bonded face. When the bond stress versus slip function is applied to a cylindrical coaxial fibre-matrix, pull-out relationships are provided for interfacial shear and axial stress distributions and fibre displacement at the various stages of pull-out [104] (Figure 2.11 ii). Naaman et al. [41,110] modified this theory assuming that the radial misfit between fibre and matrix decreases as fibre is pulled from the matrix. Here it was shown that during pull-out the interfacial frictional shear stress at the de-bonded interface decreased with radial misfit.

Despite the contributions provided by the aforementioned models, most of the earlier bond-slip investigations apply to straight fibres. There is further information on the bond behaviour of deformed fibres in the literature of the last decade. Analytical models account for the effect of pre-deformed steel fibre geometry on the bond behaviour [72,98,111,112]. Alwan et al. [98] employed the frictional pulley principle to predict the pull-out response of hooked-end fibres. The mechanical bond provided by the hook is considered a function of the work needed to straighten the fibre during pull-out. An alternative approach was proposed by Chanvillard [111] who, using the principle of virtual work, divided the hook into distinct curved and straight parts. This division accounts for fibre de-bonding, plastic deformation and additional frictional forces during pull-out using a numerical integration procedure to predict the pull-out load versus slip curve. Van Gysel [72] also proposed a semi-analytical model based upon a similar concept of virtual work and requiring experimental data for predicting the pull-out behaviour of hooked-end fibres. That data considers the influence of parameters such as fibre orientation, embedded length and matrix compressive strength. Sujivorakul [112] extended the straight fibre pull-out model developed by Naaman et al. [41] by adding a non-linear spring to the end of the fibre to simulate the mechanical anchorage contribution.

In recent work Laranjeira [42] and Ghoddousi et al. [113] proposed alternatives to the pulley model of Alwan et al. [98]. Zile et al. [12] developed an analytical model to simulate the mechanical contribution from fibre geometry to the pull-out response of crimped and hooked-end steel fibres. Their model is based both on the amount of plastic work required to straighten the fibre during pull-out and frictional resistance in the curved ducts. Won et al. [14] extended this to the work required in straightening arch-type steel fibres.

2.8.1 Straight fibre

Numerous proposals have been reported in the literature to understand the bond mechanisms associated with pull-out behaviour of straight fibres. Of these that proposed by Naaman et al. [114] has been adopted by several researchers to predict the pull-out response of straight fibres based on the interfacial bond stress-slip relationship (Figure 2.12).

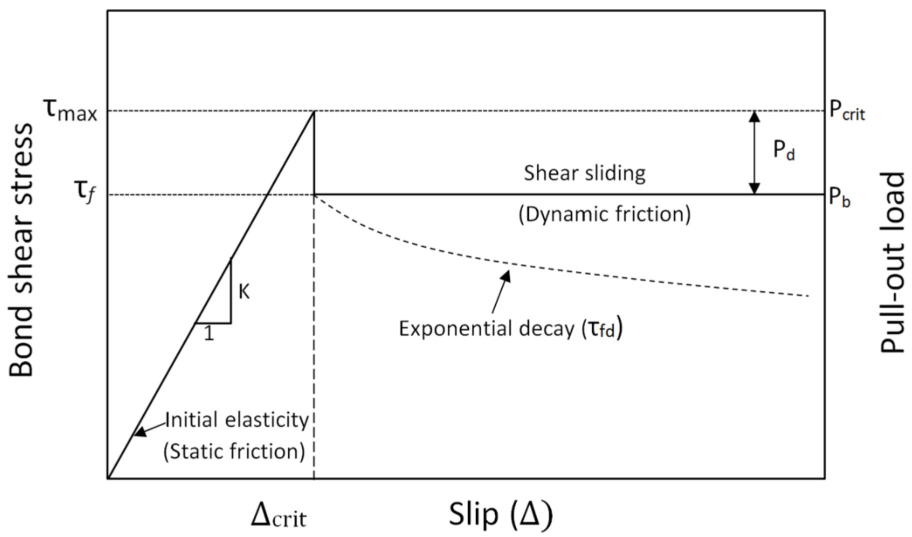

Figure 2.12 Assumed bond shear stress versus slip relationship[114]

This relationship is assumed to be linear elastic to the point where the bond strength τ_{max} of the interface is reached. Here the bond fails and for further slip a kinetic frictional condition prevails under a constant frictional shear stress τ_f. Equilibrium of a wire element (Figure 2.13) shows:

$$(F + dF) - F = \tau \times 2\pi r \times dx$$

$$\therefore \ \frac{dF}{dx} = \tau\psi \tag{2.9}$$

where, F is the local axial force in the fibre, τ is the local bond shear stress at the fibre-matrix interface, and $\psi = 2\pi r$ is the perimeter of the fibre section.

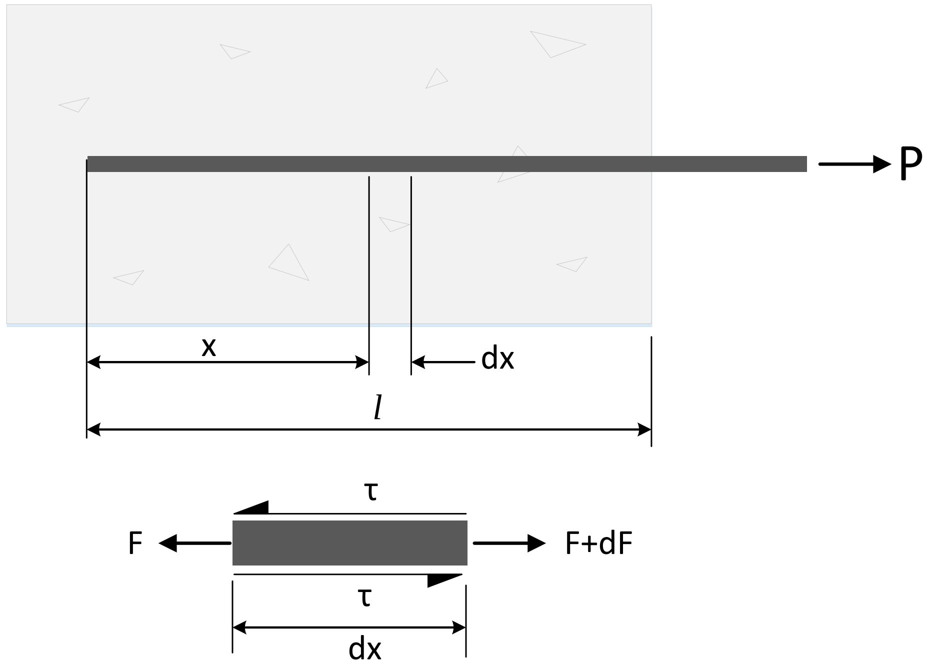

Figure 2.13 Free-body diagram of infinitesimal segment of fibre [114]

The bond shear stress-slip relationship in the elastic region can be expressed as:

$$\tau = k\Delta \tag{2.10}$$

where, k is assumed to be constant (Figure 2.12) and the local slip Δ is defined as follows:

$$\Delta = \delta_f - \delta_m = \int_0^x [\varepsilon_f(x) - \varepsilon_m(x)]dx \tag{2.11}$$

where, δ_f and δ_m are the local displacements in the fibre and the matrix, respectively, and ε_f and ε_m are their corresponding axial strains.

Applying Eqs (2.9)- (2.11) to a static equilibrium condition at section x, the local axial force F in the fibre and the corresponding interfacial shear stress can be obtained as:

$$F(x) = \left(Ae^{\lambda x} + Be^{-\lambda x} + \frac{1}{Q}\right) \tag{2.12}$$

$$\tau(x) = \frac{dF}{dx}\frac{1}{\psi} = \frac{P\lambda}{\psi}\left(Ae^{\lambda x} + Be^{-\lambda x}\right) \qquad (2.13)$$

where, $\psi = \pi d_f$, $\lambda = \sqrt{KQ}$, $K = \frac{\psi k}{A_m E_m}$ and $Q = 1 + \frac{A_m E_m}{A_f E_f}$ in which A_m and A_f are the section areas of matrix and fibre, E_m and E_f are their corresponding elastic moduli.

The constants A and B can be determined using the two boundary conditions, $F(0) = 0$ and $F(l) = P$.

The critical load P_{crit} represents the load when the interfacial shear stress at $x = l$ reaches its maximum value, τ_{max}.

$$P_{crit} = \frac{\pi d_f \tau_{max}}{\lambda}\left[\frac{1 - e^{-2\lambda l}}{\left(1 - \frac{1}{Q}\right)\left(1 + e^{-2\lambda l}\right) + \left(\frac{1}{Q}\right)2e^{-\lambda l}}\right] \qquad (2.14)$$

The entire pull-out-slip response of a straight fibre may be divided into three different stages relative to P_{crit}:

1) Elastic stage

When $P \leq P_{crit}$, the fibre is assumed to be perfectly bonded to the matrix. Here, the pull-out load-slip relationship is linear and can be expressed as follows [114]:

$$\left(\frac{P}{\Delta}\right) = \left(\frac{\lambda A_m E_m}{Q - 2}\right)\left(\frac{1 + e^{-\lambda l}}{1 - e^{-\lambda l}}\right) \qquad (2.15)$$

2) Partial de-bonding stage

When $P > P_{crit}$, a part of the fibre is still fully bonded to the matrix while the remaining part is de-bonded. In this case, the pull-out load (P) is equal to the sum of two conditions P_b and P_d , respectively:

$$P = P_b + P_d \qquad (2.16)$$

The pull-out load P_b for a bonded length u is determined from Eq. 2.15 under a constant frictional stress τ_f. For the de-bonded length $l - u$, P_d replaces l in (Eq. 2.14). Thus, the pull-out load and the corresponding slip for this stage follow from Eq. 2.16:

$$P = \tau_f \psi u + \frac{\tau_{max}}{\lambda} \frac{1 - e^{-2\lambda(l-u)}}{\frac{2}{Q} e^{-\lambda(l-u)} + (1 - \frac{1}{Q})(1 + e^{-2\lambda(l-u)}} \tag{2.17}$$

$$\Delta = \frac{\left[P(Q-1)u - \frac{\tau_f \psi u^2}{2}(Q-2) + \left(P - \tau_f \psi u\right) \frac{1 - e^{-\lambda(l-u)}}{1 + e^{-\lambda(l-u)}} \frac{Q-2}{\lambda} - \tau_f \psi l\right]}{A_m E_m} \tag{2.18}$$

3) Fully de-bonded and frictional pull-out stage

When the fibre has completely de-bonded from the matrix and the relative displacement due to the elastic elongation of the fibre is neglected, the pull-out load versus slip relationship becomes:

$$P_1 = \psi \tau_{fd}(\Delta) \times (l - \Delta) \tag{2.19}$$

where, (l-Δ) is the embedded length of fibre remaining , $\tau_{fd}(\Delta)$ is a dynamic frictional shear stress where assumes a constant when slip (Δ) is small. For large slips, it has been shown [110] from experiment that the deterioration of τ_f when slip increases, leads to $\tau_{fd}(\Delta)$ as follows:

$$\tau_{fd}(\Delta) = \tau_{fi} \frac{e^{-(\Delta-\Delta_0)^\eta} - \xi e^{-(l)^\eta}}{1 - \xi e^{-(l-\Delta+\Delta_0)^\eta}} \times \frac{1 - EXP\left[\frac{-2v_f \mu (l - \Delta + \Delta_0)}{E_f r_f \left(\frac{1+v_m}{E_m}\right) + \left(\frac{1-v_f}{E_f}\right)}\right]}{1 - EXP\left[\frac{-2v_f \mu l}{E_f r_f \left(\frac{1+v_m}{E_m}\right) + \left(\frac{1-v_f}{E_f}\right)}\right]} \tag{2.20}$$

where, Δ is the relative slip of the fibre; Δ_0 is the relative slip of the fibre at end of full de-bonding, taken to approximate equal the slip at maximum load; μ is the friction coefficient of the fibre-matrix interface; ν is Poisson's ratio, with subscript "*f*" for fibre and "*m*" for matrix; the damage coefficient ξ describes decay observed in the bond shear stress-slip curve and the exponent η= 0.2 applies to an exponential decay for straight steel fibre.

2.8.2 Hooked end fibre

The short fibre reinforcement of concrete has certain advantages over the traditional method of continuous tensile rods. A random orientation of strong steel hooked fibres has the desirable property of withstanding tension applied in any direction. Single, double and triple bend hooked ends increase the capacity of a concrete structure to bear complex loading including tension, compression and shear. The higher performance need is matched to a multi-bend hook in a refined matrix. The two-bend hook and a traditional concrete mix are safe in many applications including minimum weight design, where the hooked fibre can be expected to bridge tensile cracking in the matrix until the fibre force attains its pull-out limit. The later would be chosen from the hook geometry and matrix quality in the various combinations available. The greatest pull-out force deems that a bend pull attains 100% plasticity across the fibre diameter when both the steel and the concrete are at their strongest. Lesser pull-out forces spread less plasticity in low-medium strength combinations where slip is facilitated by crushing failure at the fibre/matrix interface [15]. The pull-out force theory has adopted two alternative approaches. The first uses the equations of static force and moment equilibrium [15,98] in a friction pulley analogue and the second adopts the principle of virtual work[111]. These admit both static and dynamic friction respectively: (i) for initial elastic loading and (ii) for slip beyond the elastic limit (Figure 2.12).

2.8.2.1. Friction pulley model

The first successful attempt to model the pull-out behaviour of hooked end fibre was advanced by Alwan et al. [98] to predict the mechanical anchorage contribution provided by the fibre hook. Their model is based upon a frictional pulley bend where an unbending of plastic hinges provides the cold work of straightening during pull-out. This model adopts contribution from unbending two plastic hinges with frictional slip to predict the entire pull-out load versus slip curve. The latter is quite similar to that of a straight fibre up to the load P_1 where the complete de-bonding occurs (Figure 2.14). The corresponding slip (Δ_1) for this initial stage assumes an elastic response [114]. Thereafter, hook interlocking is triggered (Figure 2.14).

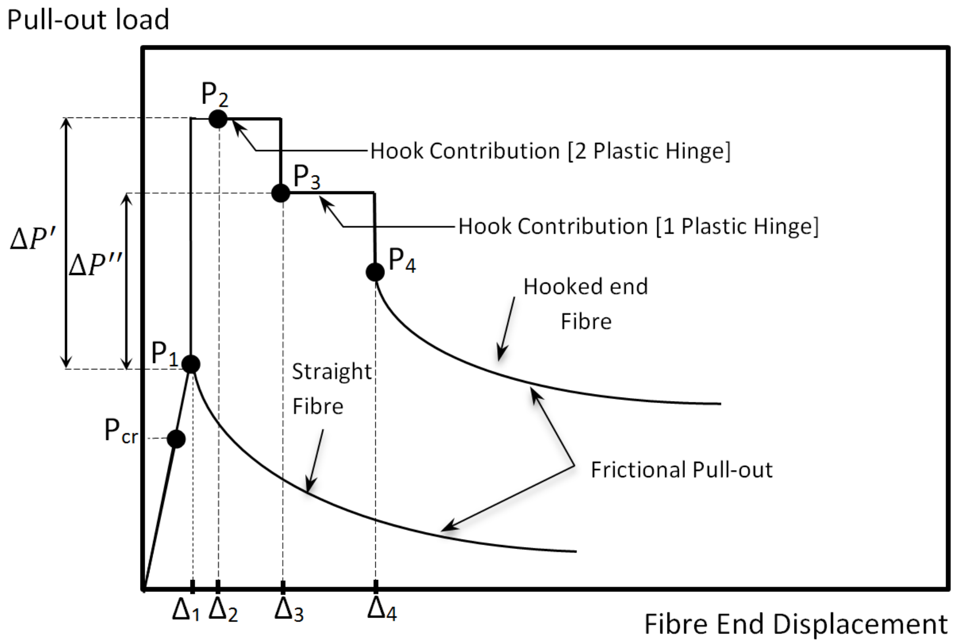

Figure 2.14 Schematic sketch of the theoretical pull-out curve of a hooked steel fibre from a cementitious matrix [98]

Once interface de-bonding is completed, the horizontal portion of the fibre must overcome kinetic friction as the hooked end of the fibre undergoes reverse bending (Figure 2.15b). The resulting increase in the pull-out load value *ΔP′*, due to the cold work from both plastic hinges (PH1 and PH2), is then added to P_1, resulting in a load plateau under (P_2). This load remains until the fibre is pulled by an additional distance L_2= (Δ_2 - Δ_1). Thereafter the load drops to P_3 with only one plastic hinge (PH2) active (Figure 2.15c). Load P_3 remains constant as the fibre is pulled-out by an additional distance L_1= (Δ_4 - Δ_3) (Figure 2.15d). After this the pull-out load-slip curve can then be described using the frictional pull-out model of straight fibre [114] as explained in the previous section.

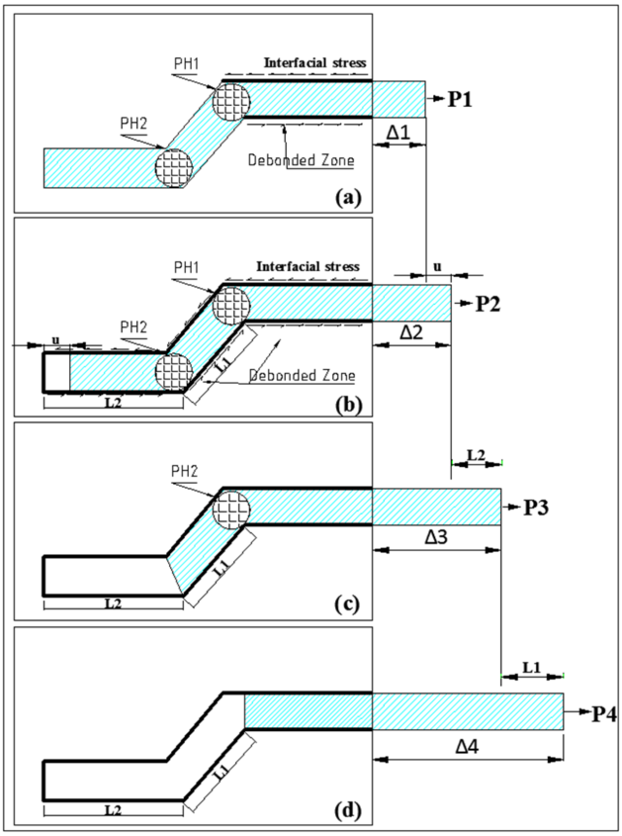

Figure 2.15 Hooked-end steel fibre at onset of complete debonding (a), mechanical interlock with two plastic hinges (b), mechanical interlock with one plastic hinge (c), and frictional pull-out (d) [98]

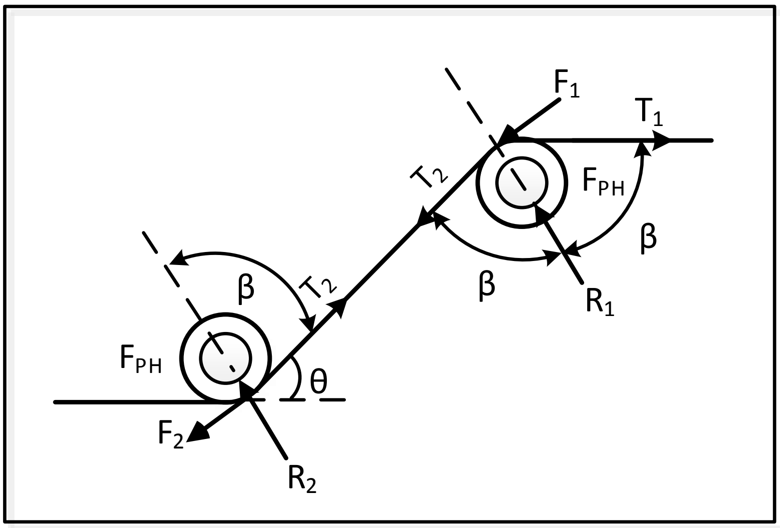

Figure 2.16 Line sketch of the frictional pulley model of 3DH fibres [98]

The first plateau load at P_2 (Figure 2.14) is due to the contribution $\Delta P'$ from two plastic hinges:

$$P_2 = P_1 + \Delta P' \tag{2.21}$$

where P_1 is the initial de-bonding load. Similarly, the second pull-out load plateau at P_3 (Figure 2.14) is given as:

$$P_3 = P_1 + \Delta P'' \tag{2.22}$$

where, $\Delta P''$ is the pull-out load due to unbend one remaining plastic hinge.

In order to determine the values of $\Delta P'$ and $\Delta P''$, Alwan et al. [98] developed an equivalent pulley model (Figure 2.16). The model consists of two frictional pulleys having rotational and tangential components of friction resisting pull-out. The rotational friction component corresponds to the cold work needed to straighten the steel fibre at the plastic hinge location represented by F_{PH} in Figure 2.16. The tangential friction components F_1 and F_2 represent the work of Coulomb friction between fibre and matrix at the contact corner during straightening. T_1 and T_2 are fibre tensions before and after the first pulley respectively that equate to the anchorage forces $\Delta P'$ and $\Delta P''$ as follows [98].

$$\Delta P' = T_1 = \frac{\left(\dfrac{\sigma_y \times \pi r_f^2}{3 \times cos\theta}\right)\left[1 + \dfrac{\mu \times cos\beta}{1 - \mu \times cos\beta}\right]}{[1 - \mu \times cos\beta]} \tag{2.23}$$

and that,

$$\Delta P'' = T_2 = \frac{\left(\dfrac{\sigma_y \times \pi r_f^2}{6 \times cos\theta}\right)}{[1 - \mu \times cos\beta]} \tag{2.24}$$

Having obtaining the pull-out load at three stages enables a continuous pull-out-slip curve from a suitable polynomial fit, the simplest being a quadratic polynomial for the three loads (P_1, P_2 and P_3) as shown in Figure 2.17 [15] .

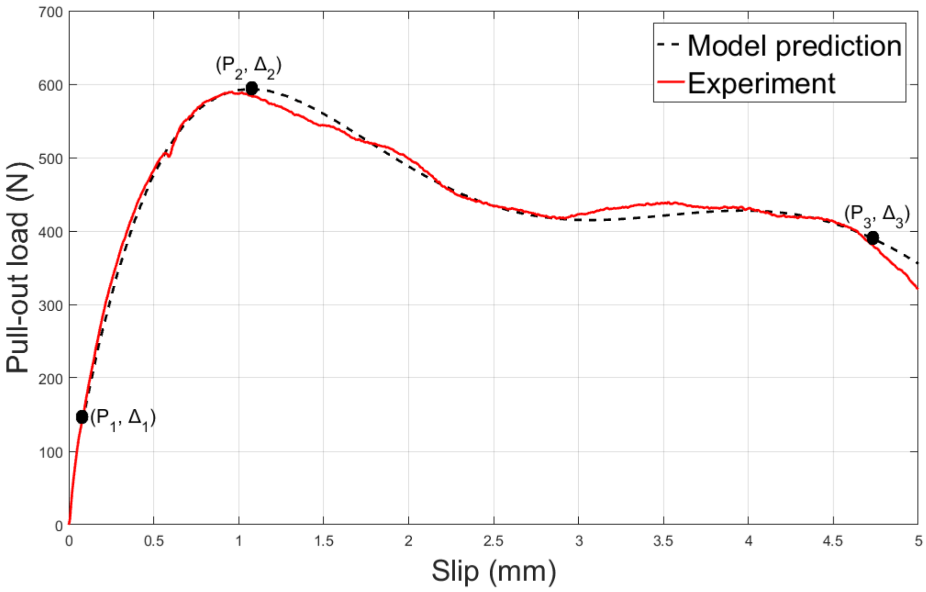

Figure 2.17 Comparison between predicted and experimental pull-out curves [15]

2.8.2.2 Virtual work

The virtual work (vw) principle may be applied to each release of the anchorage provided by the hooked end fibre. Thus, the peak plateau loads P_2 and P_3 (Figure 2.14) remain in quasistatic equilibrium while the respective slips Δ_2 to Δ_3 and Δ_3 to Δ_4 occur. The vw principle states that the corresponding work measures are virtually given that each slip occurs under its respective system of equilibrium forces. Hence the slip under P_2 and P_3 may be disconnected from the force and moment balance that lies within each of the pull-out stages given in Figures 2.15b and c. When the bend angles θ_1 and θ_2 differ, in the manner of Figures 2.18a,b, virtual work provides:

$$F_2 u_2^v + F_1 u_1^v = M_1 \theta_1^v + M_2 \theta_2^v \,; \quad u_1^v = u_2^v = \Delta_2 - \Delta_1 \qquad (2.25)$$

$$F_3 u_3^v = M_3 \theta_2^v \,; \quad u_3^v = \Delta_3 - \Delta_2 \qquad (2.26)$$

Where u^v and θ^v are the 'virtual' displacement and rotation due to slip, F and M are the 'real' internal pull-out force and plastic hinge moment that remain in equilibrium during slip Δ. Because u^v and θ^v may take any value in the range of slip/rotation within each stage it is expected that they should cancel within Eqs.(2.25) and (2. 26) enabling F_2 and F_3 to be written in terms of M_1 and M_2 and

M_3. Hinge moments $M_1$and M_2 are elastic-plastic corresponding to rotations θ_1^v and θ_2^v , from and into the vertical plane, equal to the bend angle (Figure 2.18a). Thus $M_1$and M_2 are equal but M_3 is a reversal of M_2 (Figure 2.18b) and may not be the same due to the Bauschinger effect [12].

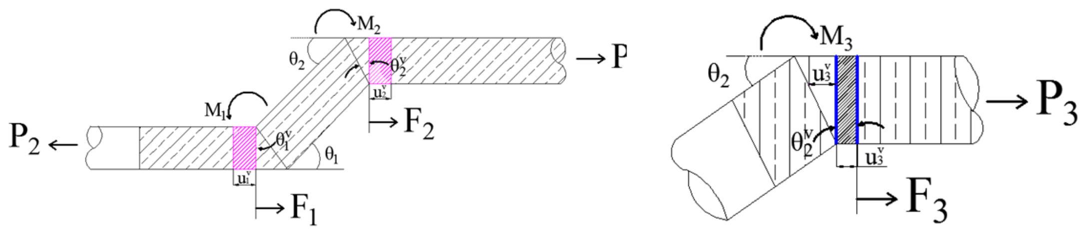

(a) **(b)**

Figure 2.18 Virtual work application to fibre bends pull-out

In fact, Eqs. (2.25) and (2.26) provide the additive forces $\Delta P'$and $\Delta P''$ to the fibre's pre-tensioned force P_1 necessary for bond release. Moreover, when bend angles $\theta_1$and θ_2 are equal and the simplifying assumptions $F_1 = F_2 = \Delta P'$, $F_3 = \Delta P''$ and $M_1 = M_2 = M_3$ is made for fully plastic hinge moments M_P :

$$2\Delta P' u_2^v = 2M_P\theta^v \tag{2.27}$$

$$\Delta P'' u_3^v = M_P\theta^v \tag{2.28}$$

indicating that $\Delta P' = \Delta P''$. Since $\Delta P' > \Delta P''$ by experiment Eqs.(2.25) and (2.26) are refined for $\theta_1 = \theta_2$, $F_1 \neq F_2 \neq F_3$ and $M_1 = M_2 \neq M_3$ as :

$$2\Delta P' = 2M_1\theta^v \qquad (F_2 + F_1)u_2^v = 2M_1\theta^v$$

$$\Delta P'' u_3^v = M_3\theta^v \qquad F_3 u_3^v = M_3\theta^v$$

Writing $u_2^v = u_3^v = \frac{d}{2}\theta^v$ from Figure 2.18b we find from Eqs.(2.27) and (2.28): $\Delta P' = \frac{2M_1}{d}$ and $\Delta P'' = \frac{2M_3}{d}$ suggesting that $M_1 > M_3$ in accord with Figure 2.14. Expressions for M_1 and M_3 may be connected to the bend angle θ and the degree of plastic penetration [15]. For M_3 a further account of reversed plasticity arising from bend-unbend moments is required on straightening the fibre before release. Therein, Eqs. (2.27) and (2.28) show that $M_1$and M_3 ensure the match to observed de-anchoring forces $\Delta P'$and $\Delta P''$ in the ratio

$\Delta P''/\Delta P' = M_3/M_1$. The same ratio is provided by Alwan's Eqs. (2.23) and (2.24) as $1/2(1 - \mu cos\beta)$; this providing a basis for comparison between each analysis.

2.9 Concluding remarks

Bond characteristics between a steel fibre and cementitious matrix have been thoroughly reviewed. A number of mechanisms, which can govern the bond strength, indicated that the interfacial properties play the major role. Since the tensile behaviour of SFRC is directly related to the fibre pull-out loading, improving the pull-out resistance is essential to optimize the mechanical properties of the composite.

The bond has been recognized as a main agency in the composite from which the stresses between fibre and matrix are transmitted. An investigation of fibre-matrix interface mechanics is fundamental to understand and quantify the tensile behaviour of the composite. The mechanisms governing the pull-out behaviour of SFRC are complex and multiple: While the straight fibres rely entirely on friction and adhesion to generate a bond, the hooked-end fibres also develop a mechanical interlock to resist slippage. Although the bond characteristics of straight fibre has been the subject of early extensive investigations, bond mechanisms associated with pull-out behaviour of hooked ends fibre require further research to exploit their improved resistance. Currently, pull-out tests are used extensively for investigation of the bond characteristics at the fibre-matrix interface. However, there is no standard test method to investigate the bond strength of SFRC. Consequently, there appeared a considerable variation between the different sets of test results found in literature.

Several attempts to enhance the bond-slip characteristics have been reported, in which most effective method was to pre-deform fibre. However, there have been relatively few attempts to optimize fibre size and shape in this regard.

Chapter 3 Materials and Methodologies

3.1 Materials

3.1.1 Cement

Two classes of commercially available Ordinary Portland Cement (CEM II 32,5R and CEM III 52.5N) conforming to European standard BS EN 197–1 were used in this study. The average particle size is 20.26 and 16.21μm for CEM II 32,5R and CEM III 52.5N, respectively. The chemical, physical, and mechanical properties of both cements are given in Table 3.1.

Table 3.1 Chemical, physical, and mechanical properties of cement (CEMEX, UK)

	Chemical properties	
	CEM II 32,5R	CEM III 52.5N
CaO	59-61%	62-63.5%
SiO_2	17-18%	19-20.8%
Al_2O_3	3-4%	4.5-5.6%
Fe_2O_3	2.3-3%	3-3.5%
MgO	0.9-1.5%	1-1.2%
SO_3	2.75-3%	3-3.5%
K_2O	Less than 0.64%	Less than 0.70%
Na_2O	Less than 0.25%	Less than 0.27%
Cl	Less than 0.05%	Less than 0.06%
LOI	6.5-7.9%	2.9-3.1 %
	Physical properties	
Autoclave Expansion	0.05%	0.06%
Surface area	465-520 m^2/kg	415-450 m^2/kg
	Mechanical properties	
Setting time	125-150 mins	105-120 mins
$f'c$ (2 days)	15-22 MPa	32-34 MPa
$f'c$ (7 days)	25-32 MPa	44-48 MPa
$f'c$ (28 days)	40-43 MPa	61-64 MPa

3.1.2 Fly ash

Fly ash (EN 450) used in this study was supplied from the West Burton Power Station, Nottinghamshire, UK under Cemex brand. The chemical and physical properties of fly ash (EN 450) conform to BS EN 450-1:2012 (normal fineness Category N and loss on ignition Category B). The average particle size is 6.72 µm and the bulk density usually in the range of 800-1000 kg/m^3. The chemical and physical properties of Fly ash used in the experimental programme are given in Table 3.2.

Table 3.2 Chemical and physical properties of fly ash

Chemical composition	Average % by weight
SiO_2	50
Al_2O_3	30
Fe_2O_3	7
CaO	3
MgO	1
K_2O	3
Na_2O	1
TiO_2	1
SO_3	0.5
Cl	0.1
Total alkali (Na_2Oaq)	Less than 5
Loss on ignition	Less than 7
Fineness (residue on 45 microns)	Less than 40

3.1.3 Silica fume

Silica fume for this study was supplied from France under FerroAtlantica brand which was obtained by filtering the dust extracted from silicon and ferrosilicon production in an electric arc furnace. Its properties confirm with EN 13263-1,2 and ASTM C1240 standards. The average particle size is about 0.1 µm and bulk density in the range of 550-700 kg/m^3. The specific gravity is 2.20 and specific surface area (fineness) in the range of 15000-30000 m^2/kg. The chemical and physical characteristics of silica fume are given in Table 3.3.

Table 3.3 Physical and chemical characteristics of silica fume

Analysis	EN 13263-1,2	ASTM C1240	Typical
SiO_2 (%)	Min. 85	Min. 85	92-96
Free Si (%)	Max. 0.4	-	0.14
Free CaO(%)	Max. 1.0	-	< 0.1
SO_3(%)	Max. 2.0	-	0.25
Na_2Oeq (%)	-	-	0.5
Cl^-(%)	Max. 0.3	-	< 0,1
Loss on Ignition (%)	Max. 4.0	Max. 6.0	2.0
Specific surface (BET) (m^2/g)	15-35	Min. 15	< 25
Pozzolanic Activity Index Normal curing (28d)	Min. 100	-	110
Pozzolanic Activity Index Accelerated curing (7d)	-	Min. 105	120
Bulk Density (kg/m^3) :			
Undensified	-	-	150-170
Semi Densified	-	-	250-350
Densified type DM	-	-	350-550
Densified type DP	-	-	550-700
H_2O (%)	-	Max. 3.0	0.5
> 45 µm (%)	-	Max. 10.0	< 2

3.1.4 Aggregate

A combination of 6 and 10 mm crushed granite was used as a coarse aggregate. Two types of sand: normal sharp sand (0-4mm) and very fine sand (150-600 µm) were used in the experimental programme. Both had similar specific gravity and bulk density which are 2.65 and 1600 kg/m^3, respectively. The chemical analysis of fine and coarse aggregate is presented in Table 3.4, in accordance with BS 1881-131:1998 standard. Both fine and coarse aggregates were firstly washed to ensure there is no dust or any other undesirable materials. Then, they were dried in an electrical oven at 105°C for 24 hours to remove the moisture from the surface. They were stored in a dry place at ambient room temperature until the day of mixing.

Table 3.4 Chemical characteristics of aggregates

Analysis		Typical %		
		150-600 µm	0-4 mm	6-10 mm
Silica	SiO2	99.06	97-99.8	90
Titania	Ti	0.13	1-1.5	1.6
Aluminium	AL_20_3	0.38	0.5-1.5	1.0
Lime	CaO	<0.01	<0.20	0.4
Magnesia	MgO	<0.01	<0.20	0.4
Potash	K_2O	<0.01	<0.20	0.1
Soda	Na_2O	<0.01	<0.01	0.1

3.1.5 Admixtures

A new generation of superplasticiser called (TamCem23SSR) was used in this study to enhance the workability of the concrete. It is a non-chloride admixture which contains polycarboxylate ether polymers and is particularly formulated to reduce water content with greater workability. TamCem23SSR is formulated to comply with the requirements of EN 934-2 and ASTM C 494 standards.

To accelerate setting time and rapid hardening of ultra-high performance concrete (UHPC), a chloride free liquid admixture called (203 Accelerator and Frostproofer) was used. The specific gravity at ambient temperature is about 1.2 and pH content between 9-11%. A 203 Accelerator and Frostproofer have been developed to comply with the requirements of EN934-2 standard.

3.1.6 Fibres

Four different types of commercially available Dramix hooked end steel fibres are investigated in this project. These fibres are designated according to the manufacturer based on hook geometry as 3D (single bend), 4D (double bend) and 5D (triple bend) fibres. The old generation of hooked end fibres (3D) was produced by BEKAERT in 1970. In the recent years, the new line of the improved shape hooked end fibres i.e. 4D and 5D fibres were introduced in the market. All Dramix hooked end fibres have been developed to comply with the requirements of EN 14889-1 and ASTM A820 for structural use. The chemical elements of all fibres were quantitatively analysed using the SEM-EDAX technique. The chemical compositions of all fibres are shown in Figure 3.1 and summarized in Table 3.5.

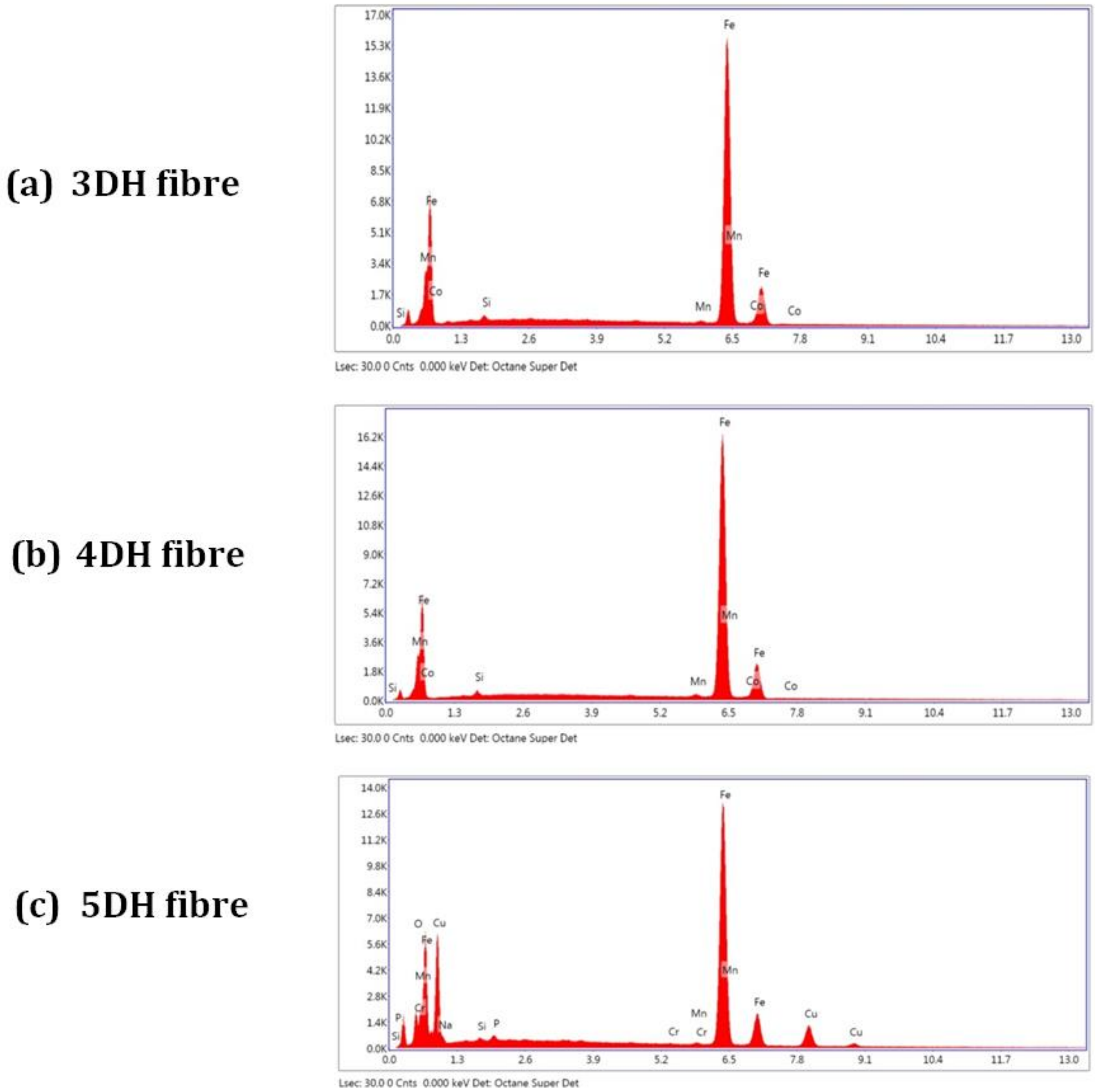

Figure 3.1 Chemical element analyses of 3DH, 4DH and 5DH fibres

Table 3.5 Chemical compositions of hooked end steel fibres

Fibre type	Element	Weight %	Atomic %	Net Int.	Error %	Kratio	Z	R	A	F
3DH	SiK	0.90	1.77	142.31	10.14	0.0049	1.1667	0.9187	0.4614	1.0089
	MnK	0.93	0.94	92.89	14.17	0.0106	0.9818	0.9954	0.9954	1.1650
	FeK	96.92	96.12	7493.57	1.69	0.9916	0.9988	1.0006	0.9997	1.0247
	CoK	1.25	1.17	80.94	12.06	0.0124	0.9774	1.0055	0.9868	1.0310
4DH	SiK	0.33	0.64	53.21	15.55	0.0018	1.1680	0.9182	0.4597	1.0090
	MnK	1.35	1.36	138.22	9.79	0.0153	0.9829	0.9950	0.9956	1.1631
	FeK	96.85	96.59	7751.52	1.69	0.9921	1.0000	1.0002	0.9997	1.0247
	CoK	1.48	1.40	99.51	11.68	0.0147	0.9786	1.0051	0.9863	1.0309
5DH	O K	4.06	12.43	399.86	7.77	0.0232	1.2534	0.8682	0.4556	1.0000
	NaK	3.48	7.42	144.00	13.74	0.0059	1.1452	0.8992	0.1473	1.0015
	SiK	0.16	0.28	25.20	36.29	0.0008	1.1517	0.9263	0.4543	1.0079
	P K	0.48	0.76	77.68	14.20	0.0031	1.1078	0.9345	0.5752	1.0130
	CrK	0.12	0.11	17.65	59.13	0.0017	0.9880	0.9961	0.9883	1.4808
	MnK	0.41	0.37	41.52	24.10	0.0046	0.9684	1.0015	0.9950	1.1622
	FeK	78.55	68.83	6253.00	1.81	0.8039	0.9851	1.0066	0.9992	1.0397
	CuK	12.73	9.81	575.74	3.99	0.1173	0.9488	1.0189	0.9268	1.0475

Two different sizes of 3D fibres were used in this study. The first one (3D 65/60 BG) had a length of 60 mm and diameter of 0.9 mm and the second (3D 65/35 BG) had a length of 35 mm and diameter of 0.55 mm. Both 4D and 5D fibres had a same length (60 mm), diameter (0.9 mm) and aspect ratio (l/d= 65) and only differ in the hook geometry and tensile strength. For each type of fibres, the end hook geometry of the fibres was electronically scanned and measured by using computer software (SUPRA 35 VP). In addition, to obtain the tensile properties, tension tests were conducted for all fibres. The tensile tests were carried out via an Instron 2670 series testing machine of 30 kN capacity using displacement control with a rate of 5 mm/min (Figure 3.2). The tensile and geometrical properties of hooked end fibres are depicted in Figures 3.3 and 3.4 detailed in Table 3.6.

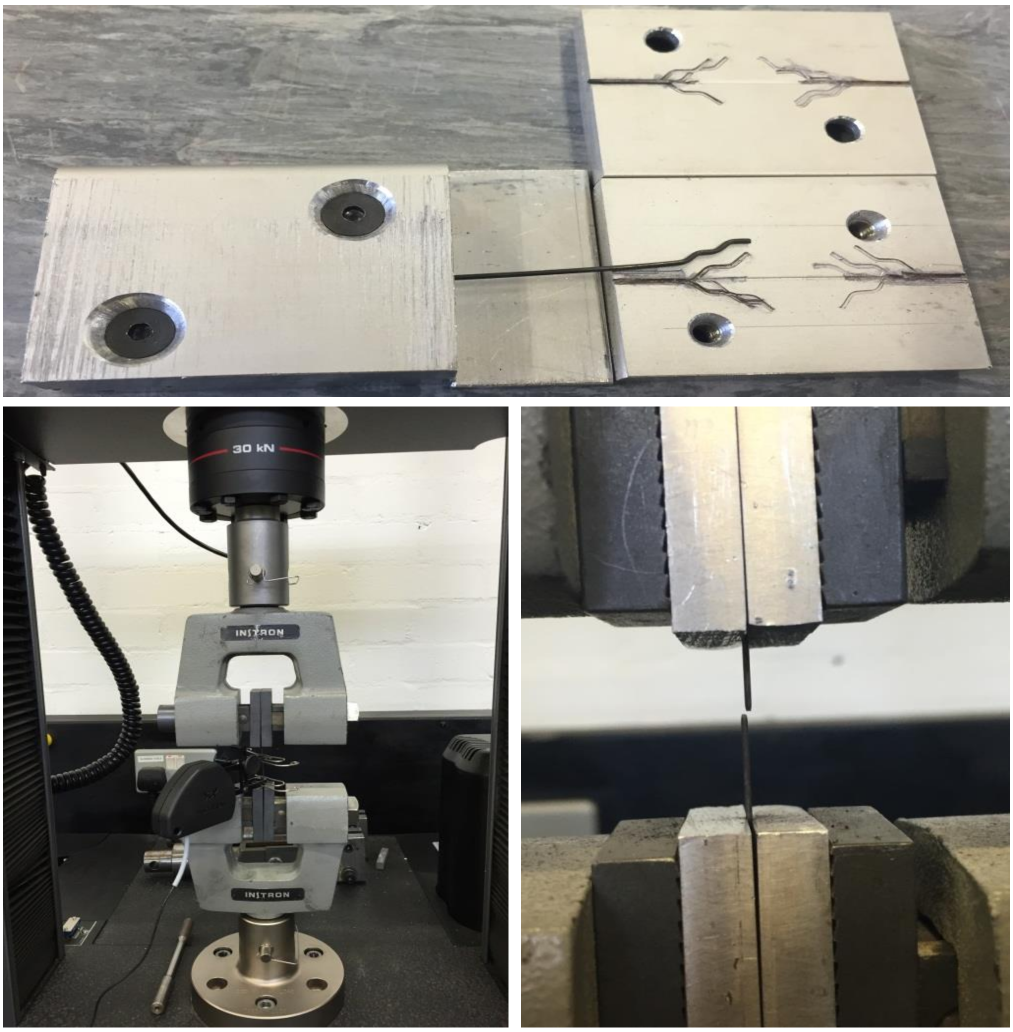

Figure 3.2 Auxiliary jaws for fastening fibre (Top), tensile test setup (Left) and failure mode (Right)

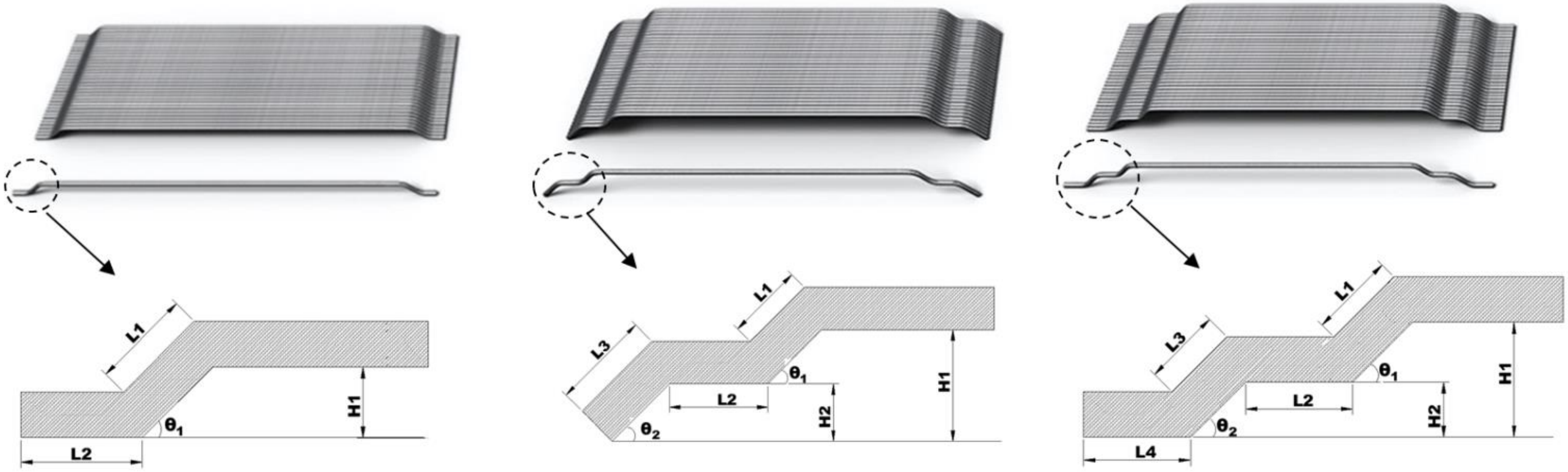

3DH **4DH** **5DH**

Figure 3.3 Geometrical properties of hooked end steel fibres

Table 3.6 The measured geometrical and mechanical properties of hooked end fibres

Fibre type	σ_u* (MPa)	σ_y† (MPa)	l_f (mm)	d_f (mm)	Hook length (mm)				Hook angles (°)		Hook height (mm)	
					L1	*L2*	*L3*	*L4*	θ_1	θ_2	H1	H2
3D 65/35 BG	1345	890-995	60	0.55	2.55	2.22	-	-	43.9	45.1	1.74	-
3D 65/60 BG	1150	775-985	60	0.90	2.12	2.95	-	-	45.7	45.5	1.85	-
4D 65/60 BG	1500	1020-1165	60	0.90	2.98	2.62	3.05	-	30.1	30.8	4.37	2.20
5D 65/60 BG	2300	1177-1455	60	0.90	2.57	2.38	2.57	2.56	27.9	28.2	2.96	1.57

* Ultimate strength
† Yield strength

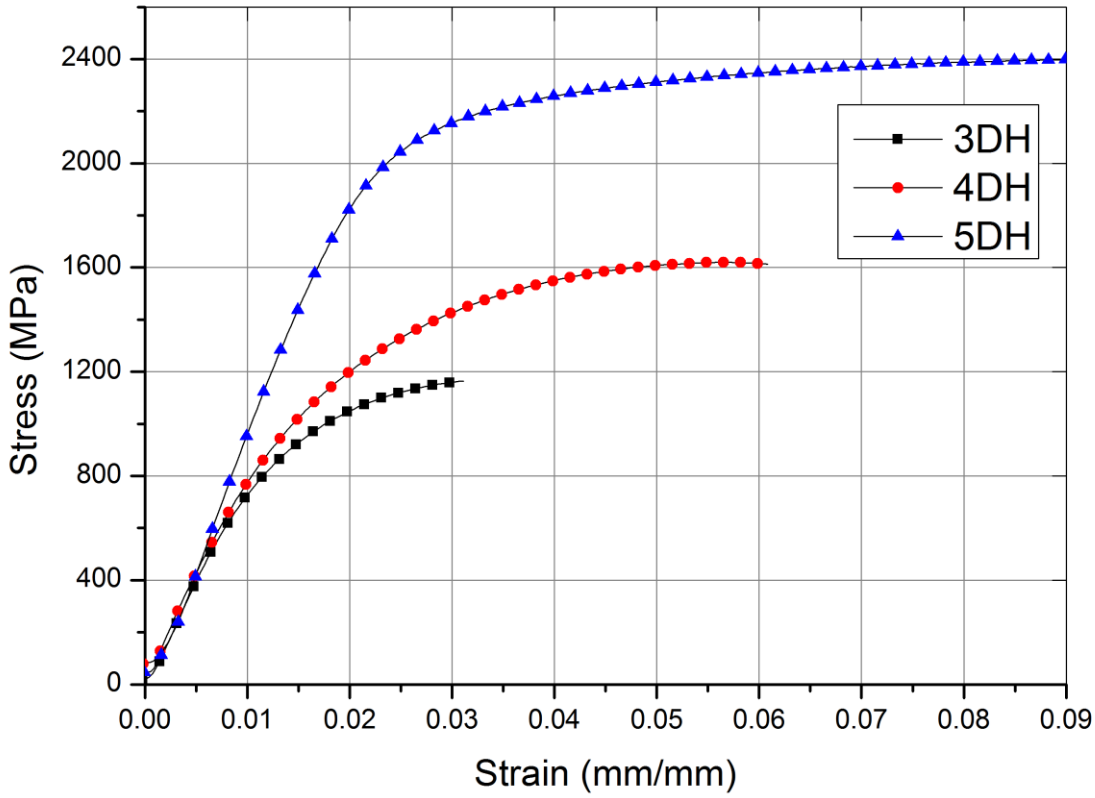

Figure 3.4 Stress–strain curves from fibres tensile tests

3.2 Sample preparation

In this project, two different mixers were used to prepare concrete and mortar mixtures. A laboratory pan mixer has a capacity of 120 litre was used to prepare the concrete with coarse aggregates. For concrete with fine materials, a Hobart mixer of a 40 litre capacity was used to prepare the concrete mixes (Figure 3.5). The mixing procedure for both concrete and mortar is as follows: the dry components i.e. cement, fly ash, silica fume and aggregates were firstly mixed for roughly 1 minute before the superplasticizer and water were added. This was then mixed for another 11 minutes. For concrete with adding fibres, the mix was continued for another 3 minutes as shown in Figure 3.6.

Figure 3.5 Concrete mixer (Left) and mortar mixer (Right)

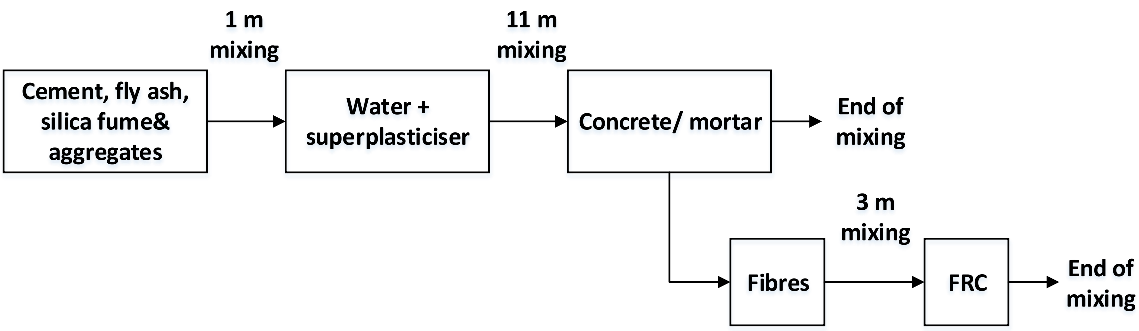

Figure 3.6 Mixing procedure for concrete and mortar

3.2.1 Pull-out test specimens

The pull-out test specimens prepared were (100mm ×100mm ×100mm) cubes for concretes and cylinders with a diameter of 100mm and a height of 50mm for the UHPC specimens (Figure 3.7). For concrete with cubic moulds, each specimen consists of three embedded fibres, while the UHPC specimens contained one embedded fibre. Three different fibre embedment lengths were used in this study which is 10, 20 and 30mm. Meanwhile, three additional 100mm cubes were prepared in order to determine the mechanical properties of the mixture. Immediately after casting and vibration, the specimens were covered with a thin polyethylene film in order to minimise moisture loss and left for 24 hours at room temperature. The specimens were demoulded after 24 hours and then cured for a further 28 days in the conditioning chamber, which was controlled to have a temperature of 20 ± 2°C and relative humidity of 95 ± 5%.

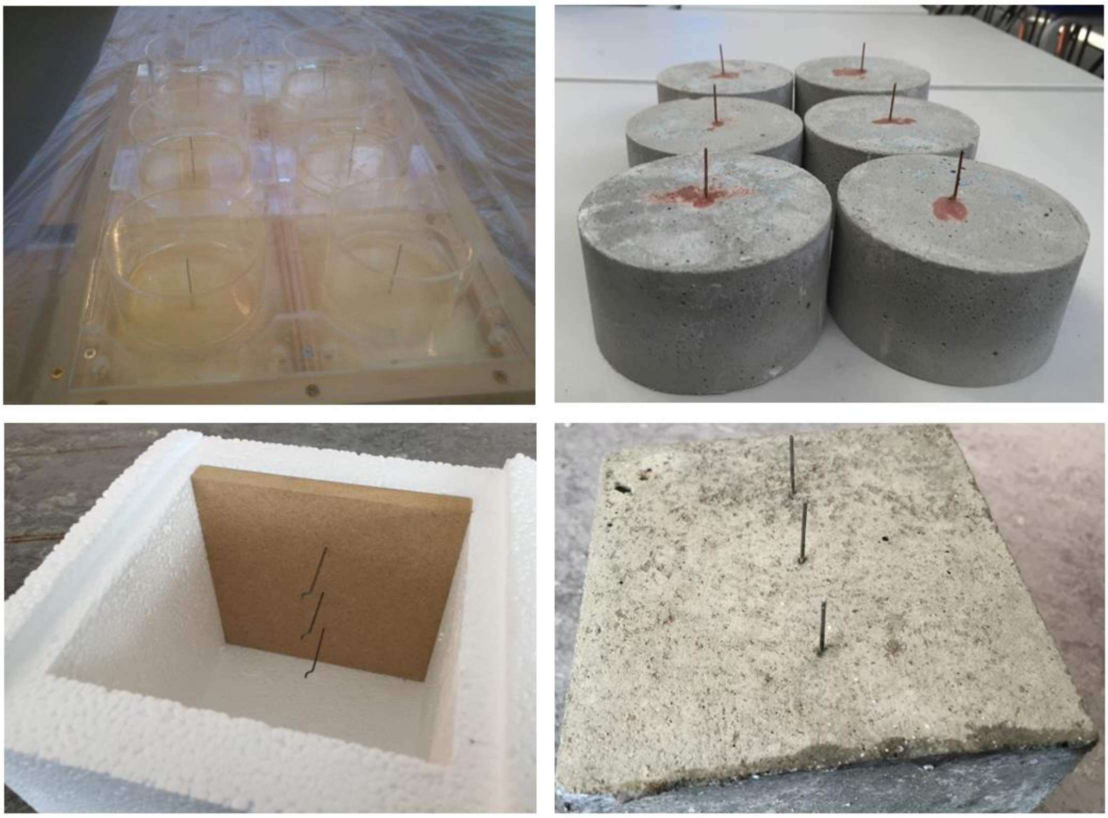

Figure 3.7 Fibre pull-out test moulds and specimens: cylinders (Top) and cubic (Bottom)

3.2.2 Flexural test specimens

The three point bending test specimens were prepared using a beam of 600mm (length) and a cross-section of 150mm^2, according to RILEM TC 162-TDF [115] and EN 14651:2005 standards. All beams were cast by using the flowed mix from one end of the mould to the other end until the mould was full (Figure 3.8). All the test specimens were removed from the moulds after 24h and cured for further 27 days in a water tank at ambient temperature.

Figure 3.8 Casting method (Left) and covering the specimens after casting (Right)

3.2.3 Uniaxial tensile test specimens

Cylindrical specimens of 150×300mm were prepared for the uniaxial tensile tests as shown in Figure 3.9a. The size and shape of each specimen must comply with RILEM TC 162-TDF [115]. Both the nominal length and diameter of the specimen would have to be equal to 150mm. To obtain these dimensions, the top and bottom of the specimen were sawn at a distance of 75mm (Figure 3.9b). Then a circumferential notch with a width of 2-5mm and a depth of 15mm +/- 1 mm was made at mid of the specimen to ensure crack localization during the tests (Figure 3.9c). Special care was given during the cutting process to guarantee smooth surface and perpendicular plane to the cylinder axis.

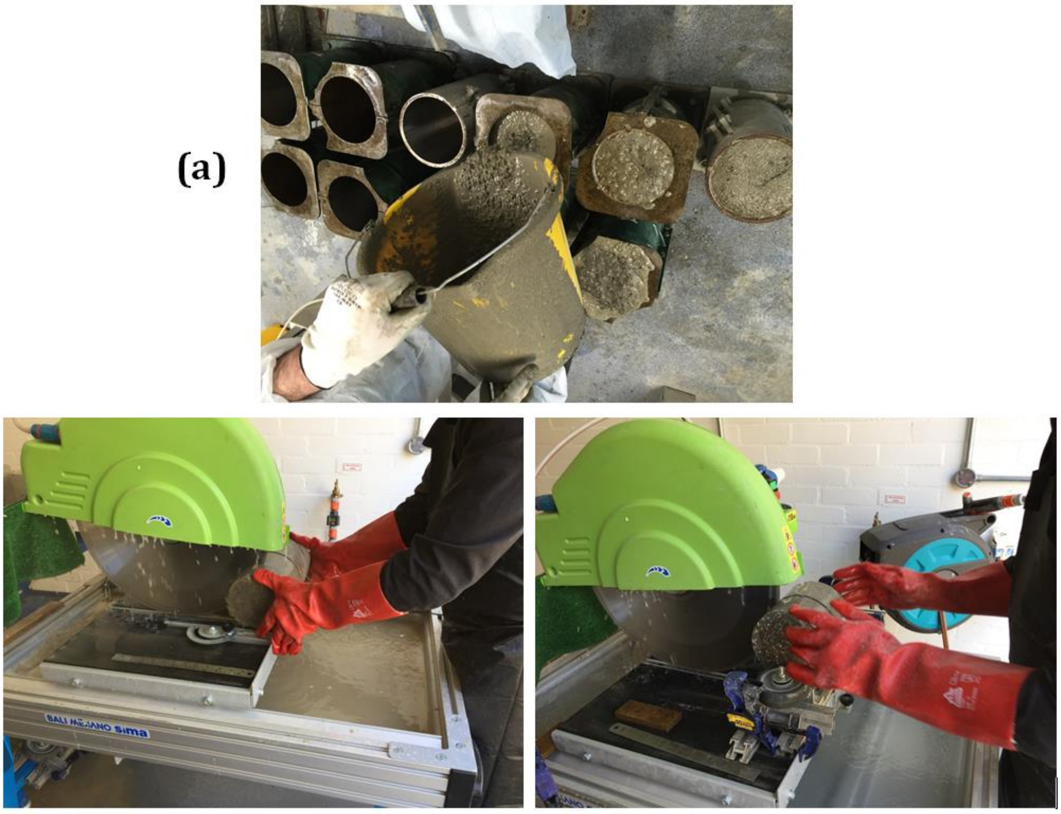

(a)

(b) (c)

Figure 3.9 Specimens preparation: a) casting method, b) and c) sawing procedure

3.3 Testing of fresh state properties

To evaluate the rheological and flowability properties of fresh concrete and mortar, the standard slump, slump-flow, V-funnel tests were performed according to BS 1881: Part 102 and EN 12350-8: 2010 standards. Both standard and flow slump tests were performed using a cone having height 30cm, top diameter 10 cm and bottom diameter 20cm. For normal concrete, the standard slump test was used to measure the slump of the concrete mixes. The flow slump test was used to assess the flowability and the workability of self-compacting concrete and mortar mixtures. In this test, the slump-flow diameter (SFD) and the time to reach 500mm spread (T_{500}) were measured and recorded (Figure 3.10). The V-funnel test was also used to assess the filling ability and viscosity of self-compacting concrete. For this test, measure the time it takes from opening the funnel until the container is visible through the funnel (T_v) was recorded.

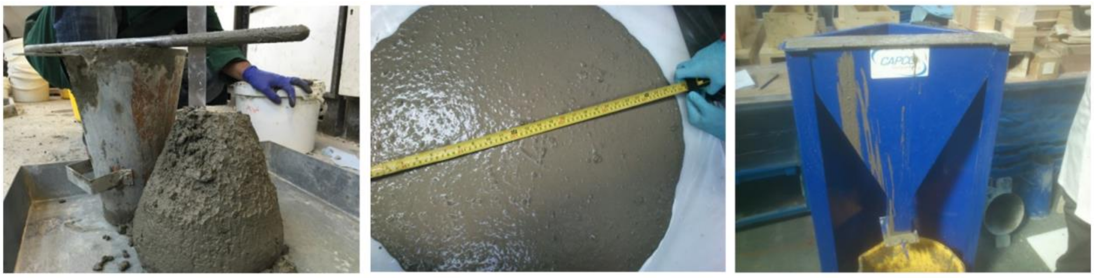

Standard slump test Slump-flow test V-funnel test

Figure 3.10 Rheological and self-compactable tests of fresh mixtures

3.4 Testing of hardened state properties

3.4.1 Heating scheme

The residual thermal, mechanical and bond characteristics were investigated by exposing the samples to various elevated temperatures in an electric furnace. At 90 days after casting, the specimens for the pull-out, mass loss and compressive strength tests were placed in a high-temperature furnace (Figure 3.11). For the pull-out specimens, the free end of the steel fibre were protected with heat insulation (intumescent coating) before the specimens were placed in the furnace. The specimens were then heated to a maximum target temperature of 100, 200, 300, 400, 500, 600, 700 and 800°C, at a heating rate of 20°C/min. The target temperatures were maintained for 1 hour, following which the specimens were allowed to cool down naturally before being tested at room temperature. It is noteworthy that for specimens heated to higher temperatures; the overall exposure duration was greater than for specimens heated to relatively lower temperatures as the specimens also follow the "heating up" period.

Figure 3.11 The furnace (Left) and specimens allowed to cool down naturally to room temperature (Right)

3.4.2 Mass loss

The mass loss measurement was carried out in order to further assess the thermal properties of concrete. One of the most common ways to measure the mass loss of concrete is to calculate the weight loss of a concrete specimen. Measurement of mass loss for all concretes was performed using (100mm ×100mm ×100mm) cubic specimens. The specimens were taken out from the curing chamber and then left to dry at room temperature for four hours before testing. The mass of each specimen was firstly measured at room temperature; the specimens were then exposed to elevated temperatures (100-800°C) in an electric furnace. Then specimens were allowed to cool down naturally to ambient temperature for five hours. Thereafter, the weighing of heated specimens was measured using a balance with an accuracy of 1000th of a gram. This procedure was repeated and applied for all the samples at various target temperatures. The mass loss was calculated following the Equation (3.1).

$$M_{loss}(\%) = \frac{M_i - M_f}{M_i} \times 100 \qquad (3.1)$$

where, (M_{loss}%) mass loss percentage, (M_i) is the initial mass of a specimen at room temperature and (M_f) is the final mass of the specimen after exposure to elevated temperatures.

3.4.3 Compressive strength

Compressive strength of cubic specimens (100mm×100mm×100mm) was determined by using VJ Tech compression machines of 3000 kN capacity in accordance to BS EN 12390-3:2009. One day before testing, specimens were taken out from the curing tank and stored in a room temperature to confirm water-dryness. For compressive strength tests at elevated temperatures, the specimens were exposure to high temperate in an electric furnace and then left to cool naturally for one day before testing. In all tests, specimen was carefully placed between platens before testing, and a constant rate of 360 kN/min was adopted (Figure 3.12).

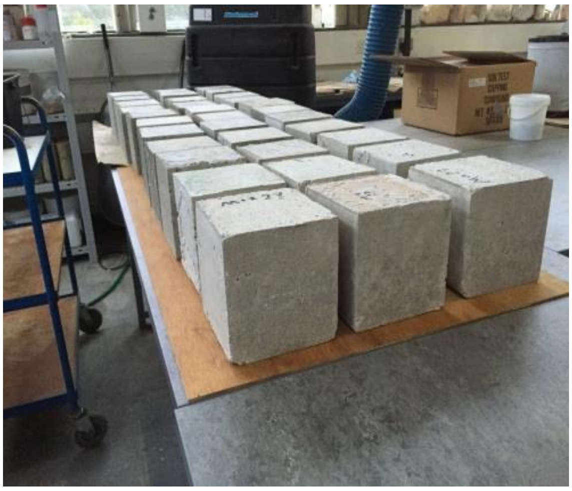

Figure 3.12 Compressive strength test specimens (Left) and setup (Right)

3.4.4 Single fibre pull-out test

The pull-out tests were performed using a specially designed grip system, as illustrated in Figure 3.13, which was attached to an Instron 5584 universal testing machine. The grips were designed such that the forces applied to the fibre provided a true reflection of the real situation experienced by fibres bridging a crack. The body of the gripping system was machined in a lathe using mild steel and had a tapered end to allow the insertion of four M4 grub screws (Figure 3.13). These were then tightened around the steel fibre to an equal torque for an even distribution of gripping pressure to minimise the deformation of the fibre ends and avoid breakage at the tip. Two linear variable differential transformer (LVDT) transducers were used to measure the distance travelled by the steel fibre relative to the concrete face during testing (i.e. the pull-out distance). They were held in place using aluminium sleeves on either side of the main grip body (Figure 3.13). The LVDT's had ball bearings at the tips to allow for accurate readings on the face of the samples. The sample was secured to the Instron base using clamps with riser blocks and M16 studs. The specimen was positioned on a brass round disc to remove any discrepancies in the sample base and allow for distortion. In all pull-out tests, a displacement rate of 10 μm/s was adopted.

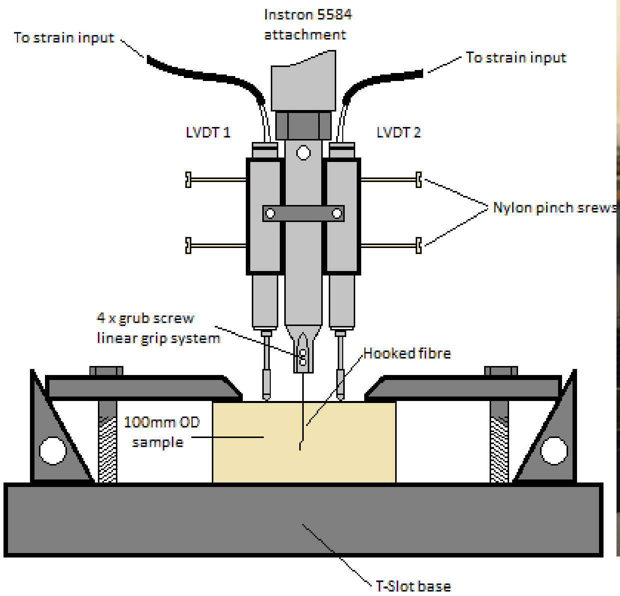

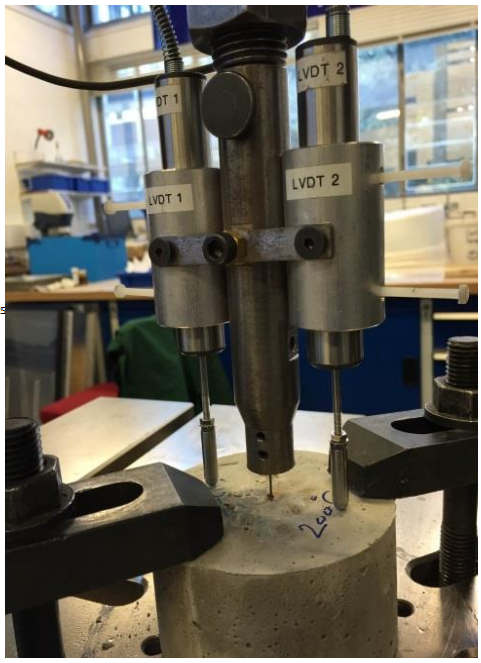

Figure 3.13 Set-up for pull-out tests: schematic view (Left) and photographic image during testing (Right)

3.4.5 Flexural behaviour test

Three-point bending tests on notched beams having dimensions 150×150× 600mm^3 were performed in accordance with RILEM TC 162-TDF. In the mid-span of each beam, a single notch with depth of 25mm and width of 3mm was cut to localize the crack. The beams were placed on roller supports, so to have a test span of 500mm (Figure 3.14). It should be noted that each beam is turned 90° from the casting surface, and the notch is then sawn through the width of the beam at mid-span. The tests were carried out by imposing a constant displacement rate of 0.5mm/min under the INSTRON 5584 electromechanical testing machine. The test was controlled by means of crack mouth opening displacement (CMOD), using a clip-on extensometer with a ±2.5mm range and 10 mm gauge length. The mid-span deflection was also measured using a yoke mounted on the tested beams (Figure 3.14).

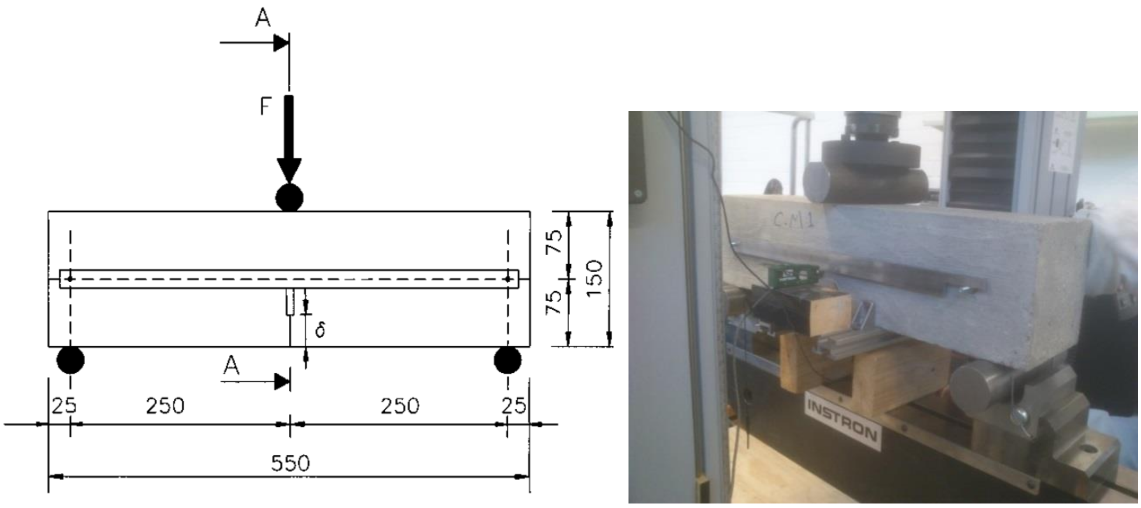

Figure 3.14 Arrangement of three-point bending test: specimen dimensions (Left) and test setup (Right)

3.4.6 Uniaxial tensile test

Following the cutting and notching process, all specimens were carefully cleaned with pressurized air and acetone. Afterwards, two metal plates attached in the loading cell were glued using high strength adhesives top and bottom surfaces of the specimen and then left to cure for two hours before testing (Figure 3.15a). An Instron 5584 series testing machine of 1500 kN loading carrying capacity was used to perform the uniaxial tensile tests as shown in

Figure 3.15b. This test was carried out under closed-loop displacement control by measuring the averaged readings of three displacement transducers arranged along the perimeter of the specimen. The three displacement transducers had a 30mm gauge length (Figure 3.15c). The displacement rates adopted were as follows: 5μm/min up to a displacement of 0.1mm, 100μm/min up to a displacement of 2mm, and this kept until a crack width of 10mm in order to ensure that the hook part was fully deformed and straightened. The testing procedure adopted and displacement rates complied with the recommendations of RILEM TC 162-TDF.

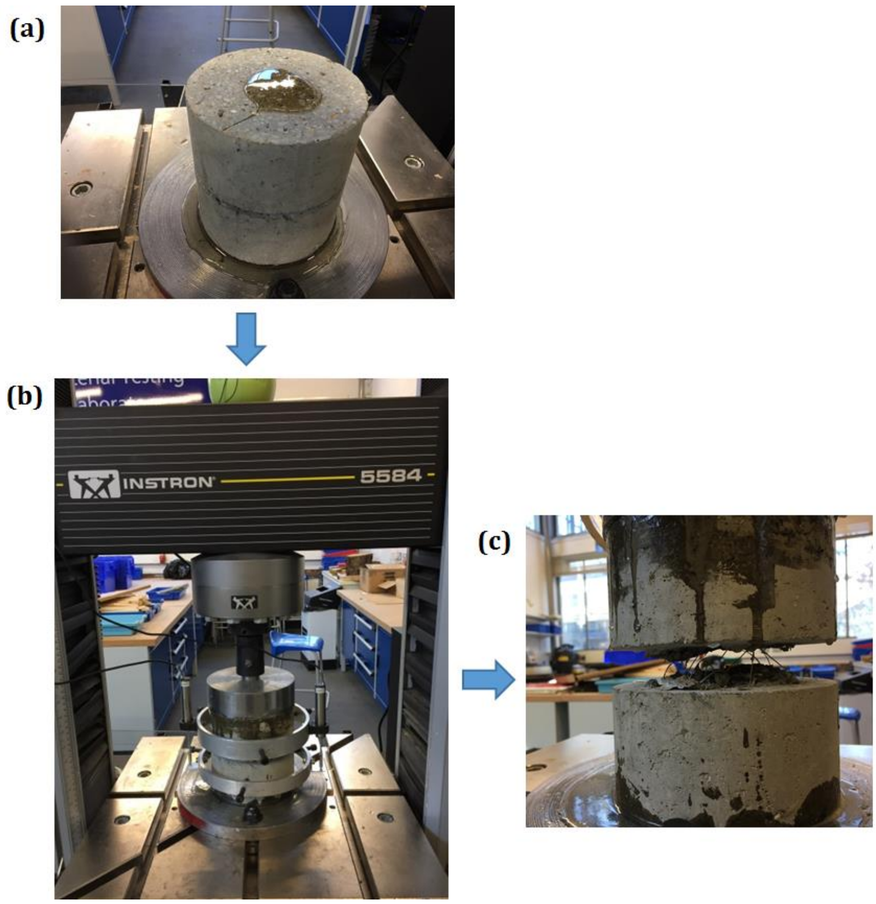

Figure 3.15 Uniaxial tensile test set-up: (a) gluing the top and bottom surfaces of the specimen to loading steel plates, (b) configuration of the test and (c) failure mode of the specimen after testing

3.5 Concluding remarks

All the materials and experiments used in this project have been presented and explained in detail in this chapter. The materials characteristics, fabrication and testing methods according to the relevant standards have been developed. The fresh state characteristics of concrete and mortar were investigated through slumps and V-funnel tests. Mechanical properties of steel fibre reinforced concrete (SFRC) were investigated by testing compressive strength, uniaxial tensile and flexural behaviour, while bond characteristics were examined by using pull-out tests. Some specific experimental procedures or set-ups, which may be required in some work packages, are further detailed in methodologies part of each chapter.

Chapter 4 Pull-out Behaviour of Straight and Hooked-end Steel Fibres

4.1 Introduction

Nowadays one of the main challenging topics of concrete industry is how to improve the tensile response of cementitious materials in terms of strength and ductility. It is well established that the addition of short fibres into concrete significantly enhances their strength in tension as well as controls the cracking propagation [65,116,117]. The tensile strength of steel fibre-reinforced concrete (SFRC) can be quite variable, depending mainly on the fibre-matrix bond strength [118,119]. Therefore, the investigation of the bond mechanisms is a key factor to understand the tensile behaviour of SFRC [15,95].

This chapter experimentally investigates the pull-out behaviour of various hooked end fibres, dealing with varying parameters such as the fibre inclination, fibre embedded length, fibre tensile strength, and matrix compressive strength and quantify the effect of the hook geometry of 3DH, 4DH and 5DH fibres on pull-out response. The pull-out behaviour of straight fibre was also studied. The findings of this experimental investigation provide a better understanding of the bond mechanisms and efficiency of hooked end steel fibres with variation of matrix strength. This provides some fundamental information for efficient exploitation and application of these fibres which are recently introduced to the market. In addition, this investigation will also contribute to increase the database and in-depth knowledge on bond mechanisms of especially 4DH and 5DH steel fibres, which shall be most useful for future review of relevant codes and standards.

4.2 Pull-out behaviour of aligned hooked-end fibres in various concretes

4.2.1 Experimental program

Four different mixtures of normal strength concrete (NSC), medium strength concrete (MSC), high strength concrete (HSC) and ultra-high performance concrete (UHPC) were used. For the NSC, MSC and HSC matrix, the following components were used: Portland cement CEM II 32,5R and CEM III 52.5 N, fly ash EN-450, sand (0-5mm), combination of two particle sizes of crushed granite aggregates (C.G.A), 60% 6mm and 40% 10mm, superplasticizer TamCem (23SSR) and water, for UHPC the component materials include Portland cement CEM III 52.5 N, silica fume, ground quartz, fine sand (150-600) micrometres (μm), superplasticizer, accelerator and water. The materials and mix proportion adopted in this study are summarized in Table 4.1. The sample preparations and pull-out tests are performed according to the procedure described in Chapter 3.

Table 4.1 Mix design of mixtures (kg/m^3) and cube compressive strength (28 days)

Matrix type	Cement	Silica fume	Fly ash	Quartz	Aggregate			Superplasticizer	Water	W/B	f_c
					C.G.A 6-8mm	Sand					(MPa)
						0-4mm	150-600 μm				
NSC	364[a]	-	-	-	979	812	-	-	200	0.55	33
MSC	350[b]	-	107	-	660	1073	-	-	205	0.45	52
HSC	480[b]	-	45	-	850	886	-	6	210	0.40	71
UHPC	710[b]	230	-	210	-	-	1020	30.7	127	0.11	148

[a] Portland-limestone cement CEM II 32,5R

[b] Portland cement CEM III 52.5 N

4.2.2 Results and discussion

4.2.2.1 Effect of hook geometry on pull-out behaviour

The effect of the end hook geometry on the pull-out behaviour was evaluated by comparing pull-out results from fibres of the same length, diameter, aspect ratio, embedment length, matrix strength with the only variable being the end hook geometry. The average pull-out-slip curves (three specimens) of all fibres embedded in different matrix strength are presented in Figure 4.1 for comparison. Table 4.2, also summarizes the average maximum pull-out load (P_{max}) and total pull-out work (W_{total}) values as well as the corresponding coefficient of variation (C.o.V.%).

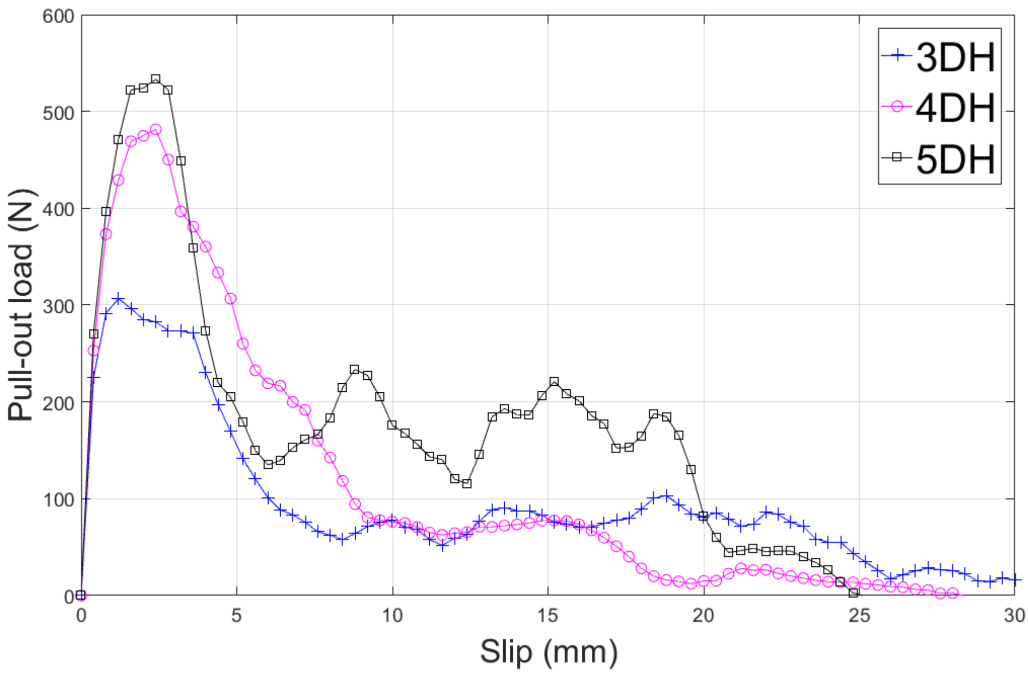

(a)

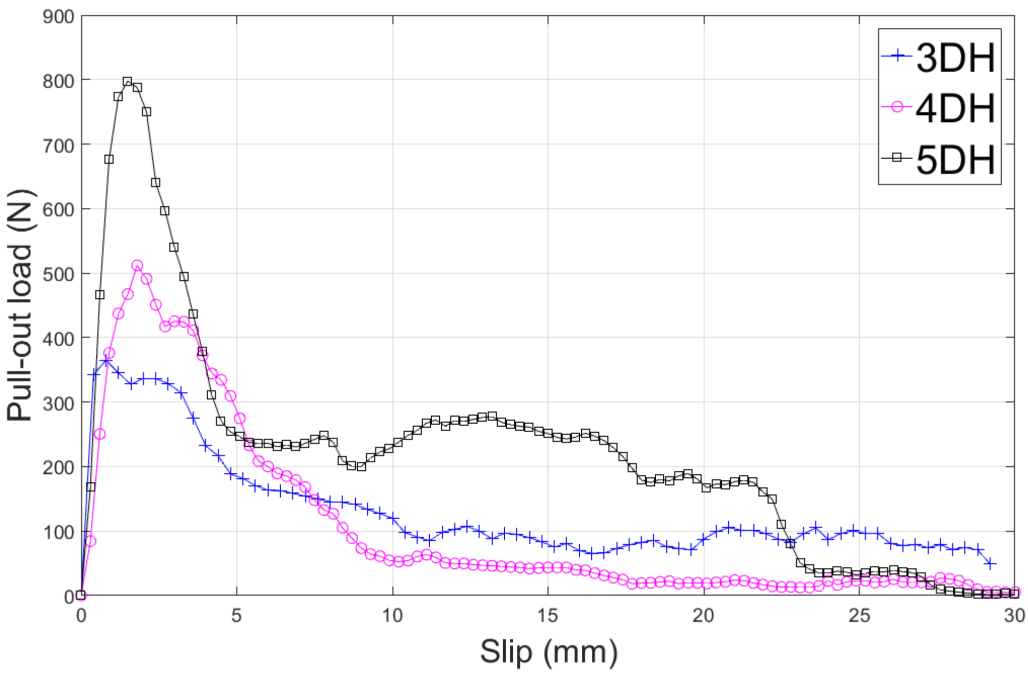

(b)

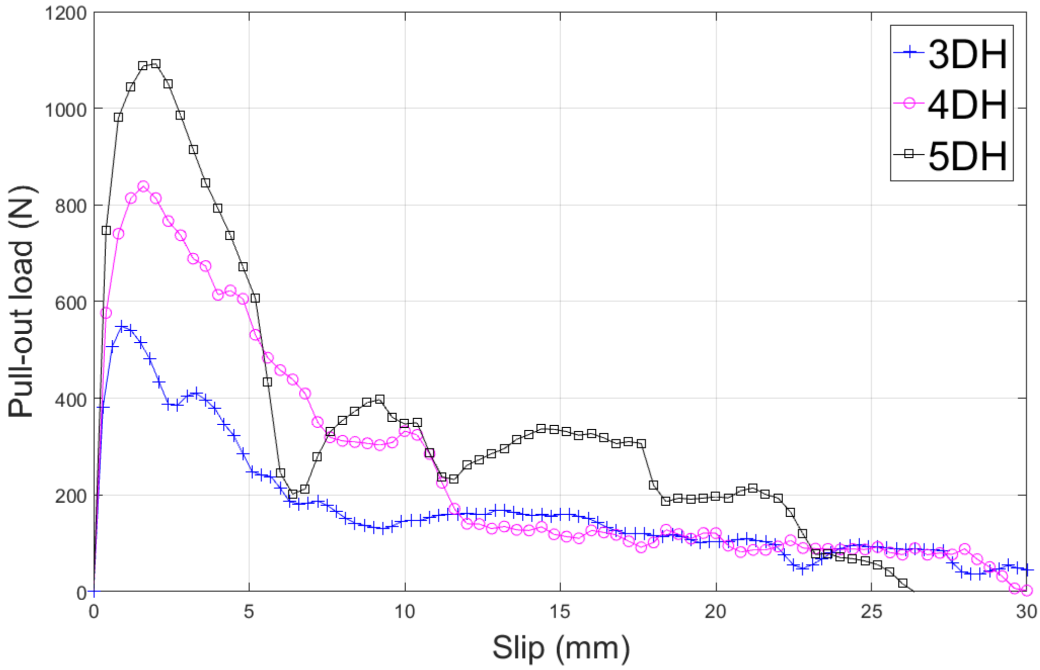

(c)

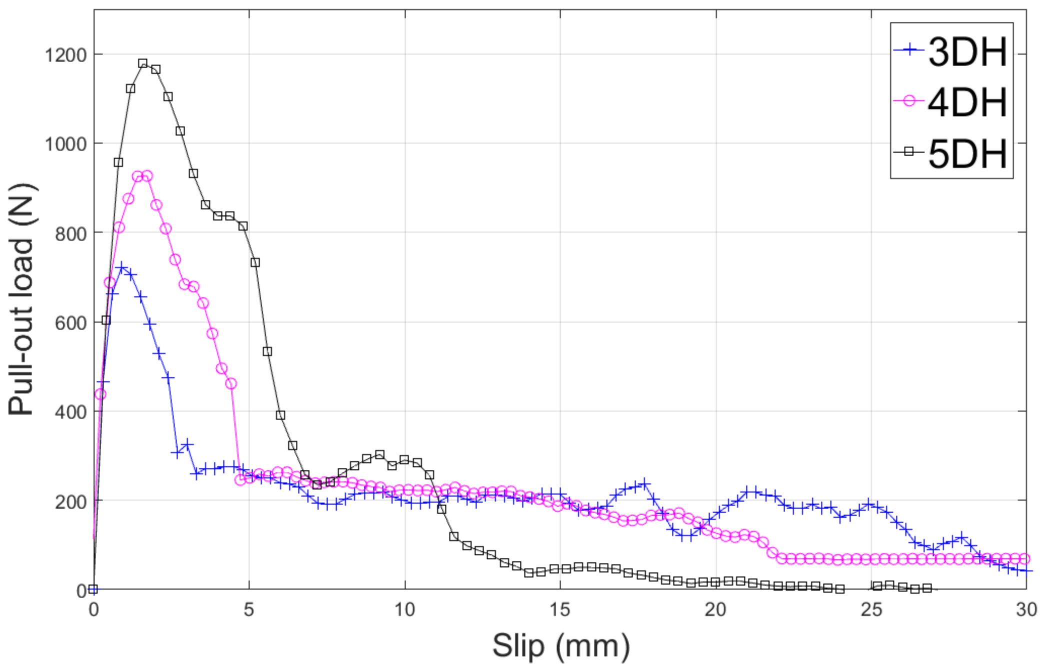

(d)

Figure 4.1 Comparative average pull-out behaviour of 3DH, 4DH and 5DH fibres: a) NSC, b) MSC, c) HSC and d) UHPC matrices

Table 4.2 Average and scattering of the pull-out results

Fibre type	Matrix	P_{max} (N)	C.o.V. (%)	W_{total} (N.mm)	C.o.V. (%)	Failure mode
3DH	NSC	309	10.1	2437	8.8	Pull-out
	MSC	391	9.2	3445	6.4	Pull-out
	HSC	549	7.5	4446	5.1	Pull-out
	UHPC	723	4.3	5948	4.8	Fibre rupture
4DH	NSC	484	14.4	3065	20.5	Pull-out
	MSC	595	9.5	3445	16.4	Pull-out
	HSC	840	6.4	7509	12.6	Pull-out
	UHPC	933	1.5	6592	9.7	Fibre rupture
5DH	NSC	537	23.7	4682	26.6	Pull-out
	MSC	799	18.6	6625	17.3	Pull-out
	HSC	1101	9.9	9721	10.7	Pull-out
	UHPC	1181	4.7	7568	7.8	Pull-out

It can be seen that the shape of the curves for 5DH fibres embedded in NSC and MSC matrices behaves differently from the HSC and UHPC ones (Figure 4.1). The initial incline of the pull-out curve up to peak load is similar for all matrices, but post-peak behaviour both NSC and MSC curves exhibit a steeper load drop than the slopes of the fibres pulled from the HSC and UHPC. Further, the residual pull-out strength of 5DH fibres embedded in concrete matrices (i.e. NSC, MSC, and HSC) is remarkably higher than that corresponding to the concrete matrix (UHPC). These differences can be attributed to the remaining irregularities at the fibre end due to incomplete the deformation and straightening of the hook. While the shape of pull-out curves of the 3DH and 4DH fibres does not vary significantly in the concrete matrices. Both fibres in the post-peak region exhibit a sudden load drop at slip less than 5 mm when embedded in UHPC matrix. It can also be observed that overall the end hook geometry has a significant influence on the pull-out response. The high anchorage effect provided by the lengthy hook of 4DH and 5DH fibres significantly enhances the pull-out behaviour, generating higher pull-out load and pull-out work as compared to 3DH fibre. The anchorage strength also increases with increasing matrix compressive strength.

A scrutiny of results indicates that the maximum pull-out strength of 3DH-NSC combination is much lower, only slightly higher than½ those of 4DH- and 5DH-NSC which are very similar (Figure 4.1a). A comparison of the pull-out behaviour of these fibres in the NSC (Figure 4.1a) with that in the MSC (Figure

4.1b) clearly showed that the pull-out strength of 5DH fibre is considerably increased probably due to the enhancement of the matrix compressive strength. With the NSC matrix, the maximum pull-out load of 5DH fibre is about 73% and 11% that of the 3DH and 4DH fibres respectively and the corresponding difference in total pull-out work is 92% and 53% respectively. Similarly, for the 5DH fibre in MSC, the maximum pull-out load are 117%, 55%, and pull-out work 92 % and 93% higher than that for the 3DH and 4DH fibres respectively. This significant difference in pull-out work can be attributed to variation in slip capacity as a result of different pull-out mechanisms. As aforementioned, improving the matrix compressive strength significantly increases both the maximum pull-out load and pull-out work of all fibres (Figure 4.1c and d). Again, the maximum pull-out load of 5DH fibres embedded in both HSC and UHPC is about 101% and 63% that of the 3DH fibre, while for the 4DH fibre the corresponding values are only 31% and 27% respectively.

The C.o.V. of both the average P_{max} and W_{total} indicates the consistency of the test results with the C.o.V. values below or around 10% (Table 4.2), except, the deviations in case of 4DH and 5DH fibres embedded in the NSC and MSC. As some of 4DH and 5DH fibres were not fully deformed and straightened during pull-out tests.

4.2.2.2 Effect of matrix strength on pull-out behaviour

Four different matrices (NSC, MSC, HSC and UHPC) with compressive strengths ranging from 33 MPa to 148MPa are used (Table 4.1) to investigate the influence of matrix compressive strength on the pull-out behaviour of fibres with various hook geometry. It can be seen from the Figure 4.2 that the pull-out response of all fibres has varied dramatically with matrix strength. For all fibres, the pull-out response is strongly dependent on the matrix strength. The variability of the pull-out response is found to be higher in the case of 5DH fibre than 3DH and 4DH fibres. Therefore, the variability of the pull-out response can be attributed to the variations in the level of deformation and straightening of the hook. The maximum pull-out load and pull-out work significantly increase as the matrix strength increases for all fibres (Figure 4.2). The percent increase in the maximum pull-out load of 3DH fibre in ascending order is 27%, 78% and

134% as the matrix compressive strength increased from NSC (f_c=33MPa) to MSC (f_c=52MPa), HSC (f_c=71MPa) and UHPC (f_c=148MPa), while the corresponding increase in the total pull-out work is 41%, 82%, and 144% respectively. Both 4DH and 5DH fibres behaved in the HSC and UHPC better than in NSC and MSC. In comparison with the NSC matrix, the percent increase of HSC matrix is about 74% and 105%, while the percent increase in UHPC is 92% and 119% respectively.

Figure 4.3 illustrates the influence of matrix strength on the pull-out work of 3DH, 4DH and 5DH fibres. The values of pull-out work are determined by calculating the area under the pull-out load-slip curves. It is evident that the pull-out work increases significantly with increasing matrix compressive strength for all fibres. With the increase in matrix compressive strength from 33 to 52 MPa, an increase of about 41%, 13% and 42% pull-out work was observed for 3DH, 4DH and 5DH fibres respectively. With the further increase in compressive strength from 33 to 71 MPa, an increase of approximately 82%, 145% and 108% pull-out work was observed for 3DH, 4DH and 5DH fibres respectively. Interestingly, the pull-out work of 5DH fibre is greatly higher than the 3DH and 4DH ones in all matrices. However, the pull-out work of both the 4DH and 5DH fibres pulled from the HSC is 14% and 28% higher than the corresponding value in the UHPC. These differences can be attributed to the remaining irregularities at the fibre end that, together with the presence of coarse aggregates in concrete, increase the residual pull-out strength. Similar behaviour is also reported by other researchers [67,70].

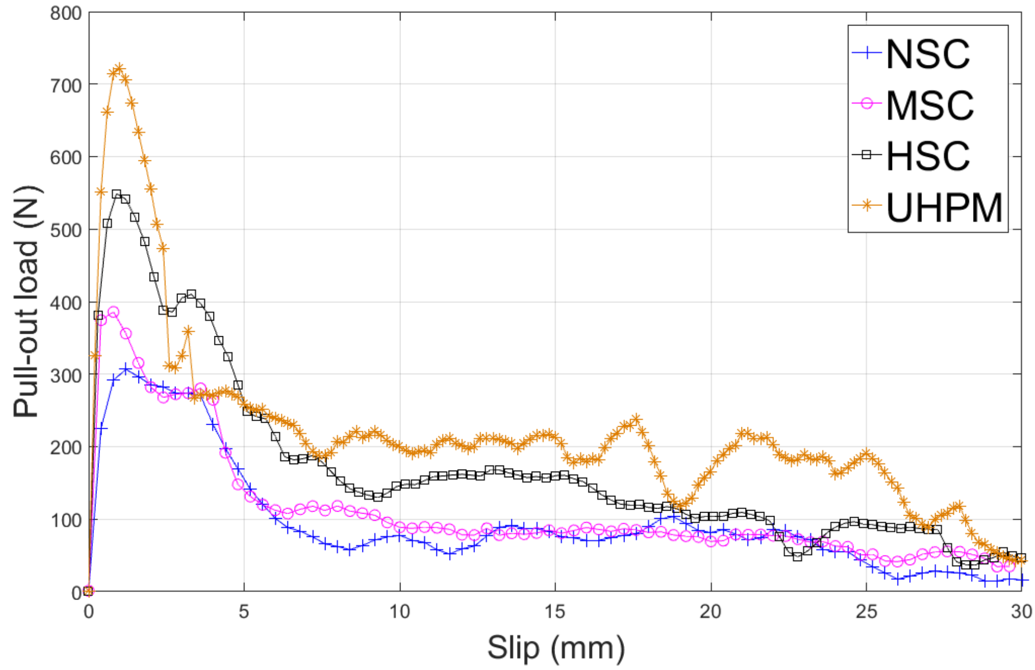
Pull-out load (N)
Slip (mm)
NSC
MSC
HSC
UHPM

(a)

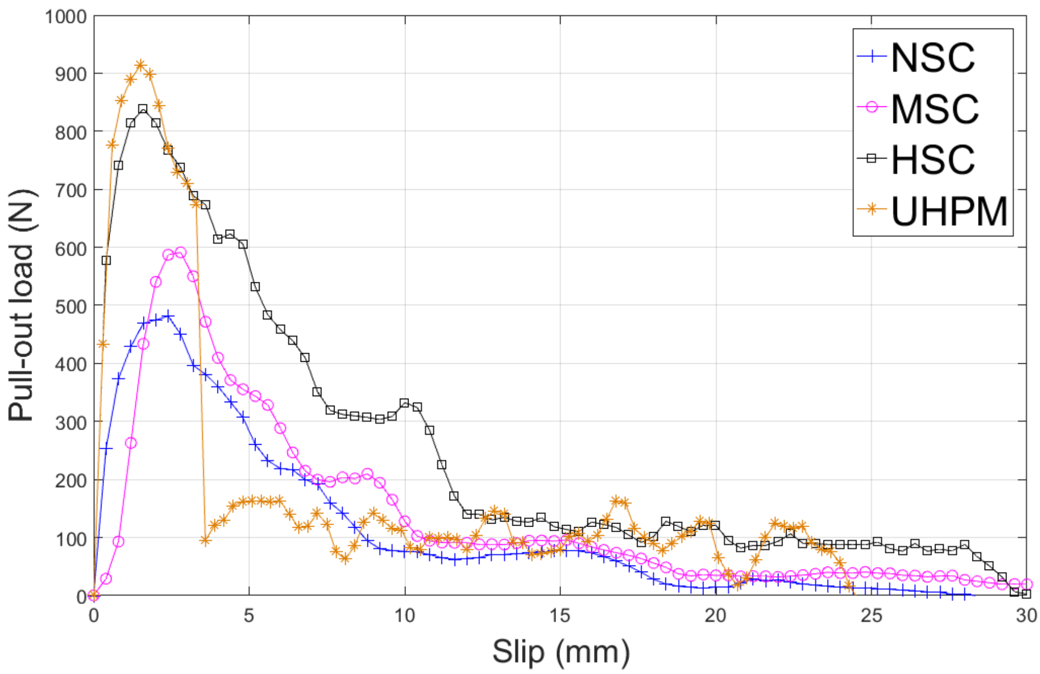
Pull-out load (N)
Slip (mm)
NSC
MSC
HSC
UHPM

(b)

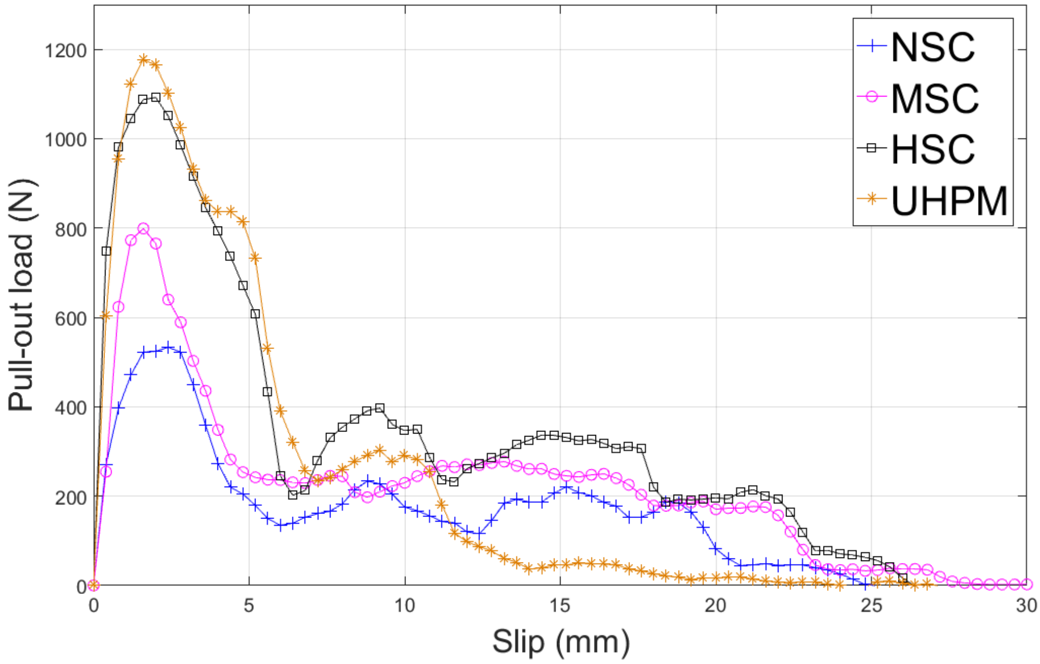

(c)

Figure 4.2 Effect of matrix strength on average pull-out load-slip curves: a) 3DH, b) 4DH and c) 5DH fibres

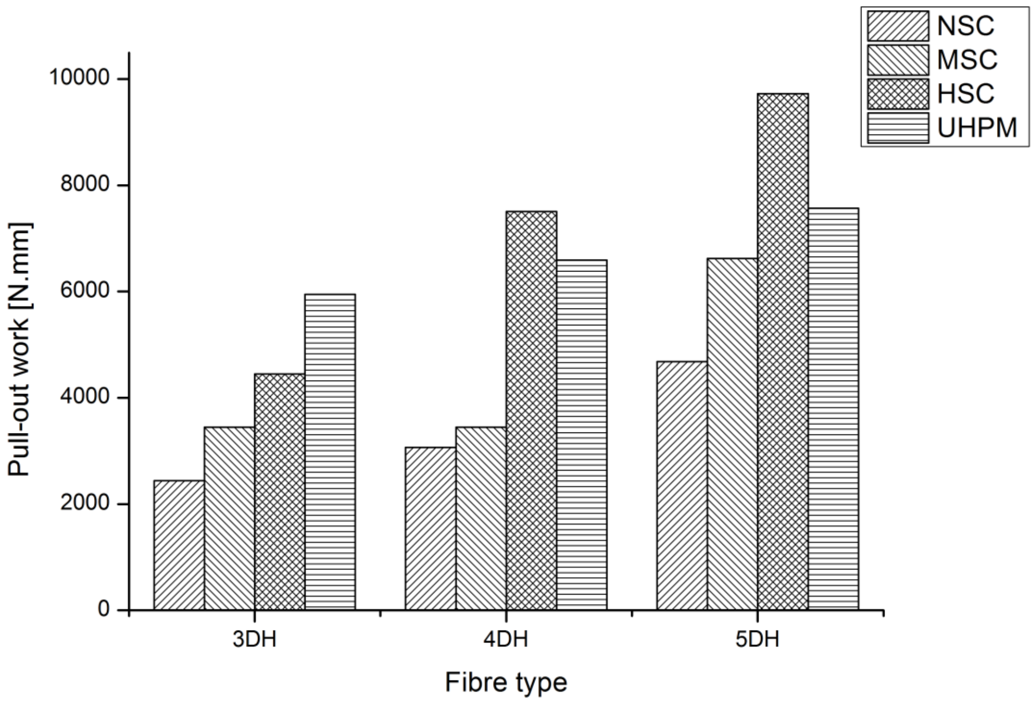

Figure 4.3 Total pull-out work of various combinations

4.2.2.3 Deformation of the hook

To further understand the influence of the hook geometry and matrix compressive strength on the pull-out response, deformation and straightening process of the 3DH, 4DH and 5DH fibres from different matrices were investigated. It is evident that the 3DH and 4DH fibres embedded in NSC and MSC are completely pulled out without occurrence of fully deformation and straightening of the hooks (Figure 4.4). However, the influence of matrix compressive strength on deformation and straightening of the hooks becomes much more pronounced when the fibres were pulled out from the HSC and UHPC matrices. While the full deformation and straightening of the hooks occurs, the rupture of both fibres in the latter matrix at the hook portion has been observed. These differences may be due to the enhanced matrix properties which lead to better bonding strength between fibre and matrix. This leads to the conclusion that the level of deformation and straightening of the hook are significantly different depending on which matrix they are pulled from.

For the 5DH fibres, the following interesting points could be drawn: 1) the complete deformation of fibre hook embedded in the NSC matrix did not occur rather only low level of deformation and straightening of the hook have been observed (Figure 4.4), 2) this partial deformation dramatically increases with increasing the matrix compressive strength, 3) the full deformation and straightening of 5DH fibre hook only take place when the fibres embedded in UHPC, 4) in all four matrices, the 5DH fibre is completely pulled out from the specimen without an occurrence of the fibre rupture, 5) as a result of unique hook's geometry and high tensile strength of 5DH fibre, matrix with high compressive strength is needed to ensure the full utilization of hook anchorage which makes this type of fibre attractive for use in ultra-high performance cementitious composites, and 6) this leads to the conclusion that the 5DH fibre used in this study may only be fully exploited as the reinforcement in UHPC.

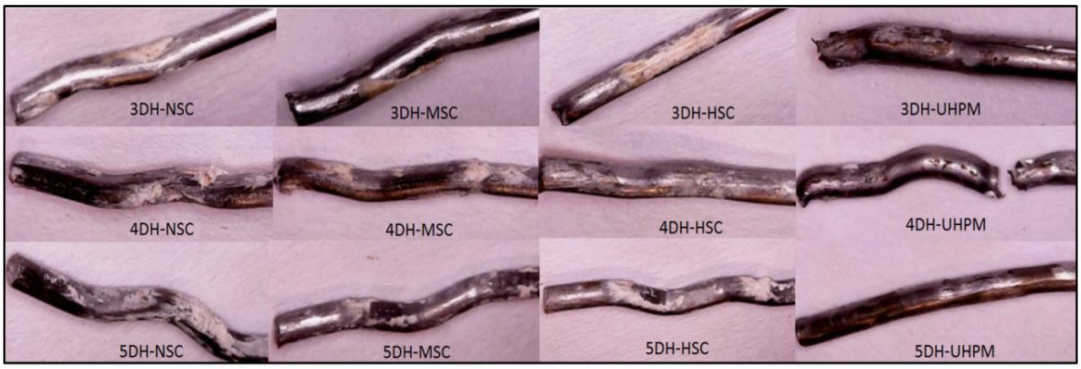

Figure 4.4 Deformation and straightening of hook after pull-out test

4.2.2.4. Fibre rupture

A scrutiny of the morphology of deformation shows that the 3DH and 4DH fibres embedded in NSC, MSC and HSC are completely pulled out from the specimens without the occurrence of fibre rupture (Figure 4.4). However, when both fibres pulled out from the UHPC matrix, the fibre rupture takes place during the early stages of the pull-out process. This is in agreement with the pull-out load (Figure 4.2a), which of 3DH fibre dropped sharply at slip of approximately 3.5-4.5mm and this means that the fibre rupture at hook portion. This could be due to an attainment of the ultimate tensile capacity of the steel at the hook part. Bearing in mind that the hook length of 3DH fibres is approximately 5mm, this indicates that the fibre rupture was likely to take place at last portion of the hook (within L2 region, Table 3.6) as demonstrated in (Figure 4.4). Like the 3DH fibre, the pull-out behaviour of 4DH fibre is characterized by an ascending increase of pull-out load up to maximum value, generally followed by a sudden drop of load, indicating fibre partially rupture. By contrast, the rupture of 4DH fibre occurs roughly at 2-4.5mm (Figure 4.2b) which corresponding approximately to the L1 and L2 (Table 3.6, Figure 4.4) region. The fact that this fibre is bent several times at each curvature results in a significantly worn down of the fibre at hook part. As a consequence, the tensile strength of steel fibre at the hook portion decreases due to excessive deformation and hence the fibre becomes more susceptible to rupture. Although the fibre rupture took places at early stages of pull-out, Figures 4.2a and b show the fibre continues transfer the stress till fibre completely pulled out.

On the other hand, due to the high mechanical anchorage of the 4DH fibre compared with its tensile strength (f_y = 1500MPa), the rupture of fibre is more likely to occur in very high matrix strength. That is, the fibre rupture tends to occur when the fibre with high mechanical anchorage and low tensile strength is combined with high matrix strength [67]. This indicates that the mechanical anchorage contribution of 4DH fibre can be completely reflected if fibre rupture is prevented. Therefore, the tensile strength of 4DH fibre has to increase in parallel with the strength of its anchorage. Only in this way can the fibre resist the forces acting upon it. On the basis of these considerations, it is believed that increasing the tensile strength of the 4DH fibre would effectively prevent fibre rupture and capitalize the end hook anchorage strength to the maximum degree.

4.2.2.5 Concluding remarks

The pull-out behaviour of various hooked-end steel fibres in combination with various cementitious matrices has been thoroughly investigated. Some specific conclusions can be drawn as follows:

1) The pull-out behaviour of a hooked end fibre was significantly influenced by the hook geometry and compressive strength of the matrix. The combined effect and balance of the constituents' contribution determined the maximum failure load, failure region and many other failure parameters. The maximum pull-out load and total pull-out work of the 5DH fibre were much higher than that of the 3DH and 4DH fibres in all matrices.
2) All fibres embedded in NSC and MSC matrices were completely pulled out without the occurrence of full deformation and straightening of the hook. The hook of the 3DH and 4DH fibres fully deformed and straightened when embedded in HSC, while the 5DH fibre only occurred in UHPC. This leads to the fact that the 5DH fibre can only be fully effective when used in UHPC.
3) The fibre rupture tended to occur when the fibre with high mechanical anchorage but low tensile strength (e.g. 3DH and 4DH) was combined

with high matrix strength (e.g. UHPC). Although the load sharply dropped after fibre rupture took place, remaining part of fibre continued to transfer part pull-out load.

4) For 4DH fibre, the mechanical anchorage contribution provided by the hook could be greatly increased by increasing the tensile strength of the fibre. To fully utilize the high mechanical anchorage, 5DH fibres should be used for reinforcing high or ultra-high performance matrices in practice.

4.3 Pull-out behaviour of inclined straight and hooked-end fibres in ultra-high performance concrete

4.3.1 Experimental program

The ultra-high performance concrete (UHPC) matrix considered here is produced by the following ingredients: Portland cement CEM III 52.5 N conforming to BS EN 197-1[120]; densified silica fume; very fine sand (150-600) micrometres (μm); ground quartz with average particle size (10μm); superplasticizer, accelerator and water. The mix proportion adopted in this study is summarized in Table 4.3. Three types of Dramix hooked-end steel fibres (3D, 4D and 5D) with the same length (60mm), diameter (0.90 mm) and aspect ratio (l/d=65) but different in hook geometry were used in this investigation (Table 3.6). The geometrical properties of each fibre type are depicted in Figure 3.3 and detailed in Table 3.6.

Table 4.3 Constituents and proportions of ultra-high performance concrete (kg/m³)

Cement type III 52.2N	Silica fume	Ground quartz	Fine sand	Superplasticizer	Accelerator	Water	$f_{cm}(28)MPa$
710	253	211	1020	31	30	127	176

In each concrete cylinder (100mm diameter and 50mm height), one steel fibre was placed carefully through a hole made through the bottom of moulds at different an inclination angles 0°, 15°, 30°, 45° and 60 ° with respect to the load direction. The fibre embedded length of 30 mm was adopted which is half the length of the hooked end fibres used in this study. For compressive strength test, three cubes of (100×100×100 mm) were prepared. During concrete fabrication, the components were firstly dry mixed for approximately 1 minute followed by the addition of water and superplasticizer to the dry mixture, which were then mixed for 11 minutes. After casting and vibration, the specimens were covered with a thin polyethylene film and left for 24 hours at room temperature. Then specimens were removed from their moulds and cured for a further 28 days in the conditioning chamber (20 ± 2 °C, 96 ± 4%RH). For all series, the test was carried out at an age of 30 ± 2 days and the average of three specimens was adopted. The pull-out tests are performed according to the procedure described in Chapter 3.

4.3.2 Results and discussion

4.3.2.1 Pull-out behaviour of straight fibres

In order to determine the fibre-matrix interfacial characteristics of straight fibres, the end hooked of 3DH and 5DH fibres has been cut off. It is generally accepted that the pull-out behaviour of straight fibre is characterized by a quasi linear ascending branch, followed by a sudden drop in pull-out load, indicating full fibre debonding due to increase of damage at the fibre-matrix interface. Afterwards, the pull-out load is continued by a steady decrease with an increase in slip (decrease in embedded length). Once the debonding of the fibre is completed, the pull-out will then occur under sliding friction between fibre and matrix (Figure 4.5).

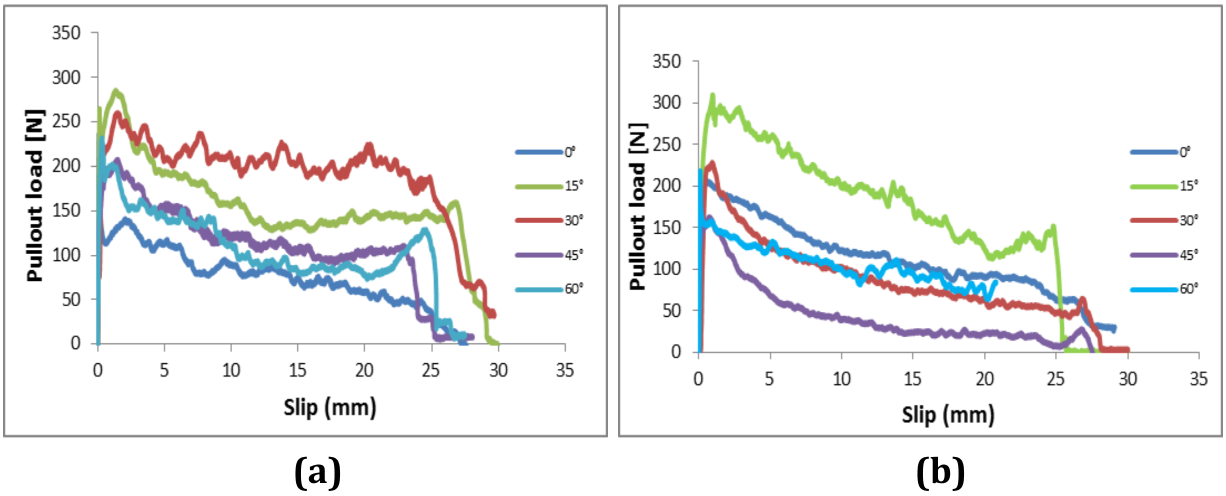

Figure 4.5 Average pull-out-slip curves for: (a) 3D and (b) 5D straight steel fibers embedded in UHPC at different inclination angles

As shown in Figure 4.5, the pull-out response of both the 3Dand 5D straight fibres at different inclination angles has similar trends up to peak pull-out load. However, in the case of fibre at inclination angles of 15° and 30°, a clear difference is observed in the post-peak region of both 3D and 5D straight fibres; there is no sudden drop after the peak load. For both the 3D and 5D straight fibres, the highest maximum pull-out load was observed for an inclination angle of 15°. However, the increase of the maximum pull-out load at an inclination angle of 15° was more significant on the 5D straight fibre than in case of 3D straight fibre. For the former, the specimens with a 15° inclination angle have a maximum pull-out load 48.32% higher than the aligned one (θ= 0°). However, the latter is only higher by 20.25% than that with an inclination angle of 0°. In general, the maximum pull-out load increases up to inclination angle of 30° and then decreases with inclination angles. Although the increase of inclination angle leads to relatively high stress concentrations in the fibre at the exit point, all fibres are entirely pulled out without fibre rupture. The main reason is the limited bond strength between fibre and matrix due to the absence of a mechanical anchorage which results in fibre pull-out under relatively moderate pull-out loads.

In comparing Figure 4.5a for 3D straight fibres (f_y= 1160 MPa) with Figure 4.5b for 5D straight fibres (f_y= 2300 MPa), a slight difference is observed in the maximum pull-out load. This indicates that the increase of tensile strength of 5DH wire, which is approximately two times that of 3DH wire, did not improve the pull-out response. It is well recognised that the tensile strength of steel wire has to be increased in parallel with the strength of its anchorage. However, while this holds mostly true for hooked end steel fibres, it is usually not the case of straight fibres. Since there is no anchorage mechanisms tend to occur in the case of straight fibres, it seems that an increase the tensile strength of straight fibres is not of a great importance any longer.

4.3.2.2 Pull-out behaviour of hooked end fibres

In the case of hooked end fibres, the pull-out behaviour has the same principle (i.e. de-bonding followed by frictional pull-out) that has been observed in straight fibres. However, the hooked end fibre has an additional mechanism, which is plastic deformation at its end hook. The mechanical anchorage that is provided by fibre hook can generate high energy during the pull-out process. Figure 4.6 shows the generally observed pull-out-slip curves of 3DH, 4DH and 5DH hooked end fibres at different inclination angles. It can be seen that the pull-out response of hooked end fibres is directly related to the end hook geometry and the inclination angle of the fibre. For all hooked end fibres, increasing the inclination angle up to 15° remarkably enhances the pull-out behaviour. However, fibre rupture and spalling of the matrix tend to occur at inclination angles of 45° and 60° due to concentrated stresses where the fibre is bent.

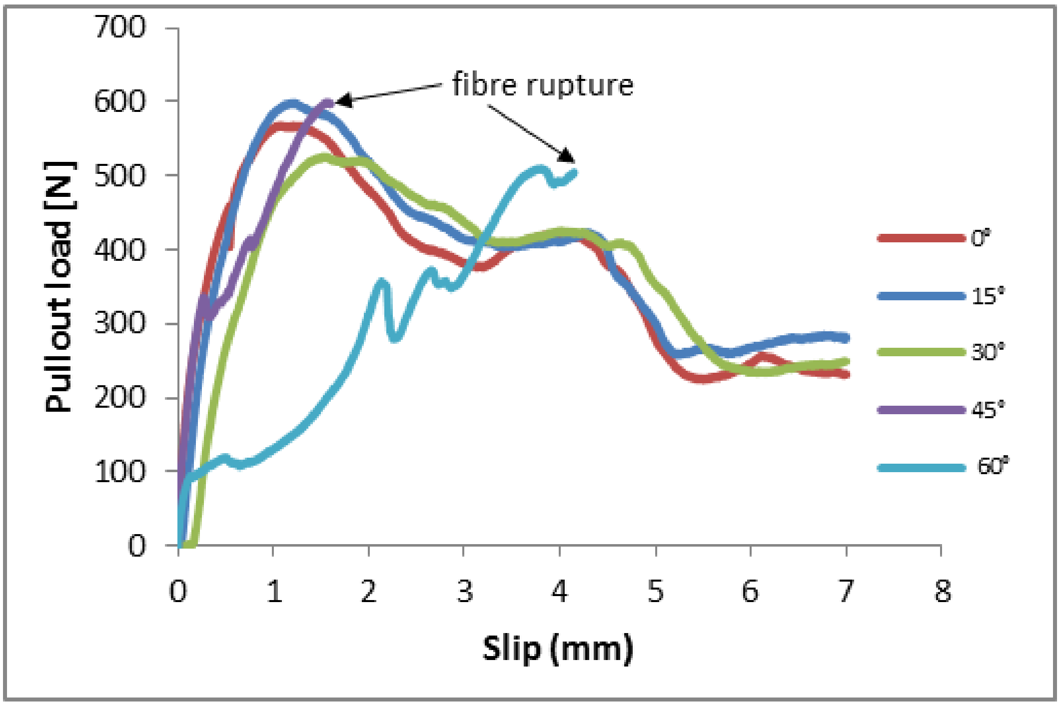

fibre rupture
Pullout load [N]
Slip (mm)
0°
15°
30°
45°
60°

(a)

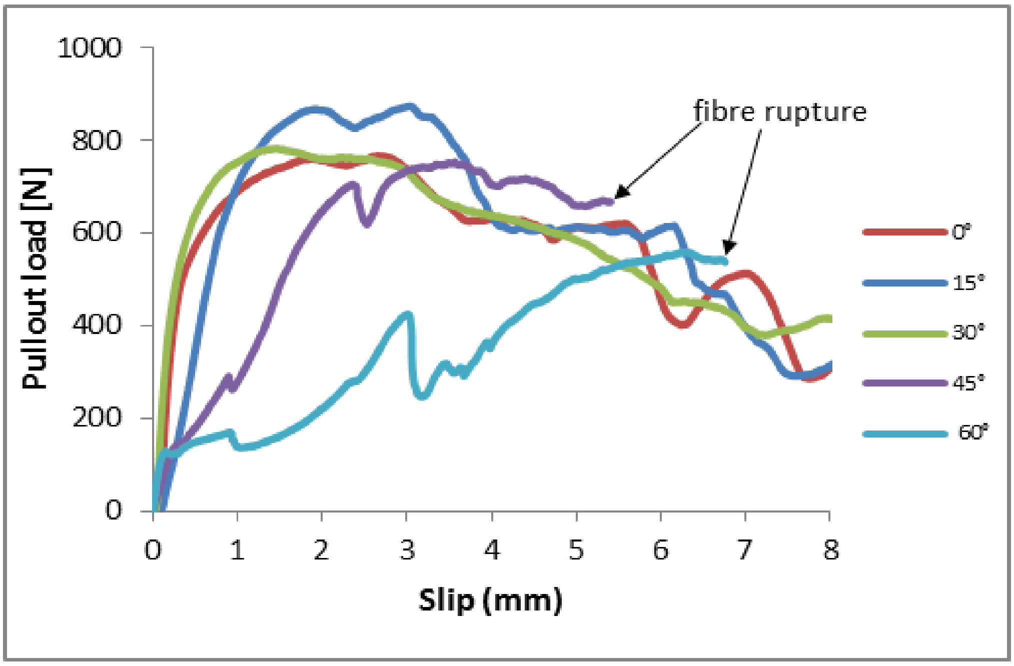

fibre rupture
Pullout load [N]
Slip (mm)
0°
15°
30°
45°
60°

(b)

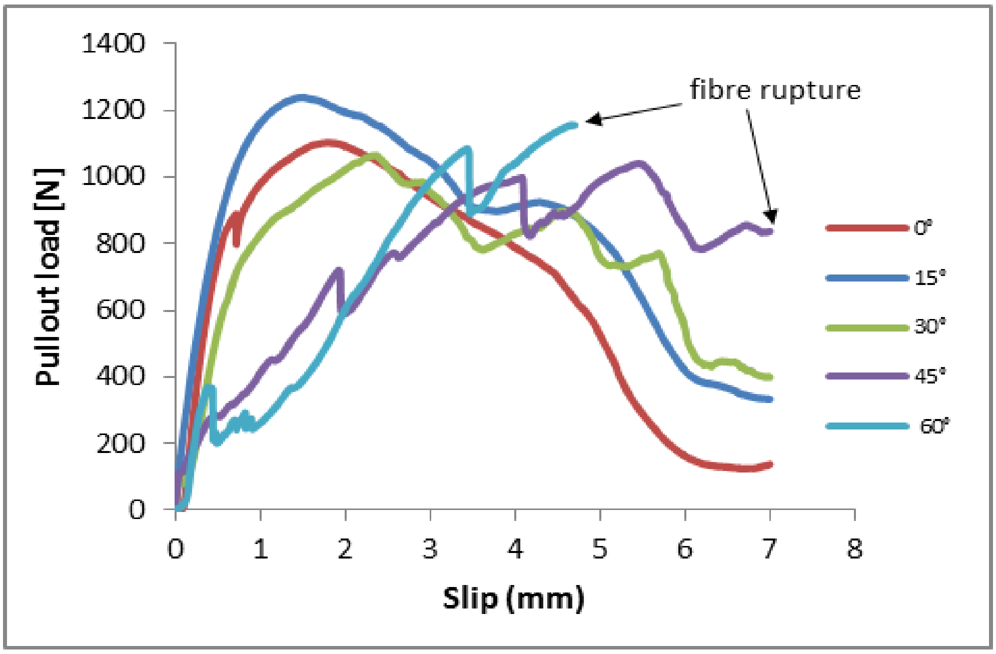

(c)

Figure 4.6 Average pull-out load-slip curves for: (a) 3D, (b) 4D and (c) 5D hooked end steel fibres embedded in UHPC at different inclination angles

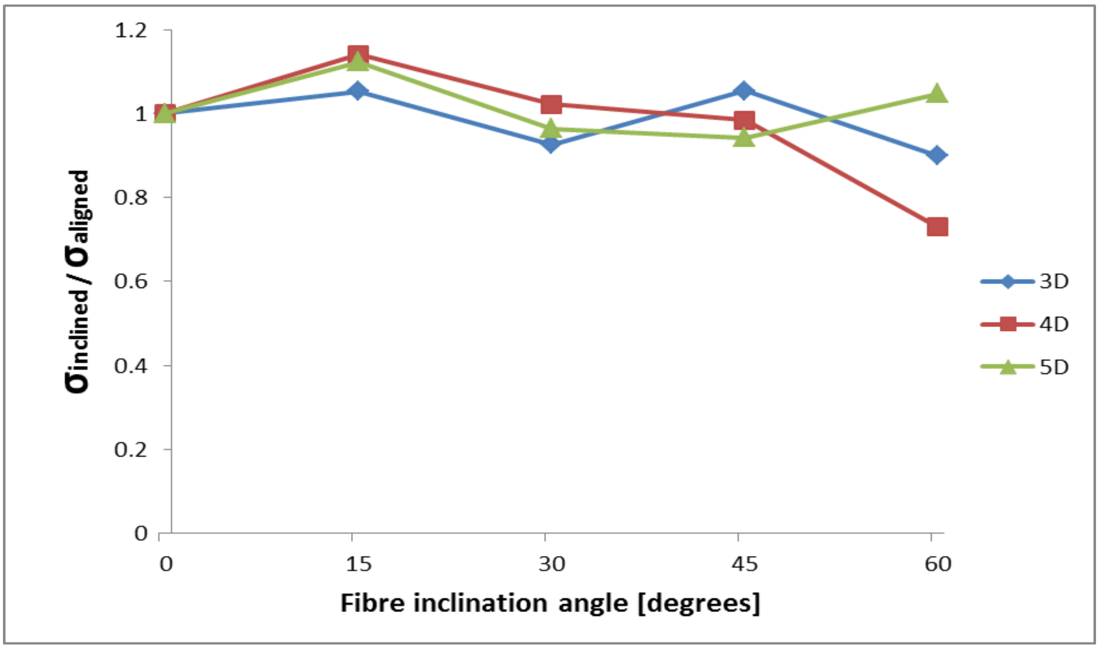

Figure 4.7 Ratio between the pull-out load in aligned and inclined fibres with loading direction

Figure 4.7 shows the effect of the inclination angle on the maximum pull-out load of 3DH, 4DH and 5DH hooked end fibres. It can be observed that the maximum pull-out load of all hooked end fibres was observed at an inclination angle of 15°. However, the increase of the inclination angle of all hooked end fibres beyond 30° did not play a clear influence on the maximum pull-out load. In contrast to the 3DH and 4DH fibres, the pull-out load of 5DH hooked end fibres considerably increases at inclination angle of 60°. For the latter, the maximum pull-out load was found to be even higher than the aligned fibre (θ = 0°). The reason for this behaviour is due to the high ductility and tensile strength of 5DH fibre (f_y=2300 MPa), which enables fibre to resistance the concentrated stresses at fibre bending point and delay fibre rupture.

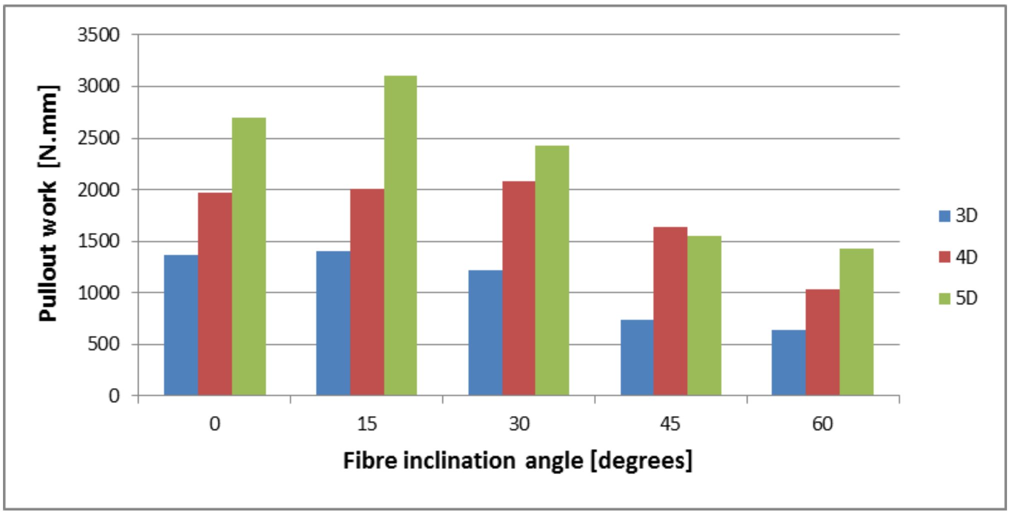

Figure 4.8 Influence of the inclination angle on pull-out work up to a slip of 3mm

The influence of inclination angle on the pull-out work (the area under pull-out load-slip curve) up to 3mm is illustrated in Figure 4.8. For 3DH and 4DH hooked end fibres, a slight increase of pull-out work was observed up to an inclination angle of 15° and 30° respectively and followed by gradually decreases with inclination angle increases. However, for the 5DH hooked end fibre, the pull-out work significantly increases at an inclination angle of 15° and progressively decreases with increasing of the inclination angle. It is believed that the reason for decreasing the pull-out work with increasing the inclination angle is due to spalling of the matrix during the pull-out of inclined fibres, which reduce the available embedded length. In comparing the pull-out work of 5DH fibre versus that of the 3DH and 4DH fibres at the inclination angles of 0°, it can be observed that the pull-out work of 5DH fibre is higher by 49.50% and 26.89% respectively.

The influence of inclination angle on the maximum stress applied to the fibre during the pull-out process is presented in Figure 4.9. It is obvious that no clear relation between the inclination angle of fibre and maximum tensile stress could be found. While the tensile stress of the 3DH fibre is maximized at fibre inclination angles of 45°, whereas the 4DH and 5DH fibres have been shown to maximize under inclination angle of 15°. The difference between these values corresponds to variation the effect of various mechanisms such as local friction, fibre bending and matrix spalling which are differently influenced by the inclination angle.

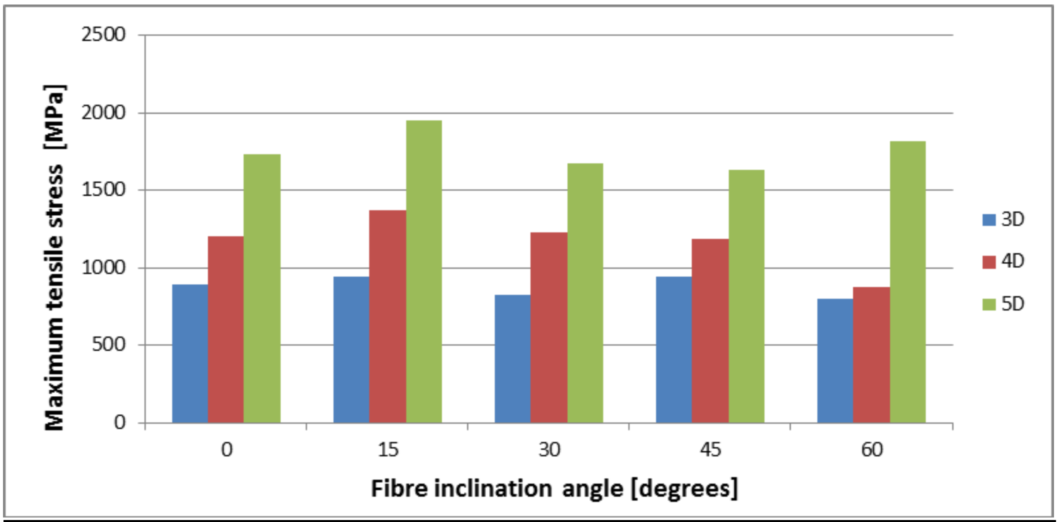

Figure 4.9 Influence of the inclination angle on the maximum tensile stress

The utilisation degree of the tensile capacity can be expressed as the ratio of the maximum tensile stress achieved in the fibre through the pull-out process (σ_{max}) and the ultimate tensile strength of the fibre (σ_y). The obtained results from this ratio can be used to evaluate the fibre efficiency in terms of the utilisation level of tensile capacity, which provides information if the fibre properties (e.g. aspect ratio and tensile strength) convenient to the matrix strength. The effect of the inclination angle on the ratio (σ_{max} /σ_y) at different inclination angles is shown in Figure 4.10. Generally, all hooked end fibres showed a high degree of the tensile utilisation up to an inclination angle of 15°, especially for 4DH fibre. For the latter, however, the increase of inclination angle causes a gradual decrease in the utilisation level of tensile capacity and then followed by a significant drop at an inclination angle of 60°. This can be attributed to concentrate the friction load at the fibre exit point; which results in severe spalling of the matrix; thus the stress carried by the fibre is reduced. Due to the high mechanical anchorage of the 4DH fibre compared with its tensile strength (f_y = 1500MPa), the rupture of fibre is more likely to occur. Therefore, the tensile strength of 4DH fibre has to increase in parallel with the strength of its anchorage. The authors believe that by increasing the tensile strength of the 4DH fibre; to prevent fibre rupture would be highly effective; to capitalize the end hook anchorage strength to the maximum degree.

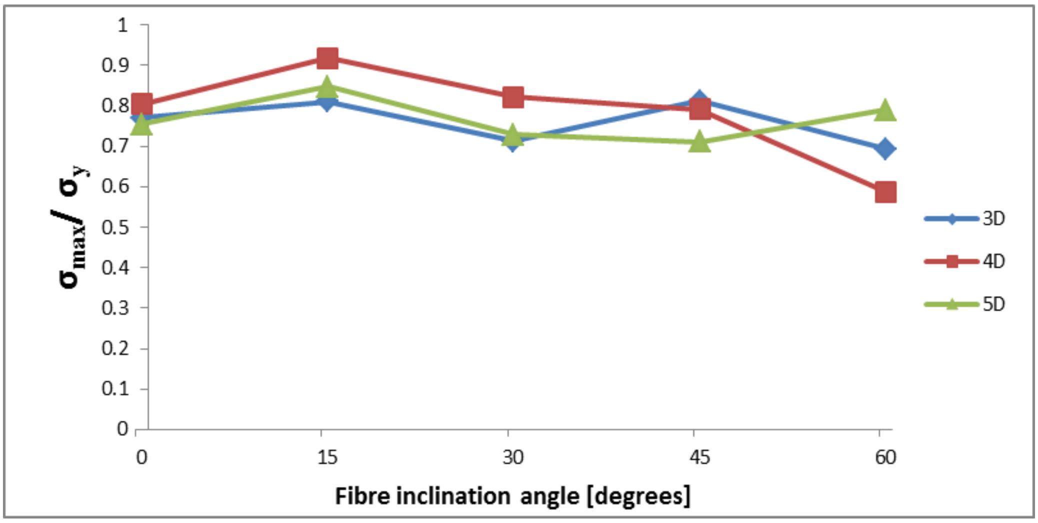

Figure 4.10 Relationship between the utilization level of tensile strength and fibre inclination angle

4.3.2.3 Concluding remarks

The pull-out behaviour of various hooked end steel fibres embedded in ultra-high performance concrete has been investigated. The effect of the end hook geometry and the inclination angle of the fibre on the pull-out response were thoroughly studied. The pull-out behaviour of both straight and hooked end fibres appeared to be directly related to the end hook geometry and the inclination angle of the fibre. For the straight fibres with the same length, diameter and aspect ratio (L/D), the doubling of the tensile strength of straight fibre did not result in any improvement in the pull-out behaviour. However, due to variation in the end hook geometry and tensile strength of the hooked end fibres, a significant difference in the pull-out behaviour was observed. Enhancing both the tensile and anchorage strength of the 4DH and 5DH fibres played a major influence on the pull-out behaviour. The maximum pull-out load and pull-out work of the aligned 5DH fibre (θ=0°) were higher by 48.55%, 30.52%, 49.50% and 26.89% than those in the 3DH and 4DH fibres respectively. For this matrix strength (UHPC), the highest pull-out load and pull-out work of both the straight and hooked end fibres occurred at an inclination angle of 15°. Nevertheless, further increase of inclination angle of all hooked end fibres did not show a clear trend due to the occurrence of fibre bending and matrix spalling. The rupture of fibre tended to occur at larger inclination angles (45° and 60°) for all hooked end fibres. On average, all hooked end fibres showed a high level of utilisation of the tensile capacity, particularly for 4DH fibres.

4.4 Pull-out behaviour of hooked-end fibres in ultra-high performance concrete with various embedded lengths and W/B ratios

4.4.1 Experimental programme

The ultra-high performance fibre reinforced concrete matrix (UHP-FRC) with different W/B ratio (W/B = 0.15, 0.20 and 0.25) considered here is produced by the following ingredients: Portland cement CEM III 52.5 N confirming to BS EN 197-1; densified silica fume; fine sand (150-600) micrometres (μm); ground quartz with average particle size (10μm); superplasticizer (TamCem23SSR), accelerator (203 accelerator and frostproofer) and water. The mix proportion adopted in this study is summarized in Table 4.4. Two types of commercially available and commonly used 3D Dramix hooked-end steel fibres (3DH) were used to reinforce the UHPC. The geometrical properties of each fibre type are depicted in Figure 4.11 and detailed in Table 4.5.

Table 4.4 Mix design of UHPC mixtures

Type	UHPC1	UHPC2	UHPC3
Constituent		Kg/m^3	
Cement type III 52.5 N	710	710	710
Silica fume	231	231	231
Ground quratz	211	211	211
Fine sand	1020	1020	1020
Superplasticizer	30.7	30.7	30.7
Accelerator	30	30	30
Water	140.7	186.7	243.7
W/B	0.15	0.20	0.25

Table 4.5 General properties of hooked end steel fibres

Fibre type	Lf (mm)	Df (mm)	Lf/ Df (-)	L1 (mm)	L2 (mm)	α (°)	H1 (mm)	Tensile strength (MPa)
3DH1	35	0.55	65	2.55	2.22	38.3	1.85	1345
3DH2	60	0.90	65	2.12	2.95	45.7	1.77	1160

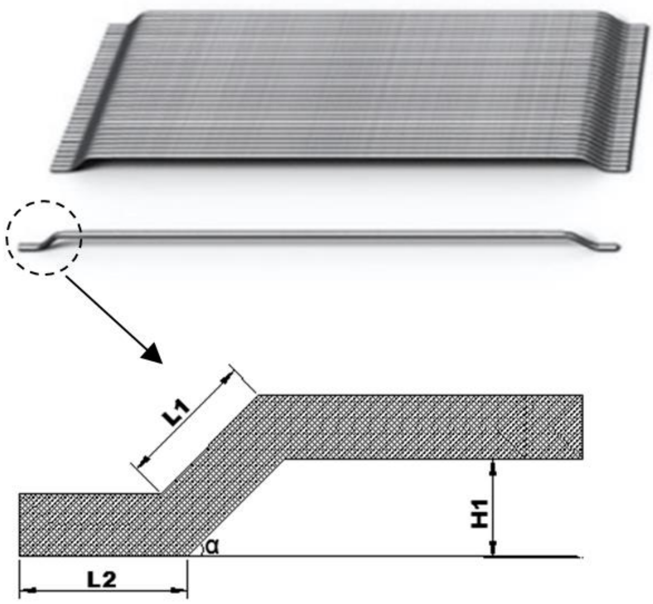

Figure 4.11 Geometrical properties of hooked end fibres

The pull-out test specimens prepared were cylinders with a diameter of 100 mm and height of 50 mm. In each test specimen, a single steel fibre was carefully placed through a hole which was made in the bottom of moulds (Figure 3.7). Three different embedded lengths L_E (10, 15 and 30 mm) were investigated in this study. For compressive strength test three cubes of (100×100×100 mm) were prepared for each mixture differentiated in W/B ratio. The sample preparations and pull-out tests are performed according to the procedure described in Chapter 3.

4.4.2 Theoretical consideration of σ_{max}, τ_{av} and τ_{eq}

In order to assess and compare the pull-out behaviour of the two types of hooked end steel fibres embedded in different ultra-high performance concretes (UHPCs), the following parameters are considered based on the experimental results [33]:

- Maximum fibre tensile stress, σ_{max} that can be obtained by dividing the maximum pull-out load, P_{max} over nominal cross-sectional area of the fibre, A_f.

$$\sigma_{max} = \frac{P_{max}}{A_f} \tag{4.1}$$

- Average bond strength, τ_{av}, can be defined as the maximum pull-out load based on the initial embedment length surface area [54].

$$\tau_{av} = \frac{P_{max}}{\pi \times d_f \times L_E} \tag{4.2}$$

where, τ_{av} is the average bond strength, P_{max} is the maximum pull-out load, d_f is the fibre diameter, and L_E is the embedment length of steel fibre.

- Equivalent bond strength, τ_{eq} can be defined as the average bond strength based on the total pull-out work during the entire fibre pull-out [121].

$$\tau_{eq} = \frac{2 \times W_P}{\pi \times d_f \times {L_E}^2} \tag{4.3}$$

where, τ_{eq} is the equivalent bond strength, W_p is the total pull-out work, d_f is the fibre diameter, and L_E is the embedment length of steel fibre.

4.4.3 Results and discussion

4.4.3.1 Fresh and hardened properties of UHPCs

To evaluate the workability and rheological properties of fresh concretes, the slump-flow test according to EN 12350-8:2010 [122] were performed. It can be seen from Table 4.6 that all ultra-high performance concretes (UHPCs) mixtures had excellent rheological and self-compacting properties. However, the reducing of W/B ratio leads to a decrease in slump-flow diameter (SFD), while time to reach 500mm spread (T_{500}) is increased. This is in agreement with other results reported by Deeb et al. [123]. The average compressive strength was remarkably enhanced for all UHPCs by decreasing W/B ratio (Table 4.6). This indicates that an excessive water in the matrix may result in adverse effect on the formulation of microstructure and hence the property of the concrete.

Table 4.6 Properties of fresh and hardened UHPCs

Mixtures	*Slump flow test*		*Density*	$f^{*}_{cm,28d}$(MPa)
	$T_{500\ (S)}$	SFD(mm)	(kg/m^3)	
UHPC1	6	780	2497	178
UHPC2	4	850	2485	152
UHPC3	3	910	2464	149

* average of three specimens

4.4.3.2 Effect of water/binder ratio on pull-out behaviour

The average pull-out load-slip curves of the two types of 3DH hooked end steel fibres embedded in ultra-high performance concrete matrix with three different water/binder ratios (W/B=0.15, 0.20, 0.25) are presented in Figures 4.12 and 4.13. The maximum pull-out load and the total pull-out work (the area under the pull-out curve) of both types of hooked end fibres increase as the W/B ratio decreases (Table 4.7). It can also be seen from the curves that decreasing W/B ratio from 0.25 to 0.15 remarkably enhances the maximum pull-out load and pull-out work. However, for 3DH1 fibre with L_E (15mm) and 3DH2 fibre with L_E (30mm) a slight difference in pull-out behaviour is observed when W/B ratio decreased from 0.25 to 0.20. The high compressive strength associated with 0.15W/B ratio (f_c=172 MPa) and the close compressive strengths for 0.20W/B ratio (f_c=152 MPa) and 0.25W/B ratio (f_c=149MPa) can interpret the better pull-out behaviour of the specimens with 0.15W/B ratio and the similar behaviour of the specimens with 0.20W/B and 0.25 W/B ratios.

On the other hand, the pull-out response of both types of fibres exhibit somewhat different slip behaviour before the second drop of the pull-out load. As can be seen in Figures 4.12 and 4.13, the slip capacity of both fibres noticeably increases when W/B ratio decreases. It has been found that the decease of W/B ratio not only increases the maximum pull-out load but also effectively enhances the Δ_{peak} (Table 4.7). This effect may be attributed to the significant improvement in the fibre-matrix interfacial properties in term of bond strength. Furthermore, a significant difference in the total pull-out work can be observed due to different slip capacities.

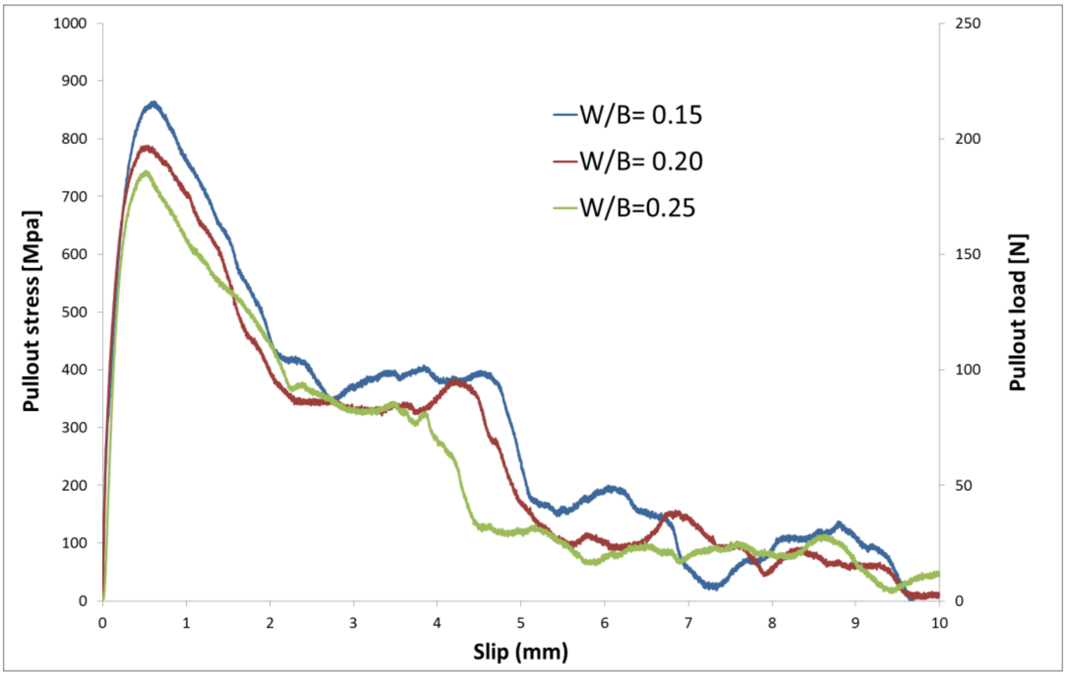

(a)

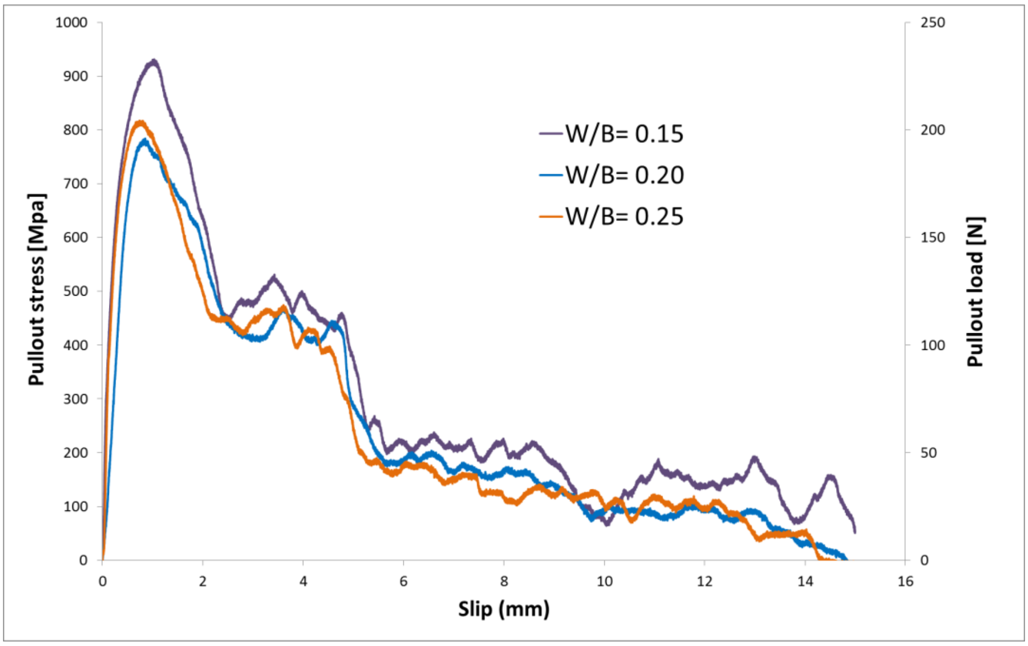

(b)

Figure 4.12 Average pull-out load-slip curves of 3DH1 fibres: (a) embedded length (10 mm) and (b) embedded length (16 mm)

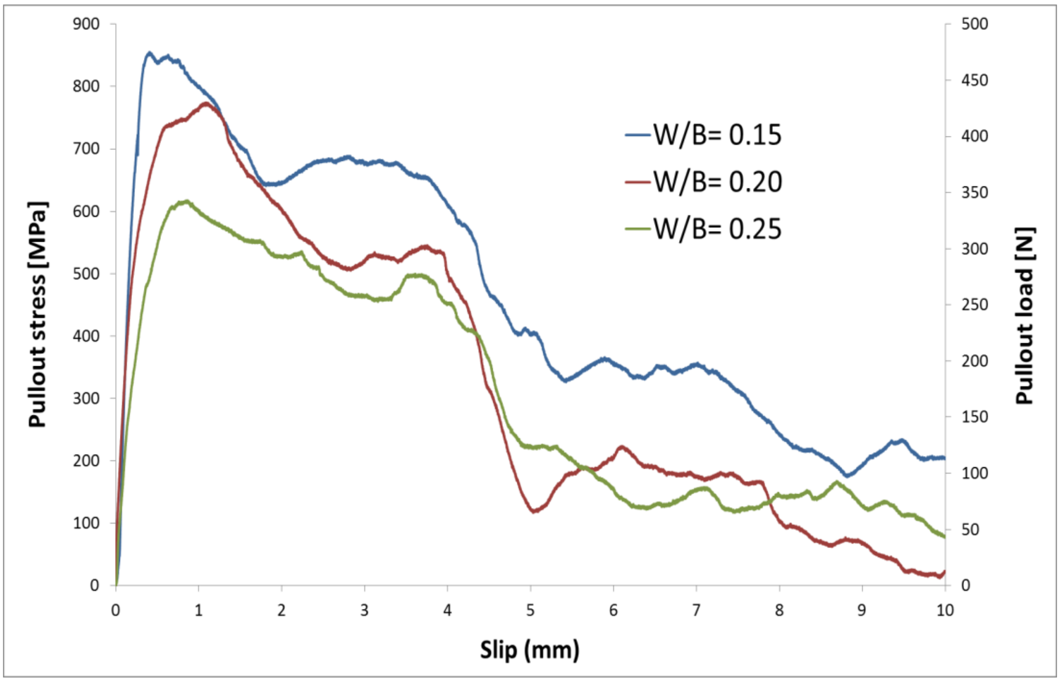

(a)

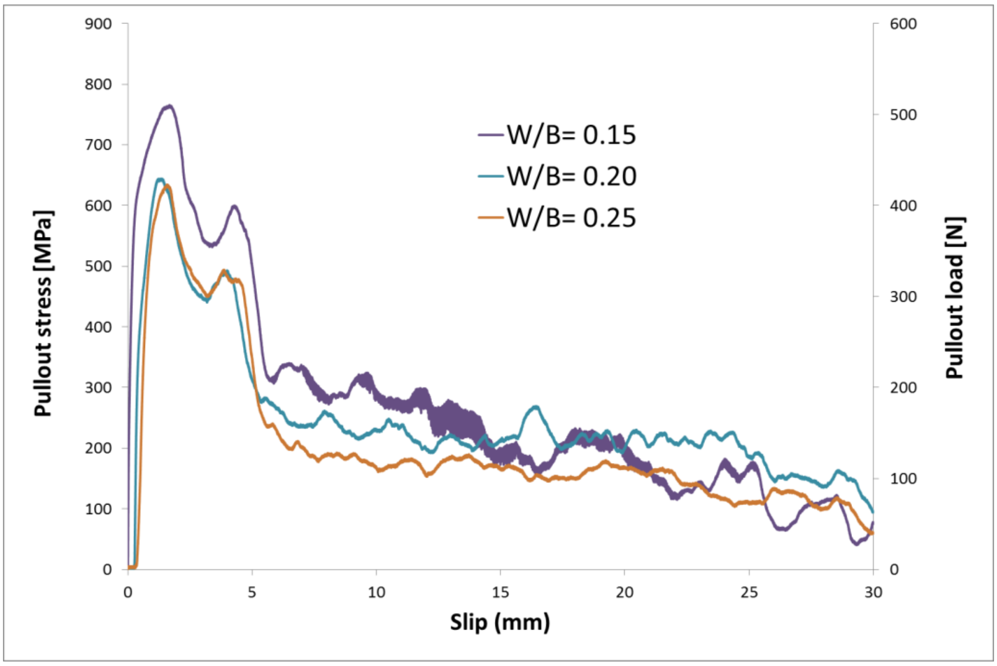

(b)

Figure 4.13 Average pull-out load-slip curves of 3DH2 fibres: (a) embedded length (10 mm) and (b) embedded length (30 mm)

Table 4.7 The experimental parameters of pull-out test

Series	Medium	Embedded length(mm)	P_{max} (N)	Δ_{peak} (mm)	W_{total} (N-mm)	σ_{max}/f_y (-)	σ_{max}	τ_{eq}	τ_{av}
							(N/mm^2)		
3DH1-U1-LE10		10	216	0.61	753	0.67	909	8.72	12.51
3DH1-U1-LE15	UHPC1	15	233	1.02	1153	0.73	980	5.93	8.90
3DH2-U1-LE10		10	475	0.40	2595	0.64	747	18.36	16.85
3DH2-U1-LE30		30	510	1.67	5443	0.69	802	4.28	12.14
3DH1-U2-LE10		10	196	0.48	664	0.61	825	7.69	11.33
3DH1-U2-LE15	UHPC2	15	195	0.85	922	0.61	821	4.74	7.58
3DH2-U2-LE10		10	430	1.08	1848	0.58	676	13.08	15.29
3DH2-U2-LE30		30	429	1.36	5027	0.58	675	3.95	10.16
3DH1-U3-LE10		10	185	0.49	598	0.58	779	6.93	10.77
3DH1-U3-LE15	UHPC3	15	204	0.73	908	0.63	860	4.67	7.82
3DH2-U3-LE10		10	342	0.86	1706	0.46	539	12.07	12.14
3DH2-U3-LE30		30	423	1.58	4120	0.57	665	3.23	9.95

For the 3DH2 fibre with embedded length of 10 mm, the maximum pull-out load is increased by 38.88%, while the corresponding increase for 3DH1 fibre is only 16.75%, when W/B ratio decreased from 0.25 to 0.15. In contrast, the decrease of W/B ratio from 0.25 to 0.20 the maximum pull-out load of the 3DH2 fibre with embedded length of 30mm is only increased by 1.41%, while for the 3DH1 fibre with embedded length of 15mm it is decreased by 4.41%. This indicates that the decrease W/B ratio from 0.25 to 0.20 does not offer any improvement in maximum pull-out load. On the other hand, the improvement in total pull-out work due to decrease in W/B ratio is relatively more significant than that in maximum pull-out load for both types of fibres with L_E (10mm). The total pull-out work is increased by 52.11 and 25.9% for 3DH2 and 3DH1 fibres, respectively when W/B decreased from 0.25 to 0.15 (Table 4.7). These results are directly related to significant improvement in bond strength which increases the consumed energy during the pull-out process.

According to Figure 4.14, it can be seen that the average and equivalent bond strength are remarkably increased due to the decrease in W/B ratio. However, the great effect of decreasing W/B ratio is found to be optimal at the W/B ratio of 0.15, which has the highest values for both the average and equivalent bond strength. The significant enhancement in bond strength due to a decrease in W/B ratio from 0.25 to 0.15 may help to explain the noticeably high values of pull-out load and total pull-out work. For the 3DH2 fibre with embedded length of 10 mm, the average and equivalent bond strength are increased by 38.84% and 52.28%, respectively, whereas for the 3DH1 fibre it only increased by 25.83% and 16.82 %, respectively, when W/B ratio decreased from 0.25 to 0.15.

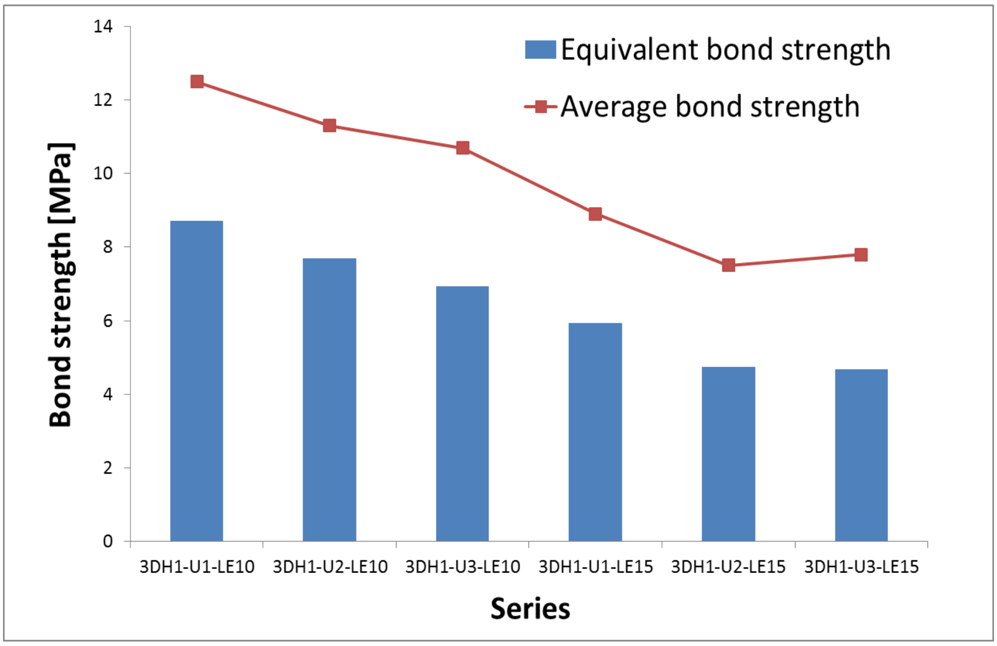

(a)

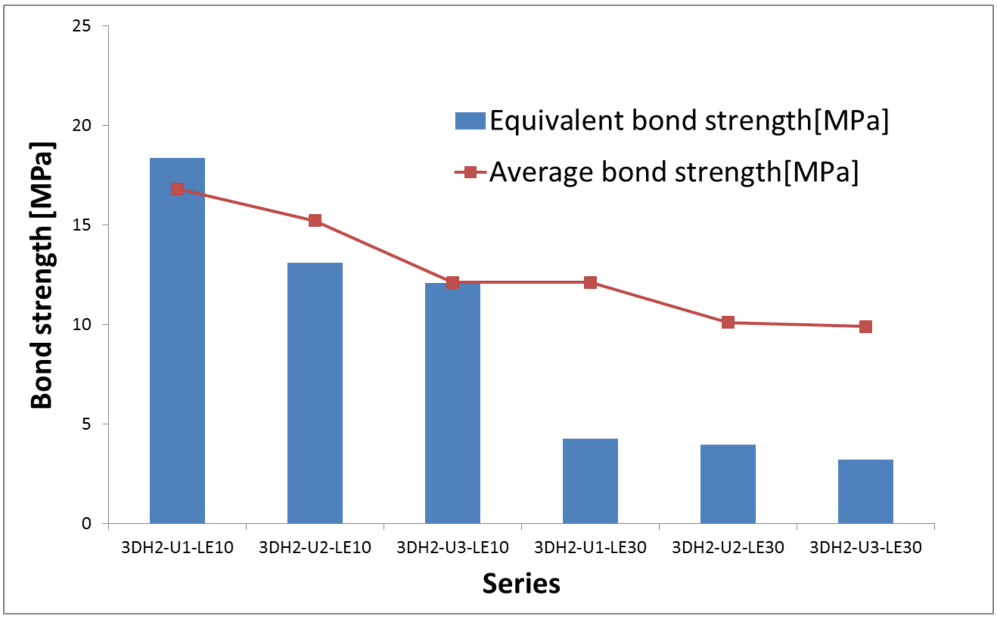

(b)

Figure 4.14 Effect of W/B ratio on the bond strength of (a) 3DH1 fibres and (b) 3DH2 fibres

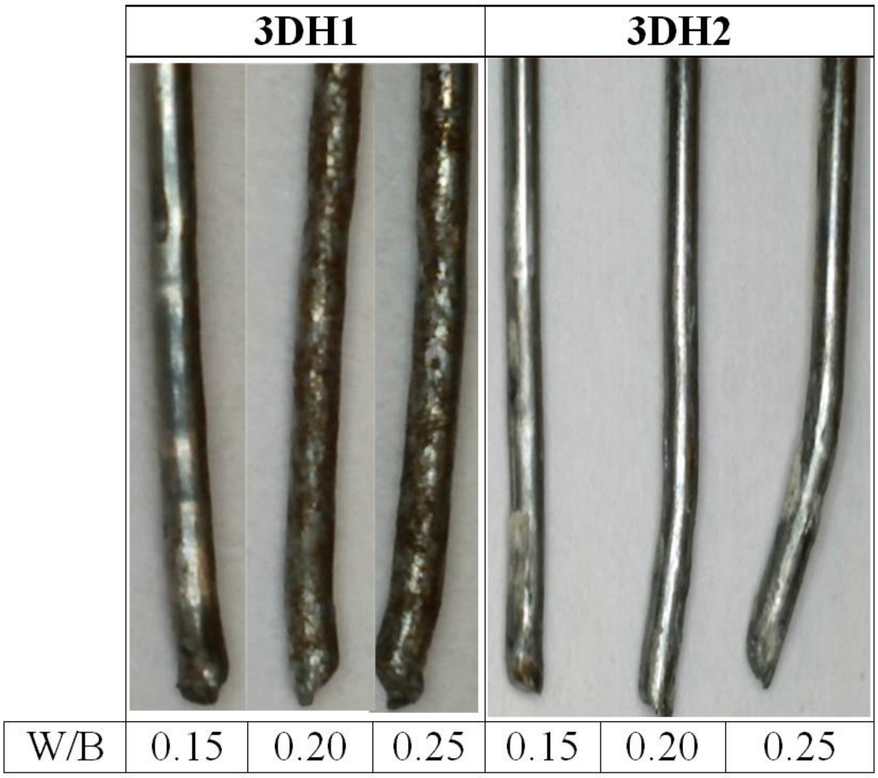

Figure 4.15 Image shows the comparison between 3DH1 and 3DH2 fibres after pull-out

Figure 4.15 shows the images of fibres after pull-out tests with various W/B ratios. It can be seen that the end hook of both types of fibres was somehow straightened, with those pulled out from the matrix with the W/B ratio of 0.15 being more straight compared with those in matrix with other W/B ratios. The reason for this behaviour may be explained by the enhancement of the fibre-matrix interfacial properties. This was also confirmed by the remarkable improvement in pull-out behaviour, equivalent bond strength and average bond strength (Table 4.7). Although the fibres embedded in the matrix with 0.20 and 0.25 W/B ratios were completely deformed, the full straightening of their end hook did not occur. Nevertheless, the straightening of the end hook of both types of fibres embedded in matrices with 0.20 and 0.25 W/B ratios are similar. This reinforces the conclusions that the decreasing W/B ratio from 0.25 to 0.20 may not improve the interfacial bond characteristics as in case of 0.15 W/B.

The tensile stress induced in fibre or the maximum fibre stress is then interpreted and summarized in Table 4.7 and Figures 4.12 and 4.13. Although the values of induced stress in both types of fibres are comparable in matrices with 0.20 and 0.25 W/B ratios, a significant improvement in the maximum fibre stress was achieved for all fibres in matrix with 0.15 W/B ratio. The maximum fibre stress of the 3DH2 fibre with embedded length of 10 mm is increased by 25.41%, while for the 3DH1 fibre only 5.90% when W/B ratio decreases from 0.25 to 0.20. However, a further decrease in W/B ratio to 0.15 leads to remarkable increase in the maximum tensile stress about 38.58%, and 16.68% for the 3DH2 and 3DH1 fibres, respectively. This represents an utilisation of about 64 % and 67 % of extra tensile capacity of these fibres, respectively.

4.4.3.3 Effect of fibre embedment length on pull-out behaviour

In order to evaluate the influence of embedment length of hooked end steel fibres on pull-out behaviour, two different embedded lengths (L_E) for each type of fibres have been considered in this study. For the 3DH1 fibre, the embedment length investigated is 10 and 15mm, while that for the 3DH2 fibre is 10 and 30 mm.

Overall, both types of fibres showed extremely similar pull-out behaviour but difference in maximum pull-out load and pull-out work (Figures 4.12 and 4.13).

It is apparent that the increase of embedment length has no great effect on the maximum pull-out load but it relatively increases the total pull-out work. This can be explained by the slightly higher maximum pull-out load was observed for both types of fibres in 0.20 W/B ratio series with an embedded length of 10 mm than those of 15 and 30 mm (Table 4.7). This is also in accordance with the results of other researchers.

On the other hand, since the measured lengths (L_1+L_2) of the end hook of the 3DH1 and 3DH2 fibres were approximately 4.80 and 5 mm (Table 4.5), respectively. It is believed that an embedment length of 10 mm which is roughly twice of the length of the end hook is efficient to achieve full mobilization and straightened end hook. This indicates that the pull-out behaviour is drastically governed by the hook component and increasing in embedment length does not have significant contribution to the maximum pull-out load. On the basis of this, it can be concluded that if the fibre is fully deformed and straightened, it seems that the fibres with a shorter embedded length (10 mm) can be used to obtain the same efficiency as fibres with a larger embedded length (15 or 30 mm). This was also confirmed from the results of average and equivalent bond strength in Table 4.7. Although the bond strength is drastically enhanced by W/B ratio, the increase in fibre embedment length remarkably decreases both the average and equivalent strength. In addition, there is nearly no significant increase in the maximum pull-out load relative to the increase in embedded length which leads to decrease in the bond strength. It seems that the maximum pull-out load is significantly influenced by the plastic deformation of the fibre hook and increase the embedded length only enhances the frictional pull-out stage.

Table 4.7 also summarizes the key parameters of pull-out behaviour of all series of tests performed in this study. It can be observed that the maximum fibre stress of the 3DH1 fibres is somewhat higher than that generated by the 3DH2 fibres. On the other hand, although reducing W/B ratio particularly from 0.25 to 0.15 considerably enhances the fibres stress-slip behaviour, the increase in embedded length has no remarkable effect on the maximum fibre stress. It is noteworthy from Table 4.7 that for the matrix with 0.20 W/B ratio the increase in embedded length of both types of fibres did not improve fibre stress and the values of the maximum fibre stress is found to be very similar.

In comparing the pull-out behaviour of 3DH1 fibre with an embedded length of 10 mm (Figure 4.12a) with that of 15mm (Figure 4.12b) embedded length, no clear difference is observed, particularly, for the matrix of W/B ratio of 0.20 or 0.25. Similarly the 3DH2 fibre showed that the increase in the embedded length from 10 mm to 30 mm slightly enhancing the maximum fibre stress (Figure 4.13). This leads to the conclusion that the increase in fibre embedment length after specific limit which is 10mm in this study does not contribute to maximum fibre stress but only improve the total pull-out work. Although many studies reported that increase the embedded length of straight fibres can develop higher tensile stresses during pull-out, it appears not to be the case for hooked-end steel fibres [43]. Since the embedded length of 10 mm seems to be enough for achieving the full deformation and straightening of the hook, an increase of embedded length is no longer play an important role for maximum fibre stress. This behaviour was also confirmed from the results (Table 4.7) of the fibre efficiency ratio (σ_{max}/f_y), which represents the maximum tensile stress induced during pull-out, σ_{max} over the fibre tensile strength, f_y. A slight difference is also observed between the values of (σ_{max}/f_y) ratio when the embedded length increases. Although the increase in embedded length slightly increases the maximum tensile stress induced by fibres, both types of fibres embedded in the matrix with 0.20 W/B showed the same value of (σ_{max}/f_y) ratio even with embedded length increases from 10 to 15 and 30mm. These results strongly proved that the end hook of fibres with embedded length of 10 mm can be fully deformed and straightened, and any increase in the embedded length does not affect much the pull-out behaviour.

4.4.3.4 Microscopic observations (SEM - Scanning Electron Microscopy)

Figure 4.16a shows SEM images of the steel fibre-matrix interface of the UHPC1 mixture (W/B=0.15). It can be seen from this figure that the particle dispersion and packing density at fibre-matrix interface is well-developed in the UHPC1 matrix. This is mainly due to the low W/B and pozzolanic reactions between silica fume and calcium hydroxide, which consumes most of the CH crystals and transforms them to C-S-H [73,124]. The densification of microstructures in the interfacial transition zone (ITZ) due to congestion of the hydration products significantly enhances the bond properties between fibre and matrix. [125] found that concrete with 0.3 W/B had higher debonding loads and fracture energies than that of the 0.5 W/B. It has been reported that the incorporation of silica fume can effectively improve the interfacial bond by reducing the porosity, refining the pores, and increasing the density and content of the C-S-H [11,126]. Also, the lower the porosity, the higher the particle packing density in the ITZ and bulk the matrix. Thus, a higher content of the cement hydration products such as C-S-H is important to enhance the microstructure and microhardness of the ITZ, resulting improves the transmission of stress between the fibre and matrix [127] .

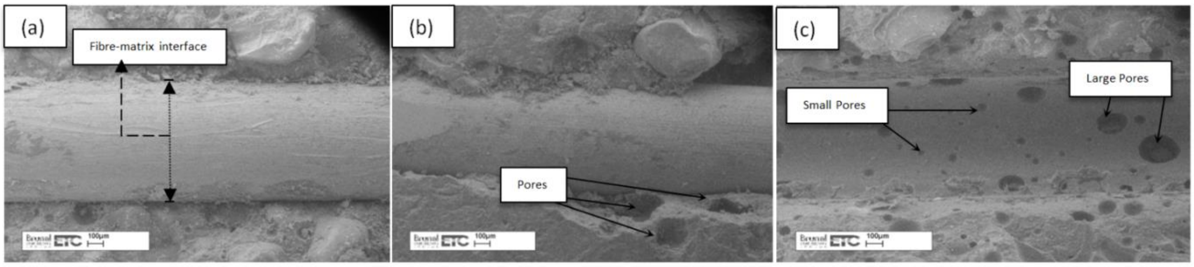

Figure 4.16 SEM images of the fibre-matrix interface:(a) UHPC1(W/B=0.15), (b) UHPC2 (W/B=0.20) and (c) UHPC3 (W/B=0.25)

Figure 4.16b shows the SEM images of the fibre-matrix interface of the UHPC2 mixture (W/B=0.20). It can be observed from this figure that some pores are formed in the ITZ. A according to [125], although the incorporation of 10% silica fume has a positive effect on the fracture and compressive energies, the improvement in debonding loads was not observed. They revealed that if silica fume particles are not dispersed properly in the concrete, an increased amount of C-S-H through the pozzolanic reaction cannot be achieved, regardless of W/B. With further increase in W/B from 0.20 to 0.25, a numerous small and large pores were observed which have formed along the ITZ (Figure 4.16c). Basically, the higher water content is responsible for forming the pores, ultimately leading to decrease in the bond strength of the UHPC3 mixture significantly. [127] has also observed a large porous zone located within 50 mm from the fibre edge for UHPC with 0.18 W/B. This weak zone could significantly reduce the contact surface area between fibre and matrix. These facts may help to explain the relatively lower pull-out load and total pull-out work of the matrix with 0.25 W/B ratio compared with 0.15 W/B.

4.4.3.5 Mechanical anchorage contribution of the end hook to pull-out behaviour

To get better understanding of the contribution provided by the end hook to pull-out behaviour, a quantitative account for hook mechanisms has been adopted. This follows that the proposed procedure is mainly dependent on the measured hook lengths which are approximately 4.78 and 5 mm for the 3DH1 and 3DH2 fibres respectively (Table 4.5). As can be seen from Figure 4.17, the end hook contribution is nearly being finished at 4.78 mm for the 3DH1 fibre and 5 mm for the 3DH2 fibre, which corresponds to decay of pull-out load due to complete deformation and straightening of the end hook. Consecutively, the friction resistance contribution initiates and continues until fibres completely pull-out. On the other hand, while test results revealed that the debonding process finishes at fibre slips up to less than 0.1 mm; its contribution to total pull-out work is found to be lower than 1% for all fibres series. Therefore, the contribution due to debonding process can be neglected. This procedure provides basic information about the effects of the parameters such as W/B ratio, diameter, embedded length and tensile strength of fibres on pull-out behaviour.

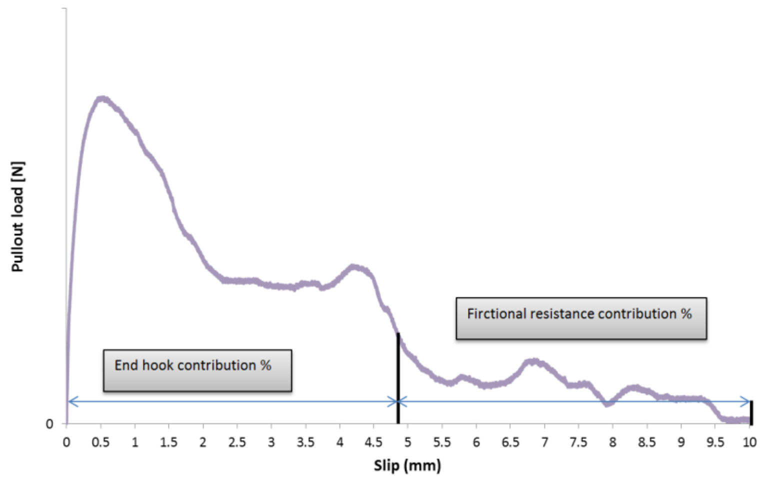

Figure 4.17 Example showing the contribution of the end hooks component and frictional resistance to the overall pull-out behaviour of 3DH2 fibres

The percentage contribution of the end hook and frictional resistance on the total pull-out work is summarized in Table 4.8. From the experimental results of the both types of hooked fibres (Table 4.8), it can be observed that as the embedded length of fibre increases, the percentage of hook contribution in terms of total pull-out work dramatically decreases. Although the percentage of hook contribution with embedded length of 10 mm is significantly higher than that of the frictional resistance, the increase in embedded length especially of the 3DH2 fibres drastically increase the contribution percentage of frictional resistance. The increase of embedded length of the 3DH1 fibres from 10 to 15mm leads to slight decrease in the hook contribution, while for the 3DH2 fibres the increase in embedded length from 10 to 30 mm results in a sharp decrease in hook contribution up to half of that in case of 10 mm embedded length. This can be attributed to large surface area of fibre in contact with surrounding matrix which increases the frictional resistance to pull-out. Based on experimental results, it appears that the embedded length has a greater effect on total pull-out work than maximum pull-out load.

Table 4.8 The end hook and frictional resistance contribution to the total pull-out work

Series	Medium	Embedded length(mm)	End hook contribution %	Frictional resistance contribution %
3DH1-U1-LE10		10	82.42	17.57
3DH1-U1-LE15	UHPC1	15	64.02	35.97
3DH2-U1-LE10		10	69.47	30.52
3DH2-U1-LE30		30	37.64	62.35
3DH1-U2-LE10		10	83.67	16.32
3DH1-U2-LE15	UHPC2	15	68.46	31.53
3DH2-U2-LE10		10	80.88	19.11
3DH2-U2-LE30		30	30.43	69.56
3DH1-U3-LE10		10	83.47	16.52
3DH1-U3-LE15	UHPC3	15	70.48	29.51
3DH2-U3-LE10		10	76.36	23.63
3DH2-U3-LE30		30	36.31	63.68

4.4.3.6 Difference in the pull-out behaviour of two hooked end fibres

The observed pull-out load-slip curves of hooked end steel fibres embedded in UHPC is generally characterised by a steady increase up to peak load as a result of the combination of two mechanisms which are: detachment of the fibre-matrix bond and mechanical anchorage of the end hook. Once the fibre-matrix bond is fully detached, two plastic hinges of the fibre hook undergo cold work causing deformation and bending of the end hook [98], in Figure 4.18, the two plastic hinges are identified as 1 and 2. As a result of deformation and slippage of the first plastic hinge a sharp decrease in pull-out load takes place. Nevertheless, initial increase in pull-out load can be observed due to the progressive deformation of the second plastic hinge in conjunction with straightening of the end hook. The last stage of the pull-out will occur under sliding friction until complete pull-out of fibre from the concrete matrix.

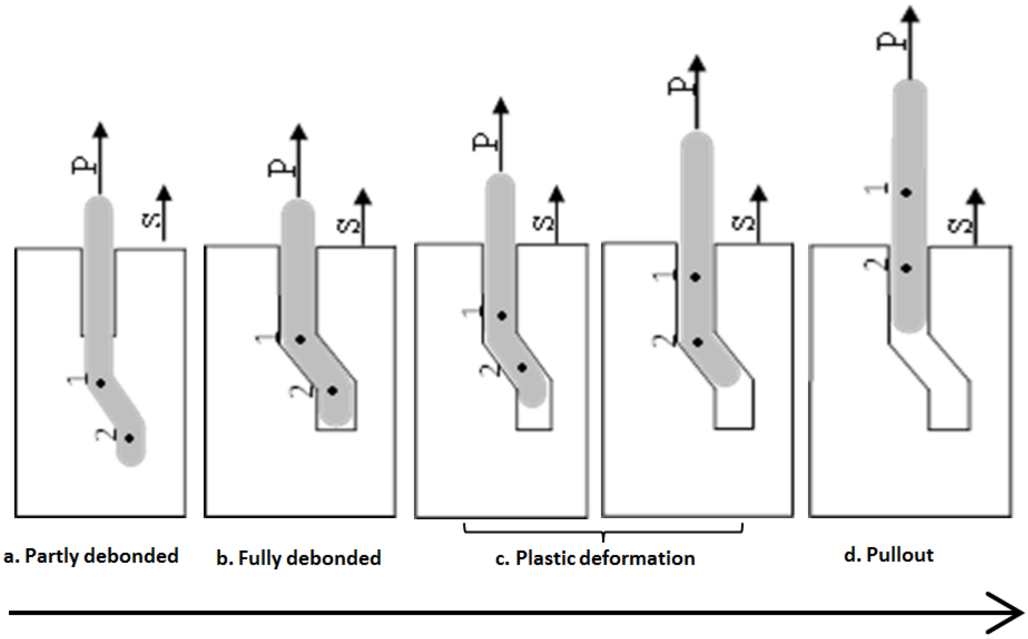

Figure 4.18 Pull-out process of a hooked end steel fibre

The comparison of the pull-out behaviour between the two hooked end fibres shows that the maximum pull-out load of the 3DH2 fibres is approximately more than two times that of the 3DH1 fibres for all W/B ratios. Moreover, the total pull-out work of the 3DH2 fibres embedded up to half fibre length (L_E=30 mm) is roughly five times that the 3DH1 fibres (L_E=15 mm). It is believed that the reason for the enhanced pull-out work is due to the increased embedded length which leads to large surface area of fibre in contact with surrounding matrix. Note that the embedded length of the 3DH2 fibre (L_E =30 mm) is two times that of the 3DH1 fibre (L_E =15mm), to allow fair comparison an embedment length of 10 mm for both types of fibres is considered here. The pull-out work of the 3DH2 fibre is also approximately three times greater than that of the 3DH1 fibre. This may be attributed to the fibre diameter that increases the bending stiffness of fibre hook, because more energy is required during the pull-out process.

On the other hand, although the decrease in W/B ratio has positive effect for both types of fibres, this effect is more pronounced for the 3DH2 (diameter of 0.9 mm) than that of the 3DH1 (diameter of 0.55 mm) fibre. The reduction of W/B ratio from 0.25 to 0.15 leads to increases in maximum pull-out load of the 3DH2 is 38.88%, which is approximately more than two times that achieved by the 3DH1 fibres (16.75%). These results suggest that the fibre with larger diameter is considerably influenced by enhancing fibre-matrix interfacial properties than that with smaller diameter.

For the fibre stress-slip, the induced stress in the 3DH1 fibres which have smaller fibre diameter (d_f =0.55), is higher than that of the 3DH2 fibres with (d_f =0.90) (Figure 4.12). This may be due to the larger cross-sectional area of the 3DH2 fibre which is approximately 2.6 times greater than that of the 3DH1 fibre. The maximum tensile stress induced in the 3DH1 fibres with the embedded length of 10 mm is higher by 21.68%, 22.11% and 44.52% than those in the 3DH2 fibres for 0.15, 0.20 and 0.25 W/B ratio, respectively. Despite the fact that the tensile strength of the 3DH1 fibres (f_y=1345 MPa) is higher than that of the 3DH2 fibres (f_y=1160 MPa), a slight difference in the values of (σ_{max}/f_y) ratio were observed. This indicates that the 3DH2 and 3DH1 fibres have somewhat similar efficiency in the utilization of tensile strength capacity.

4.4.3.7 Concluding remarks

The effect of W/B ratio of ultra-high performance concrete on the pull-out behaviour of two types of hooked end steel fibres has been investigated. Some specific conclusions can be drawn as follows:

1. The maximum pull-out load of the 3DH2 fibres was more than two times that of the 3DH1 fibres. For the same embedded length the total pull-out work of the 3DH2 fibres was about three times that of the 3DH1 fibres.
2. An increase in embedded length had no appreciable effect on the maximum pull-out load but resulted in a slight improvement in the total pull-out work due to larger surface area of fibre in contact with surrounding matrix. The little effect of fibre embedded length on bond properties was due to very limited difference in length and significant mechanical anchorage associated with hooked end.
3. The decrease in W/B ratio from 0.2 to 0.15 had a significant effect on the overall pull-out behaviour. However, no remarkable contribution could be observed when W/B ratio decreased from 0.25 to 0.20. The hooked end fibres with larger diameter would be a better choice with lower W/B ratio.
4. For the same embedded length, the equivalent bond strength of the 3DH2 fibres was approximately two times greater than that of the 3DH1 fibres for all series.
5. Though the tensile strength of the 3DH1 fibres was higher by 16% than that of the 3DH2 fibres, both fibres showed similar efficiency of utilising its tensile stress capacity. The mechanical contribution of the 3DH2 fibres would be highly effective if the fibre tensile strength could be increased.

Chapter 5 Predicting Pull-out Behaviour of Hooked- end Steel Fibres Embedded in Various Concretes

5.1 Introduction

Brittle materials such as concrete and mortar are well known for their low ability to resist tensile stresses and crack propagation [71]. The incorporation of randomly distributed steel fibres to a cementitious matrix could significantly improve their tensile behaviour, ductility, impact resistance and crack resistance [58,68,69,128].

The fibre contribution is mainly reflected when the concrete cracking initiates and often enhances the post-cracking behaviour due to the improved stress transfer provided by the fibre bridging of the cracked sections [31]. The efficiency of fibre in transferring stress is greatly dependent on bond mechanisms between fibre and matrix [60]. Therefore, the knowledge of the bond mechanisms is a key factor to understand the tensile behaviour of steel fibre-reinforced concrete (SFRC), especially for hooked end fibres. The bond characteristics are commonly assessed using the single fibre pull-out test, which is able to determine the interfacial properties between the fibre and the surrounding cementitious matrix [34,35]. A review of the literature indicated that pull-out tests have mostly been performed by means of a single-fibre on single-sided test due to the simplicity and reliability of the test [29]. On the other hand, a pull-out test on a multiple-fibre specimen is more complex to manufacture and difficult to test [76]. Moreover, use of these tests to measure pull-out behaviour quantitatively is complicated by the difficulty in achieving a uniform distribution of load to all the fibres [61].

Numerous experimental and analytical investigations have been conducted to determine the bond mechanisms between steel fibre and matrix [11,30,31,129]. Based on the results, it is concluded that the mechanical deformation of fibres and matrix strength play a major role on pull-out response. However, there have been few attempts to model the effect of fibre geometry on the pull-out behaviour of steel fibres. The first predictions of the pull-out force of hooked end fibres were proposed by Alwan et al. [98] and Chanvillard [111]. Alwan et al. [98] developed an analytical model to predict the mechanical anchorage contribution provided by the fibre hook. Their model is based on the concept of a frictional pulley along with two plastic hinges. The mechanical contribution provided by the fibre is considered as a function of the cold work needed to straighten the hook during pull-out. To predict the entire pull-out versus slip response a two-step process is required corresponding to (i) the contribution of the two hinges, and (ii) the superposition of the frictional and mechanical components. An alternative approach was proposed by Chanvillard [111] using principles of virtual work dividing the hook into distinct curved and straight parts.

Sujivorakul et al. [130] extended the straight fibre pull-out model developed by Naaman et al. [114] by adding a non-linear spring at the end of the fibre to simulate the mechanical anchorage contribution. In later work Laranjeira et al. [13], Ghoddousi et al. [113], and Lee et al. [29] proposed new models which are quite comparable to the model developed by Alwan et al. [98]. Soetens et al. [66] have proposed a semi-analytical model to predict the pull-out behaviour of hooked end steel fibres based on the principle of virtual work developed by Chanvillard [111]. Zile et al. [12] have developed an analytical model to simulate the mechanical contribution of fibre geometry to the pull-out response of crimped and hooked end steel fibres. This model is based both on the amount of plastic work required to straighten the fibre during pull-out and friction in the curved ducts. Won et al. [14] have developed an analytical model based on model developed by Zile et al.[12] to simulate bond mechanism of arch-type steel fibres. The friction model is more convenient to adopt the recent designs, where 4D and 5D hooked end steel fibres of improved shape were introduced. These fibres were designed to achieve high levels of fibre anchoring, tensile strength and ductility. Although fibre-matrix bond mechanisms of old generation of hooked end fibres (named 3D) have been largely investigated, the existing models are not sufficient to predict the pull-out behaviour of newly fibres (i.e. 4D and 5D). This is because the mechanisms associated with pull-out behaviour of these new hooked end fibres (i.e. 4D and 5D) are not yet understood.

The main objective of this chapter is to develop a simple analytical model to simulate the mechanical anchorage contribution provided by the hook of 4D and 5D fibres. The proposed model extends the frictional pulley model developed by Alwan et al. [98] to include fibres with three and four plastic hinges in their end hooks. The input parameters of the model are the geometrical and mechanical properties of various hooked end fibres. The model predictions are validated against experimental pull-out test results of all fibres embedded in various concretes.

5.2 Mathematical equations for fibre pull-out behaviour

It has been shown from experimental observations that the pull-out process of a hooked end steel fibre is quite similar to that of a straight fibre up to fibre complete debonding. After this, the mechanical anchorage effect provided by the hook is mainly responsible for the pull-out resistance. The mathematical derivation of pull-out behaviour of a straight fibre has been explained in detail in Naaman et al. [114] and given in section 2.8.1. The pull-out process of hooked end fibre can be divided into three different stages as follows (Figure 2.15a-d):

5.2.1 Elastic and partial debonding stage

When $P \leq P_1$ (Figure 2.14), a part of the fibre is debonded from the matrix while the remaining part is still fully bonded to the matrix. Here, a part of the pull-out force is resisted partially by elastic shear stresses, while the other part is resisted partially by interfacial frictional stresses (Figure 2.15). In that stage, the pull-out load (P) and the corresponding slip (Δ) are given as [114]:

$$P = \tau_f \psi u + \frac{\tau_{max}}{\lambda} \frac{1 - e^{-2\lambda(l-u)}}{\frac{2}{Q} e^{-\lambda(l-u)} + (1 - \frac{1}{Q})(1 + e^{-2\lambda(l-u)})} \tag{5.1}$$

$$\Delta = \frac{\left[P(Q-1)u - \frac{\tau_f \psi u^2}{2}(Q-2) + \left(P - \tau_f \psi u\right)\frac{1-e^{-\lambda(l-u)}}{1+e^{-\lambda(l-u)}}\frac{Q-2}{\lambda} - \tau_f \psi l\right]}{A_m E_m} \quad (5.2)$$

where, τ_{max} is the maximum elastic bond strength at the fibre-matrix interface; τ_f is the frictional bond stress at the fibre-matrix interface; u is the debonded length of fibre; ψ is the fibre perimeter;

$$Q = \frac{(A_m E_m + A_f E_f)}{A_m E_m} \quad (5.3)$$

and,

$$\lambda = \sqrt{\frac{\psi k}{A_m E_m} + \left[1 + \frac{A_m E_m}{A_f E_f}\right]} \quad (5.4)$$

in which A_m, A_f, E_m, and E_f are the matrix, fibre cross-sectional areas and elastic moduli respectively, and k is the interfacial bond modulus.

5.2.2 Full debonding stage

When $P \geq P_1$, the fibre is assumed to be complete debonding after the slip Δ_1, and no mechanical anchorage before the slip Δ_1 (Figure 2.14). The pull-out load (P_1) can be predicted by the following equation [110,114].

$$P_1 = \psi \tau f_d(\Delta) \times (l - \Delta) \quad (5.5)$$

where, (l-Δ) is the length of fibre remaining embedded for any slip Δ, and τ_{fd} (Δ) is the frictional shear stress for a slip Δ; the subscript "d" implies damage or decay. The frictional shear stress can be assumed constant for any slip Δ. However, as in real tests, it is shown to deteriorate with increasing slip, its value as derived in Naaman et al. [110,114] is given by:

$$\tau_{fd}(\Delta) = \tau_{fi}\frac{e^{-(\Delta-\Delta_0)^{\eta}} - \xi e^{-(l)^{\eta}}}{1-\xi e^{-(l-\Delta+\Delta_0)^{\eta}}} \times \frac{1-EXP\left[\frac{-2v_f \mu (l-\Delta+\Delta_0)}{E_f r_f\left(\frac{1+v_m}{E_m}\right)+\left(\frac{1-v_f}{E_f}\right)}\right]}{1-EXP\left[\frac{-2v_f \mu l}{E_f r_f\left(\frac{1+v_m}{E_m}\right)+\left(\frac{1-v_f}{E_f}\right)}\right]} \quad (5.6)$$

where Δ is the relative slip of the fibre after full debonding; Δ_0 is the relative slip of the fibre at end of full debonding; as a first approximation it can be taken equal to the slip at maximum load; ξ is the damage coefficient, a dimensionless constant to give the analytical descending branch of the bond shear stress versus slip curve the same decaying trend as the experimental one; μ is the friction coefficient of the fibre-matrix interface; ν is the Poisson's ratio, with subscript "f" for fibre and "m" for matrix; and η is the coefficient describing the exponential shape of the descending branch of the bond shear stress versus slip curve; for smooth steel fibres, a value of 0.2 is recommended by Naaman et al. [110,114].

5.2.3 Mechanical anchorage stage

Once complete debonding has occurred at the fibre-matrix interface, the horizontal portion of the fibre would still be subjected to interfacial frictional stresses and the hooked end of the fibre undergoes cold work deformation through two plastic hinges as indicated in Figure 2.15b. The corresponding increase in the pull-out load value, due to the cold work from both plastic hinges, would then be added to P_1, resulting in a plateau load (P_2). This plateau value remains until the fibre is pulled by an additional distance "L_2", after which there would be only one active plastic hinge in the hooked end (Figure 2.15c), and the pull-out load would drop to P_3. The new load at P_3 would then be held constant as the fibre is pulled-out by an additional distance "L_1" after which the pull-out load versus fibre end displacement can then be described using the frictional pull-out model of straight fibres developed by Naaman et al. [114] (Figure 2.15d).

The first plateau load at P_2 (Figure 2.14) due to the contribution of two plastic hinges can be estimated by:

$$P_2 = P_1 + \Delta P' \tag{5.7}$$

where P_1 = Pull-out load at onset of complete debonding and $\Delta P'$ = Pull-out load due to two plastic hinges.

Similarly, the second pull-out load plateau at P_3 (Figure 2.14) can be defined as:

$$P_3 = P_1 + \Delta P'' \tag{5.8}$$

where, $\Delta P''$ = Pull-out load due to one plastic hinge.

In order to determine the value of $\Delta P'$ and $\Delta P''$, Alwan et al. [98] developed an equivalent pulley model (Figure 2.16). The model simply consists of two frictional pulleys. Both Pulleys have rotational and tangential components of friction resisting the pull-out process. The rotational friction component correspond to the cold work needed for straightening the steel fibre at the plastic hinge location, and is represented by F_{PH} in Figure 2.16. The tangential friction component represents the work of Coulomb friction between the steel fibre and the matrix at the contact corner during the straightening of the fibre; it is represented by F_1 and F_2 in Figure 2.16. T_1 and T_2 represent the chord tension before and after the first pulley respectively.

$$T_1 = \Delta P' \tag{5.9}$$

and that,

$$T_2 = \Delta P'' \tag{5.10}$$

R_1 and R_2 in Figure 2.16 represent the reaction forces at the pulley centres; they are directly related to F_1 and F_2 through the kinetic coefficient of friction between the fibre and the matrix, μ. From equilibrium in the Figure 2.16, the following relation can be derived:

$$T_1 = 2F_{PH} + F_1 + F_2 \tag{5.11}$$

$$T_2 = F_{PH} + F_2 \tag{5.12}$$

Where,

$$F_1 = R_1 \times \mu \tag{5.13}$$

And,

$$F_2 = R_2 \times \mu \tag{5.14}$$

But,

$$R_1 = T_1 \times cos\beta + T_2 * cos\beta \tag{5.15}$$

And,

$$R_2 = T_2 \times cos\beta \tag{5.16}$$

Hence,

$$T_1 = \frac{2F_{PH}\left[1 + \frac{\mu \times cos\beta}{1 - \mu \times cos\beta}\right]}{1 - \mu \times cos\beta} \tag{5.17}$$

$$T_2 = \frac{F_{PH}}{1 - \mu \times cos\beta} \tag{5.18}$$

The values of F_{PH} was determined from the equilibrium of moments about points from the equilibrium of moments about point “A” in the free body diagram sketch of the fibre plastic hinge presented in Figure 5.1.

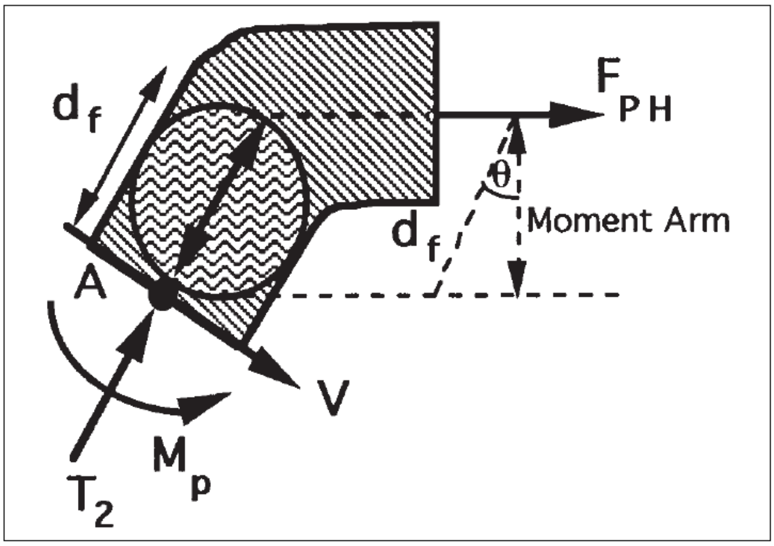

Figure 5.1 Sketch of the free body diagram of the fibre plastic hinge [123]

$\sum M_A = 0$

Thus,

$$M_P = F_{PH} \times (Moment\ arm = d_f * cos\theta) \tag{5.19}$$

Or,

$$F_{PH} = \frac{M_P}{d_f \times cos\theta} \tag{5.20}$$

The plastic moment of the steel fibre circular section, estimated as:

$$M_P = [f_y \times \frac{\pi r_f^2}{2} \times \frac{d_f}{3}] \tag{5.21}$$

where, r_f, d_f = the fibre radius and diameter, respectively and σ_y = the fibre yield strength

By substituting (5.20) in (5.17), we get:

$$\Delta P' = T_1 = \frac{\frac{\sigma_y \times \pi r_f^2}{3 \times cos\theta}\left[1 + \frac{\mu \times cos\beta}{1 - \mu \times cos\beta}\right]}{1 - \mu \times cos\beta} \tag{5.22}$$

Also by substituting (5.20) in (5.18), we get:

$$\Delta P'' = T_2 = \frac{\frac{\sigma_y \times \pi r_f^2}{6 \times cos\theta}}{1 - \mu \times cos\beta} \tag{5.23}$$

5.3 Proposed model for pull-out behaviour of 4DH and 5DH fibres

Based on the analytical procedure of the 3DH fibre illustrated above, an extended model is proposed to account for the mechanical contribution provided by the hook of 4DH and 5DH fibres. From Figure 3.3, it can be seen that the shape of the hook is idealized as three and four discrete hinges for 4DH and 5DH fibres respectively. Figures 5.2 and 5.3 show the pull-out process of 4DH and 5DH fibres, according to the three pull-out stages specified for 3DH fibres. It can be observed that the pull-out process of these fibres basically consist of five (4DH) and six (5DH) stages.

The four stages of the 3DH fibre pull-out scenario apply to 4DH and 5DH fibres as well (Figures 5.2 and 5.3); however, the mechanical anchorage stage (Figures 2.15b and c) is extended due to the plastic deformation contribution of three and four hinges (Figures 5.4a and b, respectively). In order to determine the values of pull-out load due to three and four plastic hinges; an equivalent pulley model is also extended, as described below:

5.3.1 Three hinges (4DH)

From equilibrium (Figures 5.5a), the following can be stated:

$$T_1 = 3F_{PH} + F_1 + F_2 + F_3 \tag{5.24}$$

Moreover,

$$F_1 = R_1 * \mu \tag{5.25}$$

$$F_2 = R_2 * \mu \tag{5.26}$$

$$F_3 = R_3 * \mu \tag{5.27}$$

but,

$$R_1 = T_1 * cos\beta + T_2 * cos\beta \tag{5.28}$$

$$R_2 = T_2 * cos\beta + T_3 * cos\beta \tag{5.29}$$

$$R_3 = T_3 * cos\beta \tag{5.30}$$

Substituting (5.*25*)-(5.*27*) in (5.*24*), we get:

$$\therefore T_1 = \frac{F_{PH}\left[3+\left(\frac{2\mu*cos\beta}{1-\mu*cos\beta}\right)\left[2\left(1+\frac{\mu*cos\beta}{1-\mu*cos\beta}\right)+1\right]\right]}{(1-\mu*cos\beta)} \tag{5.31}$$

5.3.2 Four hinges (5DH)

From equilibrium (Figures 5.5b), the following can be stated:

$$T_1 = 4F_{PH} + F_1 + F_2 + F_3 + F_4 \tag{5.32}$$

moreover,

$$F_1 = R_1 * \mu \tag{5.33}$$

$$F_2 = R_2 * \mu \tag{5.34}$$

$$F_3 = R_3 * \mu \tag{5.35}$$

$$F_4 = R_4 * \mu \tag{5.36}$$

but,

$$R_1 = T_1 * cos\beta + T_2 * cos\beta \tag{5.37}$$

$$R_2 = T_2 * cos\beta + T_3 * cos\beta \tag{5.38}$$

$$R_3 = T_3 * cos\beta + T_4 * cos\beta \tag{5.39}$$

$$R_4 = T_4 * cos\beta \tag{5.40}$$

substituting (5.33)-(5.36) in (5.32), we get:

$$\therefore T_1 = \frac{F_{PH}\left[4+\left(\frac{2\mu * cos\beta}{1-\mu * cos\beta}\right)\left[3+2\mu * cos\beta\left[2\left(1+\frac{\mu * cos\beta}{1-\mu * cos\beta}\right)+1\right]+2\left(1+\frac{\mu * cos\beta}{1-\mu * cos\beta}\right)+1\right]\right]}{(1-\mu * cos\beta)} \tag{5.41}$$

By using the above described procedure for 3DH fibre, the pull-out load (P) as a function of fibre slip (Δ) in all stages for 4DH (Eq. (5.42)) and 5DH (Eq. (5.43)) fibres can be obtained as follows:

$$P = \begin{Bmatrix} & P_1\ (Eq. 3) & \Delta_1 \\ \Delta P' = T_1\ (Eq. A8) & \rightarrow\ P_2 = P_1 + \Delta P' & \Delta_2 = \Delta_1 + u \\ \Delta P'' = T_2\ (Eq. 22) & \rightarrow\ P_3 = P_1 + \Delta P'' & \Delta_3 = \Delta_2 + L_3 \\ \Delta P''' = T_3\ (Eq. 23) & \rightarrow\ P_4 = P_1 + \Delta P''' & \Delta_4 = \Delta_3 + L_2 \\ & P_5 & \Delta_5 = \Delta_4 + L_1 \end{Bmatrix} \tag{5.42}$$

$$P = \begin{Bmatrix} & P_1\ (Eq. 3) & \Delta_1 \\ \Delta P' = T_1\ (Eq. A18) & \rightarrow\ P_2 = P_1 + \Delta P' & \Delta_2 = \Delta_1 + u \\ \Delta P'' = T_2\ (Eq. A8) & \rightarrow\ P_3 = P_1 + \Delta P'' & \Delta_3 = \Delta_2 + L_4 \\ \Delta P''' = T_3\ (Eq. 22) & \rightarrow\ P_4 = P_1 + \Delta P''' & \Delta_4 = \Delta_3 + L_3 \\ \Delta P'''' = T_4\ (Eq. 23) & \rightarrow\ P_5 = P_1 + \Delta P'''' & \Delta_5 = \Delta_4 + L_2 \\ & P_6 & \Delta_6 = \Delta_5 + L_1 \end{Bmatrix} \tag{5.43}$$

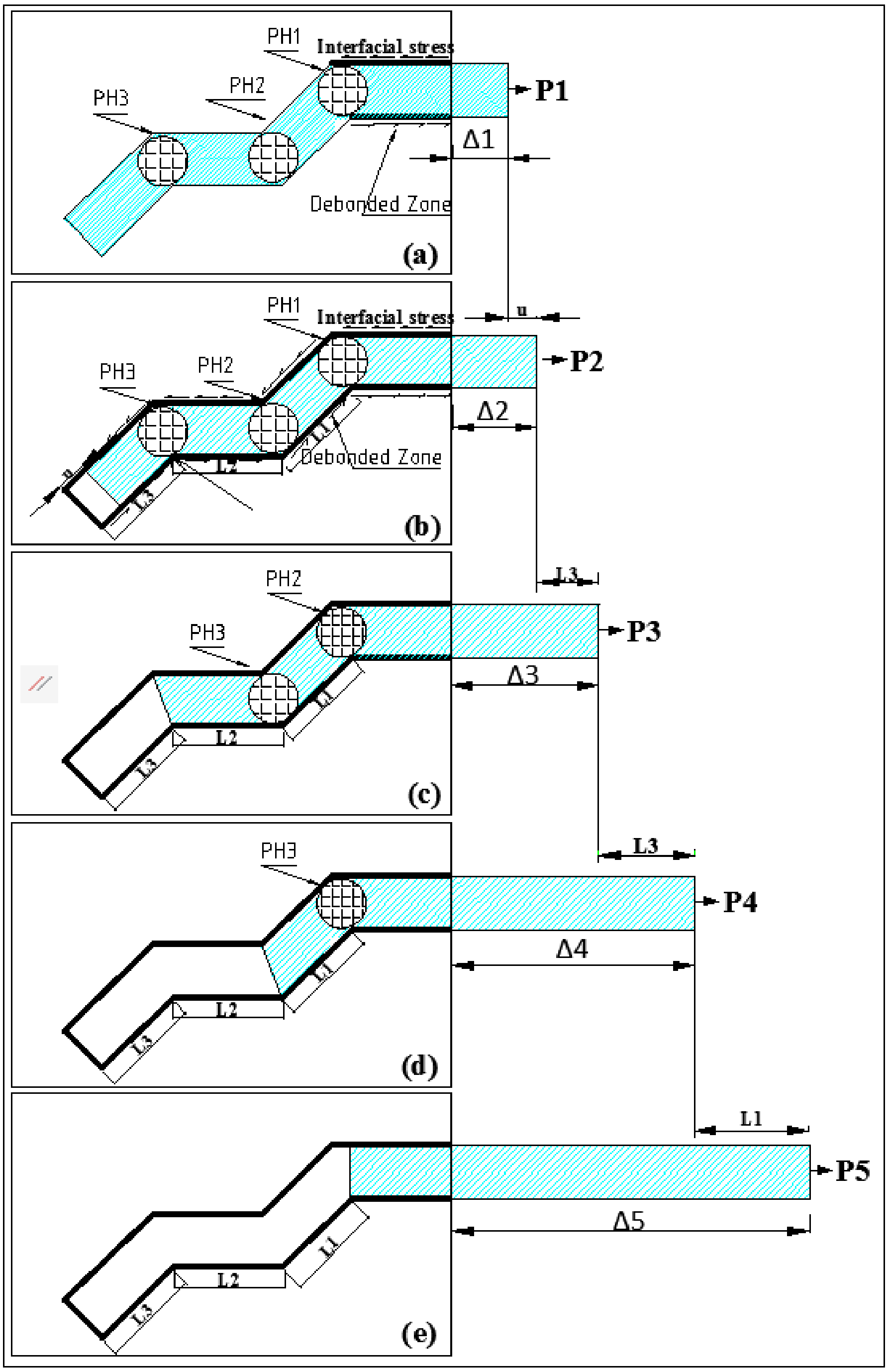

Figure 5.2 a) Hooked-end steel fibre at onset of complete debonding, b) hooked steel fibre during mechanical interlock with three plastic hinges, c) mechanical interlock with two plastic hinge, d) mechanical interlock with one plastic hinge, and e) hooked steel fibre at once of frictional pull-out

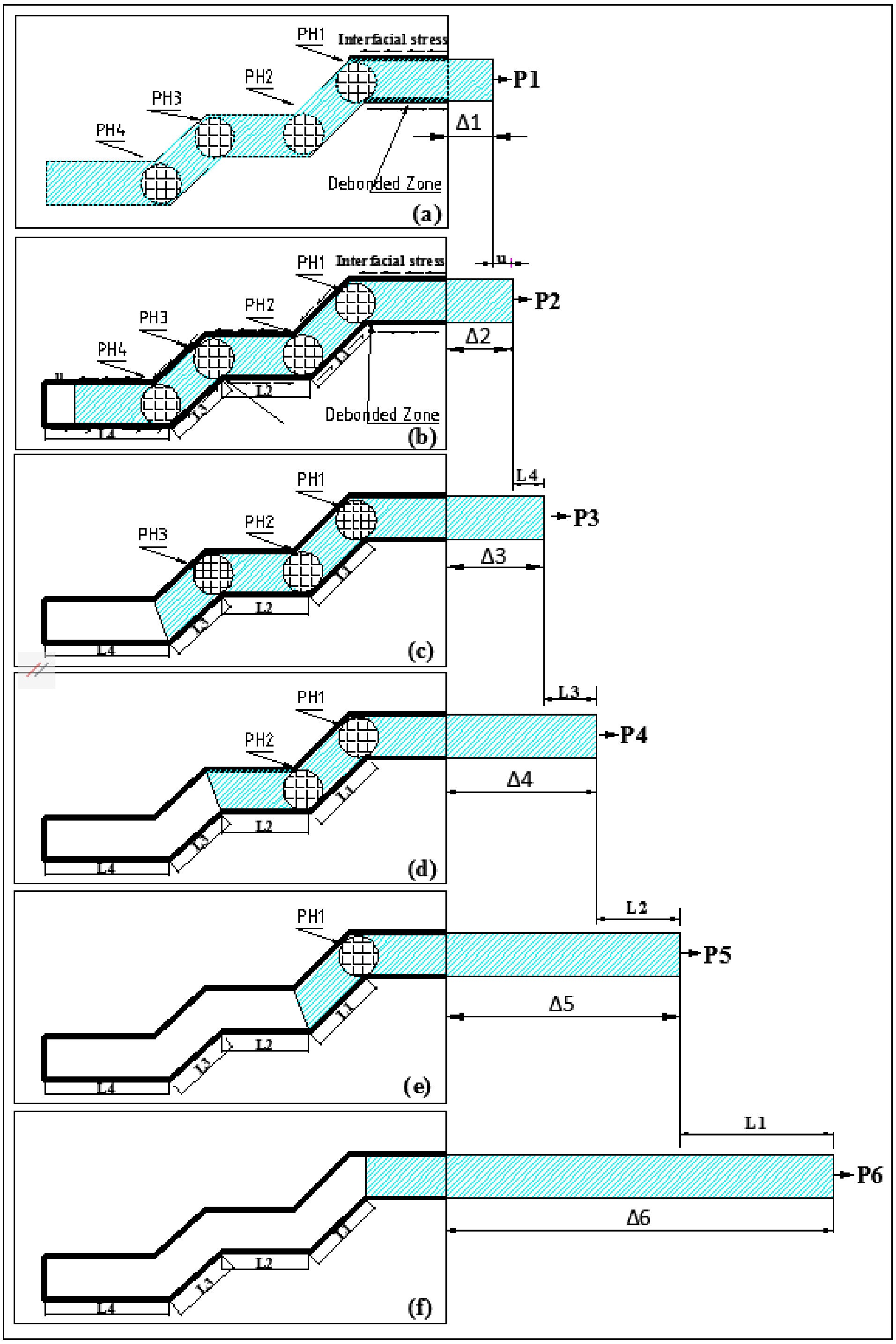

Figure 5.3 a) Hooked-end steel fibre at onset of complete debonding, b) hooked steel fibre during mechanical interlock with four plastic hinges, c) mechanical interlock with three plastic hinge, d) mechanical interlock with two plastic hinge, e) mechanical interlock with one plastic hinge, and f) hooked steel fibre at onset of frictional pull-out

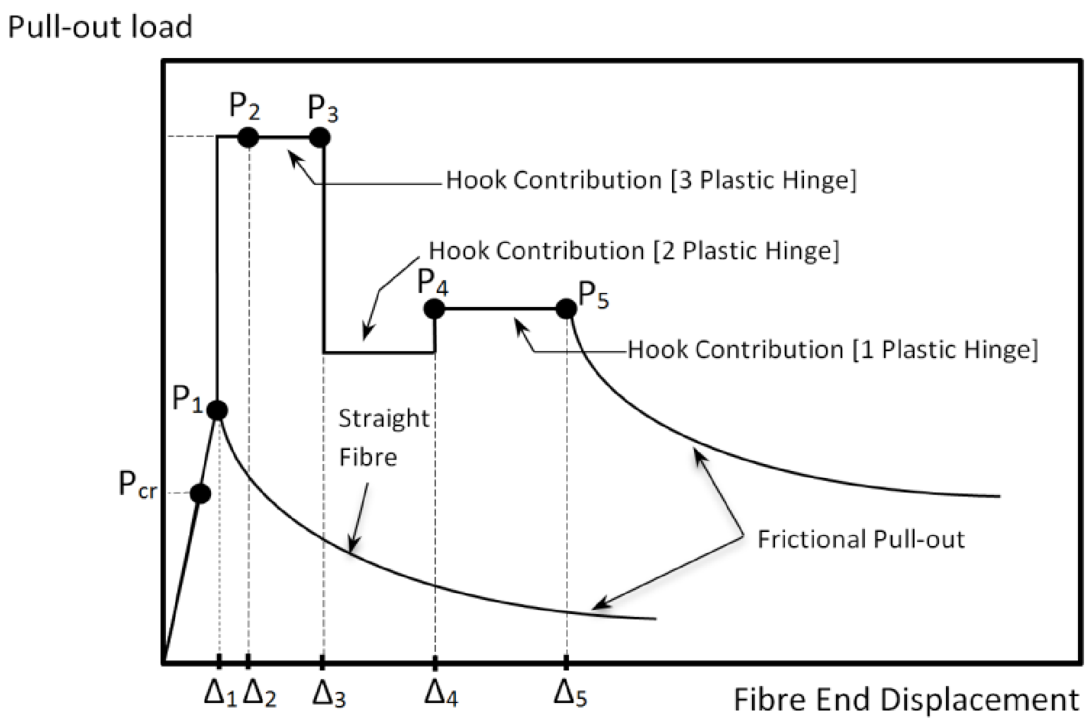

(a)

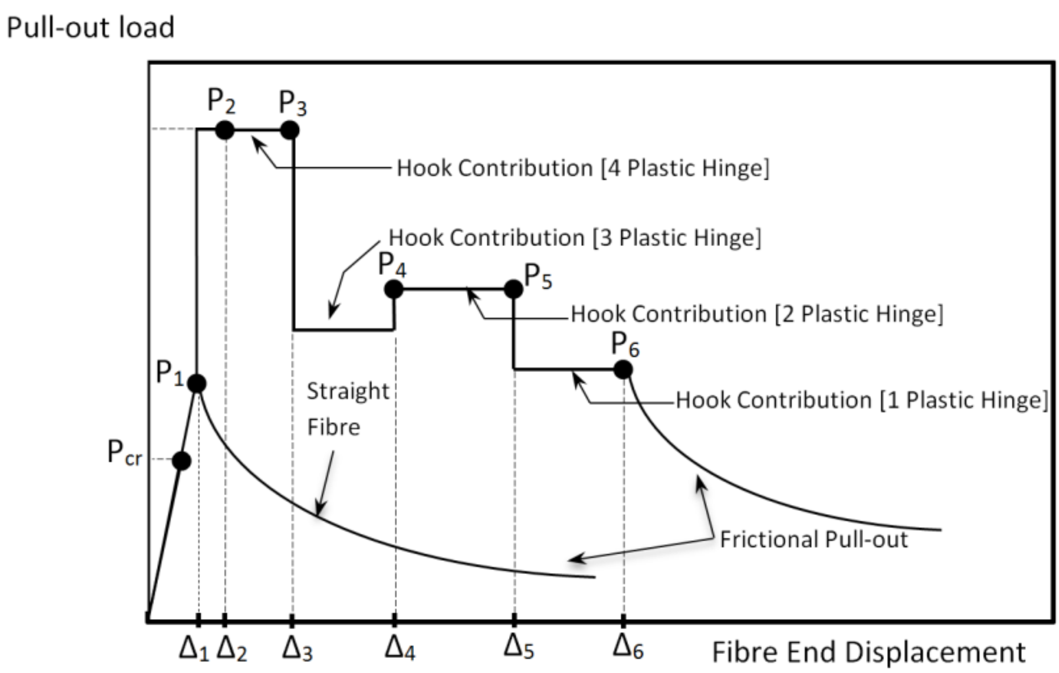

(b)

Figure 5.4 Schematic sketch of the theoretical pull-out curve: (a) 4DH and (b) 5DH fibres

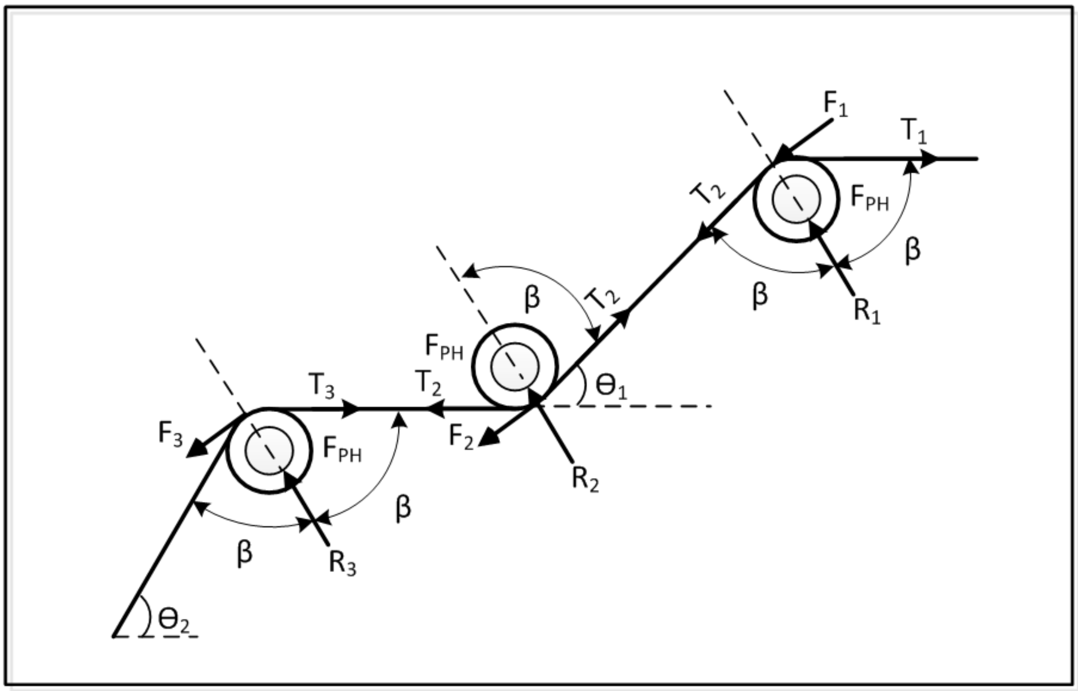

(a)

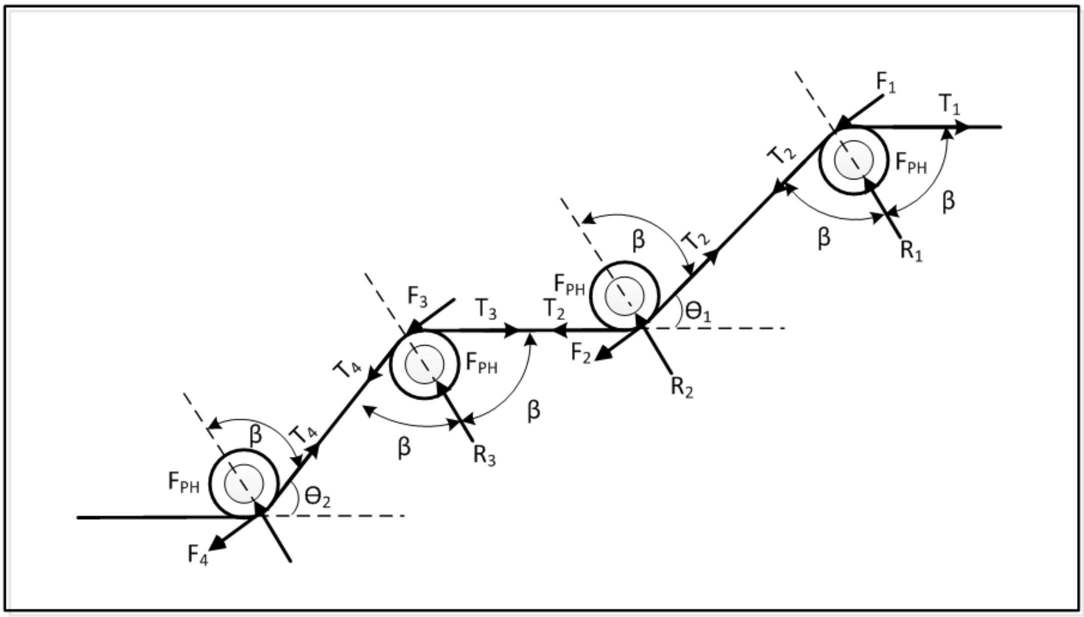

(b)

Figure 5.5 Line sketch of the frictional pulley model:(a) 4DH and (b) 5DH fibres

5.4 Predicting pull-out behaviour of hooked-end fibres in normal-high strength concrete

5.4.1 Analytical formulation of elastic-plastic responses

Figure 5.6a shows the fibre's circular section of radius r_f with centroidal axes x and y. A limiting linear elastic stress distribution in Figure 5.6b provides an initial condition for plastic penetration to occur. Penetrations to depth h shown in Figure 5.6c assume an elastic-perfectly plastic material model in which the yield stress σ_y remains constant.

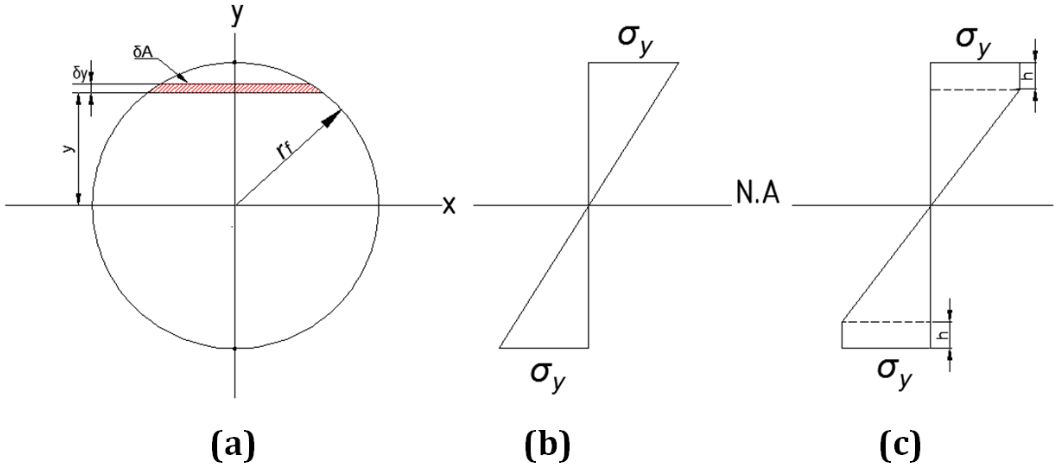

Figure 5.6 Stress distribution of the steel fibre circular section

The fully elastic bending moment M_E applies to Figure 5.6b when the yield stress σ_y applies to the section's top and bottom points upon the fibre's y- axis.

$$\frac{M_E}{I} = \frac{E_f}{\rho_E} = \frac{\sigma_y}{r_f}$$

which is re-arranged in two alternative forms

$$M_E = \frac{E_f I}{\rho_E} = \frac{\sigma_y I}{r_f}$$

where ρ_E is the fully elastic curvature. Substituting $I = \frac{\pi r_f^4}{4}$ for the fibre's neutral x-axis:

$$M_E = \frac{\pi E_f r_f^4}{4\rho_E} = \frac{\pi \sigma_y r_f^3}{4} \tag{5.44}$$

An elastic-plastic bending moment M_{ep} applies to Figure 5.6c where plastic zones have penetrated inwards to depth h as shown. This moment is the sum of two components [131]:

$$M_{ep} = M_e + M_p \tag{5.45}$$

Here the elastic moment M_e and the fibre's curvature ρ_e apply to the inner elastic region, respectively:

$$M_e = \frac{\sigma_y I_e}{r_f - h} = \frac{\sigma_y \times \pi (r_f - h)^4}{4(r_f - h)} = \frac{\pi \sigma_y}{4} (r_f - h)^3 \; ; \; \rho_e = \frac{E_f \times y}{\sigma_y} = \frac{E_f (r_f - h)}{\sigma_y} = \frac{E_f r_f (1 - \frac{h}{r_f})}{\sigma_y} \tag{5.46}$$

The plastic moment contribution applies to the plastic regions within which an elemental strip (Figure 5.6a) shows:

$$\delta M_p = 2\sigma_y \delta A y = 2\sigma_y [2(r_f^2 - y^2)^{1/2} \, \delta y] \times y$$

Integrating over each plastic zone depth $r_f \le y \le r_f - h$:

$$M_p = 4\sigma_y \int_{(r_f - h)}^{r_f} y \, (r_f^2 - y^2)^{1/2} \, dy$$

$$M_p = \frac{4}{3} \sigma_y [h(2r_f - h)]^{3/2} \tag{5.47}$$

Substituting Eqs.(5.46) and (5.47) into Eq.(5.45)

$$M_{ep} = \frac{\pi \sigma_y}{4} (r_f - h)^3 + \frac{4\sigma_y}{3} [h(2r_f - h)]^{3/2} \tag{5.48}$$

Dividing Eq.(5.48) and (5.44) gives the non-dimesnional moment ratio

$$\frac{M_{ep}}{M_E} = \left(1 - \frac{h}{r_f}\right)^3 + \frac{16}{3\pi} \left[\frac{h}{r_f}\left(2 - \frac{h}{r_f}\right)\right]^{3/2} \tag{5.49}$$

Eq. (5.49) confirms the shape factor $\frac{16}{3\pi}$ for a fully plastic circular section when $\frac{h}{r_f} = 1$ and that $M_{ep} = M_E$ when $\frac{h}{r_f} = 0$.

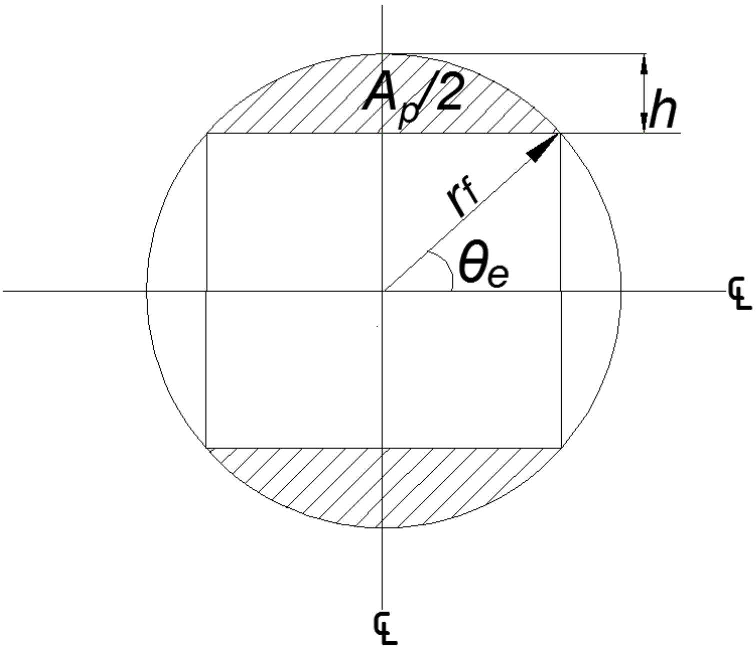

Figure 5.7 The elastic and plastic zone area of the steel fibre circular section

The plastic zone areas $\frac{A_p}{2}$ in the Figure 5.7 are in the ratio with the fibre section area A_f as:

$$\frac{A_p}{A_f} = R\ ;\ where\ A_f = \pi r_f^2$$

in which the geometry of Figure 5.7 shows:

$$\frac{A_p}{2} = \frac{1}{2} r_f^2 (180 - 2\theta_e^{\circ}) \frac{\pi}{180} - r_f cos\theta_e (r_f - h)$$

$$A_p = r_f^2 \left(1 - \frac{\theta_e}{90}\right) \pi - 2r_f^2 \left(1 - \frac{h}{r_f}\right) cos\theta_e$$

Hence

$$\frac{A_p}{A_f} = R = \left(1 - \frac{\theta_e}{90}\right) - \frac{2}{\pi}\left(1 - \frac{h}{r_f}\right) cos\theta_e$$

in which

$$r_f - r_f sin\theta_e = h, \quad \therefore \frac{h}{r_f} = 1 - sin\theta_e;\ \therefore 1 - \frac{h}{r_f} = sin\theta_e$$

Therefore,

$$R = \left(1 - \frac{\theta_e}{90}\right) - \frac{2}{\pi} sin\theta_e cos\theta_e$$

giving an equation between R and θ_e

$$\therefore R = \left(1 - \frac{\theta_e}{90}\right) - \frac{1}{\pi} sin2\theta_e$$

Preset values for $R = 0.3$, 0.5 and 0.7 require a trial solution to each θ_e as shown in Table 5.1. The results obtained by this formula will be compared with those obtained using the following formula proposed by Alwan et al.[98] Eq. (5.50) and Xu et al. [132] Eq. (5.51), respectively.

$$M_P = [f_y \times \frac{\pi r_f^2}{2} \times \frac{d_f}{3}] \tag{5.50}$$

$$M_{ep} = 4\sigma_y r_f^3 \left[\frac{1}{sin\theta_e}\left(\frac{\theta_e}{8} - \frac{sin(4\theta_e)}{32}\right) + \frac{cos^3(\theta_e)}{3}\right] \tag{5.51}$$

Table 5.1 Trial solutions for R=0.3, 0.5 and 0.7

θ_e	$1 - \frac{\theta_e}{90}$	$\frac{1}{\pi} sin2\theta_e$	R
60	0.333	0.2757	0.0543
45	0.500	0.3184	0.1816
44	0.511	0.3181	0.1919
42	0.533	0.3165	0.2168
40	0.553	0.3135	0.2365
36	0.600	0.3027	0.2973
35.8	0.602	0.3020	0.3000
25	0.722	0.2438	0.4782
24.2	0.731	0.238	0.4930
24.1	0.732	0.2373	0.4947
24.08	0.732	0.2371	0.4953
24.02	0.733	0.2367	0.4964
24.01	0.733	0.2365	0.4996
15	0.833	0.1592	0.6740
14.1	0.843	0.1504	0.6930
14	0.844	0.1494	0.6950
13.9	0.845	0.1488	0.6970
13.8	0.846	0.1475	0.6992

5.4.2 Experimental results

To determine the interfacial characteristics between fibre and matrix, pull-out test on straight fibres were carried out. The average pull-out load-slip curves of straight fibre lengths of (3DS, 4DS and 5DS) geometry pulled from the NSC, MSC and HSC matrix are shown in Figure 5.8. The curve on the left shows slip up to 30 mm and the right up to 1 mm. The latter shows that pull-out behaviour of each straight fibre is characterized generally by a rapid increase of load up to peak, followed by a load drop indicating full fibre/matrix debonding. Afterwards, the pull-out process occurs under frictional resistance where the pull-out load gradually decreases with increasing slip. It can also be observed that all straight fibres of different strengths embedded in the same matrix showed approximately similar peak load values, as expected. From a common bond (3D, 4DS and 5DS), however, the comparison between the three concretes show that the peak load increases significantly as the compressive strength of the matrix increases. In comparison with the NSC and MSC, the percent increase in HSC' peak loads is approximately 96% and 42%, respectively.

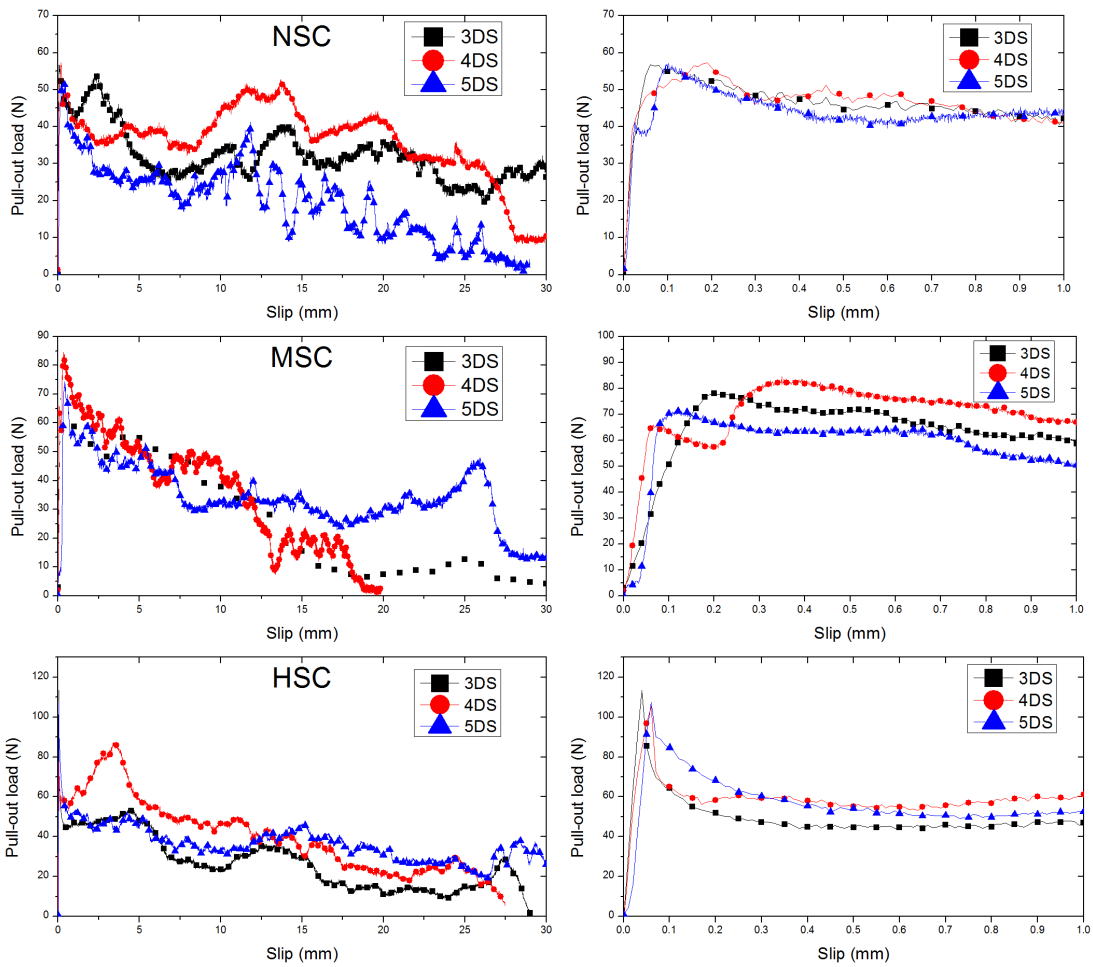

Figure 5.8 Average pull-out-slip response of straight steel fibres taken from 3DS, 4DS and 5DS bends. (Left) total pull-out curve and (Right) detail up to a slip of 1mm

The pull-out load-slip curves of hooked end steel fibres (3DH, 4DH and 5DH) are plotted in Figures 5.9a-c where each curve presented is the average curve of five specimens. As shown in Figures 5.9a-c, the pull-out response increases significantly as matrix strength increases for all hooked end fibres. In each comparison between the three hooked end fibres the highest anchorage effect is provided by the hook of 5DH fibre which has increased pull-out strength considerably. In each case, it can be seen that the pull-out strength of 5DH fibres is greater than that of the 3DH and 4DH fibres for all concretes tested.

To understand further the effect of matrix strength on pull-out behaviour of hooked end fibres, deformation and straightening processes of the 3DH, 4DH and 5DH fibres embedded in different matrices were examined under an optical microscope (Figure 5.10). Scrutiny of the morphology of deformation shows that the deformation and straightening of the hook increases significantly with the matrix strength for all hooked end fibres. All hooked end fibres pulled-out from the HSC matrix showed higher deformation and straightening of the hook than those of NSC and MSC. However, the full deformation and straightening of all hooked end fibres pulled-out from HSC did not occur in contrast to UHPC [15].

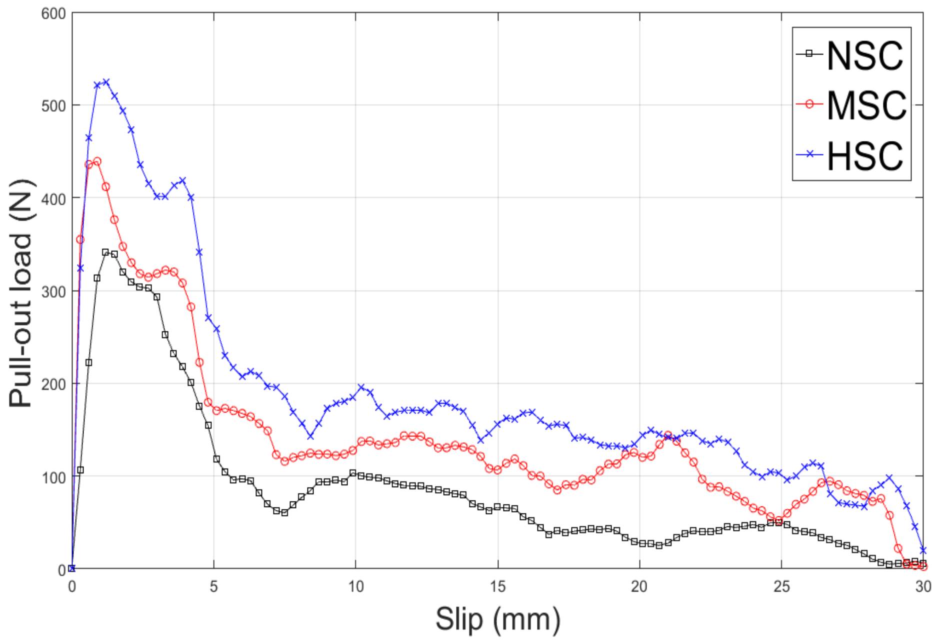

(a)

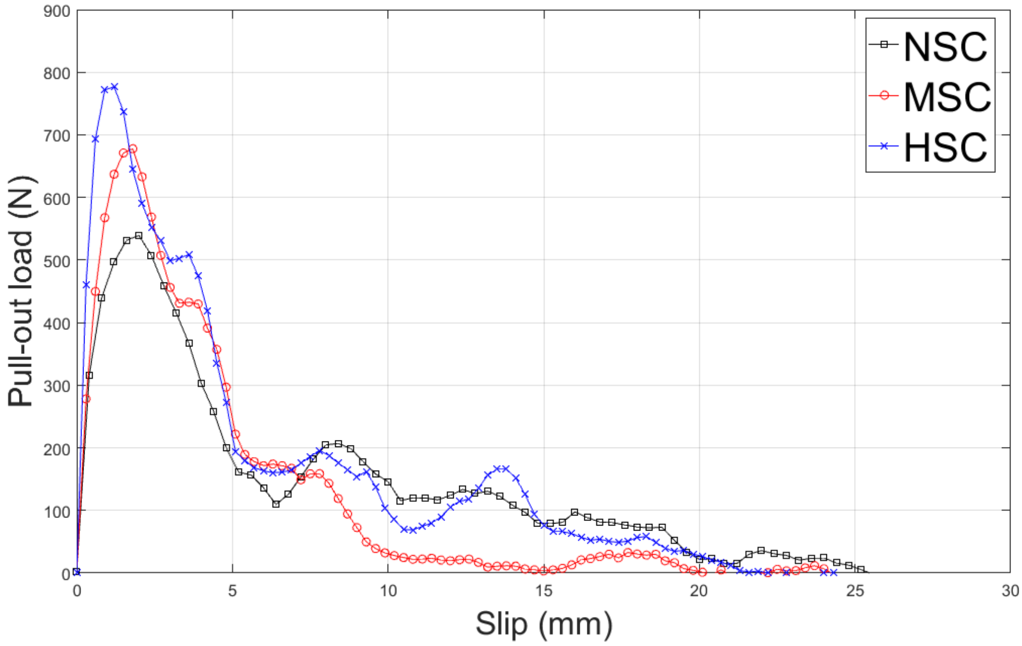

(b)

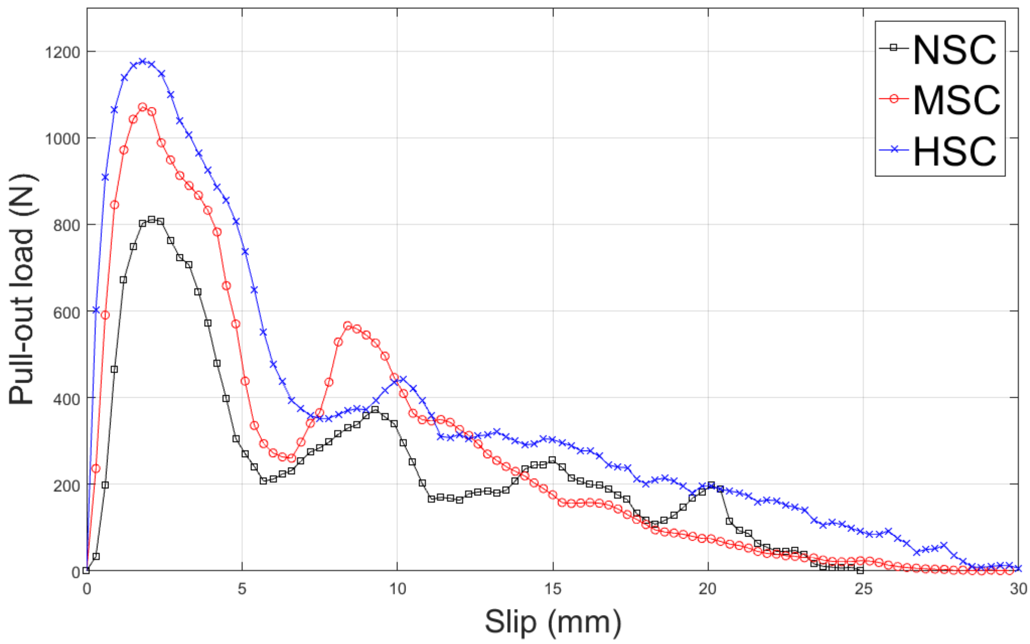

(c)

Figure 5.9 Average pull-out-slip responses of hooked-end steel fibres: (a) 3DH, (b) 4DH and (c) 5DH fibres

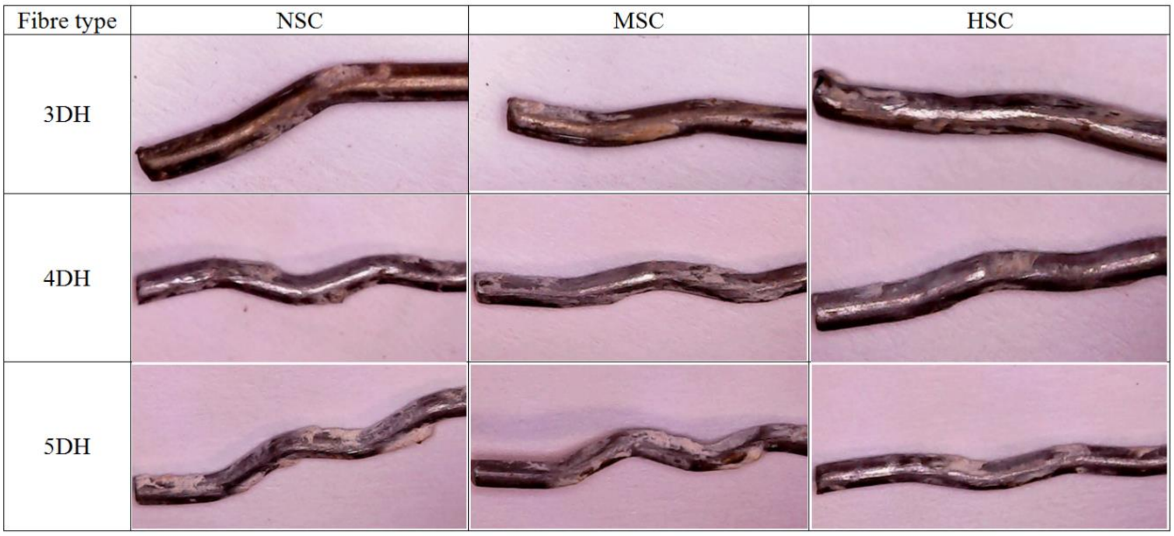

Figure 5.10 Deformation and straightening of hook after pull-out test

5.4.3 Model validation

Experimentation ascertains the applicability of the proposed analytical model to predict the pull-out behaviour of various hooked end steel fibres embedded in different concrete strengths. In addition, the predictions from the proposed elastic-plastic moment expression were also compared with those results obtained using formulas developed by Alwan et al. [98] and Xu et al. [132]. Material properties of the fibres (i.e. fibre geometry and tensile strength) were used as input parameters to Eq.(5.48) (Table 3.6). The P_1, P_2 …. P_5 forces predicted at each stage of pull-out for all hooked end fibres are summarized in Table 5.2. Here, the continuous pull-out curves shown were fitted numerically to P_1, P_2 …. P_5 using a fifth degree polynomial function [15].

Figures 5.11-5.13 show the comparison between the predicted and experimental pull-out curves of all fibres embedded in NSC, MSC and HSC. It can be seen that each polynomial has captured the main forces of pull-out predicting reasonably well the continuous pull-out-slip response of all hooked end fibres. The deviations between the proposed formula and Alwan et al. [98] and Xu et al. [132] shown brackets in Tables 5.2, do not exceed 12%. Of these predictions those from the elastic-plastic moment expression proposed are more consistent in providing good agreement with each experimental condition investigated.

Table 5.2 The predicted pull-out forces for all hooked end fibres (coefficient of variation CV% between parentheses)

R	Fibre type		P1	P2	P3	P4	P5
0.3	3DH	Proposed	55	351	174	-	-
		Alwan	55(0.0)	409(7.6)	198(6.4)	-	-
		Xu	55(0.0)	429(10.0)	208(8.9)	-	-
	4DH	Proposed	55	526	327	173	-
		Alwan	55(0.0)	623(8.4)	382(7.7)	198(6.7)	-
		Xu	55(0.0)	663(11.52)	406(10.7)	208(9.1)	-
	5DH	Proposed	55	843	573	357	188
		Alwan	55(0.0)	1005(8.7)	679(8.4)	419(7.9)	215(6.6)
		Xu	55(0.0)	1072(11.9)	724(11.6)	445(10.9)	227(9.3)
0.5	3DH	Proposed	76	437	222	-	-
		Alwan	76(0.0)	430(0.8)	219(0.6)	-	-
		Xu	76(0.0)	492(5.9)	244(4.7)	-	-
	4DH	Proposed	76	656	411	222	-
		Alwan	76(0.0)	644(0.9)	403(0.9)	219(0.6)	-
		Xu	76(0.0)	743(6.2)	461(5.7)	244(4.7)	-
	5DH	Proposed	76	1047	714	448	240
		Alwan	76(0.0)	1026(1.0)	700(0.9)	440(0.9)	236(0.8)
		Xu	76(0.0)	1195(6.6)	811(6.3)	505(5.9)	265(4.9)
0.7	3DH	Proposed	108	525	277	-	-
		Alwan	108(0.0)	462(6.3)	251(4.9)	-	-
		Xu	108(0.0)	548(2.1)	286(1.5)	-	-
	4DH	Proposed	108	779	496	277	-
		Alwan	108(0.0)	676(7.0)	435(6.5)	251(4.9)	-
		Xu	108(0.0)	815(2.2)	5172.0)	286(1.5)	-
	5DH	Proposed	108	1227	843	537	297
		Alwan	108(0.0)	1058(7.3)	732(7.1)	472(6.4)	268(5.1)
		Xu	108(0.0)	1288(2.4)	883(2.3)	560(2.1)	307(1.6)

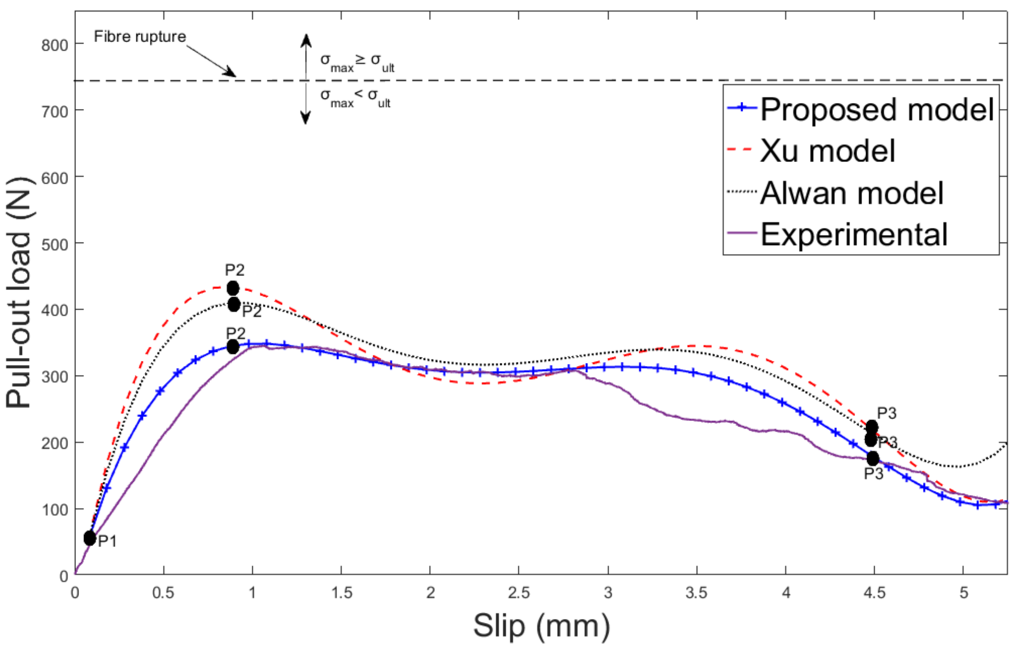

(a)

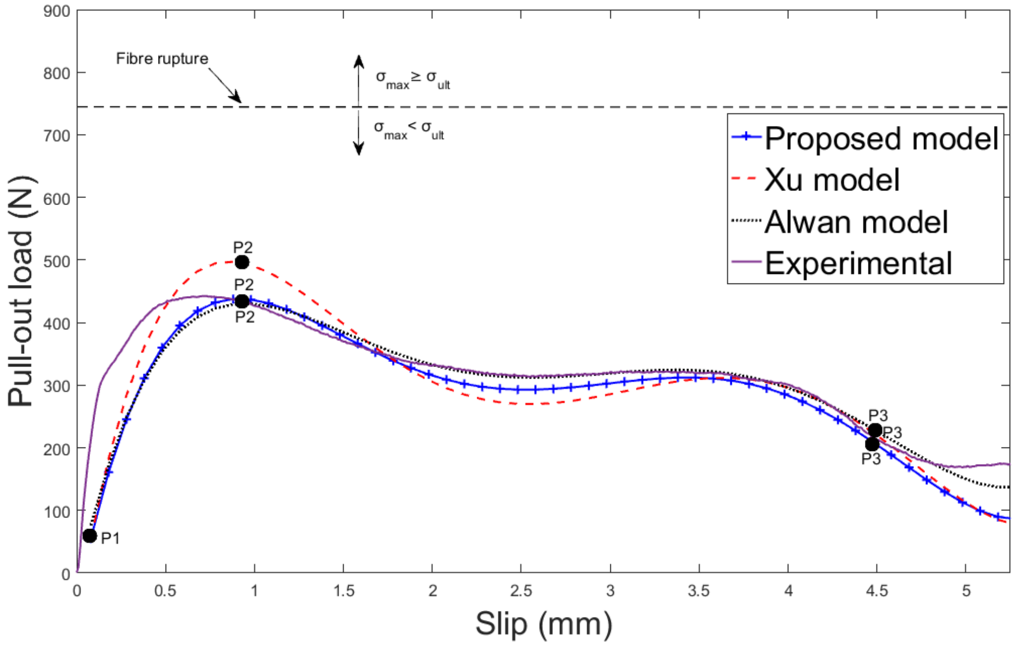

(b)

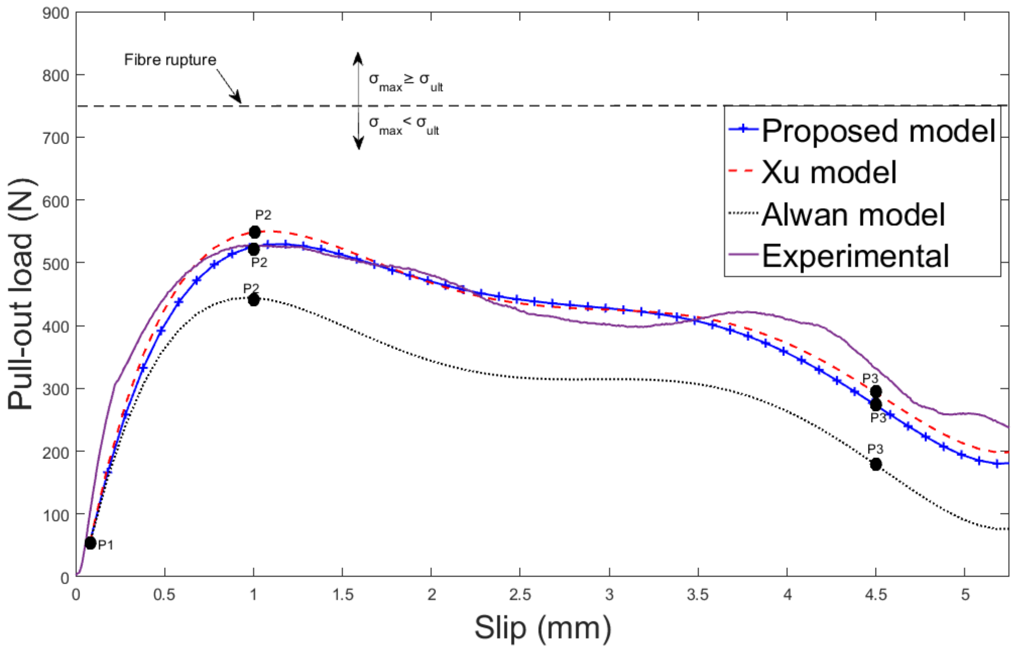

(c)

Figure 5.11 Comparison of predicted and experimental pull-out load-slip curves for 3DH fibre: (a) NSC, (b) MSC and (c) HSC

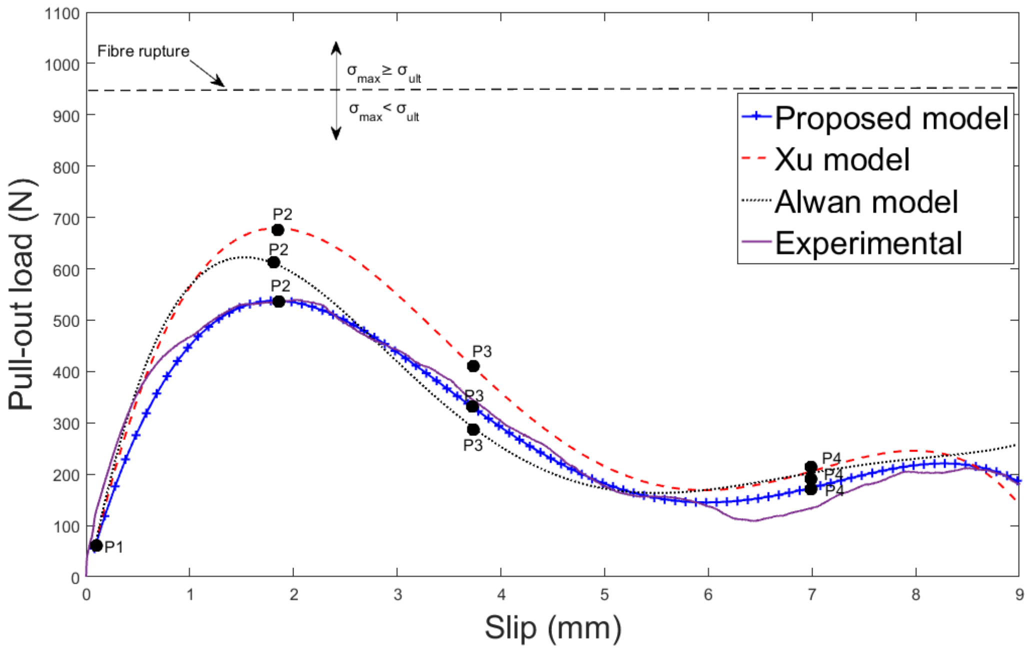
Fibre rupture
$\sigma_{max} \geq \sigma_{ult}$
$\sigma_{max} < \sigma_{ult}$
Proposed model
Xu model
Alwan model
Experimental
P1
P2
P3
P4
Pull-out load (N)
Slip (mm)

(a)

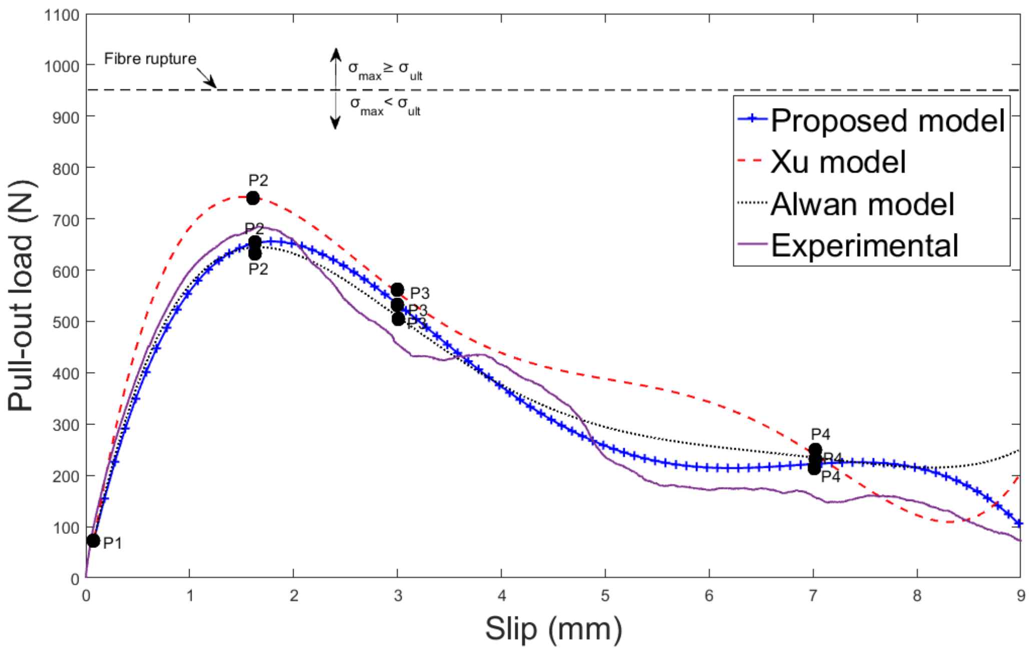
Fibre rupture
$\sigma_{max} \geq \sigma_{ult}$
$\sigma_{max} < \sigma_{ult}$
Proposed model
Xu model
Alwan model
Experimental
P1
P2
P3
P4
Pull-out load (N)
Slip (mm)

(b)

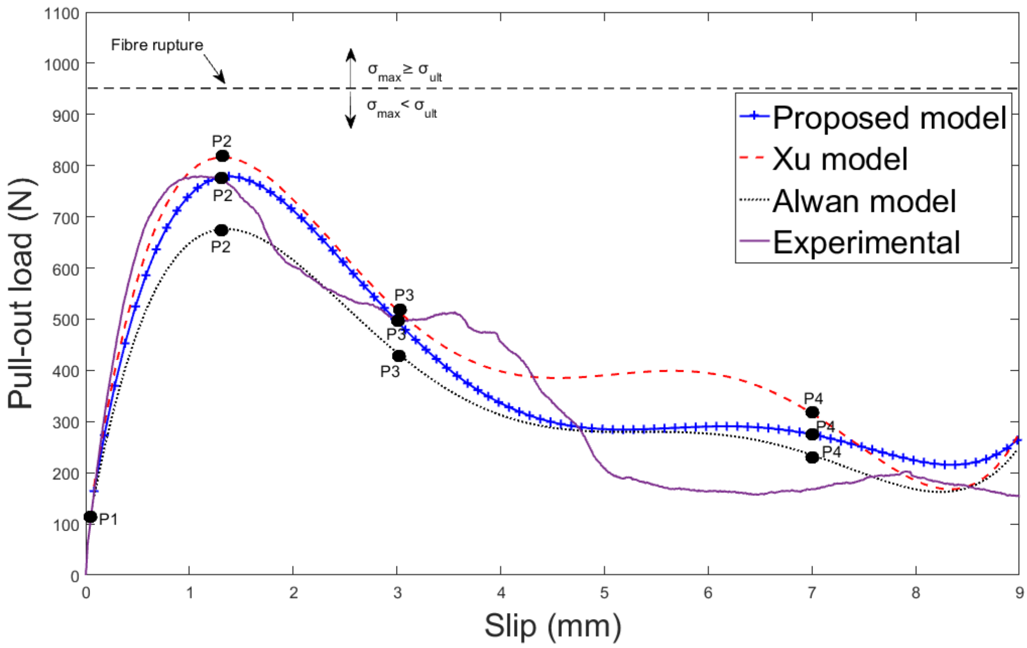

(c)

Figure 5.12 Comparison of predicted and experimental pull-out load-slip curves for 4DH fibre: (a) NSC, (b) MSC and (c) HSC

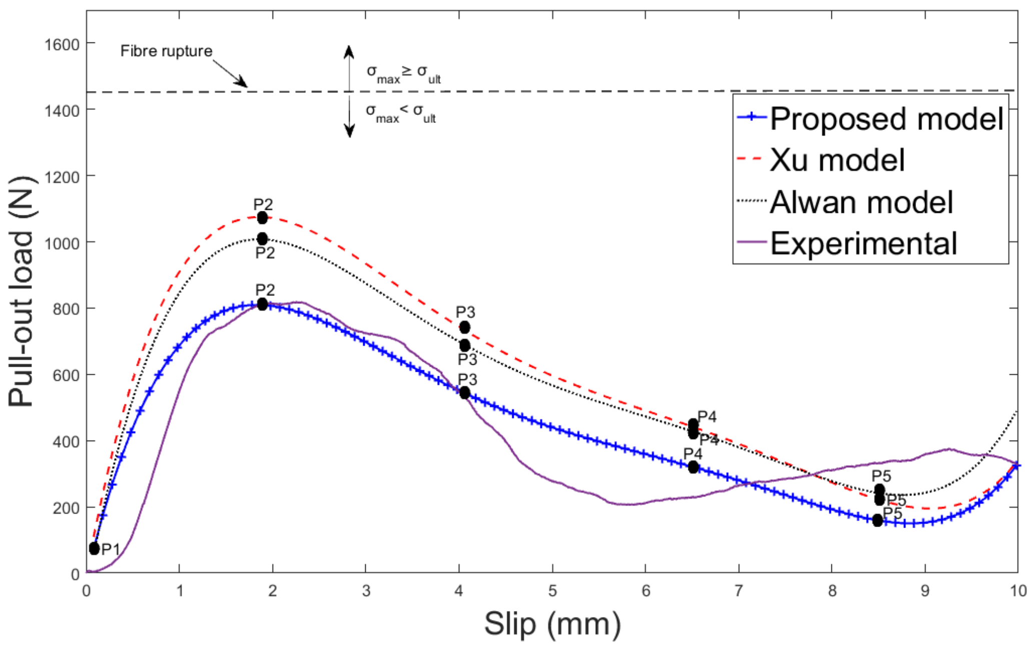

(a)

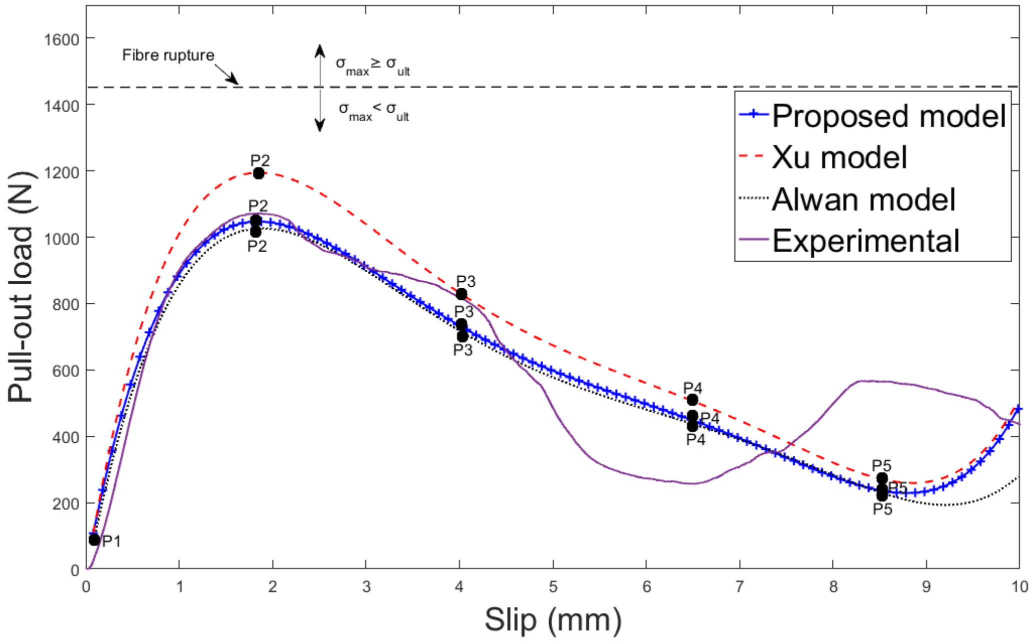

(b)

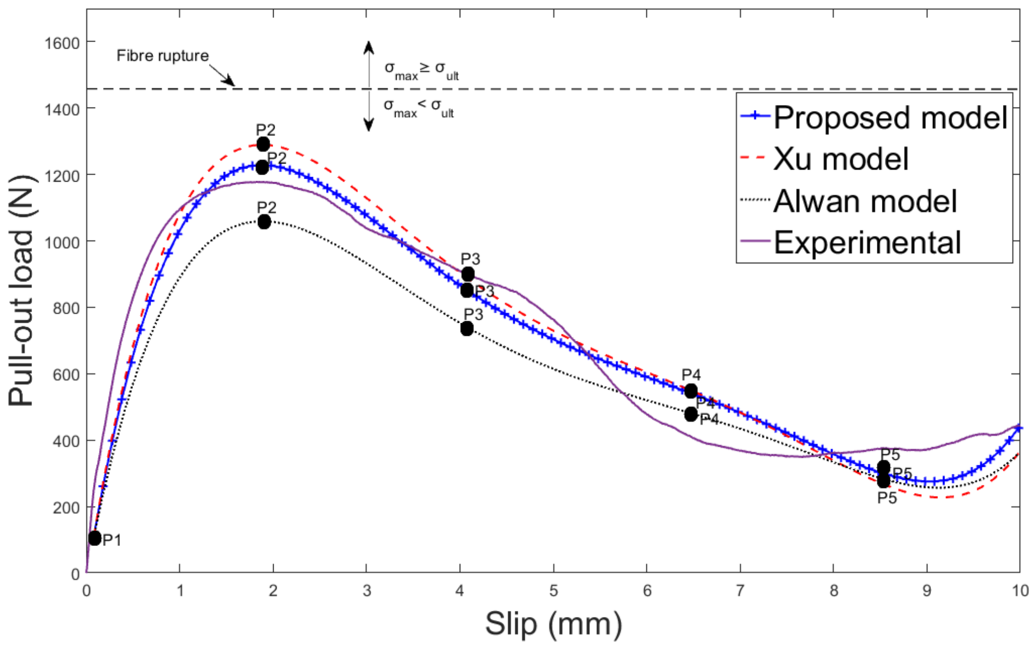

(c)

Figure 5.13 Comparison of predicted and experimental pull-out load-slip curves for 5DH fibre: (a) NSC, (b) MSC and (c) HSC

5.4.4 Concluding remarks

An elastic-plastic response model has been developed to predict the pull-out behaviour of three hooked end fibres embedded in three low-high strength concretes in various combinations. Based on experimental investigations, the complete deformation and straightening of the hook of all fibres pulled-out from NSC, MSC and HSC were not observed. The amount of deformation and straightening of the hook were found to be directly related to matrix strength. That is, the assumption that an elastic-plastic moment expression accommodates plastic bend-ratios of 30, 50 and 70% of the fibre sectional area, corresponded to the fibres embedded in NSC, MSC and HSC, respectively. The model considered the variation of the concrete strength, geometrical and tensile properties of the fibres. In addition, the model was also able to take into account a 100% bend ratio in which the condition for the fibre rupture may occur.

The model was validated by a comparison between alternative moment expressions and experimental pull-out results. The prediction from the proposed expression described the main pull-out forces consistently. The verification presented here also reinforced the validity and applicability of the proposed model for predicting the pull-out-slip response of various hooked end fibres embedded in various concrete strengths presented in pervious chapter.

5.5 Predicting pull-out behaviour of hooked-end fibres in ultra-high performance concrete

5.5.1 Analytical formulation of full plastic responses

The plastic moment formula is proposed as Eq. (5.52) to match the full plastic deformation for this fibre/matrix combination (Figure 5.14).

$$M_P = F_h \times \frac{8r}{3\pi} = (\sigma_y \times \frac{\pi r^2}{2}) \times \frac{8r}{3\pi}$$

So,

$$M_P = \frac{4\sigma_y r_f^3}{3} \tag{5.52}$$

where, $\frac{8r}{3\pi}$ is the true distance between centroids for the tension and compressive forces, F_h.

It should be noted that the previous formula for plastic moment (Eq. 5.21) was estimated in the Alwan et al. [98] model. Their approximation appears not to represent the plastic moment of the steel fibre circular as accurately. It is assumed that a fully deformed fibre is essential to pull-out without damage occurring to the UHPC matrix. In a weaker concrete an elastic-plastic deformation condition is sufficient for pull-out to occur as shown in pervious section. This research assumes that moderate hook angles (Table 3.6) require straightening under a moment given by Eq. (5.52).

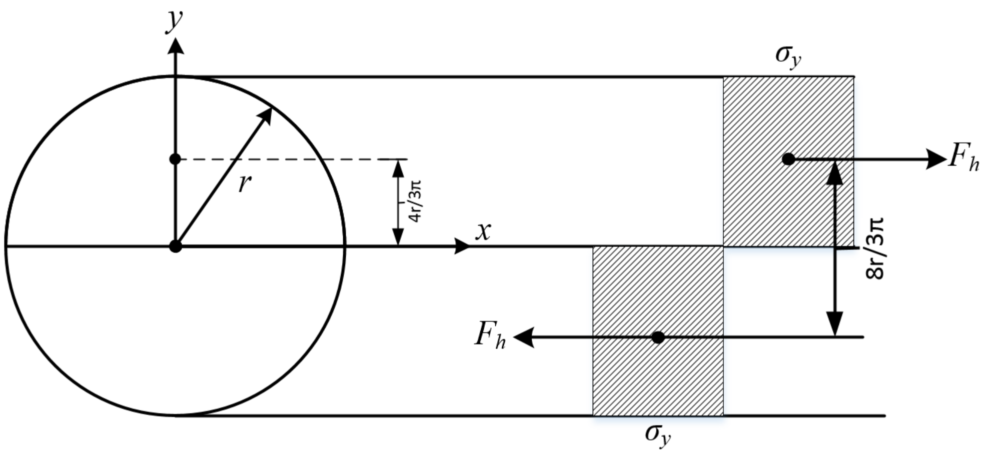

Figure 5.14 Stress distribution of steel fibre circular section subjected to fully plastic deformation

5.5.2 Experimental results

The average load-slip curves obtained from pull-out test of straight fibres (3DS, 4DS and 5DS) are presented in Figure 5.15. It can be seen that the pull-out behaviour of the straight fibres mainly characterized by a rapid increase followed by a sudden drop in pull-out load, indicating that the full fibre debonding. Afterwards, the pull-out load continues to decrease with an increase in the slip. All straight fibres have approximately the same value of the maximum pull-out load, as expected. However, there is a remarkable difference in post peak behaviour of each fibres type. Some of this difference may be a result of the deformation of the fibre end owing to the cutting process which provides some mechanical anchorage, leading to increase in the pull-out resistance. This can alter the frictional coefficient produced by a 'ploughing' effect. Similar behaviour has been observed by Wille and Naaman [77].

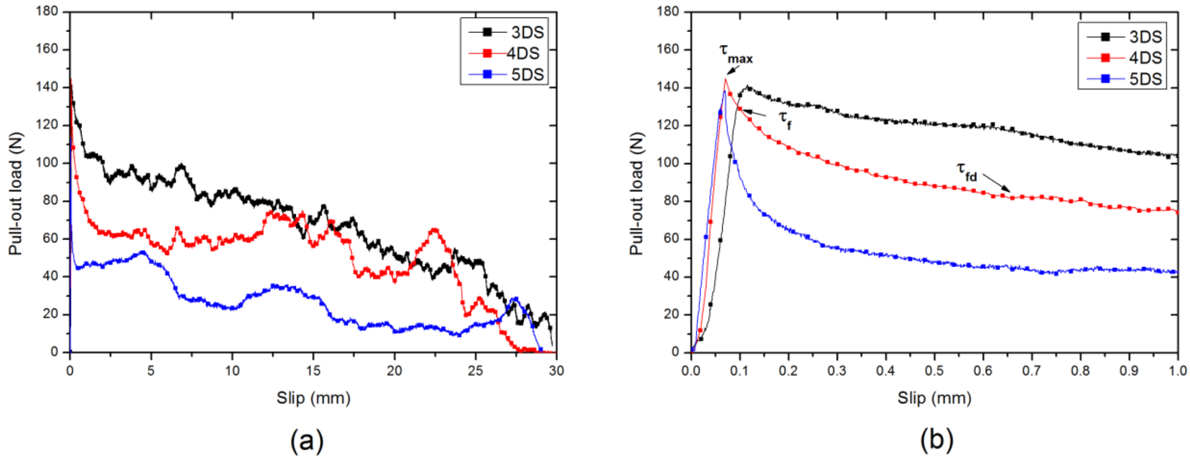

Figure 5.15 Pull-out-slip response of straight steel fibres: (a) total pull-out curve and (b) detail up to a slip of 1mm

Pull-out behaviour of hooked end steel fibres (3DH, 4DH and 5DH) is shown in Figure 5.16. It can be observed that overall the hook geometry has a significant influence on the pull-out response. The high anchorage effect provided by the lengthy hook of 4DH and 5DH fibres enhances the pull-out behaviour significantly, generating higher pull-out load and pull-out work as compared to 3DH fibre. The full deformation and straightening of fibre hook without matrix damage have been observed for all fibres. The coefficient of variation (CoV) of the average P_{max} (three tests in each series) indicates the consistency of the test results with the CoV values lying below 4% for both straight and hooked end steel fibres.

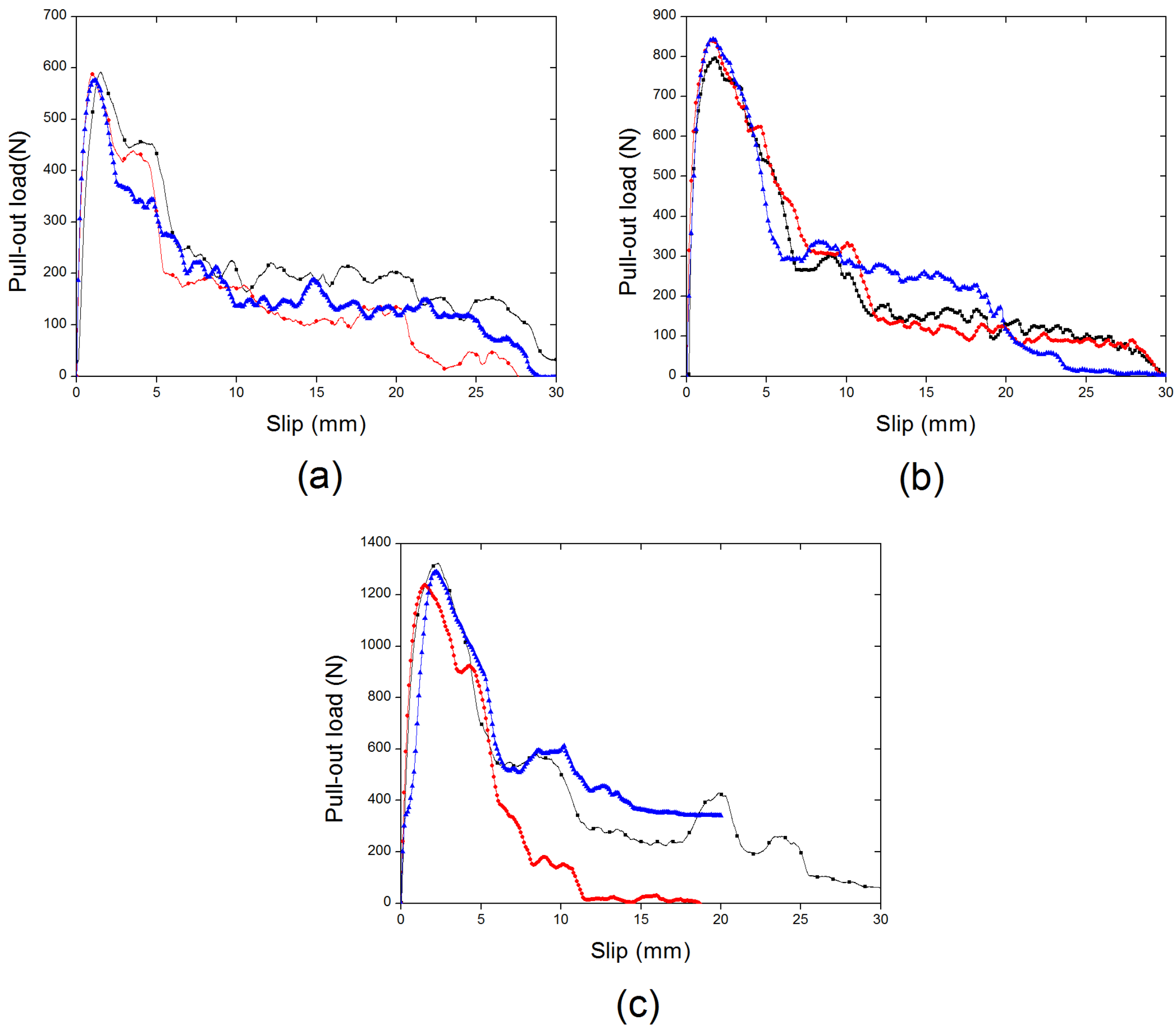

Figure 5.16 Pull-out-slip response of hooked-end steel fibres: (a) 3DH, (b) 4DH and (c) 5DH fibres

5.5.3 Model validation

5.5.3.1 Comparison of experimental and modelling pull-out forces

In order to ascertain the suitability of the proposed analytical model, comparisons are made between the experimental and predicted pull-out force curves as shown in Figures 5.17-5.20. Figure 5.17 applies to straight fibres (i.e. 3DS, 4DS and 5DS) and Figures 5.18-5.20 apply to 3DH, 4DH and 5DH hooked end fibres. The input parameters used in this model are directly related to material properties of the fibre (i.e. fibre geometry and tensile strength in Table 3.6). The results show that the proposed analytical model is able to predict the pull-out forces for all 3DH, 4DH and 5DH fibres.

5.5.3.2 Prediction of pull-out process

In addition to obtaining the pull-out load at all main pull-out stages, it is of interest to estimate the pull-out force across the whole duration of the test. Therefore, the predicted pull-out curves were fitted numerically using fifth degree polynomial function Eq. (5.53).

$$y = a_0 + a_1x + a_2x^2 + a_3x^3 + a_4x^4 + a_5x^5 \quad (5.53)$$

To provide a more realistic transition between points (i.e. P_1, P_2.....P_5) based upon the present proposal, the coefficients data (a_0, a_1......... a_5) were provided by using MATLAB (see Table 5.3).

Figures 5.18-5.20 show the comparison plots between model predictions and experimentally measured pull-out curves for 3DH, 4DH and 5DH fibres. All curves show that the proposed model is able to take into account the mechanical anchorage effect provided by the fibre hook. The results also show that the model is able to capture the main features of pull-out behaviour and to predict accurately the pull-out load-slip response, irrespectively of fibre geometry and tensile strength.

Table 5.3 Parameters of fifth degree polynomial function (see Eq. (5.53))

Fibre type	a_0	a_1	a_2	a_3	a_4	a_5
3DH	38.79	3.43	-60.79	394	-1137	1354
4DH	48.23	0.40	-11.46	122.3	-596.1	1194
5DH	29.41	0.19	-6.52	84.96	-532.7	1424

Table 5.4 The obtained pull-out forces from the proposed model (Pm) and Alwan's model (Am)

Fibre type	P_1		CV	P_2		CV	P_3		CV	P_4		CV	P_5		CV
	Pm	Am	(%)	Pm	Am	(%)	Pm	Am	(%)	Pm	Am	(%)	Pm	Am	(%)
3DH	140	140	0.0%	591	495	8.83	323	283	6.60	-	-	-	-	-	-
4DH	140	140	0.0%	867	710	9.95	561	469	8.93	323	283	6.60	-	-	-
5DH	140	140	0.0%	1353	1093	10.62	937	766	10.04	605	505	9.00	345	301	6.81

To ascertain the reliability of the proposed formula for the plastic moment, the predicted pull-out curves are also compared with that adopted by Alwan et al. [98]. It can be seen here that their predictions underestimates the mechanical anchorage contribution (Table 5.4). However, the deviations shown in Table 5.4 do not exceed 11%. On the other hand, the proposed model is also compared with Zile model [12] for single hooked end fibre (i.e. 3DH). Zile's model [12] appears to underestimate the mechanical anchorage contribution by a greater amount than Alwan's model (Figure 5.18). This can be explained by the fact that Alwan's formula and Zile's model may not take into account the case of full deformation and straightening of the hook, which results in lower values of mechanical anchorage contribution. In both of these cited papers a normal strength matrix applies.

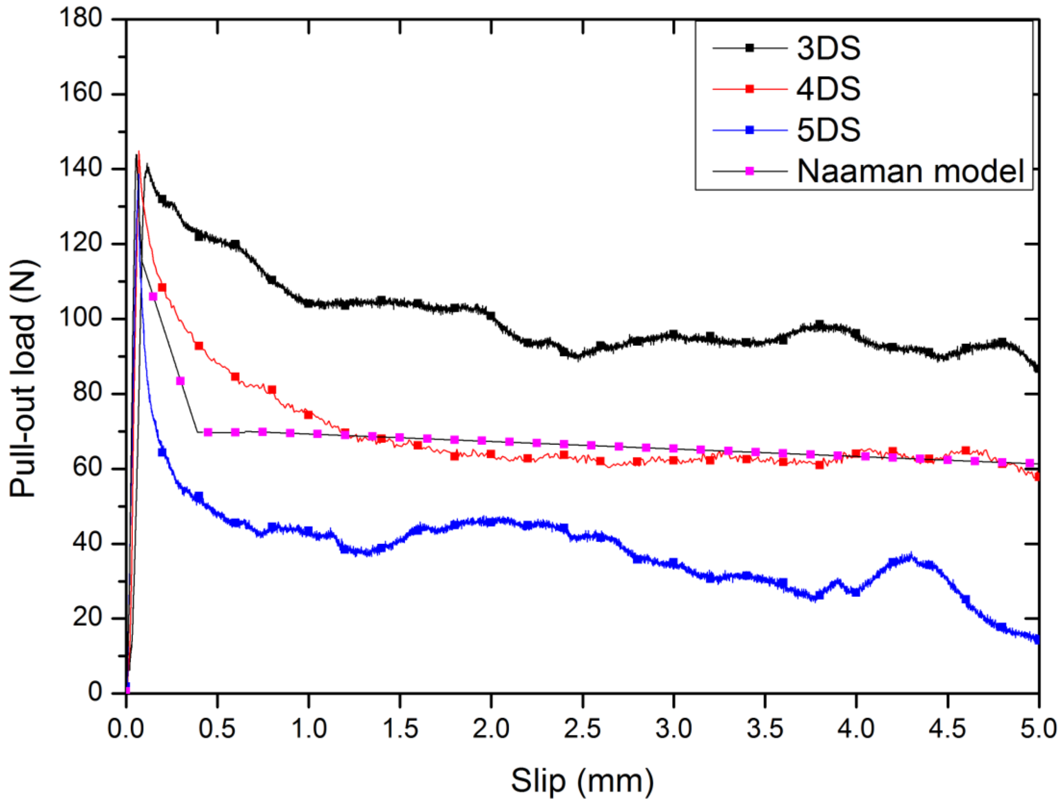

Figure 5.17 Validation of the Naaman et al.[123] against experimental results for straight fibres

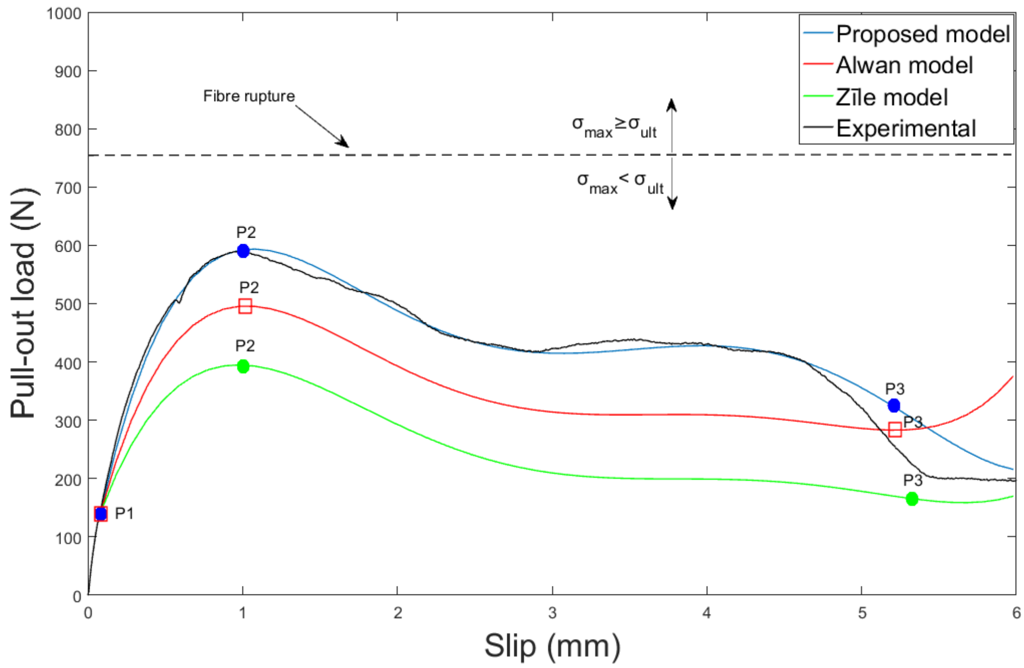

Figure 5.18 Validation of the proposed model , Alwan et al.[123] model and Zile et al.[25] model against experimental results for 3DH fibres

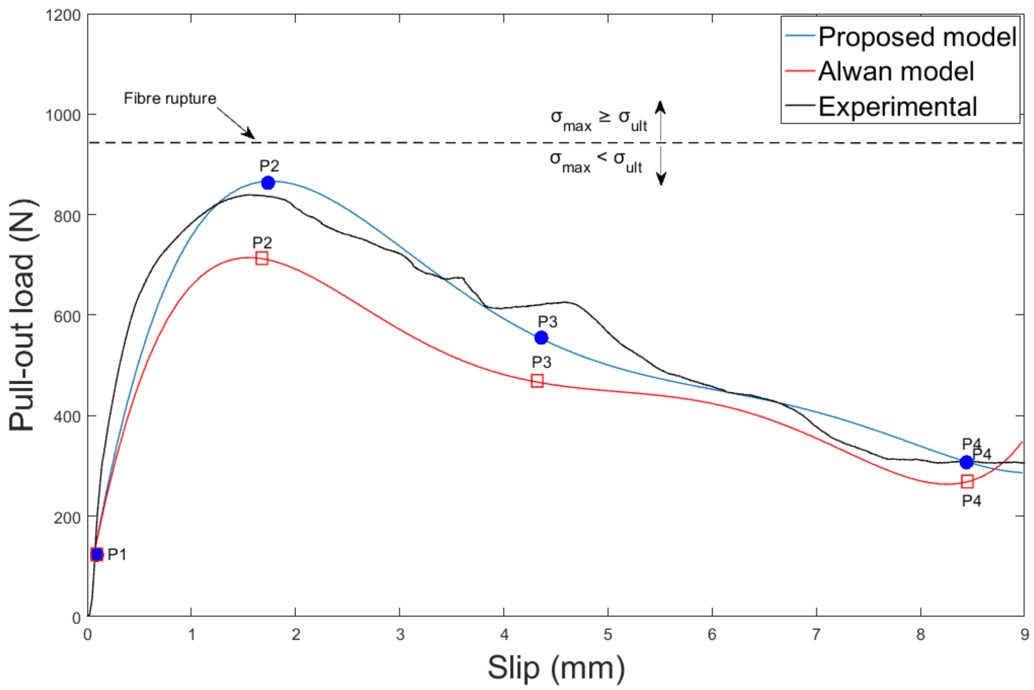

Figure 5.19 Validation of the proposed model and Alwan et al.[123] model against experimental results of 4DH fibres

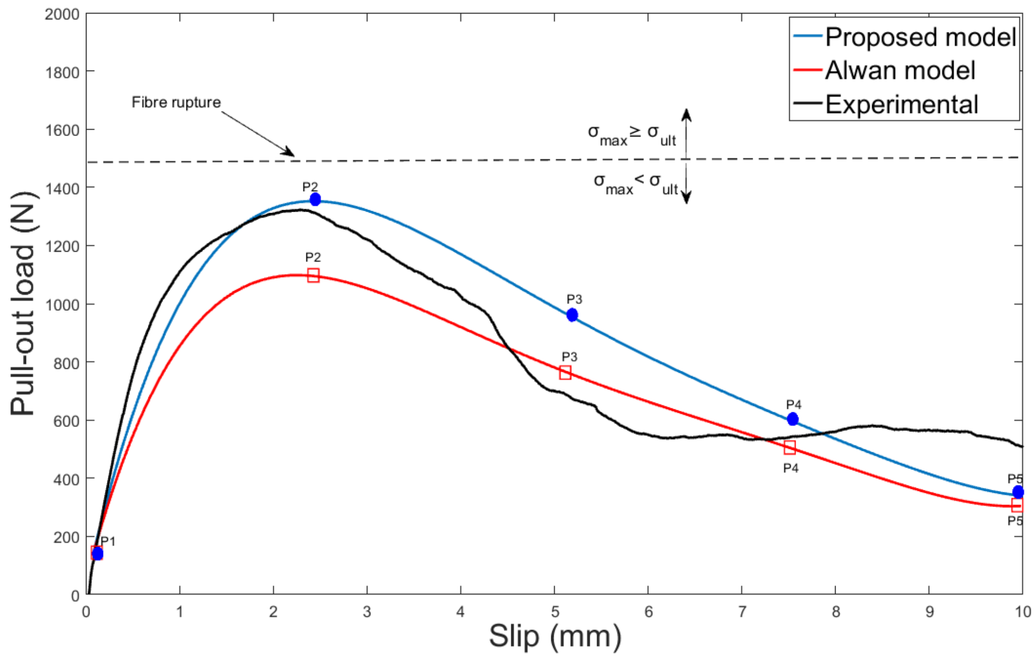

Figure 5.20 Validation of the proposed model and Alwan et al.[123] model against experimental results of 5DH fibres

5.5.4 Concluding remarks

1) A straightforward and comprehensive model has been developed to simulate the mechanical anchorage contribution provided by the hook. It was assumed that the shape of the hook was idealized as the two, three and four plastic hinges for 3DH, 4DH and 5DH fibres, respectively. The mechanical contribution of the hook was a function of the cold work needed to straighten the fibre during the pull-out. The input parameters of the model were mainly the mechanical and geometrical properties of the fibres. Since the cementitious matrix was ultra-high performance concrete (UHPC), the damage of the matrix during the pull-out was neglected.
2) Model predictions were compared against experimental results of pull-out tests. In order to ascertain the reliability of the proposed formula for plastic moment, the pull-out curves were also compared with those obtained by Alwan's et al. [98] formula.
3) The proposed model was able to describe the main features of anchorage mechanisms and to accurately predict the pull-out load-slip response.

The present model took into account the variation of the geometrical and tensile plastic flow properties as well as the rupture condition of the fibres.

Chapter 6 Pull-out Behaviour of Straight and Hooked-end Fibres after Exposure to Elevated Temperatures

6.1 Introduction

Fire remains one of the major hazards for high-rise buildings, tunnels and other infrastructure. For this reason, many researchers have spent considerable effort towards understanding the effects that elevated temperatures have on building materials and elements [133]. This is particularly true in more recent times for newer materials, such as steel fibre reinforced concrete (SFRC). SFRC is now widely used as a primary construction material in a variety of applications due to its excellent performance in improving the tensile response of concrete and also its ability to control crack propagation [12,13,27]. However, like most other construction materials, the exposure of SFRC to high temperature results in a significant deterioration of the physical and mechanical properties of both component materials and their inter-relationship (i.e. bond) [134]. Bond is the mechanism through which tensile forces are transmitted between the steel fibres and the surrounding cement paste. A part of these forces are resisted by the cement paste, whilst the remainder is resisted by the fibres. The interfacial bond properties between the fibres and cement paste play a crucial role in controlling the mechanical properties of SFRC at both room and elevated temperatures. Therefore, the knowledge of the bond relationship is the first key step towards understanding the behaviour of SFRC structural elements at an elevated temperature. The bond characteristics are commonly assessed using the single fibre pull-out test, which is able to determine the interfacial properties between the fibres and the surrounding cementitious matrix [15].

The mechanical properties of SFRC at room temperature have received considerably more attention from the research community compared to those at the elevated temperature [135]. More recent attempts on the SFRC under the elevated temperature mainly focus on the mechanical rather than the thermal properties [136-138]. The primary mechanical properties that influence the fire performance of SFRC members are the compressive strength, tensile strength, elastic modulus and the stress-strain response in compression. Although steel fibres may not offer any obvious advantage from a fire-endurance point of view, it has been shown that steel fibres can be considered as an effective way in delaying the spread of cracking, and hence potentially improve the performance of concrete after exposure to high temperature [139]. However, due to variations in concrete strength, test methods and heating conditions, there is a lack of consensus on the SFRC behaviour under an elevated temperature in the available literatures.

The degradation of the mechanical properties of concrete at high temperature is mainly due to the physicochemical bond changes that occur in the cement paste and aggregate as well as thermal incompatibility between the cement paste and the aggregate [140]. The temperature-dependent properties also vary with the concrete strength. For example, researchers have found that high strength concrete (HSC) is more likely to experience dramatic spalling failure at a given elevated temperature compared with normal strength concrete (NSC), mainly owing to the finer pore structure in HSC [141]. It has also been shown that the occurrence of explosive spalling is more likely in HSC than NSC at similar levels of elevated temperature [142]. There are a number of measures which can be taken to effectively alleviate spalling under high temperatures for HSC such as the addition of polypropylene fibres [143], steel fibres [144] or hybrid fibres (steel and polypropylene fibres)[135], as well as protecting the exposed concrete surface with a thermal barrier [140].

As stated before, it is essential to have a proper understanding of the bond relationship between the steel fibres and the concrete matrix at elevated temperature in order to evaluate the deterioration in mechanical properties of SFRC; nevertheless, little information on this topic is available in the literature. In this context, the current chapter presents an experimental study into the pull-out behaviour of both straight and hooked-end steel fibres under a range of elevated temperatures. The main objective is to investigate the bond mechanisms associated with the pull-out behaviour, and how these are affected by elevated temperatures. Four groups of cementitious mixtures with an initial compressive strength ranging between 33 and 148 MPa are included in the study. The results are essential in order to develop a better understanding of the effect of high temperature on the bond-slip characteristics and to further assess the degree of deterioration in mechanical properties of SFRC after high temperature exposure. The results of the experiments are presented and discussed in detail, with particular attention given to the most salient parameters such as concrete strength and fibre type.

6.2 Experimental program

6.2.1 Materials and sample preparation

Table 4.1 presents the four grades of concrete which were included in the experimental programme, namely normal strength concrete (NSC), medium strength concrete (MSC), high strength concrete (HSC) and ultra-high performance concrete (UHPC). The NSC mix design was prepared using ordinary Portland cement whilst the other three mixes all employed high strength Portland cement (i.e. CEM II 32.5R and CEM III 52.5N, respectively, in accordance with European standard EN 197-1[120]). Silica fume, ground quartz and fly ash were also used for the preparation of the MSC, HSC and UHPC mixtures. Around 60 % of the crushed granite aggregates were 6 mm in size and the remaining 40 % were 10 mm. Two types of sand were used in experimental programme. As presented in Table 4.1, coarse grain sand (C.G.S., 0-4 mm) was used in the NSC, MSC and HSC mix design and very fine grain sand (F.G.S., 150-600μm) was used in the UHPC concrete. A superplasticizer called TamCem23SSR was used to enhance the workability of the HSC and UHPC mixtures.

The pull-out tests on single steel fibres were performed using cubes with a side dimension of 100 mm for NSC, MSC and HSC, and cylinders with a diameter of 100 mm and height of 50 mm for the UHPC samples (this is because of the finer aggregates). In each test specimen, a single steel fibre was carefully placed through a hole which was made in the bottom of moulds. The embedded length (l_E) was one half of the overall fibre length (i.e. 30 mm). For each concrete mix, three additional cubes (again 100mm in size) were prepared in order to determine the compressive strength of the mixture. The concrete was prepared using a laboratory pan mixer for the NSC, MSC and HSC, and a hobart mixer for UHPC (which is only used for fine materials without coarse aggregates). During preparation, the dry components were firstly mixed for approximately 1 minute before water and the superplasticizer (for the HSC and UHPC) were added. This was then mixed for 11 minutes, which experience has shown is appropriate to result in a homogenous mixture. After casting and vibration, the specimens were covered with a thin polyethylene film to avoid retain the escaping moisture and left for 24 hours at room temperature. The specimens were then removed from moulds and cured for a further 28 days in the conditioning chamber, where the temperature was held at 20±2°C and the relative humidity 96±4 %.

6.2.2 Heating scheme

After 90 days, the pull-out and compressive strength specimens were directly placed in the electric furnace. The free end of the steel fibre for the pull-out specimens was covered with heat insulation (intumescent paint) before placed in the furnace. A controlled furnace was used which is capable of achieving a maximum temperature of 1100°C and a maximum heating rate of 36°C/min. In this study, the specimens were heated to a maximum temperature of either 100, 200, 300, 400, 500, 600, 700 or 800°C at a constant rate of 20°C/min, based on the recommendations of Haddad and Shinnas [145]. Once the target temperature was reached, it was held constant for one hour and then the specimens were allowed to cool in the furnace for 1 day before the compressive strength and pull-out tests were conducted. The temperature-time curve is presented in Figure 6.1.

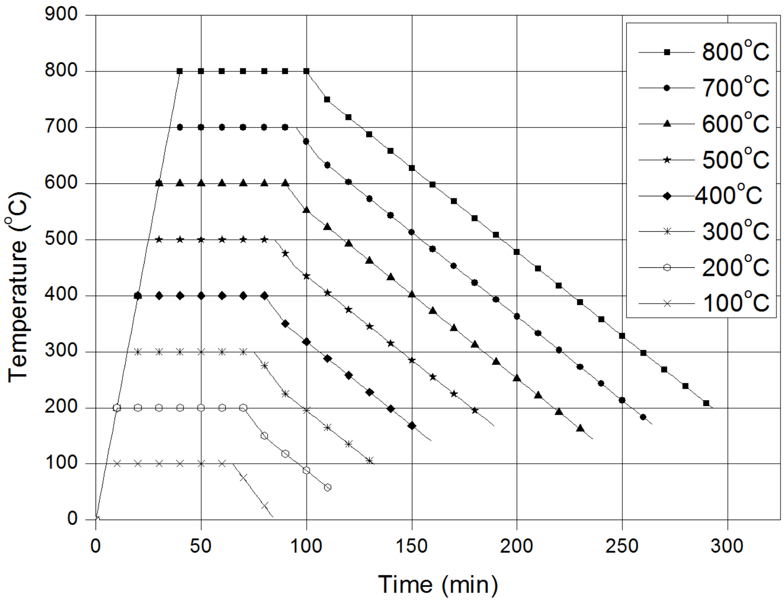

Figure 6.1 Time-temperature curves for the elevated temperature tests

6.3 Results and discussion

6.3.1 Mechanical and thermal properties of concrete and steel fibres at elevated temperatures

6.3.1.1 Compressive strength

The results from the compressive strength tests on all concrete mixes (NSC, MSC, HSC and UHPC), following exposure to elevated temperatures, are summarized in Table 6.2. It is noteworthy that the UHPC results are only presented up to 400°C (Table 6.2) because above these temperatures, the specimens exploded in the furnace; this is discussed later in more detail. While the compressive strength does not vary significantly within the temperature range from 20 to 400°C for all the mixes tested. The strength of NSC, MSC and HSC, reduces slightly at 100°C and then regains almost to its full ambient strength at 200°C. The decrease in strength at 100°C temperature may be attributed to initial moisture loss, while the regain of strength at 200°C temperature is likely to be due to an acceleration in the pozzolanic reaction and moisture migration in the concrete [136,146].

The compressive strength at elevated temperature (f'_{cT}) normalised to the corresponding ambient temperature value (f'_c) with changing temperature was given in Figure 6.2. It is clear that up to around 400°C, there are insignificant changes in the compressive strength with temperature. This is in agreement with other results reported previously [147]. Above 400°C, there is gradual degradation of strength with increasing temperature. For the NSC, MSC and HSC, the loss of compressive strength at 600°C in these tests was around 45%, 35% and 52%, respectively (Figure 6.2). This significant loss in compressive strength may mainly be attributed to the loss of chemically-bound water due to dehydration and disintegration of hydrated calcium silicate (C-S-H) gel in the concrete. Once the target temperature reaches 800°C, the compressive strength of NSC, MSC and HSC was only 33%, 42% and 47% of its original strength at ambient temperature, respectively. Therefore, it can be deduced that high temperatures in the range of 600-800°C are critical in terms of strength loss.

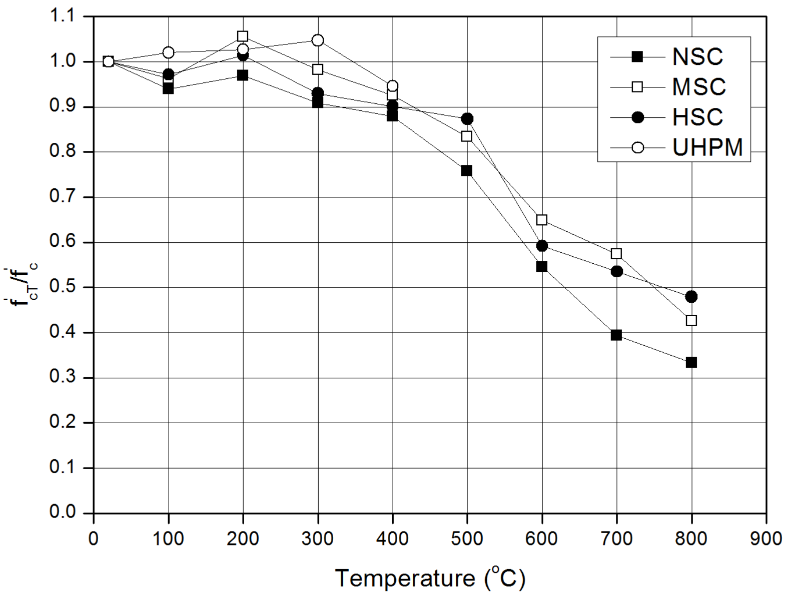

Figure 6.2 Effect of temperature on compressive strength

The behaviour of the NSC, MSC and HSC mixes differed significantly from that of UHPC in the tests above 400°C, particularly in terms of the failure mode. Above 400°C, the UPHM specimens experienced severe explosive spalling as opposed to the other specimens which failed by spalling of small fragments from the specimen top surface (Figure 6.3). This phenomenon is attributed to the lower permeability of UHPC compared with the other mixes which limits the ability of water vapour to escape from the pores. For this reason, the results of UHPC are only presented up to 400°C to allow fair comparison with the other mixes.

(a) HSC-800°C **(b)** UHPM-500°C

Figure 6.3 Failure mode of HSC and UHPC after heating at 800°C and 500°C

6.3.1.2 Mass loss

The mass of each specimen was measured before and after heating in order to determine the mass loss as a result of exposure to elevated temperature (Figure 6.4), which is presented as the percentage mass loss relative to the corresponding value at ambient temperature (M_{loss}). It is apparent that the exposure to high temperatures results in an increasing loss of mass as shown in Figure 6.4. It is interesting that the mass loss is minimal (i.e. <3 %) up to around 300°C, but above 300°C, the NSC and MSC mixes behave very similarly and experience higher mass loss than the HSC (the UHPC is not included above 400°C due to the previously discussed spalling failure mechanism). The greater mass loss in these materials may be attributed mainly to their more permeable microstructure compared to HSC. At 800°C, the loss in mass in the NSC, MSC and HSC specimens is 11%, 10% and 8%, respectively. The trend of mass loss was very similar to that the compressive strength change, showing a close correlation between compressive strength and mass loss. The results also indicate that there may be a certain loss of free water, bound water and also chemical water at high temperature exposure. The loss of water, especially bound water and chemical water, not only changes the integrity of internal structure of concrete, but also the transportation of vapour could affect the compact of concrete.

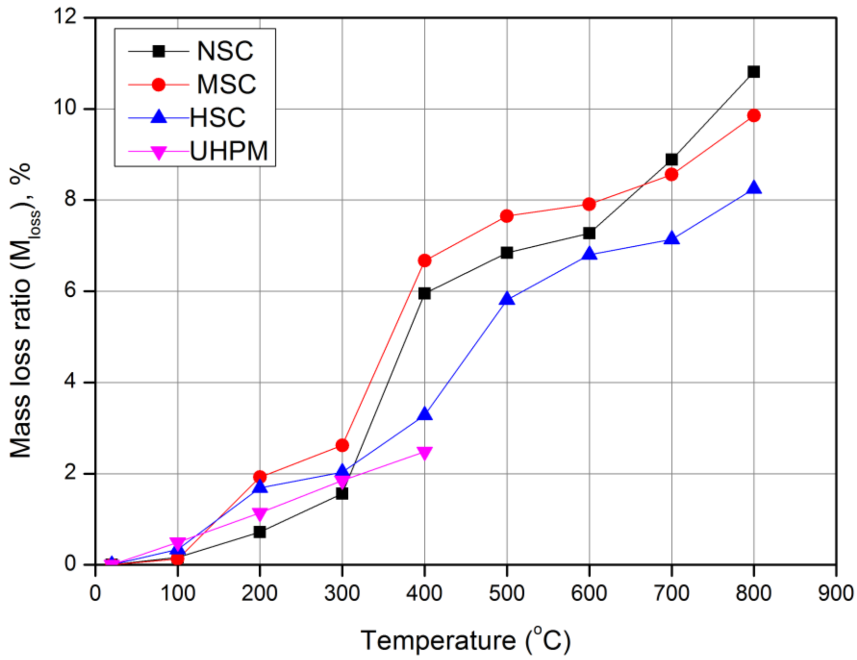

Figure 6.4 Relationship between elevated temperature and mass loss

6.3.1.3 Effect of elevated temperatures on the properties of steel fibres

The stress-strain curves obtained from tensile tests on the steel fibres at ambient and various elevated temperatures are shown in Figure 6.5. For each temperature increment, a total of six fibres were tested with the same heating regime as used in the concrete tests. The average results in terms of mechanical properties are summarized in Table 6.1. As expected, an exposure to higher temperatures significantly degraded the yield and ultimate strengths of the steel fibres. It can be seen in Figure 6.5 that the stress-strain behaviour remained relatively unchanged between 20 and 200°C. Between 300-400°C, although the yield and ultimate strengths of the fibres remained high, the stiffness and overall shape of the stress-strain response changed. At higher temperatures (i.e. exposure of 500°C or higher), the strength values greatly decreased and, moreover, there was a significant change in the shape of the stress-strain response. It is apparent that heating the steel fibre to 600°C or above resulted in a significant increase in the ductility (elongation) of the fibres. When the steel fibre attained a maximum temperature of 800°C, the remaining yield and ultimate strengths were about 15 and 25% of their corresponding value at ambient temperature, respectively.

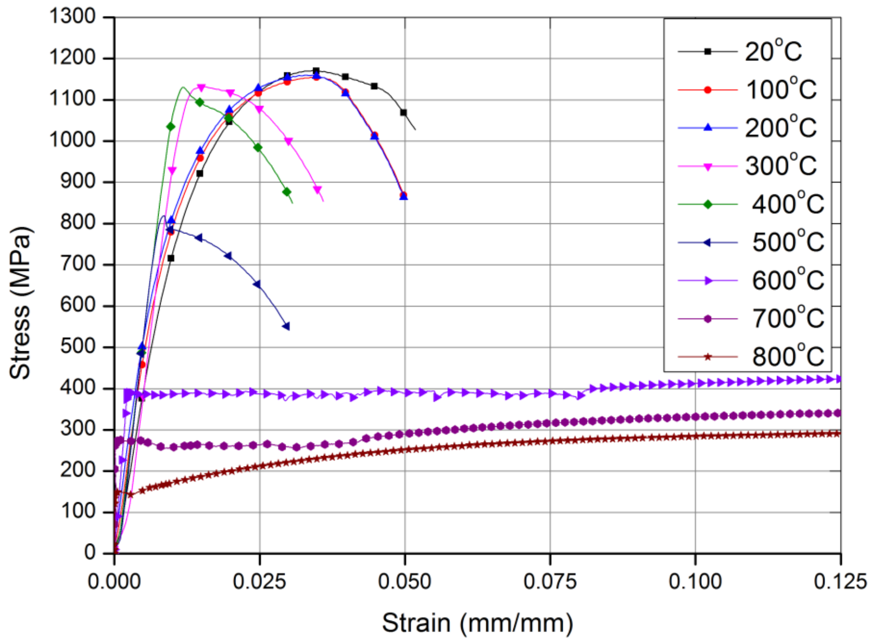

Figure 6.5 Stress-strain curve for steel fibres at ambient and elevated temperatures

Table 6.1 Mechanical properties of steel fibres at ambient and elevated temperatures

Temperature (°C)	Yield strength (MPa)	Ultimate strength (MPa)	Elongation at failure (%)
20	986	1170	5.6
100	958	1155	4.9
200	885	1159	4.9
300	801	1131	3.6
400	780	1130	3.4
500	556	818	3.1
600	387	437	21.1
700	274	348	22.4
800	144	287	24.6

6.3.2 Pull-out behaviour of straight and 3DH hooked-end fibres at elevated temperatures

6.3.2.1 Straight fibres

6.3.2.1.1 Pull-out load-slip response

In order to determine the interfacial bond characteristics between the simplest form of fibre (i.e. straight fibres) and the surrounding concrete, the end portions of the hooked-end fibres were removed. For straight fibres, the bond between the fibre and the concrete is generated only by friction and the chemical adhesion between the two materials and there is no significant mechanical interlocking or anchorage. The load-slip behaviour measured during the tests for the NSC, MSC, HSC and UHPC samples at the full range of tested temperatures are presented in Figure 6.6.

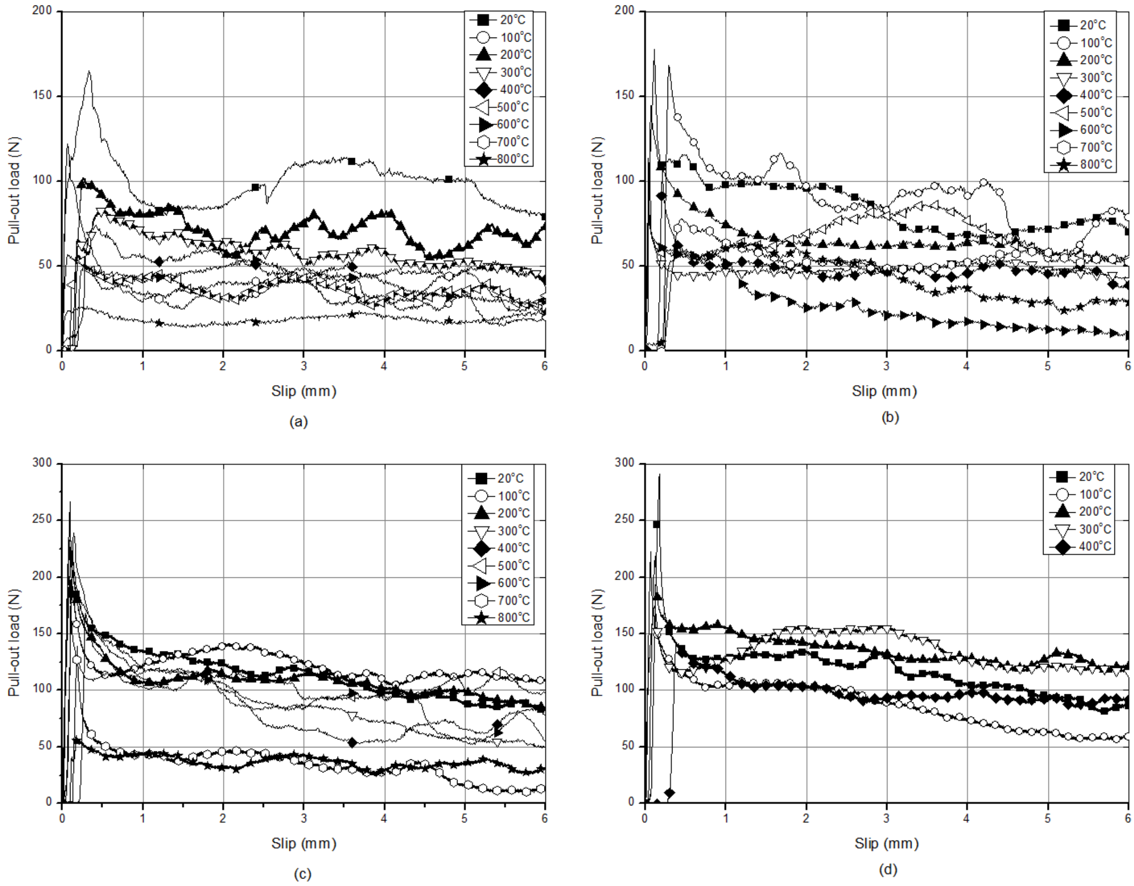

Figure 6.6 Pull-out load-slip curves obtained from pull-out test of straight fibre:(a) NSC, (b) MSC, (c) HSC and (d) UHPC

The maximum pull-out load ($P_{peak,s}$), the corresponding slip at $P_{peak,s}$ ($S_{peak,s}$) and the total amount of work done in the pull-out ($W_{total,s}$), which is calculated as the area under the pull out load-slip curve at each temperature, are given in Table 6.2. It can be seen that the pull-out behaviour of the straight fibres is mainly characterized by a rapid increase followed by a sudden drop in pull-out load, indicating that the fibre debonds significantly from the concrete in a rapid manner. Afterwards, the pull-out load continues to decrease with an increase in slip. As stated before, for the straight fibres, bond is made up only of chemical adhesion and friction with no mechanical interlock. So, once these mechanisms are overcome, the fibre pulls under low pull-out resistance.

Table 6.2 Test results of mechanical, thermal and pull-out behaviour at elevated temperatures

Material	Property	20°C	100°C	200°C	300°C	400°C	500°C	600°C	700°C	800°C
NSC	f'_c and f'_{cT} (MPa)	33	31	32	30	29	25	18	13	11
	M_{loss}(%)	0	0.16	0.72	1.56	5.95	6.84	7.27	8.89	10.81
	$P_{peak,s}$ (N)	165	122	102	84	74	57	56	52	27
	$S_{peak,s}$ (mm)	0.32	0.06	0.26	0.47	0.41	0.18	0.06	0.29	0.61
	$W_{total,s}$ (Nmm)	2288	1363	1744	721	1040	466	979	527	605
	$P_{peak,h}$ (N)	325	304	352	345	309	310	234	217	148
	$S_{peak,h}$ (mm)	0.79	1.11	0.99	1.13	1.07	0.71	0.81	1.2	2.01
	$W_{total,h}$ (Nmm)	2515	2280	3364	2635	2925	3396	1826	2251	1240
MSC	f'_c and f'_{cT} (MPa)	54	52	57	53	50	45	35	31	23
	M_{loss}(%)	0	0.13	1.92	2.62	6.67	7.65	7.91	8.56	9.85
	$P_{peak,s}$ (N)	177	171	144	113	107	105	104	77	64
	$S_{peak,s}$ (mm)	0.11	0.25	0.77	0.03	0.2	0.06	0.03	0.44	1.36
	$W_{total,s}$ (Nmm)	1066	1236	1504	1089	1162	902	803	757	533
	$P_{peak,h}$ (N)	414	438	463	446	376	269	259	182	151
	$S_{peak,h}$ (mm)	0.96	0.86	1.55	0.96	1.01	1.1	1.13	1.57	2.68
	$W_{total,h}$ (Nmm)	3542	4219	4137	4822	2861	2238	2098	1631	1690
HSC	f'_c and f'_{cT} (MPa)	71	69	72	66	64	62	42	38	34
	M_{loss}(%)	0	0.34	1.69	2.03	3.28	5.81	6.8	7.14	8.25
	$P_{peak,s}$ (N)	266	238	236	227	210	200	168	138	57
	$S_{peak,s}$ (mm)	0.09	0.13	0.09	0.13	0.21	0.07	0.29	0.18	0.19
	$W_{total,s}$ (Nmm)	2263	1932	2271	1871	1815	1558	1442	417	466
	$P_{peak,h}$ (N)	591	589	527	501	442	391	369	335	261
	$S_{peak,h}$ (mm)	1.51	0.96	1.04	1.02	0.86	0.63	0.56	2.73	2.7
	$W_{total,h}$ (Nmm)	6832	4759	5677	5309	4295	3359	3916	3736	3258
UHPC	f'_c and f'_{cT} (MPa)	148	151	152	155	140	-	-	-	-
	M_{loss}(%)	0	0.49	1.14	1.85	2.48	-	-	-	-
	$P_{peak,s}$ (N)	290	222	218	174	141	-	-	-	-
	$S_{peak,s}$ (mm)	0.17	0.06	0.12	0.12	0.39	-	-	-	-
	$W_{total,s}$ (N mm)	2468	1993	1493	1338	702	-	-	-	-
	$P_{peak,h}$ (N)	545	633	577	678	562	-	-	-	-
	$S_{peak,h}$ (mm)	1.61	1.24	1.04	1.45	1.1	-	-	-	-
	$W_{total,h}$ (N mm)	5248	5740	5489	4954	6656	-	-	-	-

6.3.2.1.2 Effect of matrix strength on pull-out behaviour of straight fibres

With reference to the $P_{peak,s}$ and $W_{total,s}$ values at ambient temperature (Table 6.2), it is observed that, as expected, as the compressive strength of the matrix increases (i.e. from NSC to MSC to HSC to UHPC), both the maximum pull-out load and the pull-out work done also increase. After exposure to elevated temperature, there is a decrease in both $P_{peak,s}$ and $W_{total,s}$ with increasing temperature for all concrete types. This is because of the gradual degradation in bond strength that occurs at elevated temperature owing to both physical and chemical transformation of concrete. These interactions progressively weaken and crack the concrete, resulting in local breakdowns in the bond between the cement paste and the fibres.

The pull-out behaviour of the straight fibres embedded in all three concrete mixes followed a similar trend at high temperatures. Following heating of the NSC, MSC, HSC and UHPC to 400°C, their peak pull-out load decreased by 55%, 40%, 21% and 51%, respectively, relative to the corresponding ambient temperature values (Table 6.2). This rapid degradation of $P_{peak,s}$ can be attributed to the significant loss of chemically-bound water at this temperature which causes dehydration and the disintegration of the C-S-H bond in the concrete. For the UHPC mixture, $P_{peak,s}$ reduces significantly compared with the other mixtures in the range of 20-400°C temperature. This may be attributed to the fact that UHPC is produced with a relatively low water/binder (W/B) ratio as well as a relatively high binder content, which combine to form a denser microstructure with lower permeability, compared to the other concrete mixes. This can induce internal cracking between the cement paste and the aggregate due to the evaporation of free water and expansion of the paste; thus, the fibre-matrix interfacial bond strength is reduced significantly.

On the other hand, at higher temperatures in the range between 600-800°C, NSC, MSC and HSC exhibit significantly lower values of $P_{peak,s}$, relative to their corresponding ambient values. The loss in pull-out strength of HSC is more abrupt in comparison to the gradual loss which occurred for the NSC and MSC in the 500-800°C temperature range. This sharp reduction in bond strength for HSC specimens may be due to its relatively low water/binder ratio which results in the dehydration of the cement paste by reducing the free water in the concrete. At 800°C, the $P_{peak,s}$ of the NSC, MSC and HSC mixes dropped by around 84%, 64% and 79%, respectively, from their corresponding ambient values. Since the pull-out resistance of straight fibres is primarily controlled by the physicochemical adhesion properties between the fibre and matrix [33], the sharp reduction in $P_{peak,s}$ can be attributed to the significant changes in the physicochemical bond properties between the fibre and matrix at this temperature. Accordingly, it is deduced that the micro-cracks may be developed in the concrete at this temperature in the region around the fibre which causes the resistance to pull-out to diminish significantly. Also, from Table 6.2 it is interesting to observe that although the NSC produced with the highest W/B ratio, it exhibits the greatest reduction in bond strength at 800°C. According to Arioz [133] the decrease in W/B ratio to 0.4 has no significant effect on concrete strength losses and higher loss was observed for mixtures with higher W/B ratios. In addition, the absence of admixtures in the NSC mix may also contribute to a poor interfacial bond strength between the cement paste and aggregate or reinforcing fibre.

6.3.2.2 3D Hooked-end fibres

6.3.2.2.1 Pull-out load-slip response

The pull-out load-slip curves for the specimens with hooked-end fibres embedded in concrete are very different from these of straight fibres (Figure 6.7). It is apparent that the level of bond strength is significantly higher for the hooked-end fibres. The different mechanisms of bond may have developed in the hooked-end fibres. The straight fibres rely entirely on friction and adhesion to generate bond, whereas, in addition to these mechanisms, the hooked-end fibres also develop mechanical interlock to resist slippage. The $P_{peak,h}$ is 49%, 57%, 55%, and 47% higher than that of $P_{peak,s}$ pulled from the NSC, MSC, HSC and UHPC, respectively. The most significant difference is that after the peak pull-out load has been achieved, the bond strength diminishes gradually and then experiences a second gain in strength at around 4-5 mm of slip; this is the activation of the mechanical interlock which develops once adhesion has been overcome and some slip has occurred. The loss of pull-out load post-$P_{peak,h}$ is more gradual in the hooked-end fibres compared with the straight fibres owing to the more complex bond mechanisms involved.

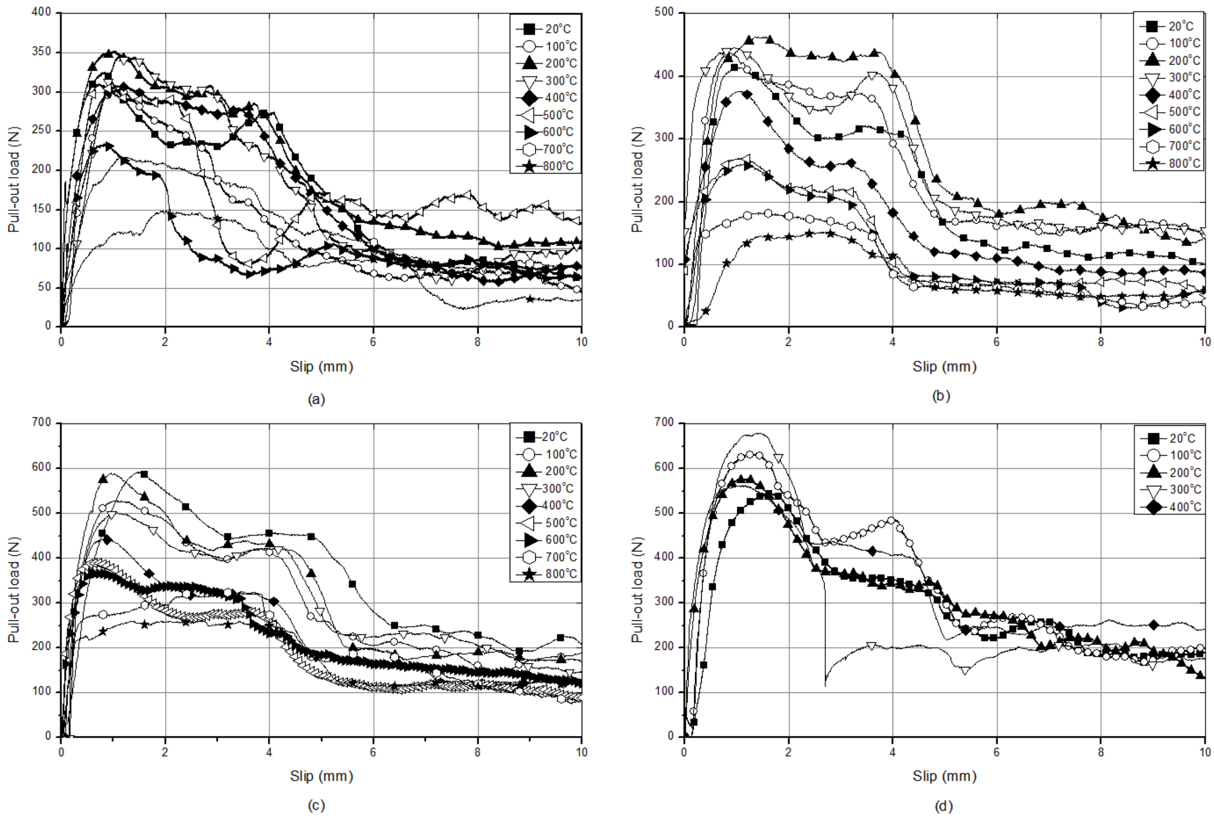

Figure 6.7 Pull-out load-slip curves obtained from pull-out tests on hooked end fibres with (a) NSC (b) MSC (c) HSC and (d) UHPC concrete mixes

From the test results (Figure 6.7 and Table 6.2), it is clear that the elevated temperature pull-out load-slip relationship can be separated into two temperature ranges, namely 20-400°C and 400-800°C. Between 20°C and 400°C, the pull-out behaviour of the hooked-end fibres is not significantly influenced by the change in temperature. For the NSC mix, the pull-out force decreases at 100°C compared with the corresponding ambient value and then actually increase to a value greater than occurred at ambient temperature at 200°C and 300°C (Table 6.2). For the MSC and UHPC concrete, $P_{peak,h}$ is higher at each temperature interval up to 300°C compared with the corresponding ambient value (Table 6.2). On the other hand, for the fibres embedded in HSC, the bond strength begins to diminish once the sample has been exposed to any amount of elevated temperature. Regarding the increase in bond strength that occurs in some samples in the 100-300°C temperature range, this is attributed to rehydration in the concrete mix, acceleration in the pozzolanic reaction, in addition to moisture migration; these phenomena combine to result in an improvement in the bond strength. It is noteworthy that this was not observed in the tests using straight fibres and therefore, it can be deduced that only the mechanical interlocking bond mechanism is affected by these chemical changes in this temperature range. After exposure to 400°C, the hooked-end fibres in NSC, MSC and HSC all demonstrate a decrease in pull-out load, compared with their equivalent ambient values. The UHPC bond strength also decreases compared to the values in the 100-300°C range, but is still slightly higher than the force achieved at ambient temperature.

In the higher temperature range between 400°C and 800°C, there is a more significant loss in the pull-out strength with increasing temperature, especially above 600°C, as the bond strength between the fibre and the concrete diminishes. In this temperature range, there is a significant loss of moisture as well as a degradation of the concrete microstructure which leads to the development and propagation of micro- and macro-cracks at the fibre-concrete interface. As a result, the fibres are completely pulled out without full deformation or straightening of the hooks. This phenomenon explains the difference in shape of the curves for NSC, MSC and HSC exposed to 700°C and 800°C compared with those in the 20-600°C temperature range.

6.3.2.2.2 Effect of matrix strength on pull-out behaviour of 3DH hooked-end fibres

It can be seen that the maximum pull-out load ($P_{peak,h}$) and total work during pull-out ($W_{total,h}$) of the hooked-end fibres at room temperature increases as the matrix compressive strength increases (Figure 6.7 and Table 6.2), as expected. At room temperature, the highest levels of bond strength are found in the HSC and UHPC samples, leading to significantly higher values for $P_{peak,h}$ and $W_{total,h}$ compared with the other mixes. However, at elevated temperatures, the various concrete mixes demonstrate some different behaviour patterns. The NSC and MSC matrices tend to have more modest peak pull-out loads but then lose their bond strength in a more gradual manner compared with the HSC and UHPC mixes. For the UHPC concrete, some of the fibres partially ruptured at the hook end during the pull-out process, as shown in Figure 6.8, causing a sudden reduction in pull-out load. Although these fibres ruptured at slips of between 2 and 4.5 mm, the remaining part of the fibre continued to transmit the pull-out loads (Figure 6.7d). For NSC and MSC, the influence of concrete compressive strength on the maximum pull-out load becomes less important when the temperature exceeds 500°C. It can be seen that these two concretes have quite similar values throughout the (600-800°C) temperature range.

Figure 6.8 Shows the rupture of fibre hook pulled-out from UHPC at 300°C

As expected, when the highest temperature of 800°C was applied to the specimens, the lowest value of P_{peak} was recorded. The NSC, MSC and HSC specimens lost 54%, 63% and 56%, respectively, of their corresponding ambient temperature maximum pull-out loads at 800°C. These values are all within +/-5% of each other, showing that the variation in the loss of pull-out load between the different concretes is not very significant. Nevertheless, HSC has superior bond strength compared with the other concretes and therefore displays better pull-out response even at higher temperatures. It is noteworthy that the load-slip curves in Figures 6.7a-c show a difference in behaviour of $P_{peak,h}$ at 700-800°C compared with lower temperatures. From 20-600°C, as stated before, the pull-out load reaches a peak value of $P_{peak,h}$ at around 1-2 mm of slip, and this is followed by a gradual reduction in the load, followed by a gentle increase at around 4 mm of slip (due to the activation of mechanical interlock). Thereafter, the pull-out load decreases progressively until it reaches a residual value at around 5-6 mm of slip. On the other hand, for the samples exposed to 700-800°C, this double peak phenomenon is not observed. This is most likely because the chemical adhesion and friction is lost due to the exposure to these high temperatures and significant bond is developed only from mechanical interlock. This is verified in the results from the tests on straight fibres (Figure 6.6) which show very low values of pull-out load for specimens heated to 700-800°C. More detailed analysis of the influence of elevated temperatures on the pull-out response is being seen in next section.

6.3.2.2.3 Evaluation of the deformation and straightening of the hook

In order to further understand the influence of elevated temperature on the pull-out response of hooked-end fibres, the deformation and straightening behaviour of fibres pulled out from different concrete matrices have been examined using optical microscopy (OM). The OM images of the hooked-end fibres pulled-out from NSC, MSC, HSC and UHPC after heating to 20, 400, 600 and 800°C are presented in Figure 6.9. These images show that the hooked-end fibres embedded in all matrices at 20 and 400°C are almost completely deformed and straightened during pull-out; this occurs to a greater extent in HSC and UHPC compared with NSC and MSC. However, at temperatures of 600°C and above, it can be seen that the fibre hook embedded in the NSC, MSC and HSC matrices did not straighten to the same extent. The lower level of deformation and straightening of the hook at higher temperatures may be attributed to the significant degradation of the matrix and local crushing at the fibre-concrete interface. Another possible reason for this may also be related to the surface damage of the fibres caused by oxidation, which results in deterioration of the bond between fibre and matrix. This also provides an explanation for the similar values of $P_{peak,h}$ for hooked-end fibres embedded in NSC and MSC throughout the 600-800°C temperature range.

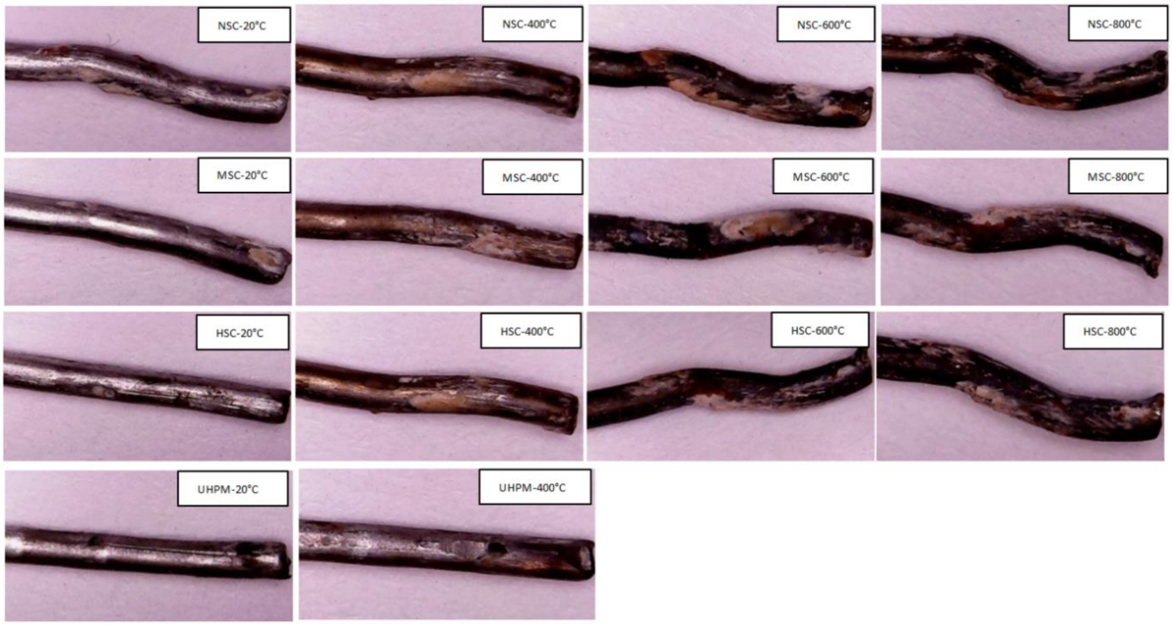

Figure 6.9 Deformation and straightening of hook after pull-out test

6.3.2.2.4 Concluding remarks

The effect of elevated temperatures on the bond characteristics between steel fibres and matrix was investigated through an extensive experimental programme. From the results of this investigation, the following conclusions can be made:

1) The NSC, MSC and HSC specimens retained 88%, 93% and 90% of their compressive strength after exposure to 400°C, and this was further reduced to 46%, 37% and 45% after exposure to 800°C, respectively. The temperature deduced degradation was related to the mass loss, which, even at 800°C, of NSC, MSC and HSC specimens were only 11 %, 10 %, and 8 % of their original values, respectively.

2) The pull-out strength of straight fibres was shown in the experiments to gradually decrease with increasing temperature. At 800°C, the peak pull-out load reduced to 16%, 36% and 21% of the corresponding ambient values, for NSC, MSC and HSC, respectively.

3) The influence of high temperature on the pull-out response of hooked-end fibre was twofold. In the range of 20-400°C, the pull-out behaviour of hooked-end fibres did not vary significantly with temperature. However, above 400°C, the pull-out response of hooked-end fibres embedded in all three concrete matrices gradually decreased with temperature. At 800°C, the peak pull-out load reduced to 46%, 37% and 44% of the corresponding ambient values, for NSC, MSC and HSC, respectively.

4) The reduction in pull-out strength for all mixtures correlated very well with the corresponding decrease in compressive strength. However, the compressive strength of matrix did not have a significant effect on the peak pull-out load of the hooked-end fibres embedded in NSC and MSC in the 600-800°C temperature range.

5) It was shown that exposure to higher temperatures (between 600 and 800°C) had a significant influence on the deformation and straightening of the hook of steel fibres.

6.3.3 Pull-out behaviour of 4DH and 5DH fibres at elevated temperatures

6.3.3.1 Pull-out load-slip response of 4DH fibres

The average pull-out load-slip curves of 4DH fibre embedded in NSC, MSC, HSC and UHPC matrices after exposure to different levels of elevated temperature (20-800°C) are presented in Figure 6.10. It can be seen that the pull-out behaviour of 4DH fibre embedded in all four matrices is generally characterized by a combination of two different mechanisms: debonding and frictional pull-out. Once complete debonding has occurred at the fibre-matrix interface, the fibre hook undergoes plastic deformation to straighten the fibre. So, once these mechanisms are overcome, the pull-out process occurs under frictional resistance.

It can also be observed from Figures 6.10a-d that the pull-out behaviour of the 4DH fibre embedded in each mixture is similar, especially for the lower temperature range (i.e. 20-400°C). However, there are some differences in the maximum pull-out load and pull-out work values. In this temperature range, the maximum pull-out load of 4DH fibre from the UHPC is 54%, 35% and 15% higher than that of the fibre pulled from the NSC, MSC and HSC, respectively (Table 6.3). Another significant difference is that the residual pull-out load of the fibre pulled from the NSC (Figure 6.10a) is greater than those from other matrices. This higher residual response can be attributed to the fibre being pulled out without the occurrence of full deformation and straightening of the hook. Also from Figure 6.10d it is interesting to observe that some of the curves exhibit abrupt load drop corresponding to a partial rupture of the fibre's hook portion. Nevertheless, as illustrated in this figure, the broken fibre continued to withstand the stress transfer until the fibre completely pulled out; the hook at the other end of the fibre remained intact. In the higher temperature range between 500°C and 800°C, there is a significant change in the shape of the pull-out curves with increasing pre-temperature, especially above 600°C, as the bond strength between the fibre and the concrete diminishes considerably (Figures 6.10a-c).

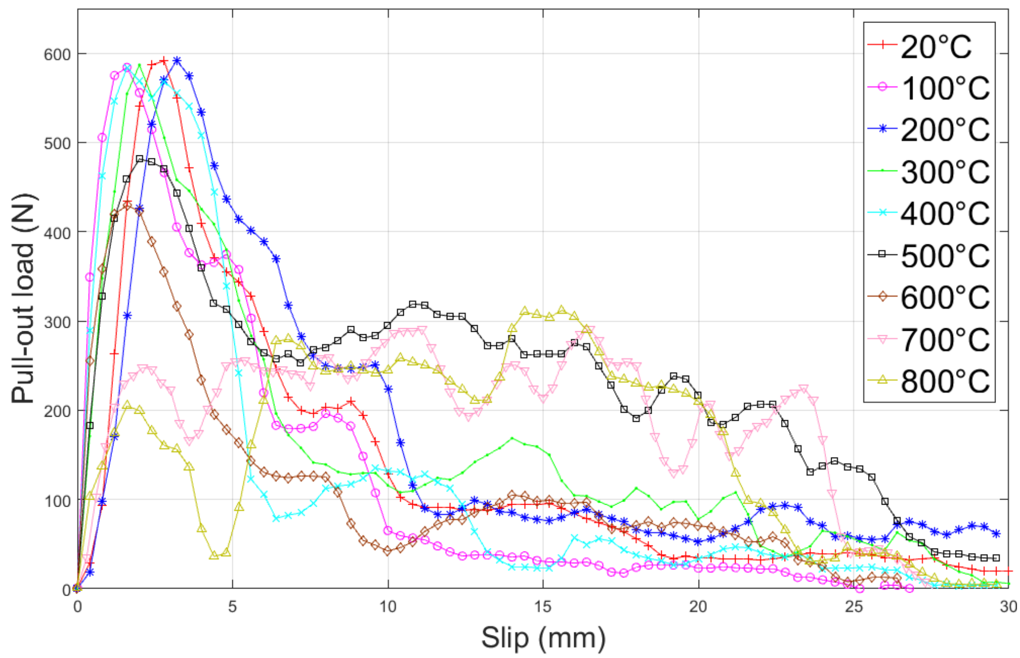

(a)

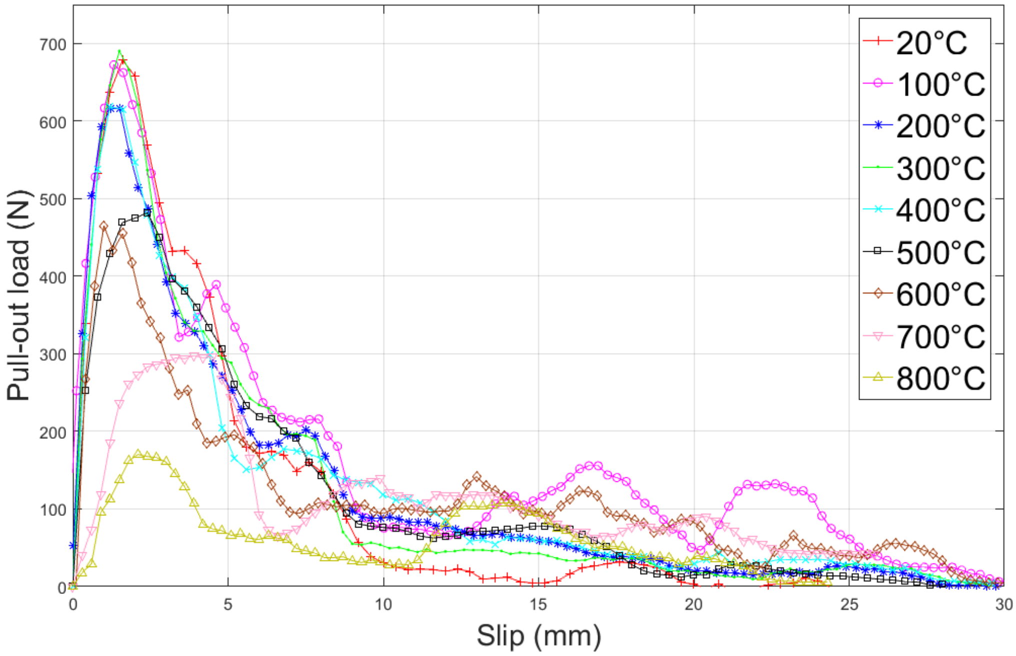

700
600
500
400
300
200
100
0
Pull-out load (N)
0
5
10
15
20
25
30
Slip (mm)
20°C
100°C
200°C
300°C
400°C
500°C
600°C
700°C
800°C

(b)

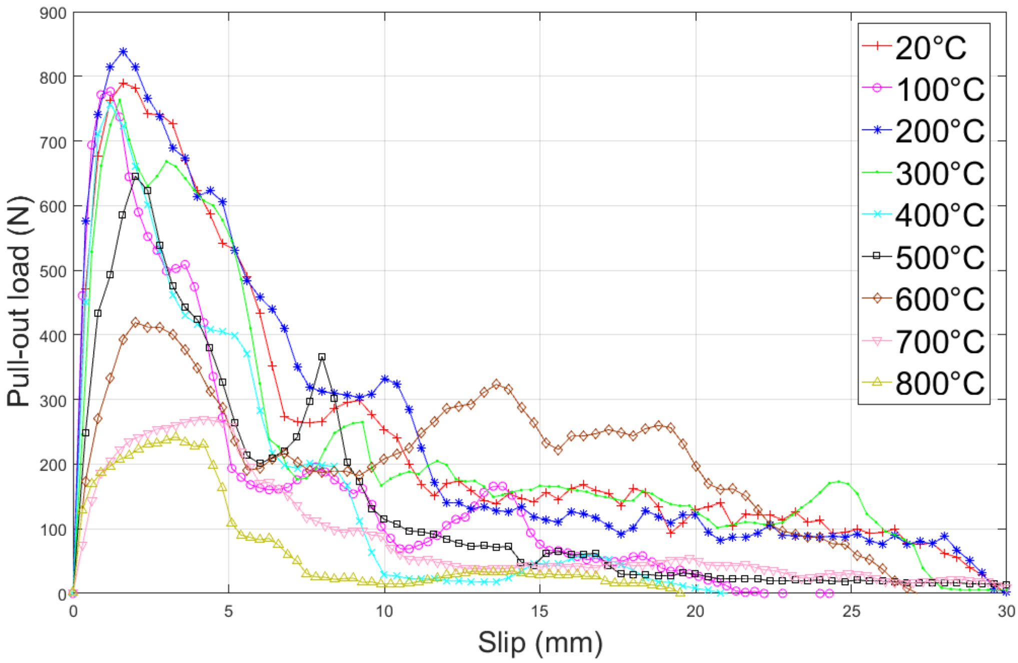

900
800
700
600
500
400
300
200
100
0
Pull-out load (N)
0
5
10
15
20
25
30
Slip (mm)
20°C
100°C
200°C
300°C
400°C
500°C
600°C
700°C
800°C

(c)

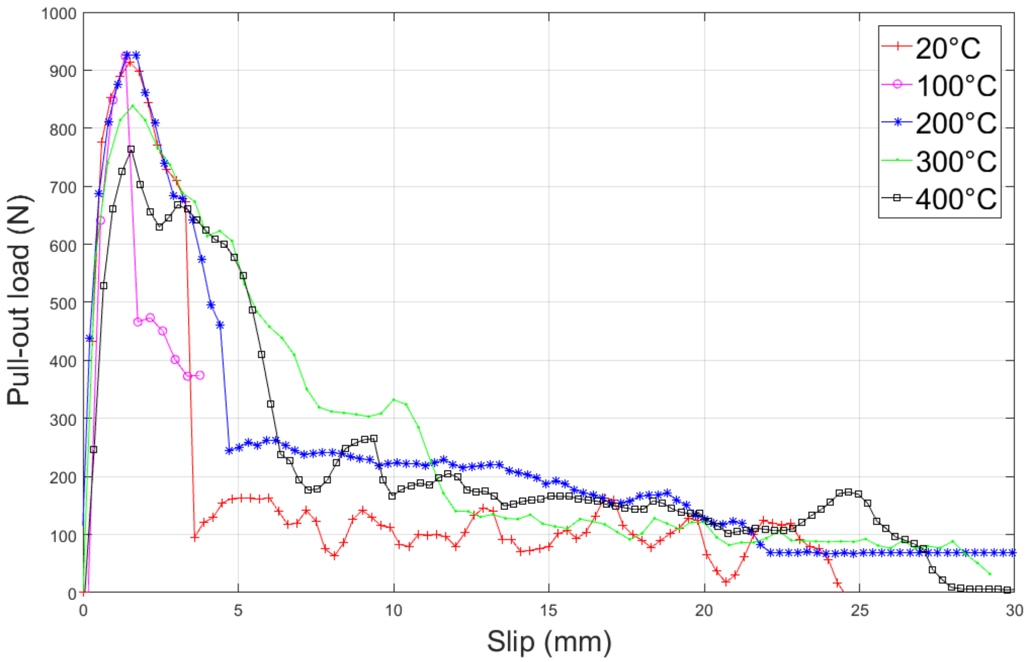

(d)

Figure 6.10 Pull-out load-slip curves obtained from pull-out test of 4DH fibre: (a) NSC, (b) MSC, (c) HSC and (d) UHPC

Table 6.3 Pull-out tests results of 4DH fibres at elevated temperatures (20-800°C)

Material	property	20°C	100°C	200°C	300°C	400°C	500°C	600°C	700°C	800°C
NSC	P_{max} (N)	596	588	595	589	586	484	433	313	292
	$\sigma_{f,max}$ (MPa)	937	925	936	926	922	761	681	492	459
	S_{max}(mm)	2.58	1.45	3.25	2.03	1.59	2.10	1.73	11.04	14.33
	W_{total} (N mm)	4154	3600	4968	4715	3789	7057	3127	2723	2445
MSC	P_{max} (N)	685	680	620	691	622	485	470	299	170
	$\sigma_{f,max}$ (MPa)	1077	1070	975	1087	978	763	739	470	267
	S_{max}(mm)	1.68	1.43	1.30	1.48	1.22	2.44	1.05	4.45	2.32
	W_{total} (N mm)	3123	5043	3661	3593	3707	3402	3531	3024	1525
HSC	P_{max} (N)	797	779	840	766	759	656	426	272	245
	$\sigma_{f,max}$ (MPa)	1254	1225	1321	1205	1194	1032	670	428	385
	S_{max}(mm)	1.76	1.11	1.57	1.53	1.16	2.12	2.24	4.91	3.44
	W_{total} (N mm)	6210	4271	6756	6627	3809	4210	5917	2563	1419
UHPC	P_{max} (N)	918	931	933	840	766	-	-	-	-
	$\sigma_{f,max}$ (MPa)	1444	1465	1468	1321	1205	-	-	-	-
	S_{max}(mm)	1.55	1.42	1.57	1.58	1.59	-	-	-	-
	W_{total} (N mm)	4763	1922	7222	7540	6627	-	-	-	-

The results from the pull-out tests are also presented in Table 6.3, which includes the maximum pull-out load (P_{max}), the corresponding slip at P_{max} (S_{max}), the maximum tensile stress induced in the fibre ($\sigma_{f,max}$) and the total amount of work done in the pull-out (W_{total}), which is calculated as the area under the pull out load-slip curve for each concrete type at each temperature. It can be seen that the P_{max}, $\sigma_{f,max}$ and W_{total} of the 4DH fibres at ambient temperature increases as the matrix compressive strength increases, as expected. At ambient temperature, the highest levels of bond strength are found for the HSC and UHPC samples, leading to significantly higher values for P_{max}, $\sigma_{f,max}$ and W_{total} compared with the other mixtures.

With heating to 100°C and above, all four matrices experienced loss in pull-out strength with temperature. The maximum pull-out load ($P_{max,T}$) normalised by the corresponding ambient value (P_{max}) for all mixtures with increasing temperature is presented in Figure 6.11, whilst the corresponding maximum tensile stress induced in the fibre ($\sigma_{f,max}$), which is found identical to that of the P_{max}, is also shown in Figure 6.11. It can be clearly seen that the maximum pull-out load in all four matrices is similar within the temperature range of 20 to 400°C. For NSC, the P_{max} initially remains constant up to 300°C and then slightly reduces up to 400°C. The P_{max} of MSC also remains constant at 100°C initially before decay at 200°C and then regains to maximize at 300°C. The P_{max} of the HSC decreases at 100°C initially and then maximizes at 200°C before remains constant between 300 and 400°C. In the case of UHPC, P_{max} increases up to 200°C initially and then gradually reduces leading to explosive spalling at 500°C. The enhancement of bond strength in UHPC up to 200°C may be attributed to accelerate the pozzolanic reactions, improving packing density and reducing the pore size which improves the fibre-matrix interfacial properties. In this temperature range (i.e. 20-200°C), as stated before, the pull-out load dropped suddenly for slip less than 5 mm indicating that the fibre ruptured internally at its hook. This represents $\sigma_{f,max}/\sigma_{uts}$ of around 0.97-1.0 (where σ_{uts} =1500 MPa is the ultimate tensile strength of the steel fibre), which reflects full activation of the mechanical bond i.e. the fraction of UTS absorbed by hinge formation.

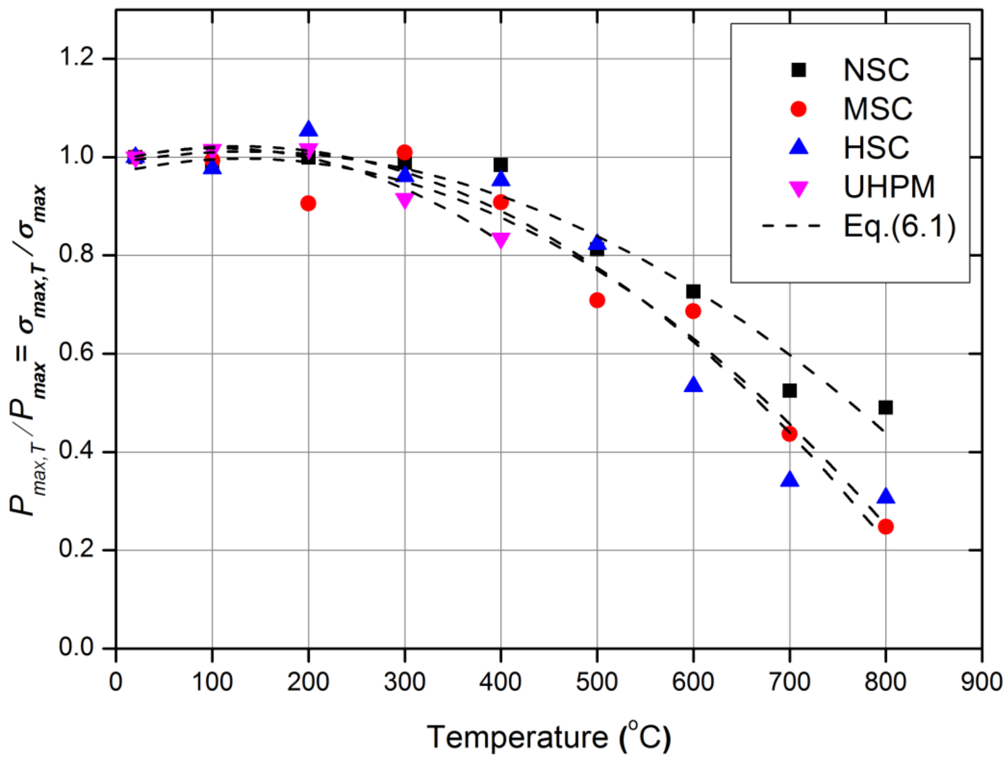

Figure 6.11 Variation in maximum pull-out load and stress of 4DH fibre as a function of temperature

At a temperature greater than 400°C the pull-out strength drops consistently with increase in temperature. The loss of bond strength in each concrete matrix almost followed a similar trend up to 700°C. Once the target temperature reaches 800°C, the P_{max} of NSC, MSC and HSC was only 52%, 25% and 31% of its original P_{max} value at ambient temperature, respectively. This sharp degradation of pull-out strength can be attributed to the decomposition of concrete due to complete dehydration and progression of micro and macro cracks, which had adverse effect on the compressive strength.

For NSC, MSC, HSC and UHPC, the quadratic relationship between the relative maximum pull-out load $P_{max,T}/P_{max}$ and the temperature T can be expressed as Eq. (6.1).

$$\frac{P_{max,T}}{P_{max}} = \frac{\sigma_{max,T}}{\sigma_{max}} = \left\{ \begin{array}{ll} 0.98 + 3.52 \times 10^{-4}T - 1.29 \times 10^{-6}T^2, & NSC \\ 0.96 + 4.44 \times 10^{-4}T - 1.67 \times 10^{-6}T^2, & MSC \\ 0.99 + 4.56 \times 10^{-4}T - 1.78 \times 10^{-6}T^2, & HSC \\ 0.99 + 4.70 \times 10^{-4}T - 2.21 \times 10^{-6}T^2, & UHPM \end{array} \right. , \quad 20℃ < T \leq 800℃ \Bigg\} \quad (6.1)$$

where, $P_{max,T}$ and P_{max} represent the maximum pull-out load at elevated temperatures and maximum pull-out load at room temperature and T elevated temperature correspondingly $\sigma_{max,T}/\sigma_{max}$ is the ratio of maximum pull-out stress between elevated and ambient temperature. As can be seen from Figure 6.11 that the proposed empirical relations by Eq. (6.1) fit well with test data and the correlation coefficient R^2 for NSC, MSC, HSC and UHPC were 0.96, 0.96, 0.95 and 0.97, respectively.

6.3.3.2 Pull-out load-slip response of 5DH fibres

The average pull-out load-slip curves obtained from the pull-out test of 5DH fibre embedded in NSC, MSC, HSC and UHPC under different exposure temperatures (20-800°C) are presented in Figures 6.12a-d. It can be seen that the pull-out curves of 5DH fibre for all four matrices are similar to the corresponding curves of 4DH fibre (Figures 6.12a-d), even at higher temperatures, although with higher maximum pull-out load, slip capacity and total pull-out work values, particularly for HSC and UHPC. It should also be noted that the 5DH fibre pulled from all matrices did not exhibit abrupt load drop or fibre rupture during the pull-out process.

The initial gradients of 5DH fibre curves embedded in all matrices are similar to each other. However, the post-peak behaviour of the 5DH fibre pulled from the NSC and MSC (Figures 6.12a and b) is significantly different from those of the HSC and UHPC (Figures 6.12c and d). The post-peak behaviour of the fibre pulled from the NSC and MSC exhibit additional peak points and more variability, while the curves corresponding to HSC and UHPC show relatively smoother and lower residual pull-out strength. These differences may be attributed to the frictional effect of coarse aggregate, together with the remaining irregularities due to incomplete deformation and straightening of the hook in the NSC and MSC (Figure 6.13a), which ultimately increase the residual pull-out strength. While the lower residual strength of 5DH fibre pulled from HSC and UHPC can be attributed to the high level of deformation and straightening of the hook, which leads to the fibre pulled out under relatively low frictional resistance (Figure 6.13b).

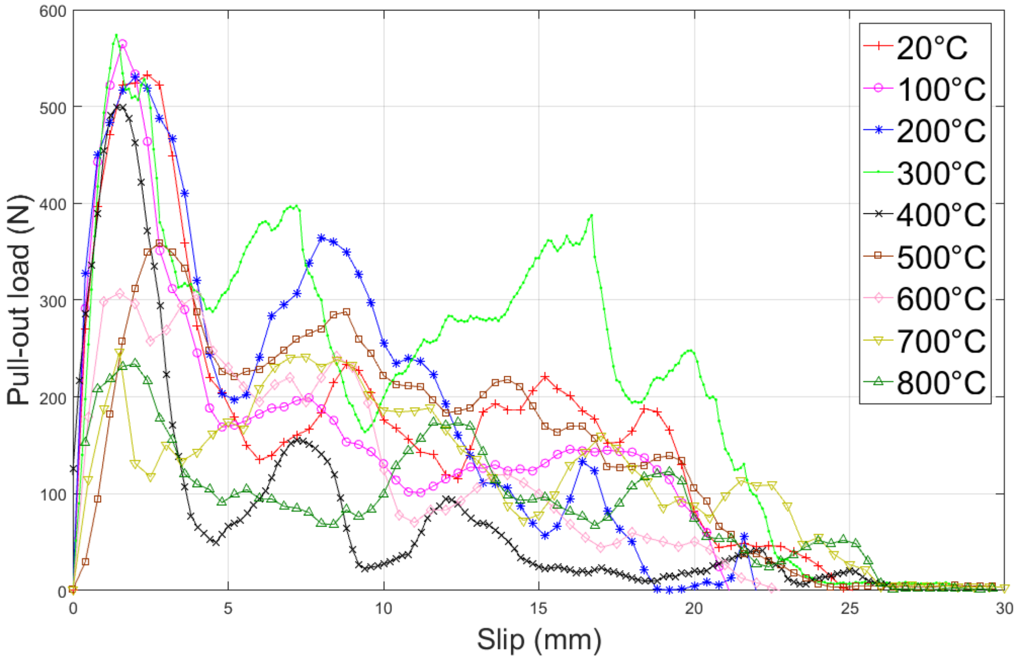

Pull-out load (N)
Slip (mm)
20°C
100°C
200°C
300°C
400°C
500°C
600°C
700°C
800°C

(a)

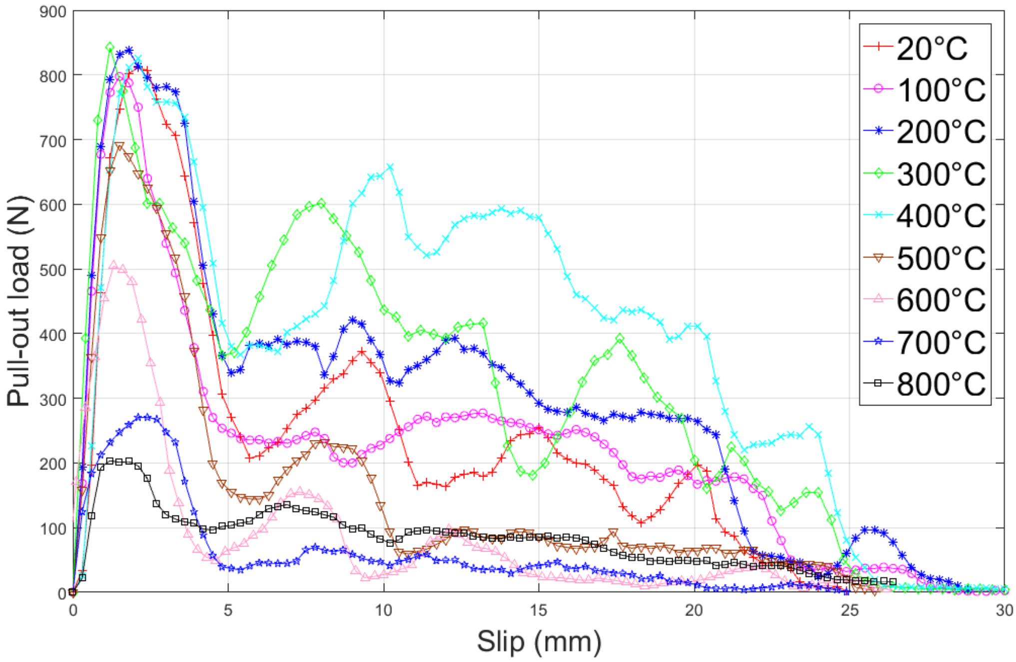

Pull-out load (N)
Slip (mm)
20°C
100°C
200°C
300°C
400°C
500°C
600°C
700°C
800°C

(b)

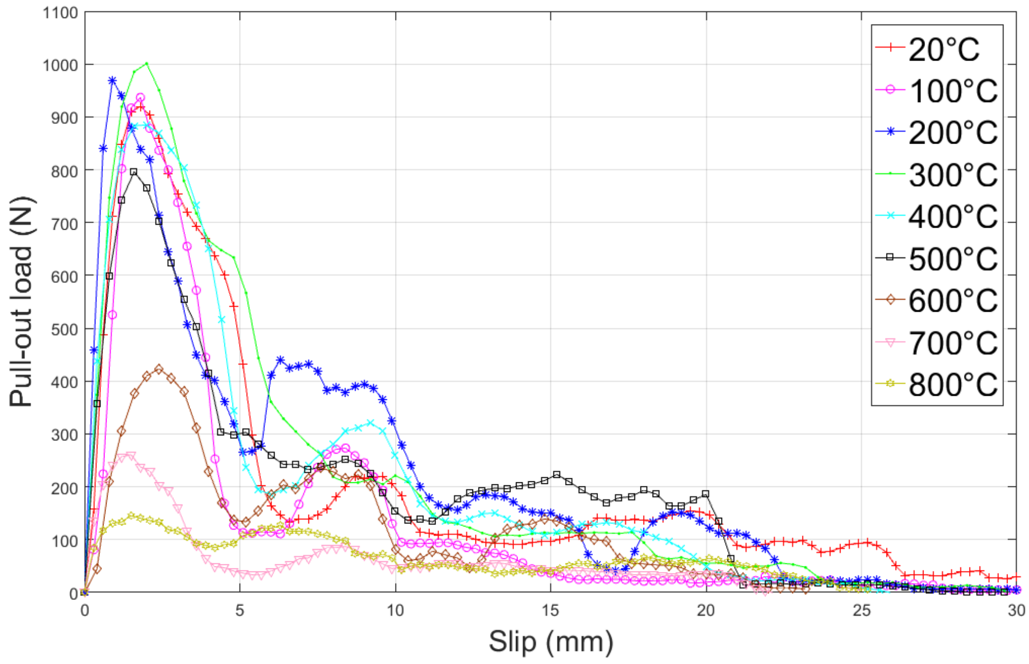

(c)

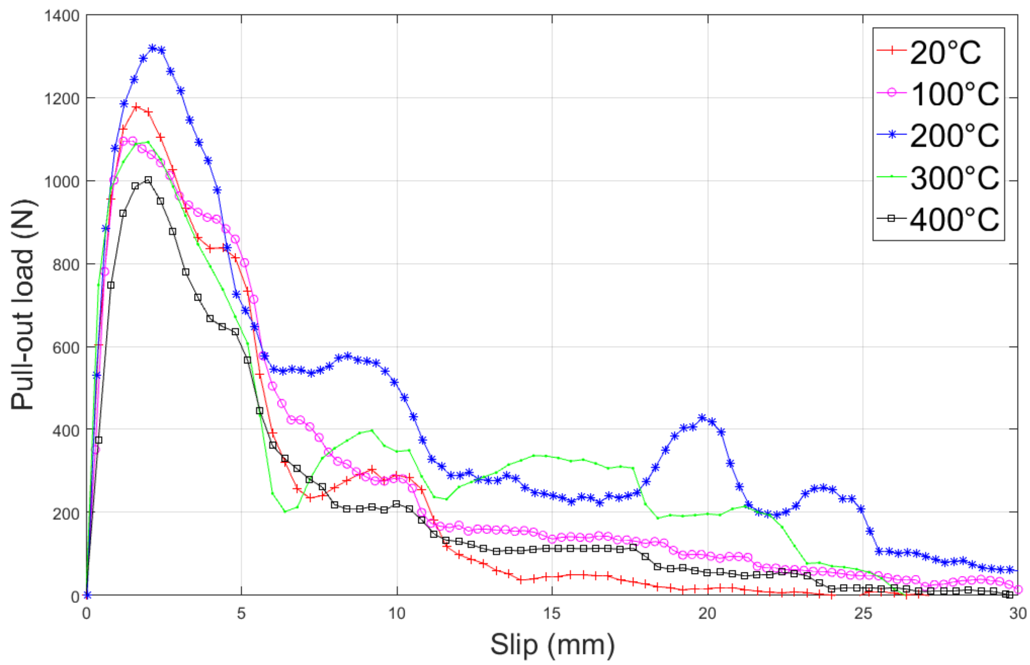

(d)

Figure 6.12 Pull-out load-slip curves obtained from pull-out test of 5DH fibre: (a) NSC, (b) MSC, (c) HSC and (d) UHPC

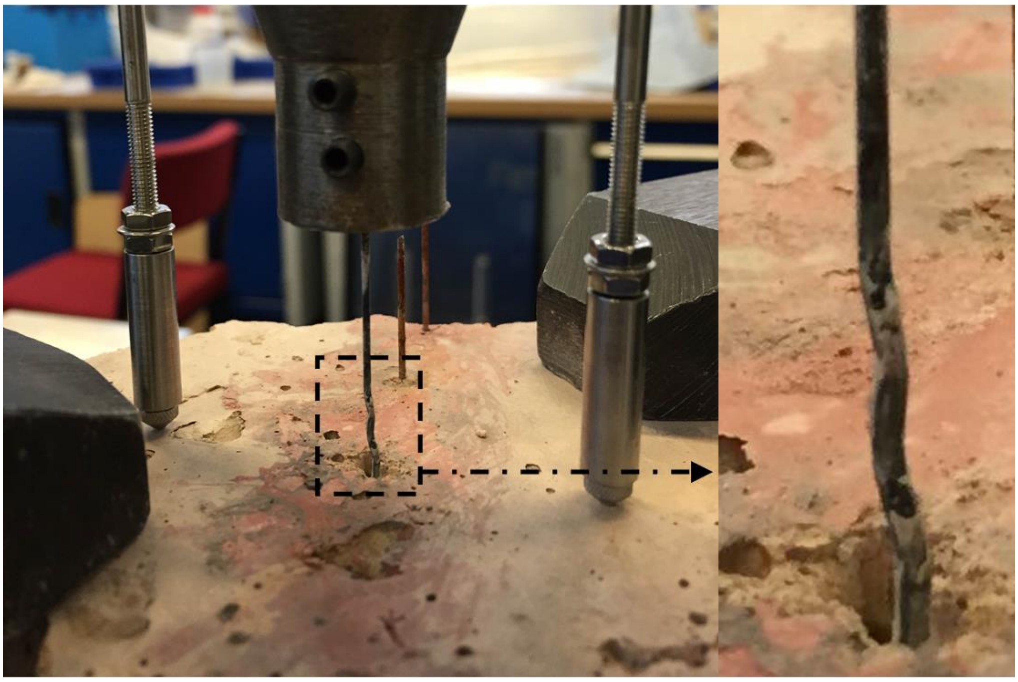

(a)

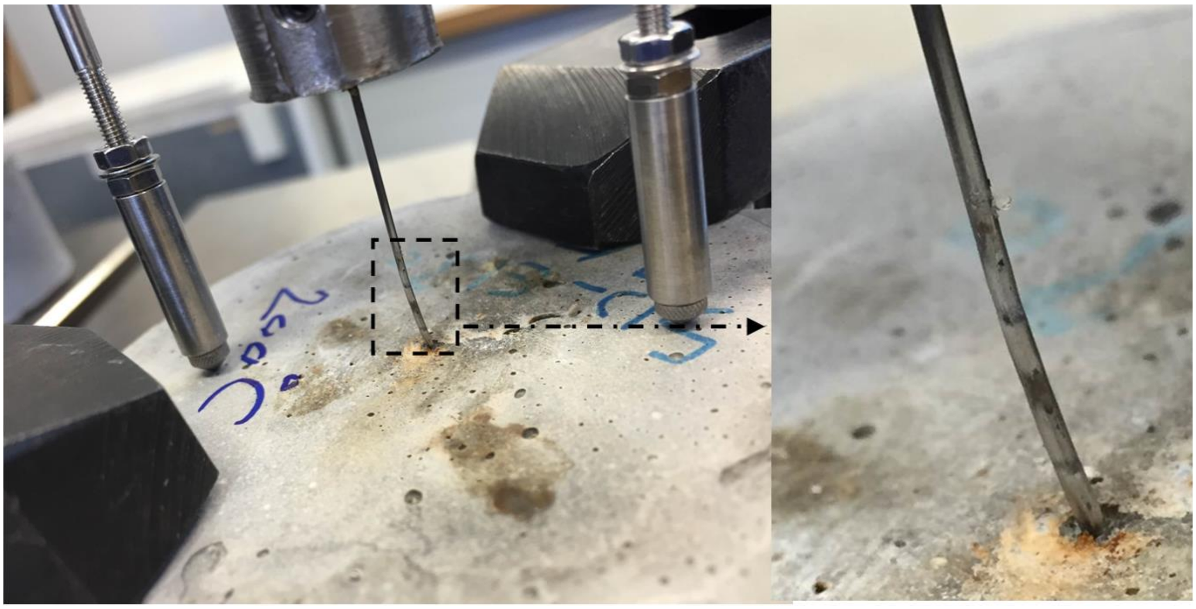

(b)

Figure 6.13 Deformation and straightening of 5DH after pull-out test: (a) NSC and (b) UHPC

Table 6.4 Pull-out tests results of 5DH fibres at elevated temperatures (20-800°C)

Material	property	20°C	100°C	200°C	300°C	400°C	500°C	600°C	700°C	800°C
NSC	P_{max}(N)	537	571	536	578	507	363	312	248	239
	$\sigma_{f,max}$ (MPa)	845	898	843	909	797	571	491	390	376
	S_{max}(mm)	2.33	1.78	2.11	1.35	1.32	2.66	1.30	1.54	1.94
	W_{total} (N mm)	4671	3862	4502	6553	4259	4417	3117	1781	1336
MSC	P_{max}(N)	819	799	843	844	828	693	507	275	205
	$\sigma_{f,max}$ (MPa)	1288	1257	1326	1327	1302	1090	797	433	322
	S_{max}(mm)	2.25	1.61	1.75	1.19	2.04	1.51	1.32	2.25	1.20
	W_{total} (N mm)	3645	6659	8874	9506	11679	4228	2287	1574	2211
HSC	P_{max} (N)	920	948	981	1005	890	798	427	263	147
	$\sigma_{f,max}$ (MPa)	1447	1491	1543	1581	1400	1255	672	414	231
	S_{max}(mm)	1.83	1.66	0.98	1.93	1.89	1.53	2.46	1.46	1.51
	W_{total} (N mm)	7384	4298	7547	6884	6098	5902	3199	1542	1742
UHPC	P_{max}(N)	1181	1110	1323	1102	1005	-	-	-	-
	$\sigma_{f,max}$ (MPa)	1858	1746	2081	1733	1581	-	-	-	-
	S_{max}(mm)	1.75	1.38	2.29	1.84	1.93	-	-	-	-
	W_{total} (N mm)	7043	8610	12937	9694	6883	-	-	-	-

Table 6.4 summarizes the pull-out test results including the maximum pull-out load (P_{max}), the corresponding slip at P_{max} (S_{max}), the maximum tensile stress induced in the fibre ($\sigma_{f,max}$) and the total amount of work done in the pull-out (W_{total}), which are calculated as the average of three tests at each temperature. It can be seen that, as expected, as the compressive strength of the matrix increases (i.e. from NSC to MSC, HSC and UHPC), both the maximum pull-out load and the pull-out work done also increase significantly. After exposure to elevated temperature, there is a gradual decrease in both P_{max} and W_{total} with increasing temperature for all concrete types. Figure 6.14 shows the variation in maximum pull-out load at elevated temperature ($P_{max,T}$) normalised by the corresponding values at ambient temperature (P_{max}) with increasing temperature. The corresponding maximum tensile stress ratio induced in the fibre ($\sigma_{f,max}$), which is geometrically identical to that of the load ratio P_{max}, is also shown in Figure 6.14. It is apparent that there was no significant change in maximum pull-out load within the temperature range of 20 to 400°C, but a subsequent gradual decrease in P_{max} when the temperature exceeds 400°C. For NSC, there is an increase in P_{max} between 20 and 300°C and then gradually decreases with temperature up to 800°C. The P_{max} of MSC slightly reduced at 100°C and remained almost constant between 200 and 400°C before it reduced sharply in the temperature range of 400-800°C. The P_{max} of HSC increased

linearly until 300°C, then gradually decayed up to 500°C and finally sharply decreased in the temperature range of 500-800°C. It can be concluded that the P_{max} loss in all three concretes (i.e. NSC, MSC and HSC) follows an almost similar trend at high temperatures. Their P_{max} was sharply reduced at a similar way above 400°C, especially for MSC and HSC. At 800°C, the P_{max} of NSC, MSC and HSC were only 45%, 25% and 16% of its original P_{max} value at ambient temperature, respectively. In the case of UHPC, there is reduction in P_{max} at 100°C initially, and then P_{max} regains to maximize at 200°C and finally decays sharply up to 400°C.

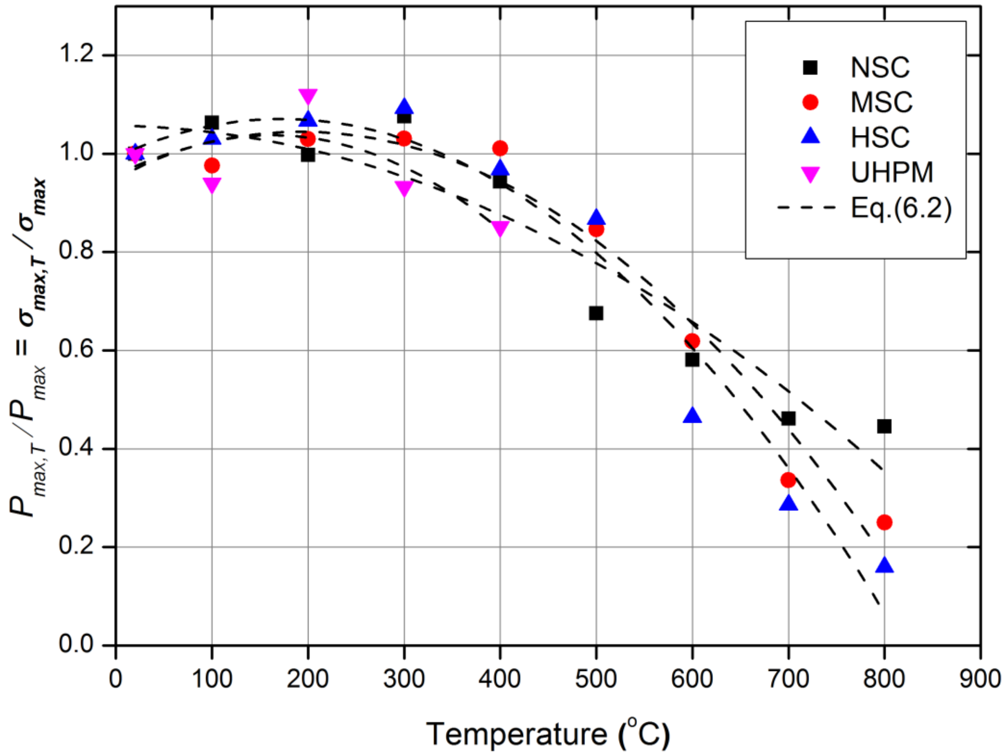

Figure 6.14 Variation in maximum pull-out load and stress of 5DH fibre as a function of temperature

For NSC, MSC, HSC and UHPC, the quadratic relationship between the relative maximum pull-out load $P_{max,T}/P_{max}$ and the temperature T is given by Eq. (6.2).

$$\frac{P_{max,T}}{P_{max}} = \frac{\sigma_{max,T}}{\sigma_{max}} = \left\{\begin{matrix} 1.05 - 2.56 \times 10^{-5}T - 1.06 \times 10^{-6}T^2, \ NSC, \\ 0.95 + 9.05 \times 10^{-4}T - 2.35 \times 10^{-6}T^2, \ MSC, 20°C < T \leq 800°C \\ 0.99 + 8.87 \times 10^{-4}T - 2.55 \times 10^{-6}T^2, \ HSC \end{matrix}\right\} \quad (6.2)$$

where, $P_{max,T}$ and P_{max} represent the maximum pull-out load at elevated temperatures and maximum pull-out load at room temperature and T elevated temperature. It can be seen in Figure 6.14 that the curves proposed by Eq. (6.2) fit well with test data, except that for UHPC. The fit to UHPC was not considered over this temperature range with its 500°C temperature limit. For NSC, MSC and HSC, the correlation coefficient R^2 were 0.90, 0.96 and 0.94 respectively.

6.3.3.3 Difference in the pull-out behaviour of 4DH and 5DH fibres

To further understand the influence of the hook geometry and elevated temperature on the pull-out response, a comparison of two fibres pulled from a different matrix were made. The comparison of the maximum pull-out load between the two hooked end fibres after exposure to various levels of elevated temperature (20-800°C) are plotted in Figure 6.15. It is evident that the pull-out behaviour of the 5DH fibre embedded in all matrices is similar to that of the corresponding 4DH fibre, but different in their P_{max} and W_{total} values. It can be seen from Figure 6.15 that as the compressive strength of the matrix increases, both the maximum pull-out load and pull-out work increase significantly for both fibres. Also from Figure 6.15a it is interesting to observe that the maximum pull-out load of 4DH fibres from the NSC is higher than the corresponding values of the 5DH fibres for all temperatures. This behaviour may be attributed to the fact that the 5DH fibre requires high energy (i.e. high matrix strength) to straighten the hook having a high mechanical anchorage compared to 4DH fibres. With the further increase in compressive strength from NSC (f_c=33MPa) to MSC (f_c=54MPa) and HSC (f_c=71MPa), the maximum pull-out load of 5DH fibre increased much more than that of 4DH fibres (Figures 6.15b and c). This indicates that good bond between steel fibre and matrix due to high mechanical interlocking and high matrix strength is necessary to straighten the hook. However, this effect has a short duration since both fibres behave similarly especially at higher temperatures (i.e. above 600°C). Comparing the two fibres embedded in UHPC (Figure 6.15d), the maximum pull-out load of 5DH is also higher than that of the 4DH fibres and it maximized at 200°C for both fibres in which 5DH fibre is more effective.

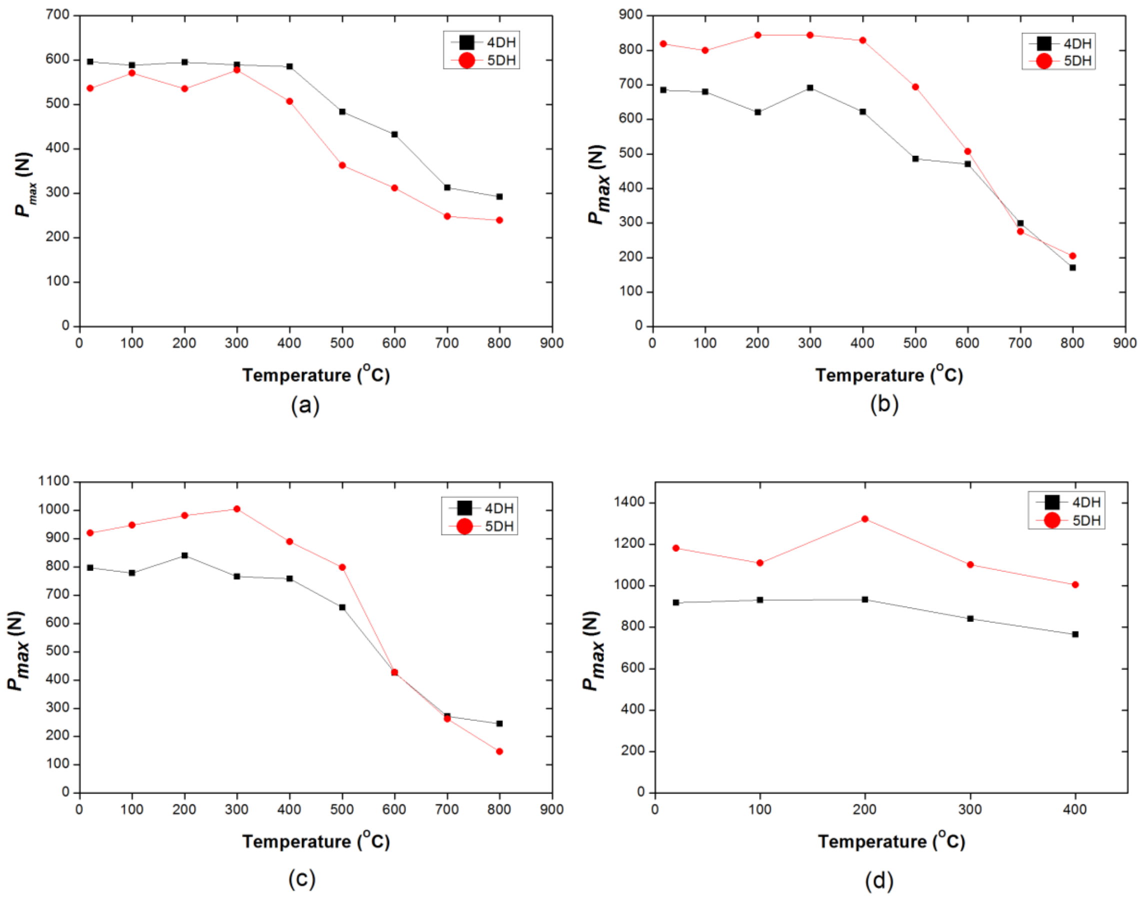

Figure 6.15 Comparison in maximum pull-out load of both fibres at elevated temperatures: (a) NSC, (b) MSC, (c) HSC and (d) UHPC

The comparison of the total pull-out work between the two hooked end fibres after different peak temperatures (20-800°C) is plotted in Figure 6.16. It can be observed that there is no clear variation between the two fibres in total pull-out work of NSC with different elevated temperatures (Figure 6.16a). The highest W_{total} observed for 4DH fibre after heating to 500°C which is almost two times higher than the others (Table 6.3). This inconsistency may be a result of the variability in the deformation required to straighten the hook. As the MSC as an example, the mechanical anchorage contribution provided by the 5DH fibre gave rise to a significant increase in the W_{total} compared to 4DH fibre (Figure 6.16b), although the W_{total} of 5DH fibre was greatly reduced for specimens heated to temperatures greater than 400°C. Similar to the MSC, the W_{total} of 5DH fibre in HSC is also slightly higher than that of the 4DH fibres up to 600°C, but W_{total} values for both fibres reduced considerably between 700 and 800°C (Figure 6.16c). It is noteworthy that since the concrete strength of NSC, MSC and

HSC does not significantly change up to temperature of 500°C (Figure 6.2). Therefore, the W_{total} of both fibres does not vary considerably. The higher values of W_{total} for both fibres at high temperatures may also be attributed to the presence of coarse aggregate in concrete together with the curvatures remaining at the fibre end. In case of UHPC, the W_{total} for 5DH fibre specimens is much higher than the corresponding values of 4DH fibre up to 300°C. The lower values of W_{total} of the 4DH fibre can be attributed partly to the sudden load drop due to a partial fibre rupture in the 4DH geometry (Figure 6.16d).

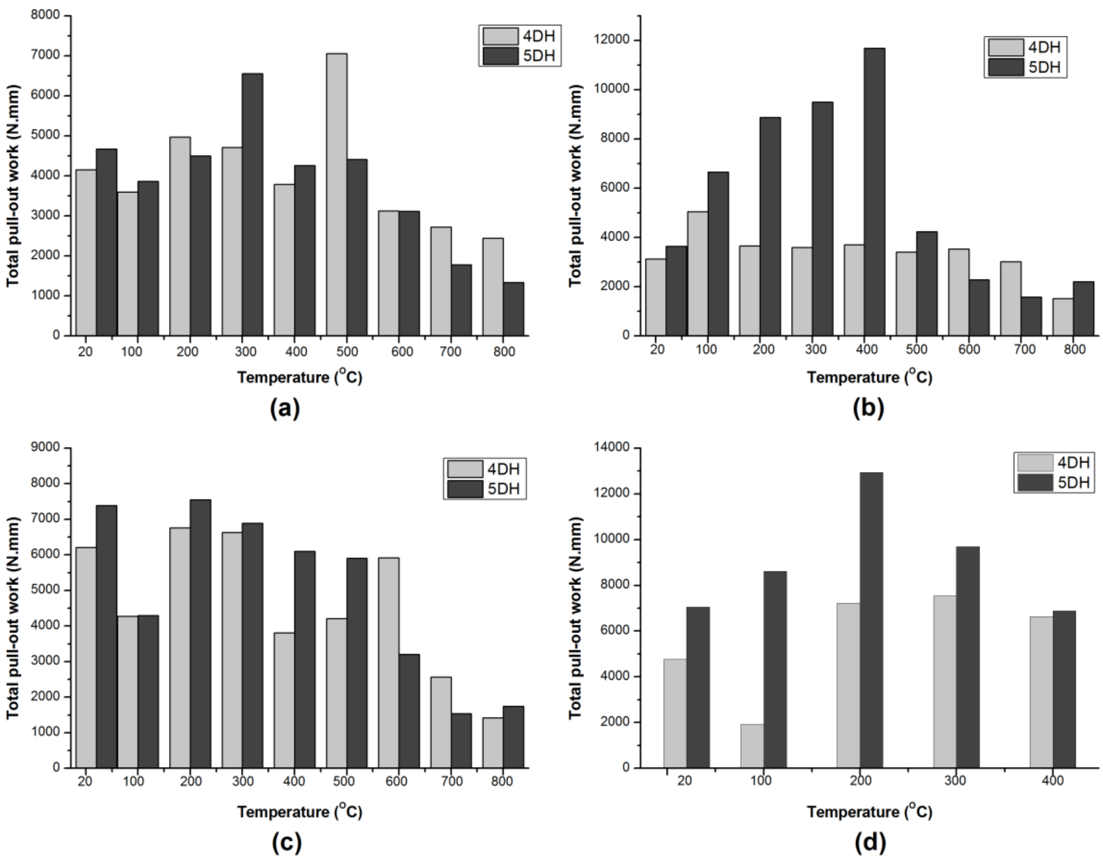

Figure 6.16 Comparison in total pull-out work of both fibres at elevated temperatures: (a) NSC, (b) MSC, (c) HSC and (d) UHPC

6.3.3.4 Discussion

Here we consider the most effective combination of matrix strength and fibre geometry for the various elevated temperatures.

1) In the range of 20-400°C:

Due to the high mechanical anchorage of the 4DH fibre compared with its tensile strength (f_{uts} = 1500 MPa), the rupture of this fibre is more likely to occur in a matrix of high strength. That is, the fibre rupture tends to occur when the fibre with high mechanical anchorage and relatively low tensile strength is combined with very high matrix strength. This indicates that the mechanical anchorage contribution of 4DH fibre can be fully effective if fibre rupture is prevented. Therefore, the tensile strength of 4DH fibre has to increase in parallel with the strength of its anchorage. Only in this way can the fibre resist the forces acting upon it. On the basis of these considerations, it is believed that increasing the tensile strength of the 4DH fibre would effectively prevent fibre rupture and capitalize the end hook anchorage strength to the maximum degree.

For the 5DH fibres, the following observations apply:

1) The complete deformation of fibre hook embedded in the NSC matrix did not occur. Rather only low level of deformation and straightening of the hook have been observed (Figure 6.13a).

2) The partial deformation dramatically increased with increasing the matrix compressive strength.

3) The full deformation and straightening of 5DH fibre hook only takes place when the fibres are embedded in UHPC (Figure 6.13b).

4) In all four matrices, the 5DH fibre is completely pulled out from the specimen without any occurrence of the fibre rupture.

5) As a result of the 5DH unique hook's geometry and its high tensile strength a matrix with high compressive strength is needed to ensure the full extent of hook anchorage, which makes this type of fibre attractive for use in ultra-high performance cementitious composites.

6) Finally, the conclusion is drawn that the 5DH fibre used in this study may only be fully exploited as the reinforcement in UHPC.

2) In the range of 400-800°C:

For 4DH and 5DH fibres, the influence of concrete compressive strength plays an important role on the pull-out strength when the temperature exceeds

500°C. It has been seen that these two fibres embedded in MSC and HSC have quite similar values of P_{max} throughout the (600-800°C) temperature range (see Figures 6.15b and c). This indicates that both fibres have almost similar bond strength when pulled from the matrix without their deformation and straightening resulting from the concrete strength degradation.

6.3.3.5 Concluding remarks

The effect of elevated temperatures on the bond mechanisms associated with the pull-out behaviour of two types of hooked end steel fibres embedded in four different concrete mixes was thoroughly investigated. Some specific conclusions can be drawn as follows:

1) Temperature had a little influence on the compressive strength for all concretes heated up to 400°C. However, explosive spalling occurred for UHPC above 500°C, while at temperatures higher than 400°C, the compressive strength of NSC, MSC and HSC generally decreased with increasing temperature. Once the temperature reached 800°C, the compressive strength of NSC, MSC and HSC was only 33%, 42% and 47% the mass losses of NSC, MSC and HSC specimens were 11 %, 10 %, and 8 % of its original values at ambient temperature, respectively.

2) The pull-out behaviour of 4DH and 5DH fibres appeared to be affected by elevated temperatures in a similar manor. The pull-out strength of both fibres did not vary significantly throughout 20-400°C temperature range, but within the temperature range of 500 to 800°C, the maximum pull-out load decreased significantly for all concretes.
3) Pull-out strength was found to be strongly dependent on the hook geometry in which the mechanical anchorage contribution provided by the hook increased with matrix strength. The bond strength of 5DH fibre was considerably higher than that of 4DH fibre, except the case of NSC. However, the bond strength of both fibres diminished gradually with increasing temperature and both fibres embedded in MSC and HSC exhibited comparable maximum pull-out load values in the 600-800°C temperature range.

4) The reduction in pull-out strength of both fibres correlated very well with the corresponding decrease in compressive strength of the matrix.

6.3.4 Bond-slip behaviour of straight and 3DH hooked-end fibres at elevated temperatures

6.3.4.1 Straight fibres

Figure 6.17 shows the bond stress-slip curve (measured as the average of five specimens) for a straight steel fibre embedded in all four concrete matrices at ambient and elevated temperatures. It can be seen that a typical bond-stress curve of a straight fibre is characterized by a rapid increase of bond stress until the maximum value is reached and this is generally followed by a sudden drop as the fibre debonds. At some point, generally around 1-2 mm slip, the bond value stabilises at a residual value. Initially, the bond strength is generated by a combination of adhesion and friction. Once the peak bond has been reached, the adhesion is overcome causing a sudden drop in the bond strength. After this, in the residual bond portion of the response, only frictional forces remain until the fibre completely pulls out of the matrix.

The detailed results from the tests are summarised in Table 6.5, which includes P_{max}, $\sigma_{f,max}$, τ_{av}, τ_{eq} and W_{total} for each concrete type at the various temperature increments. The expression given in Eq. (4.2) was used to determine the average bond strength (τ_{av}), and this is presented in Figure 6.18, which illustrates how this property is influenced by both temperature and concrete mixture. At room temperature, it is shown that there was an increase of around 10%, 63% and 79% in τ_{av} when the concrete strength was increased from 33 MPa to 52, 71 and 148 MPa, respectively (i.e. from NSC to MSC, HSC and UHPC, respectively). The corresponding increase in the equivalent bond strength values (τ_{eq}) determined using Eq. (4.3) was 9%, 64% and 73%, respectively. It is most likely that the main reason for the enhanced bond strength with increasing concrete strength is due to the improved matrix packing density around the fibre, which leads to higher frictional bond stresses being generated.

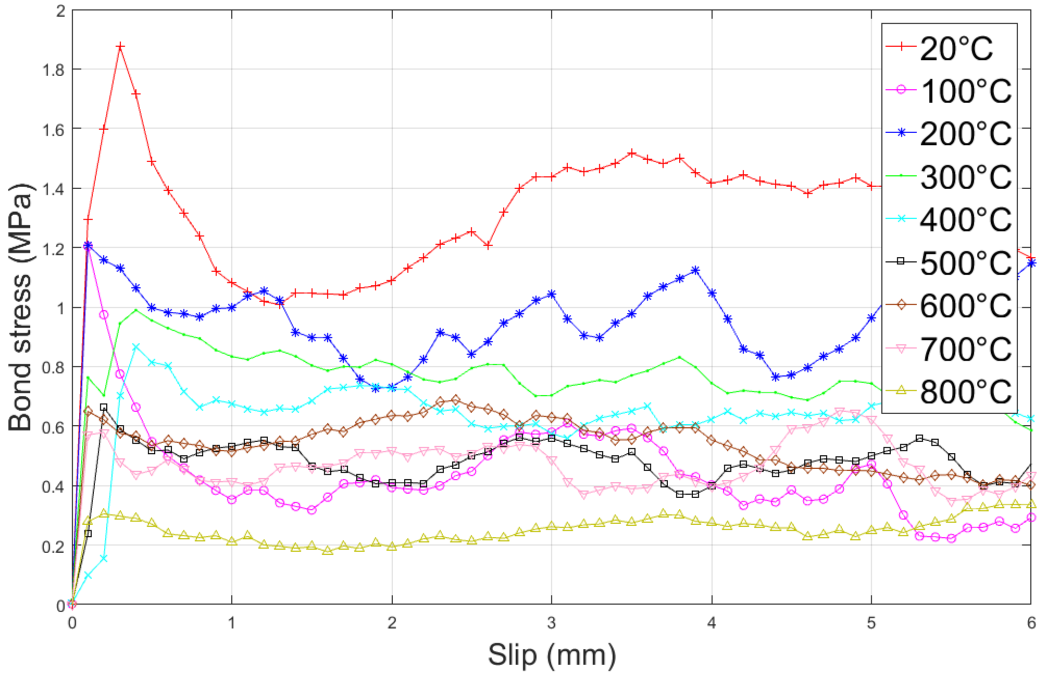
Bond stress (MPa)
Slip (mm)
0
0.2
0.4
0.6
0.8
1
1.2
1.4
1.6
1.8
2
0
1
2
3
4
5
6
20°C
100°C
200°C
300°C
400°C
500°C
600°C
700°C
800°C

(a)

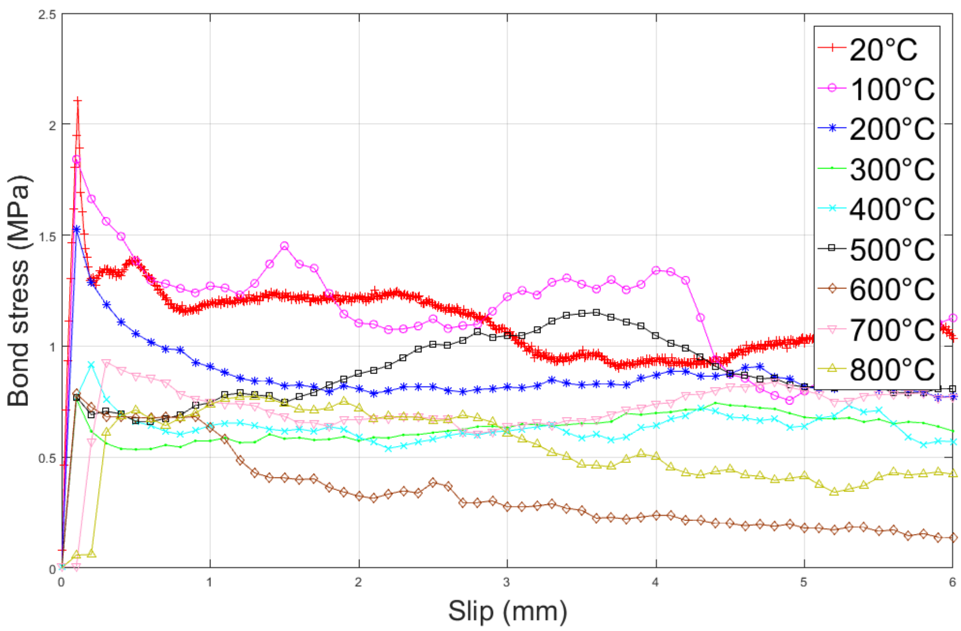
Bond stress (MPa)
Slip (mm)
0
0.5
1
1.5
2
2.5
0
1
2
3
4
5
6
20°C
100°C
200°C
300°C
400°C
500°C
600°C
700°C
800°C

(b)

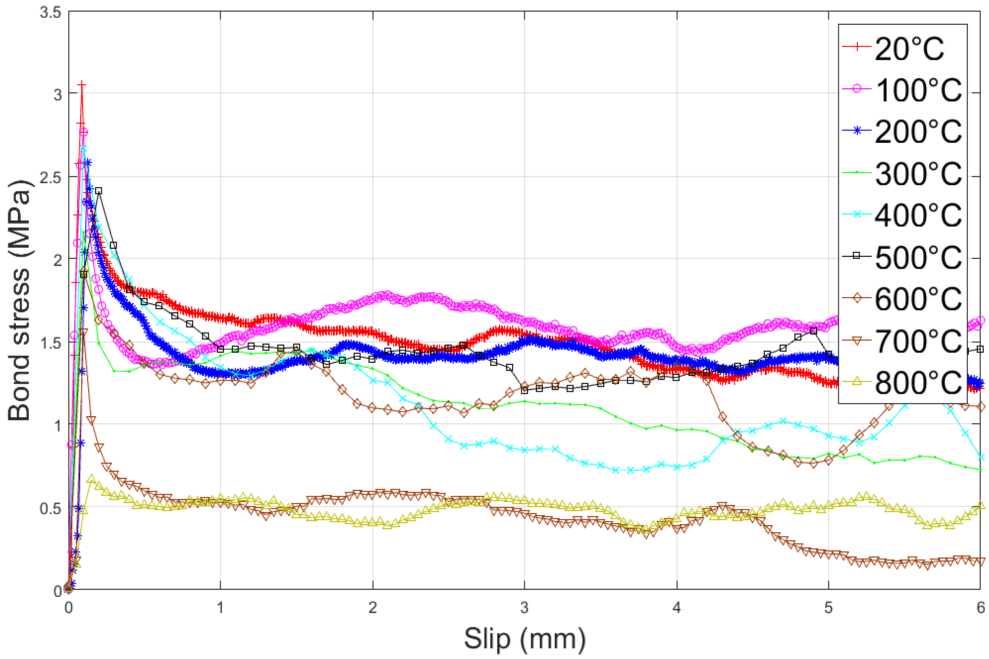

(c)

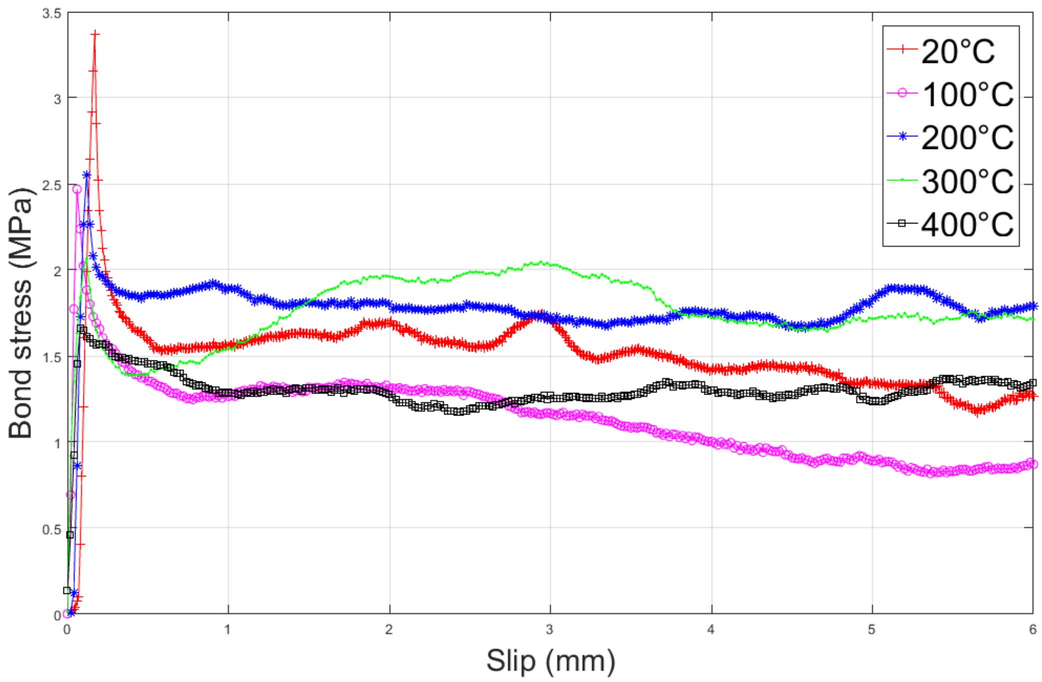

(d)

Figure 6.17 Bond stress-slip curves of straight fibres embedded in (a) NSC, (b) MSC, (c) HSC and (d) UHPC

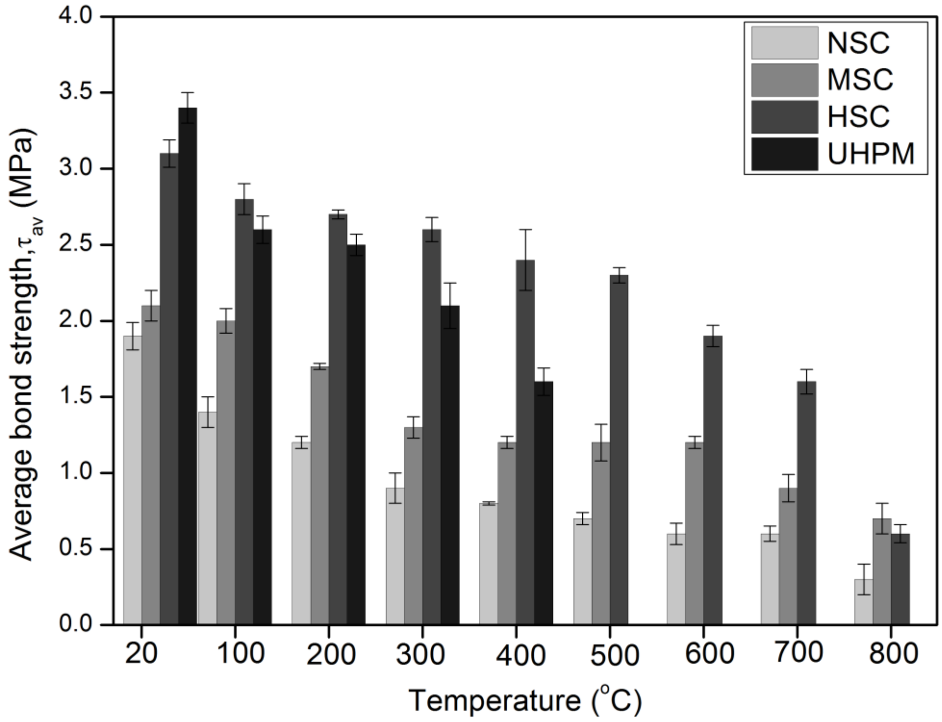

Figure 6.18 Effect of elevated temperatures on the average bond strength of straight fibres

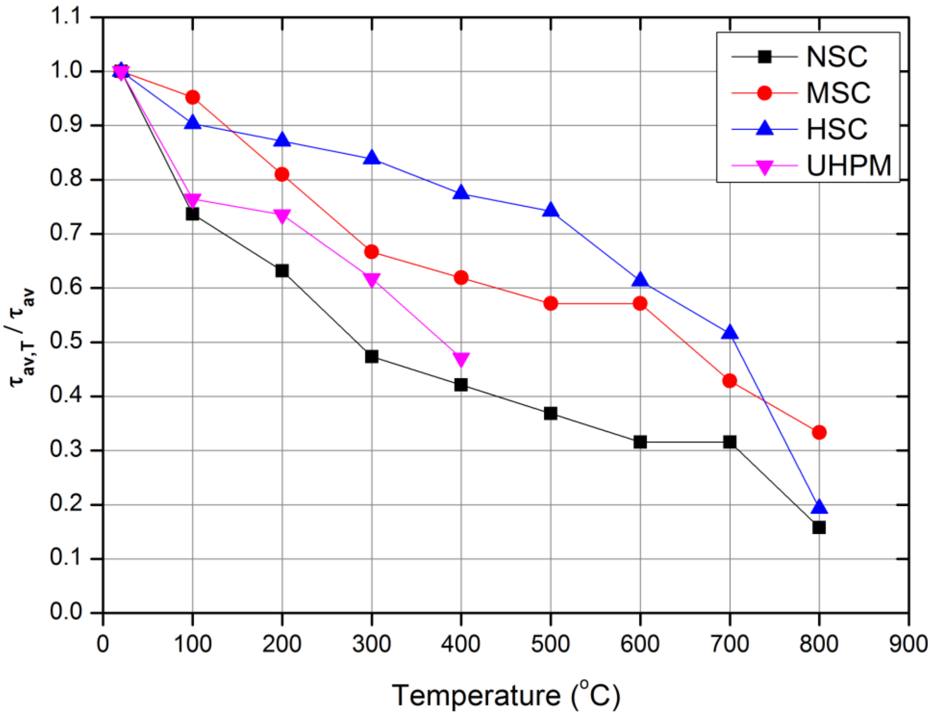

Figure 6.19 Variation in the normalised average bond strength ($\tau_{av,T}/\tau_{av}$) of straight fibres embedded in NSC, MSC, HSC and UHPC as function of temperature

After heating higher than 100°C, the loss of bond strength follows similar trend in all mixes. Figure 6.19 presents the variation in average bond strength at elevated temperature ($\tau_{av,T}$) normalised by the corresponding values at ambient temperature (τ_{av}) with increasing temperature. It is evident that all of the concrete matrices showed decreasing bond strength (τ_{av}) with increasing temperature. The τ_{av} of NSC decreased sharply up to 300°C and then gradually reduced in the temperature range of 400-600°C before stabilizing at temperatures between 600 and 700°C, and finally drops sharply again up to 800°C. The reduction in τ_{av} of MSC was also sharp up to 300°C and then remained almost constant between 500 and 600°C, before decreasing sharply again between 600°C and 800°C. The τ_{av} of the straight fibres embedded in HSC also decreased gradually up to 700°C and more sharply between 700°C and 800°C. It is notable that the level of loss in strength at the temperature range between 200 and 700°C was significantly lower for HSC than those for NSC and MSC. On the other hand, the loss of τ_{av} in the UHPC matrix is steeper than in MSC and HSC, and almost linear until the occurrence of explosive spalling above 400°C. This sharp reduction in bond strength for the UHPC matrix is attributed to the significant degradation in the physicochemical bond properties due to the low permeability and dense microstructure of this mixture. At 800°C, the τ_{av} (Figure 6.19) of NSC, MSC and HSC decreased by 84%, 68% and 81% of their original strength respectively. This sharp reduction in bond strength at 800°C is attributed to the significant degradation of material properties as well as the differential thermal expansion between the two materials. It was reported [138,148] that at 800°C the thermal expansion of concrete increased by 1.3% from zero at ambient temperature while that coefficient for steel increases by 20% [149]. These effects combine to result in greater damage and the development of more cracks around the fibre, and hence the reduction of pull-out resistance.

Figure 6.20 shows the variation in equivalent bond strength at elevated temperature ($\tau_{eq,T}$) normalised by the corresponding values at ambient temperature (τ_{eq}) with increasing temperature. For all concretes, there was a reduction in equivalent bond strength (τ_{eq}) at 100°C initially and then τ_{eq} regain at 200°C, while the τ_{eq} of UHPC appeared to significantly decrease with temperature. Above 300°C the τ_{eq} loss becomes gradual with increase in temperature for NSC and HSC. The τ_{eq} of NSC, MSC and HSC were significantly diminished, relative to the room temperature values, when pull-out specimens were heated to within the 600-800°C temperature range. At 800°C, the τ_{eq} of NSC, MSC and HSC reduced by 64%, 67% and 83%, respectively, compared with their corresponding values at ambient temperature.

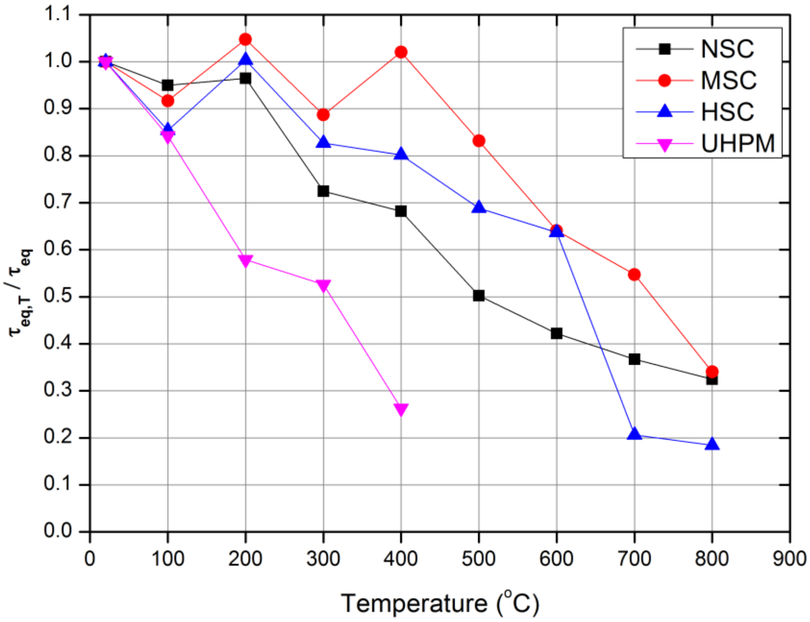

Figure 6.20 Variation in the normalised equivalent bond strength ($\tau_{eq,T}/\tau_{eq}$) of straight fibres embedded in NSC, MSC, HSC and UHPC as a function of temperature

Table 6.5 Bond parameters of straight fibre derived from test results

Material	Property	20°C	100°C	200°C	300°C	400°C	500°C	600°C	700°C	800°C
NSC	P_{max} (N)	165	122	102	84	74	57	56	52	27
	$\sigma_{f,max}$ (MPa)	260	192	160	132	116	90	88	82	42
	τ_{av}(MPa)	1.9	1.4	1.2	0.9	0.8	0.7	0.6	0.6	0.3
	τ_{eq} (MPa)	1.1	1.0	1.0	0.9	0.8	0.6	0.5	0.4	0.4
	W_{total} (N mm)	1435	1363	1384	1040	979	721	605	527	466
MSC	P_{max} (N)	177	171	144	113	107	105	104	77	64
	$\sigma_{f,max}$ (MPa)	278	269	226	178	168	165	164	121	101
	τ_{av}(MPa)	2.1	2.0	1.7	1.4	1.3	1.2	1.2	0.9	0.7
	τ_{eq} (MPa)	1.2	1.1	1.3	1.0	1.3	1.0	0.8	0.6	0.4
	W_{total} (N mm)	1566	1436	1641	1389	1598	1302	1003	857	533
HSC	P_{max} (N)	266	238	236	227	210	200	168	138	57
	$\sigma_{f,max}$ (MPa)	418	374	371	357	330	315	264	217	90
	τ_{av}(MPa)	3.1	2.8	2.7	2.6	2.4	2.3	1.9	1.6	0.6
	τ_{eq} (MPa)	1.8	1.5	1.8	1.4	1.3	1.2	1.1	0.4	0.3
	W_{total} (N mm)	2263	1932	2271	1871	1815	1558	1442	417	466
UHPC	P_{max} (N)	299	222	218	174	141	-	-	-	-
	$\sigma_{f,max}$ (MPa)	456	349	342	274	222	-	-	-	-
	τ_{av}(MPa)	3.4	2.6	2.5	2.1	1.6	-	-	-	-
	τ_{eq} (MPa)	1.9	1.6	1.1	1	0.5	-	-	-	-
	W_{total} (N mm)	2468	1993	1493	1338	702	-	-	-	-

6.3.4.2 3D Hooked-end fibres

Figure 6.21 shows the bond stress-slip curves (measured as the average of five specimens) for hooked-end fibres embedded in NSC, MSC, HSC and UHPC matrices following exposure to different levels of elevated temperature between 20 and 800°C. It is observed that the bond stress-slip behaviour of hooked-end fibres is significantly different from that of the straight fibres. This may be due to the different bond mechanisms present. For straight fibres, the bond is generated entirely from chemical adhesion and friction. These are also present in hooked-end fibres but are supplemented by the additional phenomenon of mechanical interlocking between the concrete and fibre, due to plastic deformation in the fibre hooks. Comparison of the graphs in Figure 6.21 with the equivalent responses in Figure 6.17 shows that the contribution made by this mechanical interlocking mechanism significantly improves the bond-slip characteristic of the hooked-end fibres embedded in all four matrices. Not only are the maximum bond values much higher for the hooked-end fibres but also the general shape of the bond stress-slip curve is also different. In contrast to the straight fibre behaviour, the descending branch of the hooked-end fibres demonstrated a second localised peak at a slip of around 2-5 mm, this is due to the activation of the mechanical interlocking bond once the adhesion has been overcome.

The shape of the bond stress-slip curve for the hooked-end fibres embedded in concrete is similar for the NSC, MSC and HSC mixes, even at high temperatures. However, there are some differences in terms of the maximum bond stress and pull-out work values. A significant difference is also observed between Figures 6.21(a-c) and Figure 6.21(d), which plot the average bond stress for each concrete mix. In the latter, the bond stress for UHPC shows a gradual decline immediately following the attainment of τ_{max}, whereas the other concrete mixes exhibit almost plateau after τ_{max} until the second peak which is followed by a gradual decrease in the bond stress. This difference is attributed to the variation in the level of deformation and straightening of the hook which is higher for UHPC than the other matrices. It is also important to consider that it was observed during the experiments that the end hook of the fibre at 300°C ruptured internally in the hook region at a slip of around 2.7 mm. This represents $\sigma_{f,max}/\sigma_y$ of around 0.93 (where σ_y is the yield strength of the steel fibre at ambient temperature), which reflects a full activation of the mechanical bond. Nevertheless, as illustrated in Figure 6.21d, the fibre continued to transfer the stress until the fibre completely pulled out; the hook at the other end of the fibre remained intact.

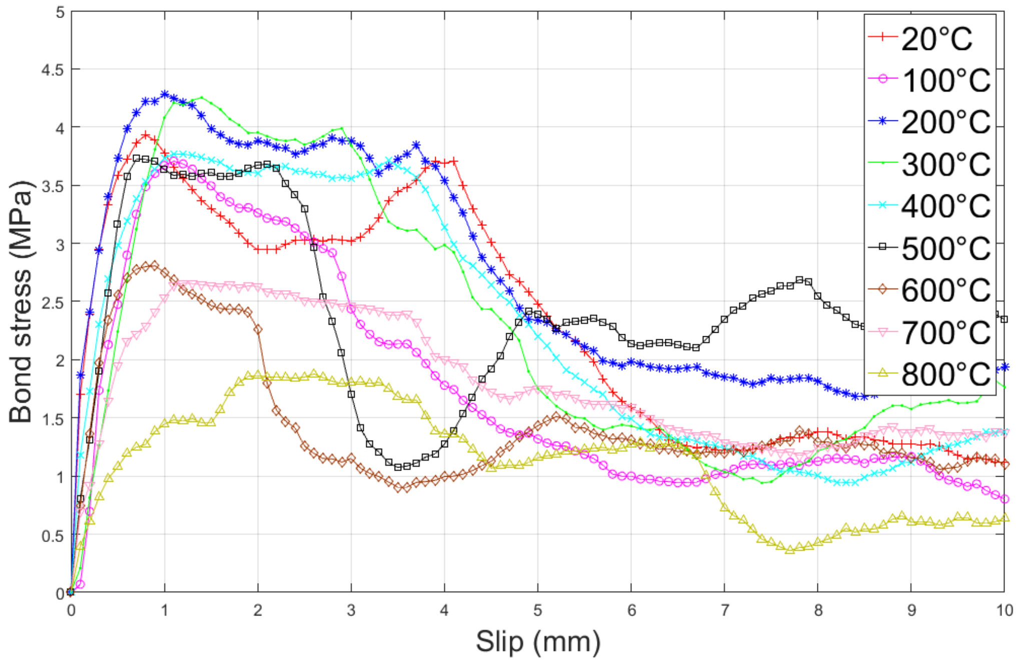

(a)

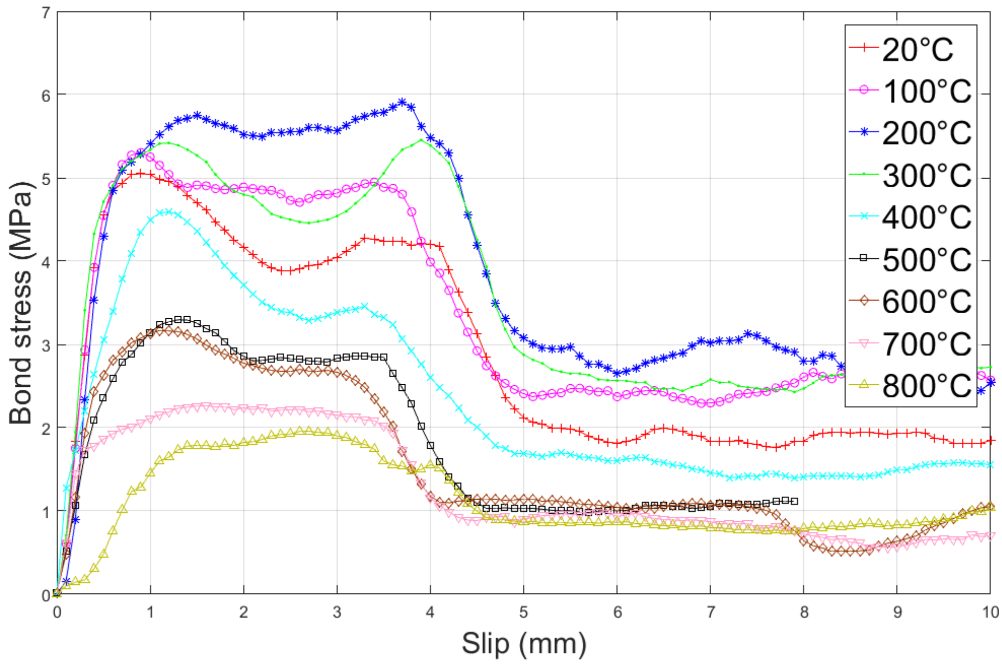

(b)

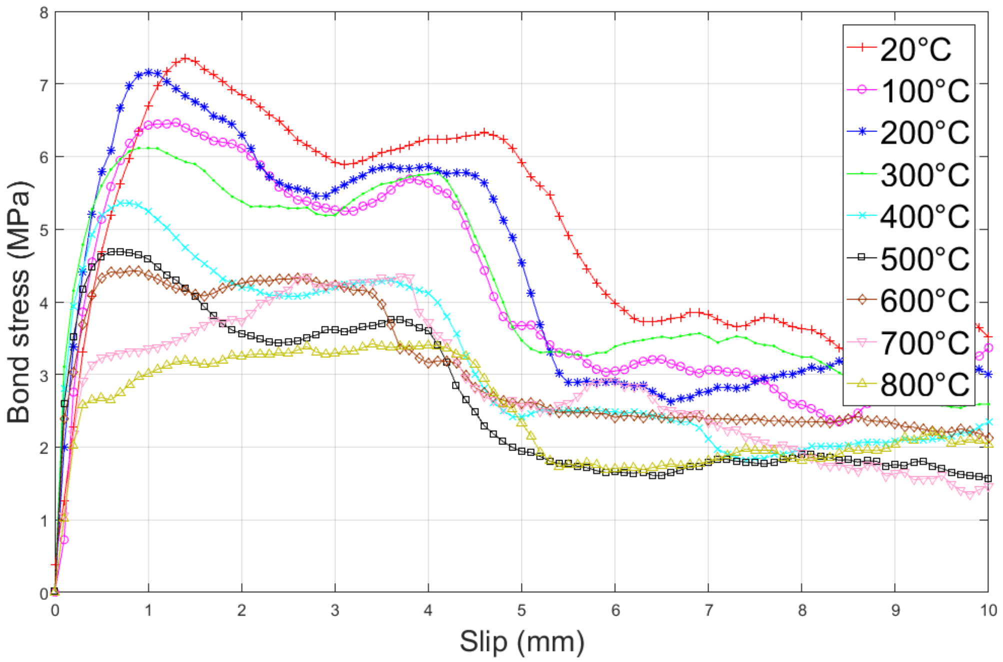

(c)

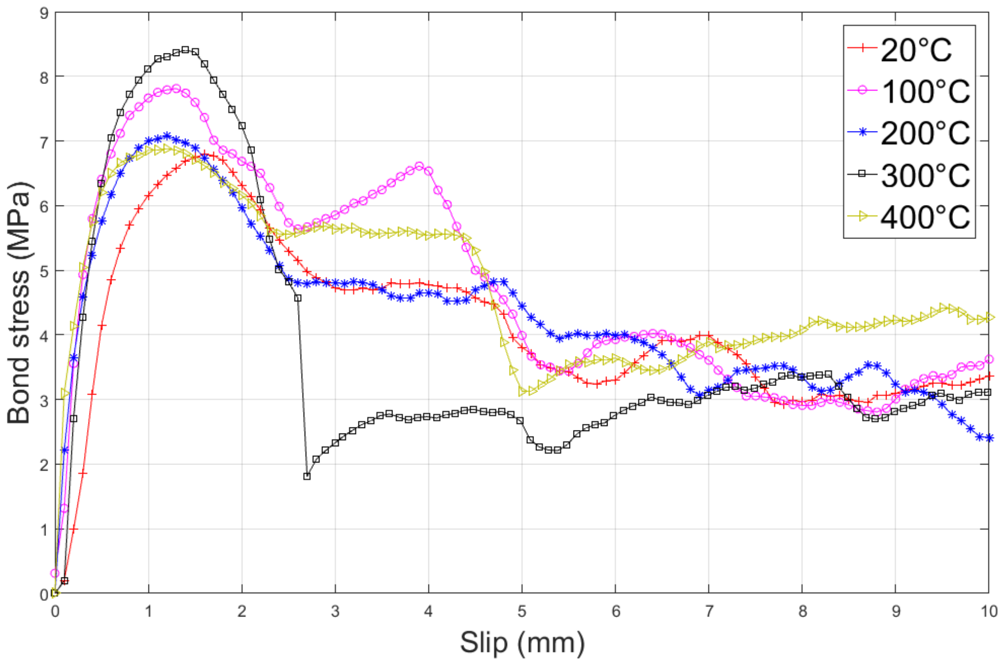

(d)

Figure 6.21 Bond stress-slip curves of hooked-end fibre embedded in (a) NSC, (b) MSC, (c) HSC and (d) UHPC matrices

The average bond strength (τ_{av}) of hooked-end fibres after exposure to various levels of elevated temperature is presented in Figure 6.22, whilst the corresponding equivalent bond strength (τ_{eq}) results are given in Table 6.6. It is evident that τ_{av} and τ_{eq} for the hooked-end fibres increase significantly with increasing concrete compressive strength. Figures 6.23 and 6.24 illustrate the average and equivalent bond stress normalised by the corresponding ambient value for all mixes with increasing temperature. It can be seen that for the four matrices, both τ_{av} and τ_{eq} follows a decreasing trend with increasing temperature. However, the decrease does not begin until around 300°C, corresponding with similar findings for the effect of temperature on the compressive strength of concrete presented in Figure 6.2. Interestingly, the behaviour of the HSC concrete differs from the other concretes in that it starts to lose bond strength significantly earlier, from around 100°C. This gradual degradation of bond strength may be attributed to the lower permeability and dense microstructure of HSC, which results in a significant strength loss as compared to NSC and MSC. The τ_{av} and τ_{eq} values for the hooked-end fibres embedded in all four matrices follow similar trend in the higher temperature range (i.e. 400°C-800°C). At 800°C, the τ_{av} of the NSC, MSC and HSC mixes decreased by around 55%, 63% and 55%, respectively, relative to the corresponding ambient values whilst the equivalent values for τ_{eq} were 55%, 52% and 53%, respectively. Interestingly, as shown in Figures 6.23 and 6.24, at 800°C the loss in bond strength for all concrete mixes is almost identical. Therefore, it is deduced that the compressive strength of concrete does not have a significant influence on bond strength loss at elevated temperatures.

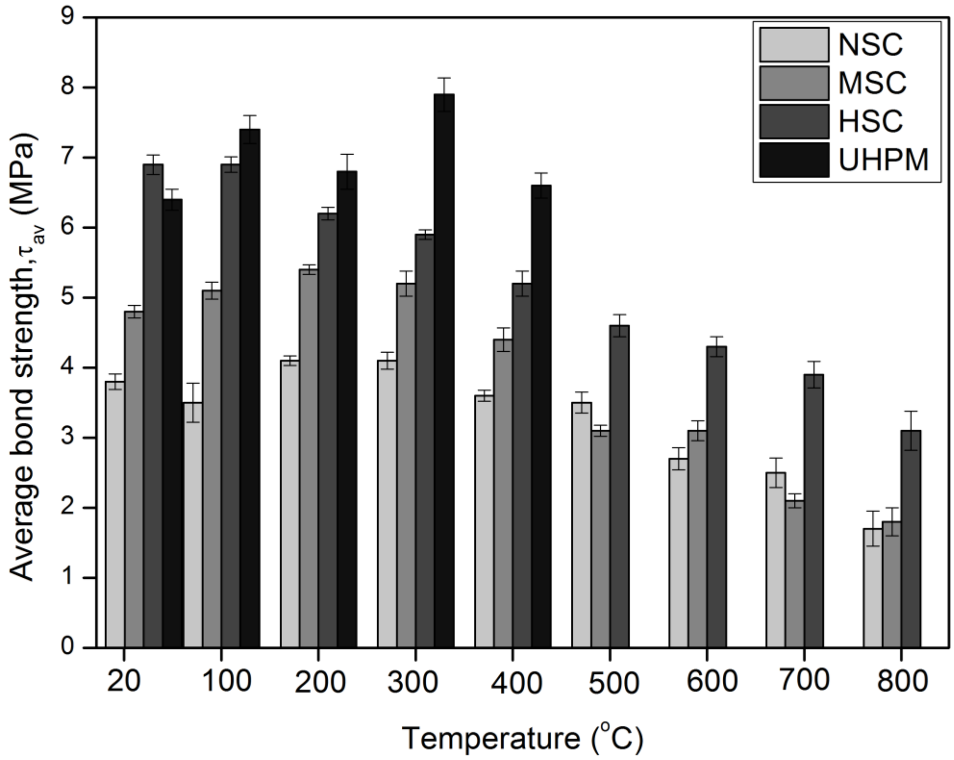

Figure 6.22 Effect of elevated temperature on the average bond strength of hooked-end fibres

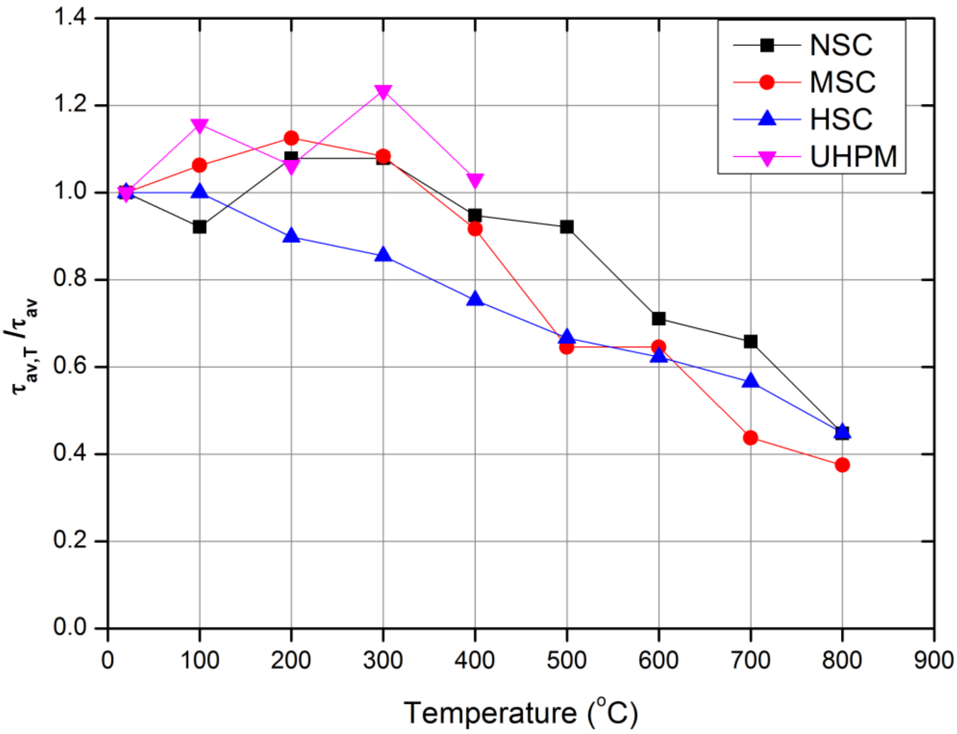

Figure 6.23 Variation in the normalised average bond strength ($\tau_{av,T}/\tau_{av}$) of hooked-end steel fibres embedded in NSC, MSC, HSC and UHPC as a function of temperature

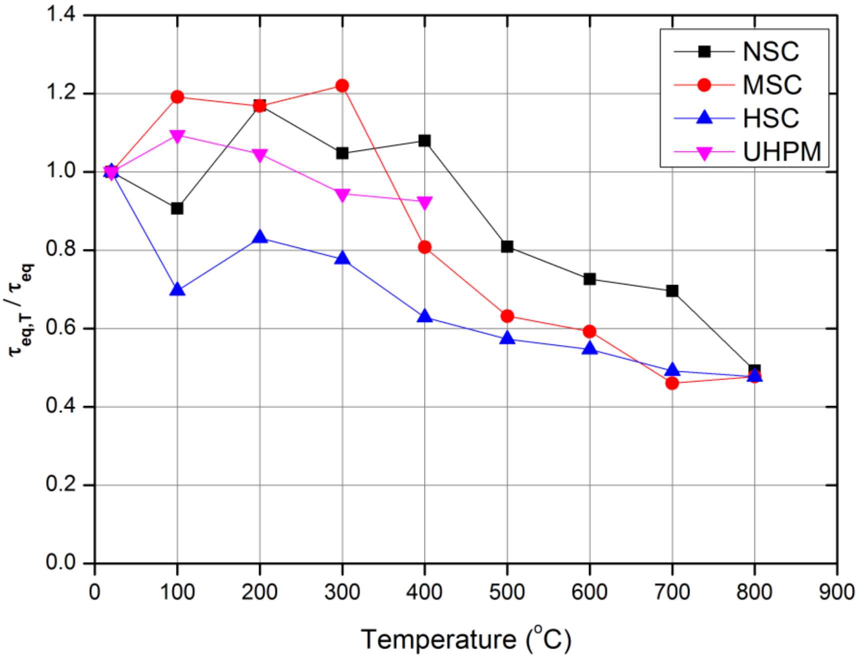

Figure 6.24 Variation in the normalised equivalent bond strength ($\tau_{eq,T}/\tau_{eq}$) of hooked-end steel fibres embedded in NSC, MSC, HSC and UHPC as a function of temperature

Table 6.6 Bond parameters of hooked-end fibre derived from test results

Material	Property	20°C	100°C	200°C	300°C	400°C	500°C	600°C	700°C	800°C
NSC	P_{max} (N)	325	304	352	345	309	310	234	217	148
	$\sigma_{f,max}$ (MPa)	511	478	554	543	486	487	368	341	233
	τ_{av}(MPa)	3.8	3.5	4.1	4.1	3.6	3.5	2.7	2.5	1.7
	τ_{eq} (MPa)	2.0	1.8	2.3	2.1	2.2	1.6	1.4	1.3	0.9
	W_{total} (N mm)	2515	2280	2941	2635	2715	2035	1826	1751	1240
MSC	P_{max} (N)	414	438	463	446	376	269	259	182	151
	$\sigma_{f,max}$ (MPa)	651	689	728	701	591	423	407	286	237
	τ_{av}(MPa)	4.8	5.1	5.4	5.2	4.4	3.1	3.1	2.1	1.8
	τ_{eq} (MPa)	2.7	3.3	3.2	3.7	2.2	1.7	1.6	1.2	1.3
	W_{total} (N mm)	3542	4219	4137	4822	2861	2238	2098	1631	1690
HSC	P_{max} (N)	591	589	527	501	442	391	369	335	261
	$\sigma_{f,max}$ (MPa)	930	926	829	788	695	615	580	527	410
	τ_{av}(MPa)	6.9	6.9	6.2	5.9	5.2	4.6	4.3	3.9	3.1
	τ_{eq} (MPa)	5.3	3.7	4.4	4.1	3.3	3.1	2.9	2.6	2.5
	W_{total} (N mm)	6832	4759	5677	5309	4295	3916	3736	3359	3258
UHPC	P_{max} (N)	545	633	577	678	562	-	-	-	-
	$\sigma_{f,max}$ (MPa)	857	996	908	1066	884	-	-	-	-
	τ_{av}(MPa)	6.4	7.4	6.8	7.9	6.6	-	-	-	-
	τ_{eq} (MPa)	4.1	4.5	4.3	3.8	5.2	-	-	-	-
	W_{total} (N mm)	5248	5740	5489	4954	6656	-	-	-	-

6.3.4.3 Evaluation of fibre damage

Following the tests, the damage to the fibres after exposure to elevated temperature and being subjected to pulling out from the concrete was evaluated using a high power optical microscope. It is noteworthy that this assessment was conducted for fibres embedded in all four concrete types, but only the NSC images are presented herein for brevity as the results were very similar irrespective of the matrix mix (Figure 6.25).

The morphology of the fibre deformation was analysed and it was shown that the specimens exposed to 400°C and above exhibited significant deterioration to the fibre surface, as compared with the fibres exposed to lower temperatures. The fibres pulled out from specimens heated to 400-800°C had clearly changed colour and also developed a corroded surface. These changes are mainly due to the oxidation process which results in surface damage and this is more pronounced at higher temperatures. This phenomenon has also been observed by other authors [150-153]. The deterioration of bond at high temperatures may be caused by both a degradation of the material properties, differential thermal expansion and also their physical changes.

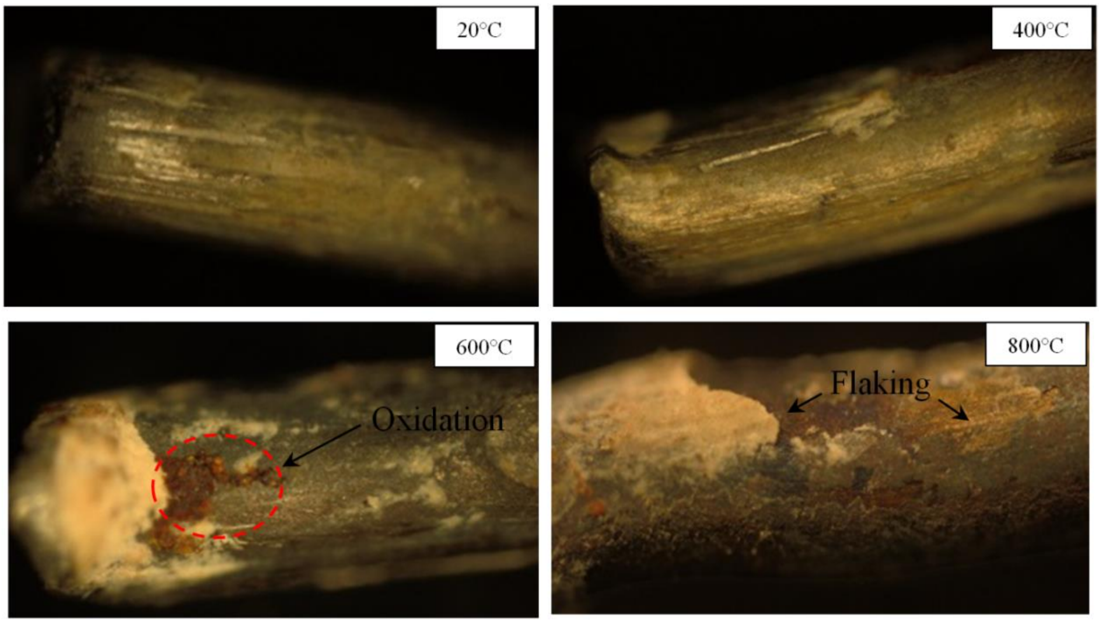

Figure 6.25 Images of the damaged fibres which were embedded in normal strength concrete (NSC) following heating, cooling and pull-out testing

6.3.4.4 Concluding remarks

The bond behaviour between steel fibre and concrete matrix subjected to elevated temperature have been characterised with two types of steel fibres and four different concrete mixes. The following conclusions can be drawn:

1) Temperature had a significant influence on the mechanical and thermal properties of both steel fibres and concrete. At the temperature higher than 400°C, the mechanical properties of both materials decreased with increasing temperature. On the other hand, both the mass loss in the concrete and the ductility of the steel fibres increased.
2) The bond strength degraded significantly with increasing temperature in all matrices for the straight fibres. At 800°C, the average bond strength of NSC, MSC and HSC decreased by 84%, 68% and 81%, respectively. Similarly, the equivalent bond strength τ_{eq} decreased by 64%, 67% and 83%, respectively.
3) The bond-slip characteristic between the hooked fibre and matrix reflected two different temperature ranges, namely 20-400°C and 400-800°C. The bond behaviour in the former range did not vary significantly for all mixes, while in the latter range, the NSC, MSC and HSC lost most of their original bond strength, especially once they were exposed to temperatures greater than 600°C.
4) The reduction in bond strength of both straight and hooked-end fibres was found to be strongly associated with the degradation in material properties (i.e. the fibre and concrete properties). However, the reduction in material properties appeared to have a more significant effect on the bond-slip mechanisms of straight fibres compared with hooked-end fibres.

Chapter 7 Flexural Behaviour of Steel Fibre Reinforced Self-compacting Concrete (SFR-SCC)

7.1 Introduction

It is well known that an addition of fibres to concrete is able to improve their tensile strength, fracture energy absorption and load bearing capacity [3,22,154,155]. The fibre contribution is mainly reflected when the concrete cracking initiates and often enhances the post-cracking behaviour due to the improved stress transfer provided by the fibre bridging of the cracked sections [156-158]. The most important parameter of fibres is their ability to transfer stresses across cracked sections rather uniformly [63,159].

The mechanical properties and post-cracking behaviour of steel fibre reinforced concrete (SFRC) greatly depend on the matrix properties in addition to the concentration, type, geometry, orientation and distribution of fibres, while the efficiency of fibre reinforcement depends on the deformed shape of the fibres, which enhances the anchorage mechanisms during the pulling-out.

While various fibres can be used for concrete reinforcement, approximately 67% of commercial fibres are the hooked-end fibres, around 9% for both straight and deformed wire, 9% for crimped fibres and 15% for other steel fibre types [159]. The variety of reinforcing fibres may have a significant effect on the efficiency of the reinforcement, hence, research on the design and architecture of fibres has been an interesting area for the researchers and engineers in the sector. For example, Bekaert has recently redesigned and expanded its Dramix® range of hooked-end steel fibres, and introduced the new generation of 4DH and 5DH series of Dramix®, the unique shape and performance of which could open up a new level of possibilities for design and construction.

The distribution and orientation of fibres in hardened concrete are very much dependant on its fresh-state characteristics after mixing, namely, flowability, casting method, vibration and wall-effects introduced by the formwork [160].

Tremendous scatterings in the bending test results of SFRC have been reported in the literature [161]. The main reason for this phenomenon is the high variation in fibre distribution and orientation [162,163]. It has been observed that an alignment of fibres in the direction of flow resulted in better post-cracking properties compared to those in the perpendicular direction [160].

To overcome the aforementioned deficiencies, the combination of steel fibres and self-compacting concrete (SCC) has quickly become one of the common concrete technologies in the construction industries [162]. Several studies have demonstrated that the main benefits of adding steel fibres in self-compacting concrete are to achieve uniform distribution of fibres in the matrix as well as rheological stability without compaction and vibration[164,165]. This indicates that fibre dispersion and orientation could be crucial for the key properties of steel fibre reinforced self-compacting concrete (SFR-SCC), and the link between its fresh- and hardened-state performances [162]. Numerous methods have been adopted in literature to evaluate performance of steel fibre reinforced concrete (SFRC), with the uniaxial tensile and flexural tests being the most commonly ones [163,166-170].

Many national and international technical committees have also proposed recommendations and guidelines to analyse the post-crack behaviour of SFRC based on the load–deflection diagrams and the load–CMOD diagrams, for example, RILEM TC162-TDF recommendation [115] and those very similar to it such as EN 14651[171], ASTM C1018[172], CNR-DT 204[173] and JSCE method [174]. Nevertheless, there is little information of repeatable database for understanding the correlation of variety of fibre types with concrete behaviour, particularly for these new types of fibres.

The main objectives of this study are to examine and compare post-cracking tensile behaviour of self-compacting concrete reinforced with four different types of hooked-end steel fibres, and to investigate the influence of new shape hooked-end steel fibres (4DH and 5DH) on post-peak behaviour of the reinforced concrete. The orientation and distribution of steel fibres on the fracture section have in particular been considered for analysing the influence of flowablitity properties on the performance of hardened SFRC. The quantitative analyses are performed to compare the behaviour of old generation steel fibres (3DH) and new ones (4DH and 5DH) to assess the development and the positive effect of the newly developed shapes of steel fibres.

7.2 Materials and methods

7.2.1 Materials and mix design

The following constituent materials were used for the formulation of the SFR-SCC: Portland-limestone cement CEM II 32,5R, fly ash EN-450, combination of two particle sizes of crushed granite aggregates which consisted of 60% of (6 mm) and 40% of (10 mm), sand, superplasticizer TamCem (23SSR) and water. For all mixes, the proportion of the ingredients maintained the same and only the fibre content varied as presented in Table 7.1.

Table 7.1 Mixture proportion per 1 m^3 of concrete made

Cement CEM II/A-L 32,5R (Kg/m^3)	Fly ash (Kg/m^3)	Sand (0-2mm) (Kg/m^3)	Coarse aggregate (6-10)mm (Kg/m^3)	Steel fibres (Kg/m^3) (%)	Superplasticizer (l/m^3)	Water (l/m^3)	W/C
C	FA	S	CA	SF	SP	W	-
470	45	850	886	40;80(0.5;1)	6	216	0.42

Four types of Dramix hooked-end steel fibres were selected, each of them added at two levels of dosage of 40 and 80kg/m^3, corresponding approximately to a volume fraction of 0.5% and 1% respectively. All these types of fibres have the same length 60 mm and aspect ratios (l/d=65), except (3DH-35), which is 35 mm. The properties of the steel fibres are presented in Table 7.2. During concrete casting, the raw materials (cement, fly ash, crushed granite and sand) were firstly dry mixed for 1 minute for homogeneity and then 80% of water and superplasticizer were added to the dry mixture which was then mixed for 4 minutes. Finally, since the hooked-end fibres are glued into strips, the remaining water and fibres were added simultaneously to dissolve the glue and distribute the fibres in the mixer and the whole mixture was further mixed for 3 minutes.

Table 7.2 Properties of steel fibres

Fibre type	Diameter (mm)	Length (mm)	Aspect ratio -	No. fibre per Kg	Tensile strength (MPa)	Young's Modulus (MPa)
3D 65/35 BG	0.55	35	65	14531	1345	± 210000
3D 65/60 BG	0.90	60	65	3183	1160	± 210000
4D 65/60 BG	0.90	60	65	3183	1500	± 210000
5D 65/60 BG	0.90	60	65	3183	2300	± 210000

7.2.2 Sample preparation

Twenty seven beams all with the dimensions of 150 x 150 x 600 mm^3 were cast for SCC and SFR-SCC mixtures. All beams were cast by using the flowed mix from one end of the mould to the other end until the mould was full. All the test specimens were removed from the moulds after 24 hours and cured for further 27 days in a chamber (20 ± 2°C, 96 ± 5% RH). All series were coded: the first number and letter denotes the fibre type (3DH, 4DH and 5DH), the second number the fibre length in mm and the last group number the fibre content in Kg.

7.2.3 Experiments

Three-point bending tests on notched beams having dimensions 150×150× 600 mm^3 were performed in accordance with RILEM TC 162-TDF[175]. In the mid-span of each beam, a single notch with depth of 25 mm and width of 3mm was cut to localize the crack. The beams were placed on roller supports, so to have a test span of 500 mm (see Figure 3.14). It should be noted that each beam is turned 90° from the casting surface, and the notch is then sawn through the width of the beam at mid-span. The tests were carried out by imposing a constant displacement rate of 0.5 mm/min under the INSTRON 5584 electromechanical testing machine. The test was controlled by means of crack mouth opening displacement (CMOD), using a clip-on extensometer with a ±2.5 mm range and 10 mm gauge length. The mid-span deflection was also measured using a yoke mounted on the tested beams (see Figure 3.14).

7.3 Results and discussion

73.1 Effect of steel fibres on rheology of paste and compressive strength of hardened SFR-SCC

To evaluate the rheological and self-compactable properties of fresh SFRC, the slump-flow test was performed according to EN 12350-8:2010 [122] . It appears that all mixtures had stable and excellent self-compacting properties (Table 7.3), although adding steel fibres slightly affect the workability of SFRC-SCC. The slump-flow diameter (SFD) and time to reach 500 mm spread (T50) of the fresh concrete are also very similar between the mixtures. The inclusion of steel fibres has not affected the density of SFRCs, although it slightly increases their compressive strength. In addition, since 3DH-60, 4DH and 5DH have the same length and aspect ratio, the different shape of the hooked-end is not a sufficient factor to induce a significant variation in slump flow diameter as it does on compressive strength as expected.

Table 7.3 Properties of fresh and hardened SFR-SCC mix

Mix	Slump flow test		Density(Kg/m^3)	$f^*_{cm,28d}$*(MPa)*	*CV (%)*
	$T_{500\,(S)}$	SFD(mm)			
CM	2	710	2398	49.86	5.32
3D-35-40	1	700	2295	47.45	4.40
3D-35-80	1	700	2349	46.79	4.44
3D-60-40	2	700	2348	48.52	5.18
3D-60-80	2	695	2372	48.24	5.50
4D-60-40	2	700	2366	49.75	7.06
4D-60-80	1	695	2321	48.67	6.28
5D-60-40	1	700	2375	49.85	3.07
5D-60-80	1	700	2385	50.5	4.88

7.3.2 Effect of various hook ends of steel fibre on the peak and residual loads of SFR-SCC

A comparison of typical load-CMOD curves of plain SCC beams and SFC-SCC beams reinforced by different hooked-end steel fibres at various dosages are presented in Figures 7.1 and 7.2. It can be seen that all plain concrete beams exhibit almost linear-elastic behaviour up to the peak load, followed by a sudden drop in load, upon which the beams separated into two parts. On the other hand, the beams reinforced with steel fibres demonstrated not only significantly higher peak load, but also a tri-linear load-CMOD behaviour with a multiple cracking process before localizing into a single major crack. Continuing crack propagation existed after peak load due to the crack control effect of fibres on the cracked surface. Once the micro-cracking propagates and joins together into larger macro-cracks, the series reinforced with long hooked-end fibres (i.e. 60 mm) became more effective in crack bridging than those series with short hooked-end fibres (i.e. 35 mm) (see Figures 7.1 and 7.2). This mainly due to the high anchorage strength provided by the hook especially of 4DH and 5DH fibres which results in a high resistance to cracks propagation. For the concrete reinforced by 60 mm fibres at the dosage of 40 kg/m^3, the peak loads are about 15, 13 and 18 kN for those with the 3DH-60, 4DH and 5DH fibres, and for the concrete reinforced by 60 mm fibres at the dosage of 80 kg, these values increased to 18, 26 and 40 kN, compared to 8 kN for the plain concrete one. For the beams reinforced by 3DH fibres, the peak loads are 12 and 15 kN in case of 35 mm and 60 mm long fibres, respectively, at the dosage of 40 kg fibres and these values increased to 16 and 18 kN, respectively at the dosage of 80 kg.

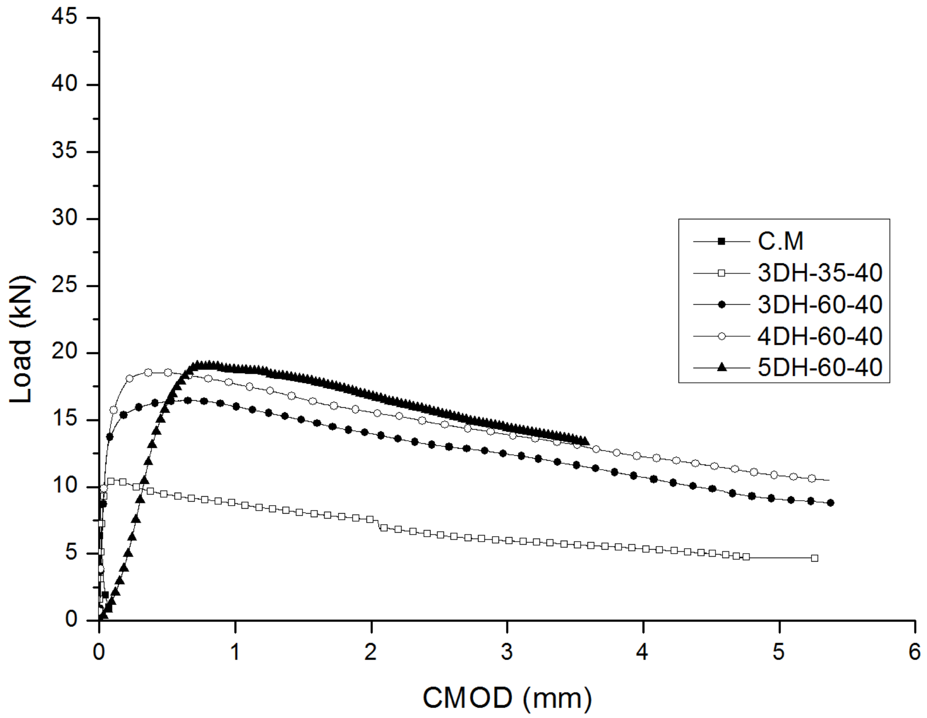

Figure 7.1 Comparison of load-CMOD curve of SFR-SCC series reinforced with 40 kg fibres

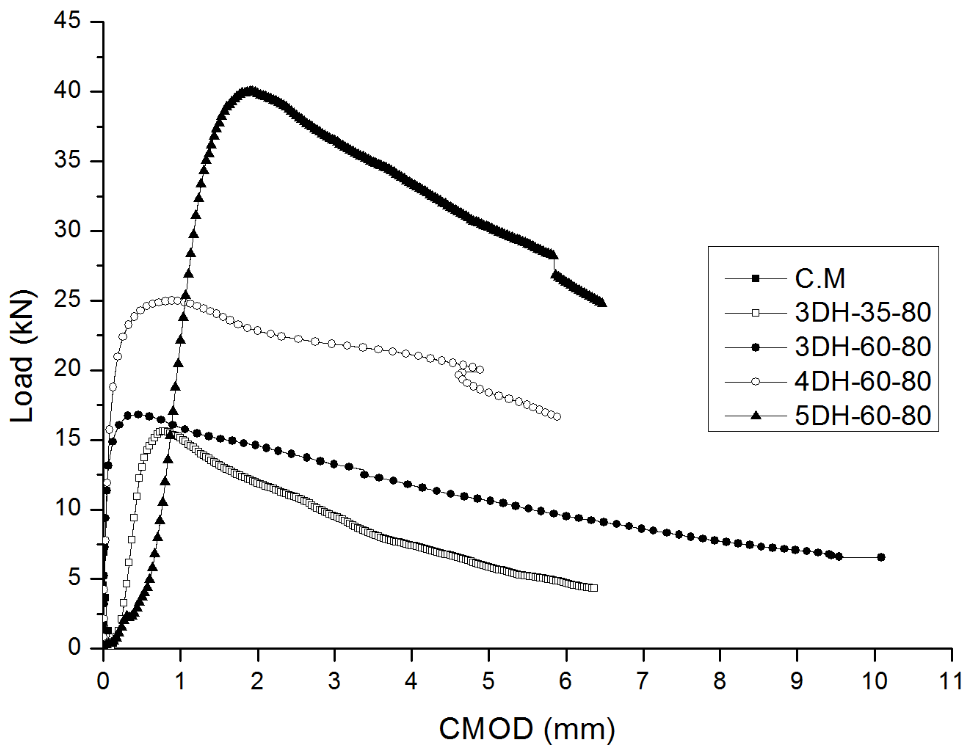

Figure 7.2 Comparison of load-CMOD curve of SFR-SCC series reinforced with 80 kg fibres

After peak load was reached, the load carrying capacity deterioration started, the lower the fibres content, the higher the loss of strength. The load bearing capacity descends immediately after the first visible crack initiated, which may be attributed to the bond slip of some fibres at the cracked surface. This also reflected the higher loss of strength for the shorter fibre reinforced concrete as the short fibre may be relatively easier to be pulled out. Gradual reduction of loading capacity continues until all fibres slip from the cracking regions. As mentioned, the maximum load increases with an increase of fibre content for all four types of hooked-end steel fibres. However, the residual load of the tested beams with long fibres also shows a more ductile trend than that with short fibres over the entire CMOD range. This may be attributed to the positive effect of long steel fibres, as the short fibres are gradually pulled out with the increase of the CMOD, while the high mechanical anchoring provided by the lengthy hook of 4DH and 5DH fibres continues to transfer the stress between fibres and matrix, generating higher strain and stress (residual load) at the post-cracking stage.

A comparison among various hooked-end types of fibre, for the same fibre content, showed that the order of performance in terms of peak load is 5DH- > 4DH->3DH-60-> 3DH-30. The beams reinforced with series of 5DH-60-80 feature higher ultimate load than the other hooked-end ones (Figure 7.2). For the long hooked-end fibres reinforced concrete with the same fibre content, even though they have somewhat equal number of fibres on fracture surface, different peak loads existed among them, showing that the peak loads of SFR-SCC is strongly affected by the hook shape of fibres.

The residual load of the beams evaluated at 4 mm CMOD is about 91%, 87%, 79% and 53% of their peak load for the series reinforced with 80 kg/m^3 of 5DH, 4DH, 3DH-60 and 3DH-30 respectively. The high residual load obtained from the series reinforced with 5DH may be the result of a unique combination of a lengthy hook, a high ductility wire and high tensile strength. Regarding the series reinforced with 5DH fibres, there is also a noteworthy observation; the CMOD value corresponds to the maximum load is equal to 2 mm, while relatively small CMOD values (less than 0.7 mm) were registered for the other types of the hook ended fibres. In the case of the series reinforced with 3DH-35, the decrease of the residual load up to 53% of its peak load was observed, mainly due to the fibre pulled out and fully deformed at small crack widths. On the other hand, the series reinforced with 5DH fibres showed high resistance to fibre pull-out and resulted in somewhat lower regression of residual peak load at larger crack widths. Thus it could be attributed to the fact that the fibre mechanical anchorage is much higher for 5DH fibres than those offered by other hooked-end fibre types.

7.3.3 Effect of various hook ends of steel fibre on the post cracking tensile behaviour

To evaluate the post-cracking tensile behaviour of SFRC, 3-point bending test according to RILEM TC 162-TDF was performed [175]. The main benefits of using RILEM TC162-TDF recommendation is to obtain dimensional parameters representative of the post-peak behaviour to be used in SFRC structural design [176]. From this method, two possible groups of material parameters can be obtained to characterize the post cracking behaviour: the first group is the residual flexural tensile strengths and the second one is equivalent flexural tensile strengths. The first crack load or the load at the limit of proportionality, F_L, can be determined as the highest value of the load in the interval (δ or CMOD) of 0.05 mm. The strength corresponding to the limit of proportionality (LOP) can be obtained by using the following equation:

$$f_{\mathrm{fct,L}} = \frac{3.F_L.l}{2.b.h_{sp}^2}\ (MPa) \tag{7.1}$$

Where, l (500 mm), b (150 mm) and h_{sp} (125 mm) are the span of the specimen, width and distance between the tip of the notch and the top of the specimen, respectively.

To assess the post-peak behaviour of SFRC, the residual flexural tensile strengths, $f_{R,1}$, $f_{R,2}$, $f_{R,3}$ and $f_{R,4}$, corresponding to the values of $CMOD_1$ = 0.5 mm, $CMOD_2$ = 1.5 mm, $CMOD_3$ = 2.5 mm and $CMOD_4$ = 3.5 mm were also computed. The residual flexural strength is calculated according to the following expression:

$$f_{R,j} = \frac{3.F_{R,j}.l}{2.b.h_{sp}^2}(MPa) \tag{7.2}$$

The mean value and the standard deviation of the post-peak parameters of all series from load-CMOD curves are given in Table 7.4. It is evident that overall the increase of fibre content significantly enhanced the residual strength of SFRC, except 3DH-35 SFRC. However, this may not solely be attributed to fibre content, since, for the series reinforced with 80 kg/m^3 hooked-end steel fibre, different post cracking behaviour was observed. It can be observed that the deformed shape of hooked-end fibre has a considerable effect on post-peak behaviour, especially, for series reinforced with 5DH hooked-end steel fibre. Since the aspect ratio and fibre content of all hooked-end fibre types were constant, the 5DH hooked end steel fibre is more effective in improving the post-peak parameters than the other hooked-end ones for both 40 kg/m^3 and 80 kg/m^3 fibre dosage. It can also be observed that with an increase of the fibre dosage from 40 kg/m^3 to 80 kg/m^3, the changes in the post-peak parameters appear to be more significant for the series with 5DH hooked-end steel fibre than for any other fibre types. This may be attributed to the bond strength between steel fibres and matrix with 5DH fibres featuring a desirable combination of hook shape, high ductility, and high tensile strength. It was also observed that for series with 3DH fibre, the majority of fibres were pulled out and the hooked-ends were straightened during the cracking process, while the fibres were not fully straightened in case of 4DH and 5DH fibres (see Figure 7.3). Therefore, the fibres with higher deformed shape and tensile strength would be more effective if these types of fibres are used in high or ultra-high performance concrete to obtain high mechanical bond between fibre and matrix. It must also be observed that, as generally known in the literature, fibres with high aspect ratio can significantly enhance post cracking parameters of SFRC. In this study, however, fibres with equal aspect ratio (i.e. l/d= 65) but different length were used, and the results have revealed that the post cracking behaviour is also largely influenced by the shape and length of fibres.

Table 7.4 Experimental results of post cracking parameters of SFR-SCC

Mix		*Residual strength parameters (MPa)**				
	F_L (kN)	$f_{fct,L}$	$f_{R,1}$	$f_{R,2}$	$f_{R,3}$	$f_{R,4}$
3D-35-40	11.30(9.55)	3.61(9.41)	3.39(11.80)	2.80(7.85)	2.17(5.53)	1.90(5.26)
3D-35-80	11.12(16.54)	3.56(16.29)	5.14(5.05)	4.64(4.95)	4.23(5.67)	3.80(5.26)
3D-60-40	13.43(7.07)	4.29(6.99)	5.62(5.87)	5.21(7.10)	4.56(7.45)	4.05(7.16)
3D-60-80	14.52(8.05)	4.59(4.35)	5.78(5.19)	5.23(7.26)	5.05(8.91)	4.40(6.13)
4D-60-40	8.51(11.86)	2.72(11.76)	4.86(6.79)	4.31(10.44)	3.64(9.61)	3.09(6.47)
4D-60-80	15.25(10.29)	4.88(10.24)	7.95(2.01)	7.57(2.90)	7.10(1.97)	6.81(3.37)
5D-60-40	0.97(8.24)	0.31(6.45)	4.94(21.65)	5.51(6.89)	4.51(11.75)	3.80(16.31)
5D-60-80	0.41(53.65)	0.13(53.84)	2.23(51.12)	11.44(4.89)	11.85(2.86)	10.51(5.70)

*Values in ( ) = CV (%)

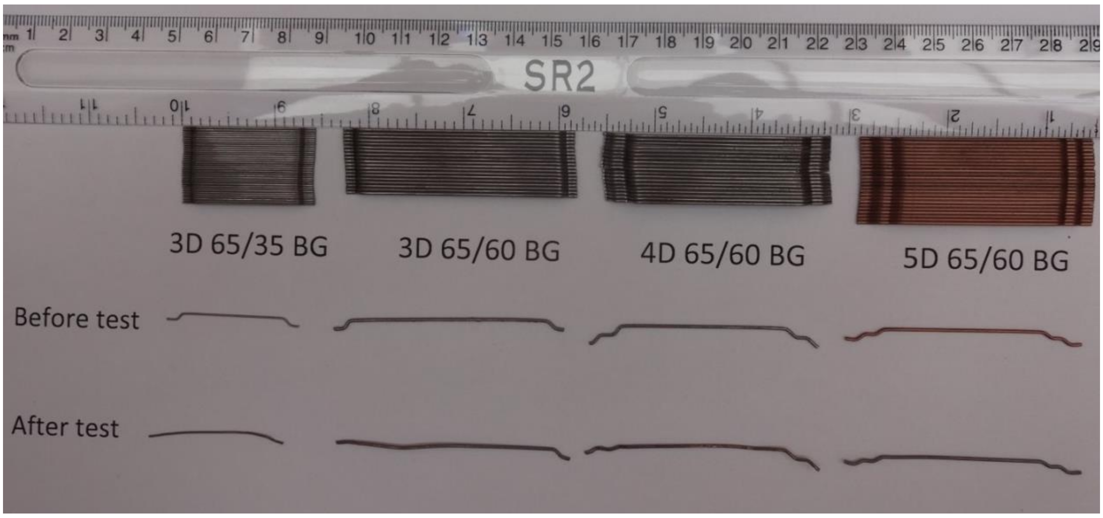

Figure 7.3 Comparison of different hooked end steel fibres before and after fibre deformation

7.3.4 Fracture energy

To evaluate the fracture energy of SFRC, the results of area under the load-CMOD curve of a notched beam tested under three-point bending load were adopted according to RILEM TC 50-FMC[166]. The fracture energy can be defined as the amount of the absorbed energy to form one unit area of a crack [159,177]. By dividing the total dissipated energy with the initial ligament area, the fracture energy is obtained as following expression:

$$G_F = \frac{W_0}{b(h-a_0)} \tag{7.3}$$

where, W_0 is the area under the load-CMOD curve, b, h and a_0 represent the width, height and notch depth of beam respectively.

It has been recommended by Bencardino et al. [178] that only the fracture energy absorbed up to a displacement of 3 mm is of interest from design point of view. Therefore in the present study, the fracture energy is calculated up to a CMOD value of 3 mm. It should be noted that a work of fracture has been computed and specify that no additional measure to clean the elastic energy effect has been taken.

Table 7.5 summarizes the results of the mean and coefficient variation of fracture energy obtained in this study. It can be observed that the fracture energy increases with increasing fibre content for all series, however, the fracture energy of series 5DH at 80kg/m^3 dosage is significantly higher than that of other series with same fibre content. As expected, the new shape of 5DH steel fibres may offer higher levels of anchorage, tensile strength and ductility, which result in guaranteeing better performance. It can also be seen that the latter series showed a more ductile behaviour under flexural load with multiple cracking around the tip of the notch and this did not occur with other series. This fact can also be related to the fibre mechanical anchorage and such high fracture energy is required to create a crack. Since fracture energy significantly increased with increment of fibre content, the overall toughness can significantly be influenced by the shape of fibres.

Table 7.5 Experimental results of fracture energy of SRF-SCC

Mix	mean G_F(N/m)	CV (%)
3D-35-40	1.13	9.02
3D-35-80	3.05	2.97
3D-60-40	1.94	11.78
3D-60-80	2.50	16.45
4D-60-40	1.34	18.34
4D-60-80	4.20	2.38
5D-60-40	2.14	11.71
5D-60-80	5.53	9.65

7.3.5 Fibre distribution and effective fibres

In order to assess the alignment and distribution of the steel fibres on the specimen's fracture surface, the total number of fibres visible on it and the number of fibres pulled out on the corresponding opposite sides were counted. To count the number of fibres on both fracture surfaces, the cross section of beam was divided into four rows and five columns. The fibres in each row, on both faces of the fractured beam were calculated. The total number of fibre per unit cross-sectional area of concrete can be computed by the following expression [62]:

$$N_f = \frac{A_{sec}}{A_{fib}} \times Vf \times \alpha \tag{7.4}$$

where, A_{sec} is the cross-sectional area of specimen (mm^2), A_{fib} is the cross-sectional area of steel fibres (mm^2), Vf is the volume fraction of fibres (%) and α is the orientation factor.

Table 7.6 Number of fibres counted on different locations of fractured cross sections

	Distance from the top	No.of fibres		% of fibres	Density	Orientation factor α	
Mix	(mm)	mean	Cv%		fibres/cm^2	mean	std. dev.
3D-35-40	Raw1	44	11.36	24.22	0.93	0.445	
	Raw2	46	8.69	24.95	0.96	0.459	0.01
	Raw3	48	10.41	26.42	1.02	0.486	
	Raw4	45	15.55	24.40	0.94	0.449	
3D-35-80	Raw1	85	12.94	22.63	1.80	0.428	
	Raw2	104	4.80	27.8	2.21	0.526	0.04
	Raw3	98	3.06	26.11	2.08	0.494	
	Raw4	88	5.68	23.44	1.87	0.444	
3D-60-40	Raw1	25	16	23.24	0.54	0.687	
	Raw2	29	6.89	26.29	0.61	0.777	0.03
	Raw3	28	21.42	25.68	0.59	0.759	
	Raw4	27	14.81	24.77	0.57	0.732	
3D-60-80	Raw1	48	16.66	25.66	1.02	0.651	
	Raw2	47	8.51	25.55	1.01	0.649	0.20
	Raw3	44	11.36	23.88	0.95	0.606	
	Raw4	46	15.21	24.77	0.98	0.628	
4D-60-40	Raw1	21	17.34	22.10	0.95	0.606	
	Raw2	23	10.26	24.21	0.98	0.628	0.01
	Raw3	28	13.85	29.47	1.01	0.642	
	Raw4	23	22.24	24.21	0.95	0.606	
4D-60-80	Raw1	47	19.14	26.60	0.99	0.664	
	Raw2	42	4.76	24.00	0.89	0.719	0.045
	Raw3	45	26.67	25.90	0.96	0.643	
	Raw4	41	17.07	23.42	0.87	0.611	
5D-60-40	Raw1	24	16.67	24.31	0.51	0.642	
	Raw2	26	26.92	26.71	0.55	0.705	0.03
	Raw3	24	20.83	24.65	0.52	0.651	
	Raw4	23	26.08	24.31	0.50	0.642	
5D-60-80	Raw1	46	15.21	25.37	0.97	0.619	
	Raw2	44	20.45	24.62	0.94	0.601	0.008
	Raw3	46	8.69	25.18	0.96	0.615	
	Raw4	45	17.77	24.81	0.95	0.610	

Table 7.6 summarizes the mean and variation of coefficient of number of fibres counted on different location of fractured cross section in of the 27 specimens. It can be seen that the number of fibres counted on fractured surface increases with increasing fibre content. Generally, very good distribution and orientation

have been observed for all SFR-SCC series. This fact can be related to the casting method (flow method), which is able to produce a good alignment of fibres to the main tensile stress, regardless of the size and the shape of the specimen. However, from Table 7.6 no clear relation between the numbers of fibres counted on the fracture surface and residual tensile strength behaviour of SFRC can be found. Three reasons may explain this finding: 1) Although the beams reinforced with 3DH-35 fibres have the highest number of fibres that counted on fracture surface, a lower residual tensile strength is observed; 2) it is also evident from Table 7.6 that these fibres also have lower values of orientation factor, indicating that less alignment of the fibres in the direction of flow leads to lower post-cracking strength; and 3) the residual tensile strength seems to be more influenced by the mechanical anchorage strength than the number of fibres that exists on the fracture surface.

On the other hand, the number of effective fibres on both fracture surfaces has been computed for each specimen, i.e. the fibres, whose hooked-ends were straightened during cracking bridging, were recorded. It must be noted that for the specimens reinforced with fibres 4DH and 5DH, the hook of most fibres did not deform in the cracking process (see Figure 7.3). Therefore, the number of fibres with the hooks partially straightened has been recorded. It is clear that the number of effective fibres of the 3DH fibre reinforced concrete is higher than those of 4DH and 5DH ones. Nevertheless, it is evident that the residual strengths of SFRC are considerably affected by shape and length of hooked-end fibre than the number of fibres within the fracture zone.

It is interesting to note from Figure 7.4 that the relation between the total number of fibres (N_f) and number of effective (N_f^{eff}) is linear. It is worthy to note that for the series reinforced with 3DH fibres, not all fibres can be considered effective in bridging cracking, as in the case of higher fibre content, the fibres are more likely to interact with each other and there is a risk of multiple fibres pulled out together.

To quantify the overall effect of various parameters on the alignment of fibres, the orientation factor was determined according to Eq. (7.4). It can be seen that the series reinforced with long fibres (60 mm) had somewhat higher orientation factor than short fibres (35 mm), for both fibre content and range from 0.610 to 0.776 (see Table 7.6). The reason for this is that the short fibres more likely rotate through the flow of fresh materials and result in lower alignment in the direction of flow. As it can be seen from Table 7.6 no clear relationship between orientation factor and fibre content can be found. However, the scatter of the orientation factor values was rather low. Once again this could be related to constant casting procedure. Therefore, it can be inferred that through the casting in flow method, the orientation of long fibres could be controlled at a very satisfactory level in laboratory conditions.

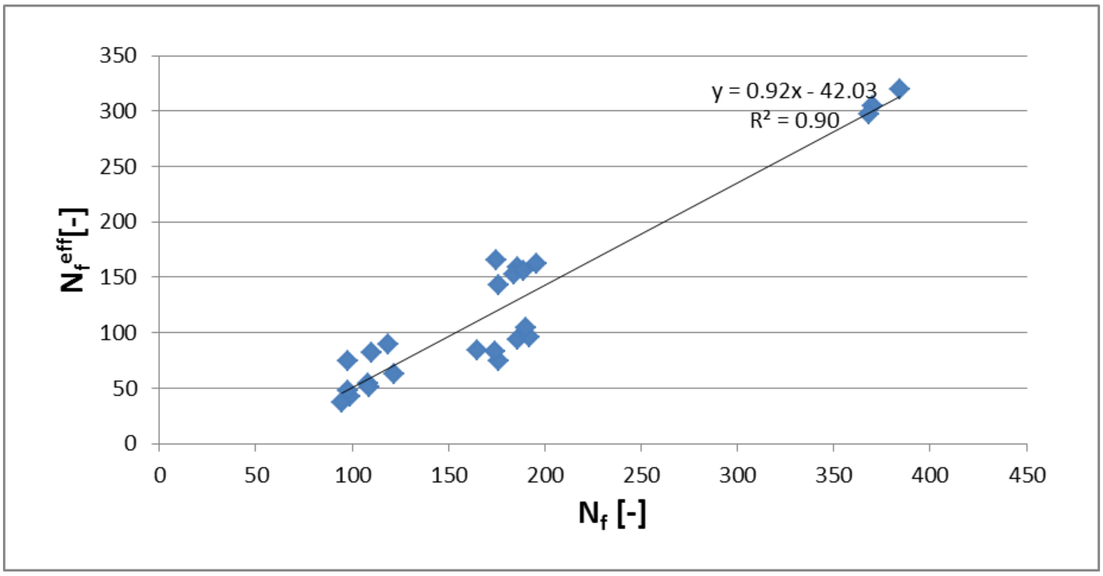

Figure 7.4 Relationship between the total number of fibres and number of effective fibres at the cracked surface

7.3.6 Correlation of the length of pull-out fibres and post cracking behaviour

To further understand the post cracking behaviour of the hooked-end steel fibres, visible lengths of fibres on both fracture surfaces were examined. The number of fibres that are visible on both fracture surfaces according to their visible length has been categorized in intervals of 10 mm (e.g. from 0-10 mm, 10-20 mm, etc.). It can be seen that for short fibres (35 mm), the 63% visible fibres exposed in a range of between 18-24 mm, while for all long fibre types (e.g. 60 mm), about 50% have visible lengths of 30-40 mm (Figure 7.5). One might say a longer visible length means the fibre pulled out through a longer distance, which should result in more energy consumption. It must be noted that for both type of 3DH steel fibres, these deformed fibres were denoted as 'fully effective fibres' (i.e. fully effective in crack bridging). While in the case of fibres hook partially deformed, they were denoted as 'partially effective fibres'. There are some non-deformed fibres found at both surfaces, which were denoted as 'non effective fibres' (see Figure 7.6).

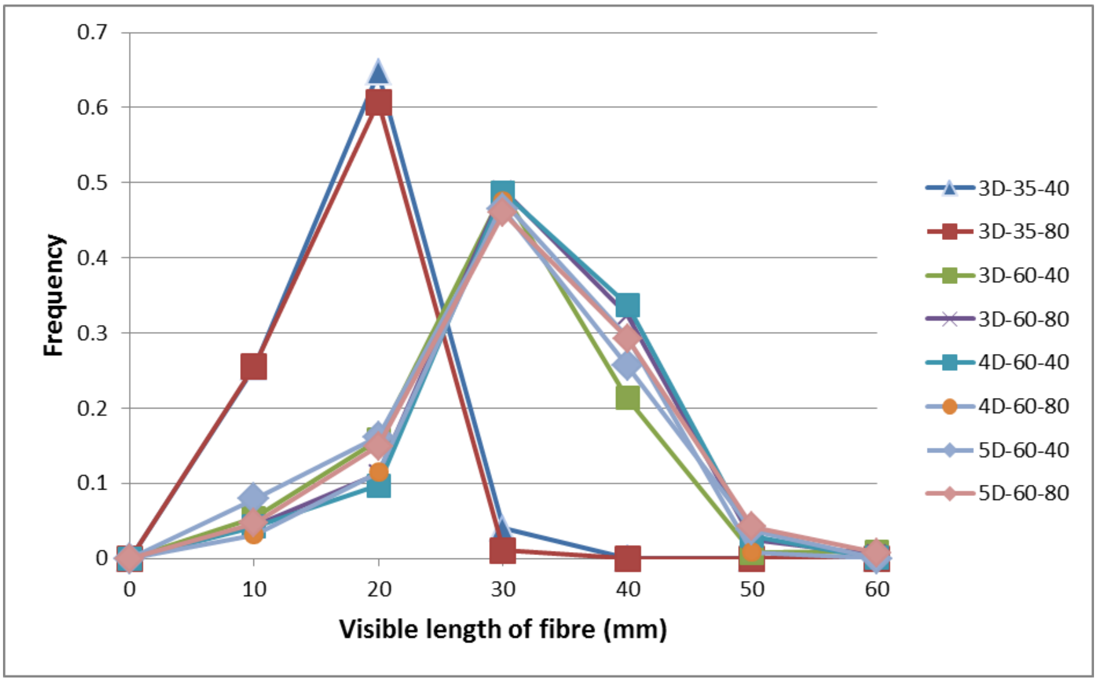

Figure 7.5 Frequency of visible length of fibres which appear on fracture surface

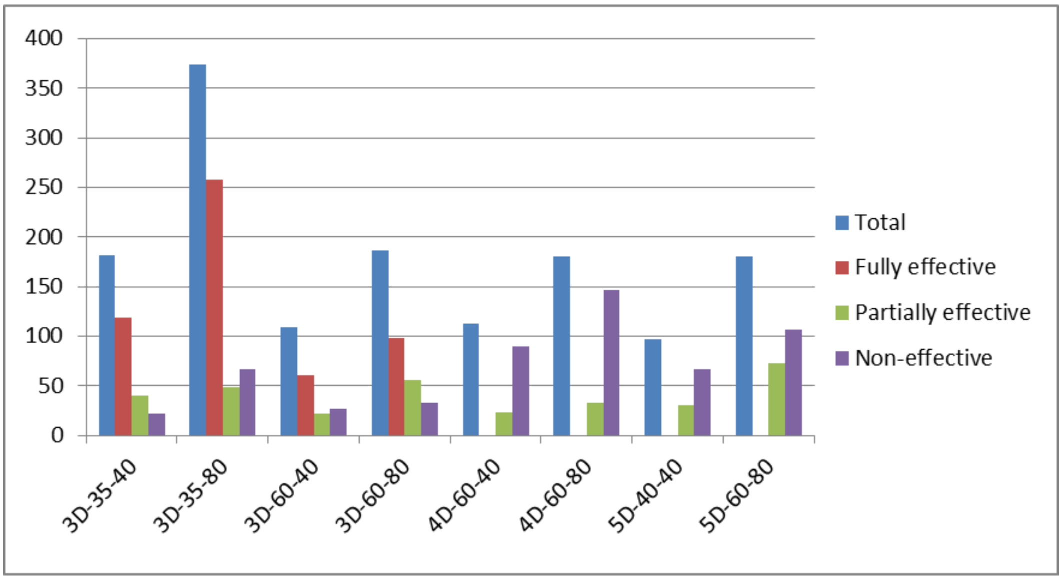

Figure 7.6 The comparison between the total number of fibres and number of effective fibres on fracture surface

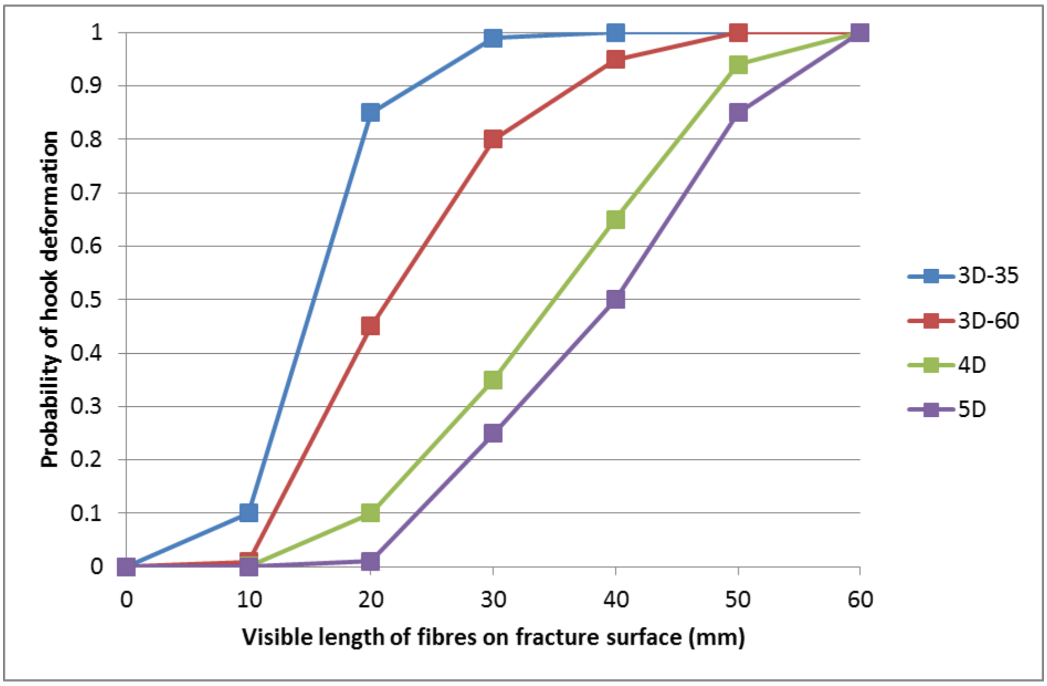

Figure 7.7 Probability of fibre's hook plastic deformation with different visible length of fibres on fracture surface

For 4DH and 5DH fibres, there are several interesting facts found from this study: 1) the full deformation of fibre hooks did not occur and only partially straightened hooks were observed; 2) these partial deformation increases with increasing fibre visible lengths; 3) although about 50% long fibres had visible length more than half of their actual length (visible length > 60/2=30 mm), some fibres did not deform. This is due to the fact that the mechanical deformation of the hook is not governed only by the embedded length but also by the bond strength between fibre and matrix. When the embedded length is less than the end-hook of fibres (i.e. embedded length <10 mm), the plastic deformation of the hook will not happen (see Figure 7.7). Generally, if the cracking path passes close to the middle of the embedded length of a fibre, the probability of fibre deformation becomes higher; 4) as a result of unique shape and ultimate tensile strength of 5DH fibres, the high resistance to fibre pull-out and multiple cracking behaviour have occurred. This could be ascribed to comparatively lower strength matrix and higher mechanical anchorage of end hook fibre. Therefore, in practice it would be more beneficial to use these types of fibres with high or ultra-high performance matrix, in order to assure a better mobilization and straightening of the hook during fibre pull out process. On the other hand, all series reinforced with 3DH steel fibres had only single crack initiated at the tip of the notch. In fact, most of these fibres were fully pulled out and straightened and resulted in relatively lower resistance to cracking extension.

7.4 Concluding remarks

The behaviour of various hooked-end steel fibre reinforced concretes has been fully investigated. Some major findings may be summarised as follows:

1) An addition of steel fibres up to 80 kg/m^3 had only a slightly effect on workability and compressive strength of SFRC.
2) The peak loads and residual strength of SFRC beams under 3-point bending increased with the increase of fibre dosage. The order of performance in terms of peak load was: 5DH- > 4DH->3DH-60-> 3DH-35. The residual loads evaluated at 4 mm CMOD was about 91%,

87%, 79% and 53% of their peak load for 5DH, 4DH, 3DH-60 and 3DH-35 respectively at a concentration of 80 kg/m^3.

3) The residual strength was not only related to the number of fibres counted on fracture surface, but also to the geometry of hooked-end and orientation in matrix.
4) Good distribution and orientation of fibres in the direction of main tensile stress were obtained. The long fibre reinforced concrete had the highest values of orientation factor, indicating most likely rotation of short fibres in the perpendicular direction.
5) The fracture energy increased with the increase of fibre content and was remarkably influenced by the shape of hooked-ends. The multiple cracking and higher ductile behaviour were observed with series 5DH-80 which did not occur with other series.
6) A good balance (compatibility) between the performance of the fibres, which was highly enhanced by the shape of the hook, and the strength of the matrix shall be sought in order to optimise the capacity of both fibres and matrix in the reinforced concrete.

Chapter 8 Characteristics of Uniaxial Tensile Behaviour of Steel Fibre Reinforced Self-compacting Concrete (SFR-SCC)

8.1 Introduction

There is a rising interest in utilising steel fibre reinforced self-compacting concrete (SFRC-SCC) in modern structural applications [179,180]. This is because of its appealing physical and mechanical properties, which in some applications could replace partially or completely the conventional rebar or mesh reinforcement [16]. Plain concrete is known for its weakness normal to a tensile force direction leading to its brittle fracture in tension [17,37,64] as soon the first crack appears. In SFRC after the peak load is reached a post-cracking plateau will occur that results from continuous pull-out of the fibres. The fibre contribution is not obvious until the occurrence of the first micro-crack in the concrete [25]. The post-cracking behaviour of SFRC can be conveniently categorised based on its tensile behaviour by either strain-softening or strain hardening [181]. The strain-softening of SFRC exhibits a low stress-strain response due to crack localisation instantly after first cracking. On the other hand, the strain hardening of SFRC is generally characterised by hardening behaviour after first cracking occurs, immediately followed by multiple cracking [182].

The randomly distributed and oriented steel fibres in the concrete can resist micro-cracking at an early stage. The post-cracking response of SFRC is strongly dependent on the bond quality between steel fibres and their cementitious matrix [4,19,35]. The shape, length and orientation of the fibre determine whether the fibre will break or be pulled-out. An efficient load transfer from the concrete into the steel fibres will result in a high tensile stress; the longer steel fibres will be more efficient at bridging the crack. Besides the shape and length, steel fibre needs to have a high tensile strength in order to resist fibre rupture. In the post cracking behaviour, the steel fibre with a high load resisting capacity, assures an increased degree of ductility. Over the past five decades, different shapes and geometries of steel fibres have been introduced to increase the crack-bridging capacity provided by fibres. These include crimped, straight, spiral, hooked end and twisted. However, according to the last statistics, two thirds of steel fibres used in concrete are hooked end fibres of single bend (3D) compared with other types [159] . Dramix hooked end steel fibres of improved geometry, namely 4D (double bend) and 5D (triple bend) were recently introduced and currently are used extensively in concrete structural applications. These fibres are designed to increase the capacity of a concrete structure to bear complex loading including tension, compression, and shear.

Several methods have been proposed to investigate the post-cracking behaviour of SFRC; the most widely used being uniaxial tensile and flexural tests [27,183]. The majority of the experimental studies of tensile behaviour in SFRC have employed the former test [42]. The tensile test is probably the one test that provides all the relevant fracture parameters directly [163], providing basic information on the tensile response of SFRC, from which a relation between section stress and crack width is derived directly [184]. Different configurations of the uniaxial tensile test, either in terms of the specimen's geometry (i.e. dog bone, cylinders with different dimensions) or with regards to the testing procedure (i.e. different gripping systems and set ups) have been tried. However, there is no standard method for uniaxial tensile test, but, a useful guideline for testing SFRC with post peak stress softening has been proposed by RILEM TC162-TDF [115].

The main intention of this chapter is to investigate the tensile behaviour of 3DH, 4DH and 5DH hooked end steel fibres through uniaxial tensile tests. The results of experiments are essential in order to improve predictions the tensile properties of steel fibre reinforced self-compacting concrete (SFR-SCC). These results will then contribute to a better understanding of tensile behaviour, which can lead to the optimization of SFRC to ensure it is used effectively in its various applications.

8.2 Experimental program

8.2.1 Materials and sample preparation

For the experimental sample preparations the following materials were used: 1) Ordinary Portland Cement (52.5N) complying with the requirements of British Standards BS EN 197-1: 2000, 2) Fly ash with a particle size in the range of 0.02-0.20 μm and the specific surface area of 11.148 m2/kg, 3) River sand in the range of 0-4mm as fine aggregate and crushed granite having a maximum size of 10 mm as coarse aggregates, and finally 4) A new generation of polycarboxylate-based superplasticiser called (TamCem23SSR) having a specific gravity of 1.07 kg/m^3. The mix proportions used in this study are summarised in Table 8.1.

Table 8.1 Mixture proportion per 1 m^3 of concrete made

Cement	Fly ash	Sand (0-2mm)	Coarse aggregate (6-10)mm	Steel fibres (Kg/m^3) (%)	Superplasticizer	Water	W/C
C	FA	S	CA	SF	SP	W	-
470	45	850	886	40;80(0.5;1)	6	216	0.42

Four types of commercially available Dramix hooked end steel fibres were investigated for this study. These fibres are designated according to the manufacturer hook geometry as 3D (single bend), 4D (double bend) and 5D (triple bend). The geometrical and mechanical properties of all fibres are depicted in Figure 3.3 and detailed in Table 3.6. Each of these fibres was added to the concrete mixture at two dosages i.e. 40 and 80 kg/m^3, corresponding approximately to a volume fraction of 0.5 and 1%, respectively.

During mixture preparation, the dry materials i.e. cement, fly ash, silica fume and aggregates were firstly mixed for roughly 1 minute before the superplasticizer and water were added. This was then mixed for another 11 minutes. For mixtures with adding fibres, the mix was continued for another 3 minutes as shown in Figures 3.6. The freshly prepared SCC and SFR-SCC were then cast into 150 × 300 mm cylindrical moulds conforming to RILEM TC 162-TDF [115]. Thereafter the specimens were instantly covered with polyethylene sheets to prevent moisture loss. Then they were demoulded after 24 h and moved into curing chamber at a temperature of 22 ± 2C and relatively humidity of 95% until the age of testing.

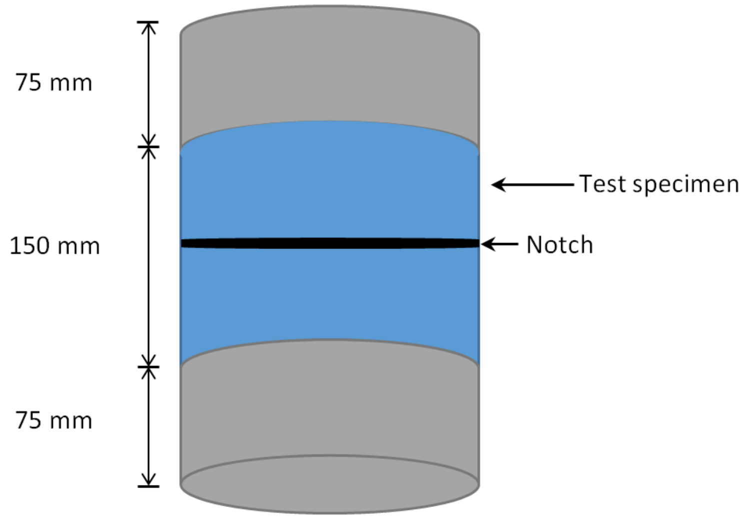

Figure 8.1 Geometrical details of the specimen to be tested in the uniaxial tensile test

The size and shape of each specimen must comply with RILEM TC 162-TDF [115]. Both the nominal length and diameter of the specimen would have to be equal to 150 mm as shown in Figure 8.1. To obtain these dimensions, the top and bottom of the specimen were sawn at a distance of 75mm. Then a circumferential notch with a width of 2-5 mm and a depth of 15 mm +/- 1 mm was made at mid of the specimen to ensure crack localization during the tests. Special care was given during the cutting process to guarantee smooth surface and perpendicular plane to the cylinder axis.

8.2.2 Setup and test procedures

Following the cutting and notching process, all specimens were carefully cleaned with pressurized air and acetone. Afterwards, two metal plates attached in the loading cell were glued using ultra performance adhesives (Epoxy), to the top and bottom surfaces of the specimen, which was then left to cure for two hours before testing (Figure 8.2).

An Instron 2670 series testing machine of 150 kN loading carrying capacity was used to perform the uniaxial tensile tests. This test was carried out under closed-loop displacement control in which the averaged readings of three displacement transducers arranged around the perimeter of the specimen were measured. The three displacement transducers had a 30 mm travel. The displacement rates adopted were as follows: 5 μm/min up to a displacement of 0.1 mm and 100 μm/min up to a displacement of 2 mm. This was continued until a crack width of 10 mm was attained in order to ensure that the hook part of each fibre was fully deformed and straightened. The testing procedure adopted and displacement rates complied with the recommendations of RILEM TC 162-TDF [115].

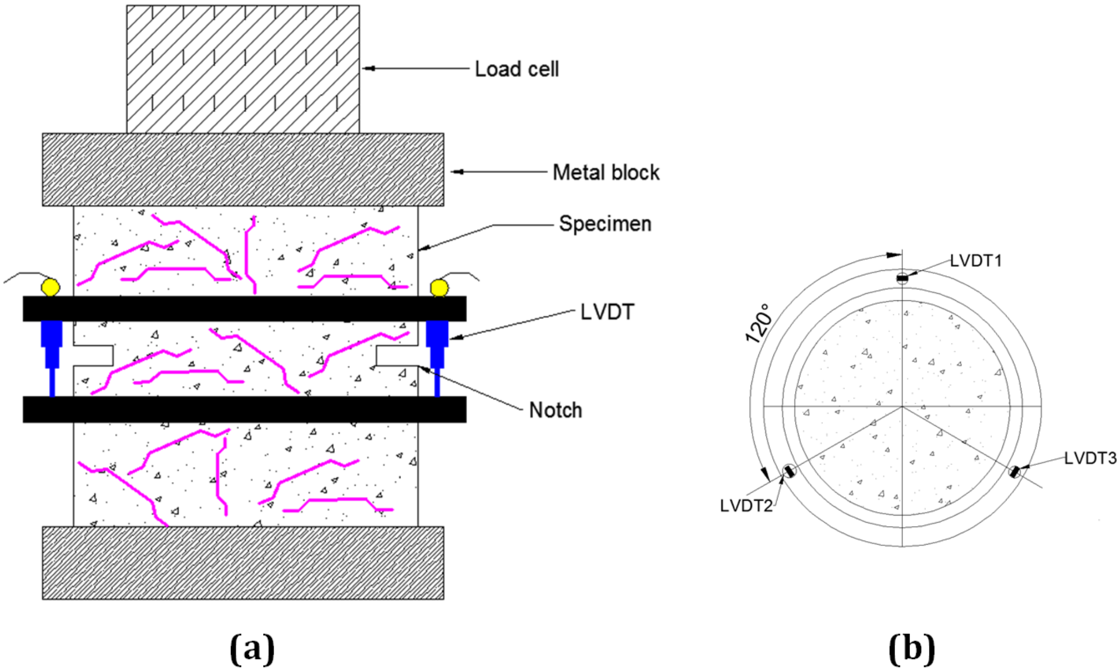

Figure 8.2 Uniaxial tension test set-up: general view (a) and positioning of displacement transducers (b)

8.3 Results and discussion

8.3.1 Stress-crack width response

Stress-crack width response is measured according to RILEM TC 162-TD[115] up to the crack width of 2 mm. The average tensile stress-crack width curves of plain concrete (PC) and reinforced concrete by different hooked end steel fibres are presented in Figures 8.3 and 8.4 for a fibre content of 40 and 80 kg/m^3, respectively. The figure (a) shows crack width up to 2 mm and the figure (b) up to 0.1 mm. It can be seen in Figures 8.3a and 8.4a that PC exhibits almost linear behaviour up to the peak stress, which corresponds to crack width of about 0.08

mm, followed by a sudden drop in stress at the initial stage of the post-peak response. For all plain concretes, a brittle failure was observed, accompanied by separation of the specimens at the notch into two parts. On the other hand, the specimens reinforced with steel fibres demonstrate not only significantly higher peak load, but also a plateau response in the post-peak part. The post-peak region of the stress-crack width curve is clearly different in case of each of the three fibres. It is evident that specimens reinforced with 40 and 80 kg/m^3 of 5D fibres show stronger strain hardening behaviour compared to the other fibres.

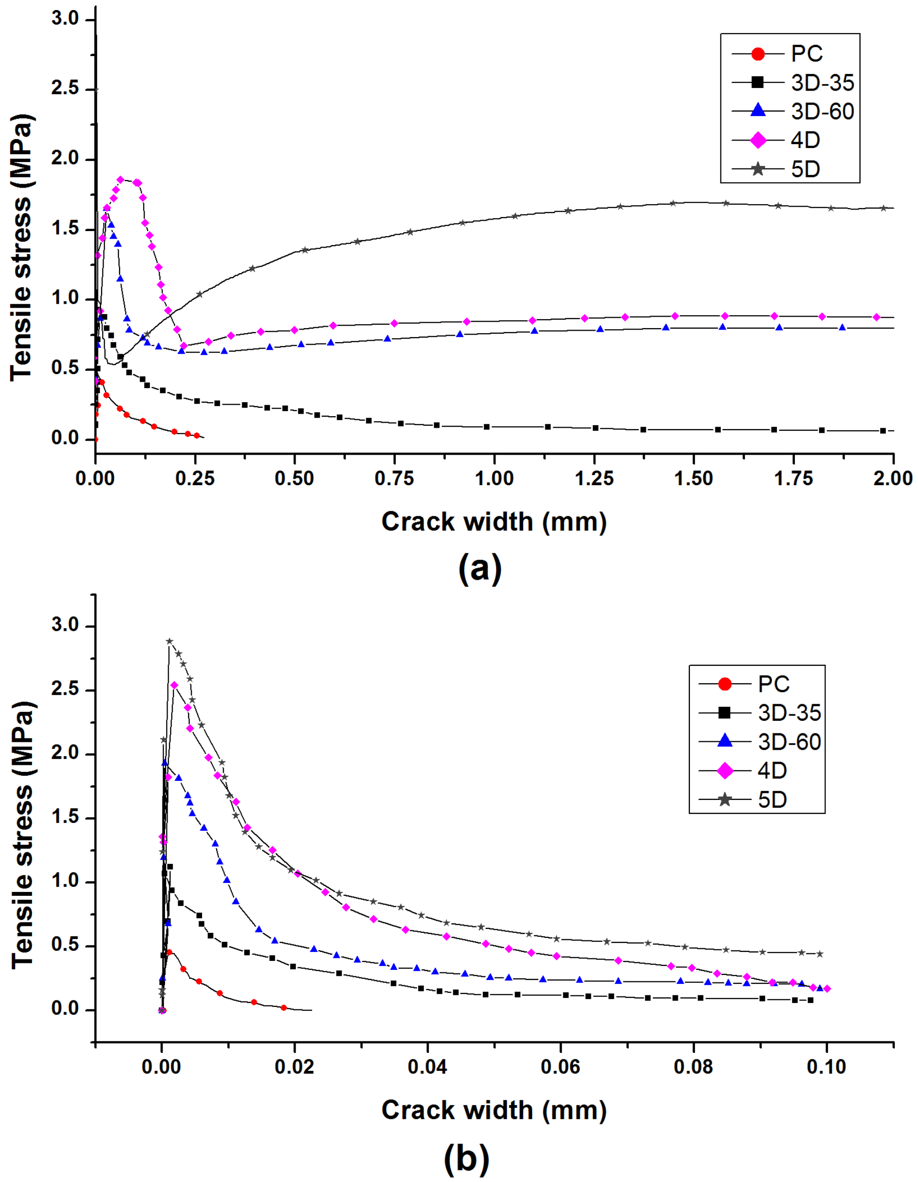

Figure 8.3 Average stress-crack width responses of SFR-SCC series reinforced with 40 kg fibres: (a) total stress-crack width curve and (b) detailed up to a crack width of 0.1 mm

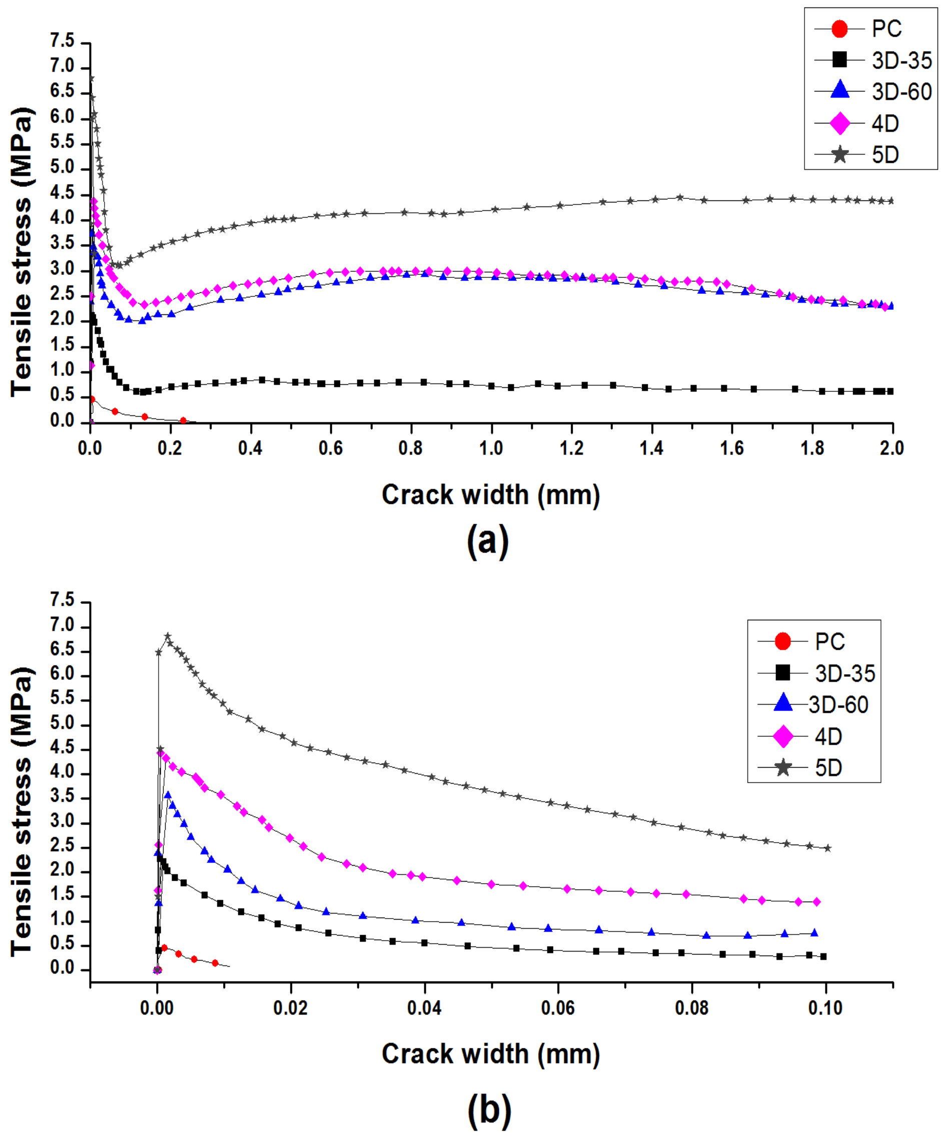

Figure 8.4 Average stress-crack width responses of SFR-SCC series reinforced with 80 kg fibres: (a) total stress-crack width curve and (b) detailed up to a crack width of 0.1 mm

Table 8.2 summerizes the average peak and post-peak parameters for different average crack widths. In this table, σ_{peak} is the maximum tensile stress, δ_{peak} is the corresponding displacement at peak stress and σ_{2000} is the stress at a crack width of 2000µm. It is clear that the effect of different fibre types and volume fractions on the post-cracking behaviour is significant. The peak and post-peak parameters increase significantly as the fibre dosage increases for all fibre series. The percentage increase in the σ_{peak} of 3D-35, 3D-60, 4D and 5D fibres is 112%, 68%, 76% and 141%, respectively when fibre dosage increases from 40 to 80 kg/m^3. As expected, the geomtery of fibres strongly influences the σ_{peak} of SFR-SCC. The hooked end steel fibres with a higher number of bends (i.e. 4D and 5D fibres) are more effective in improving the peak and post-peak response than those of single bends (3D fibres). At a comparable fibre dosage, specimens reinforced with 5D fibres achieve a higher peak and post-peak values than specimens with 3D-35, 3D-60 and 4D fibres. The residual strengths of 5D fibre, i.e. σ_{2000} at a crack width of 2 mm, is about 60% and 65% of their σ_{peak} for the 40 and 80 kg/m^3 fibre content, respectively (Table 8.2). The higher residual tensile strength at greater crack width values is mainly due to the unique combination of high anchorage strength and high tensile strength of the 5D fibre. Indeed, both aspects provide higher resistance to the pull out of fibres at larger crack widths. It is noteworthy that the fibre rupture in fractured sections is observed for both the 3D-35 and 3D-60 fibres, while for the 4D and 5D fibres are only partially deformed and straightened. The rupture of 3D-35 and 3D-60 fibres may occur due to their relatively lower tensile strength.

Table 8.2 Peak and post-peak parameters *

Fibre type	Fibre dosage (kg/m^3)	σ_{peak} (MPa)	δ_{peak}(μm)	σ_{2000} (MPa)	$G_{F,2000}$ (N/mm)
PC	0	0.25 (1.2)	5.4(3.4)	-	-
3D-35	40	1.21(8.4)	7.2(6.3)	0.15(5.8)	0.95(5.3)
3D-35	80	2.56(16.2)	6.4(4.4)	0.76 (6.2)	1.84(6.7)
3D-60	40	2.15(11.4)	6.1(8.3)	0.66(9.5)	1.61(5.4)
3D-60	80	3.62(13.9)	9.7(3.2)	2.39(7.5)	2.45(9.1)
4D	40	2.59(16.5)	5.7(8.1)	0.85(2.6)	1.94(6.1)
4D	80	4.56(14.8)	10.3(2.3)	2.4(3.7)	2.82(7.9)
5D	40	2.85(19.2)	9.6(5.8)	1.69(8.9)	3.64(8.8)
5D	80	6.87(21.3)	7.8(4.5)	4.45(9.9)	5.42(8.6)

*Values in ( ) are the coefficient of variation (%)

8.3.2 Fracture energy

The energy absorbed or fracture energy is a fundamental parameter commonly used to evaluate the advantageous effects of fibres in SFRC. The fracture energy is defined as the amount of energy absorbed during the failure of the specimen, which is calculated as area under the stress-crack width curve. The calculated fracture energy ($G_{F,2000}$) up to a crack opening of 2 mm for each fibre type at the various fibre dosages is summarized in Table 8.2. While $G_{F,2000}$ of plain SCC is found to be lower than 0.25 N/mm, $G_{F,2000}$ of SFRC-SCC tends to be considerably higher.

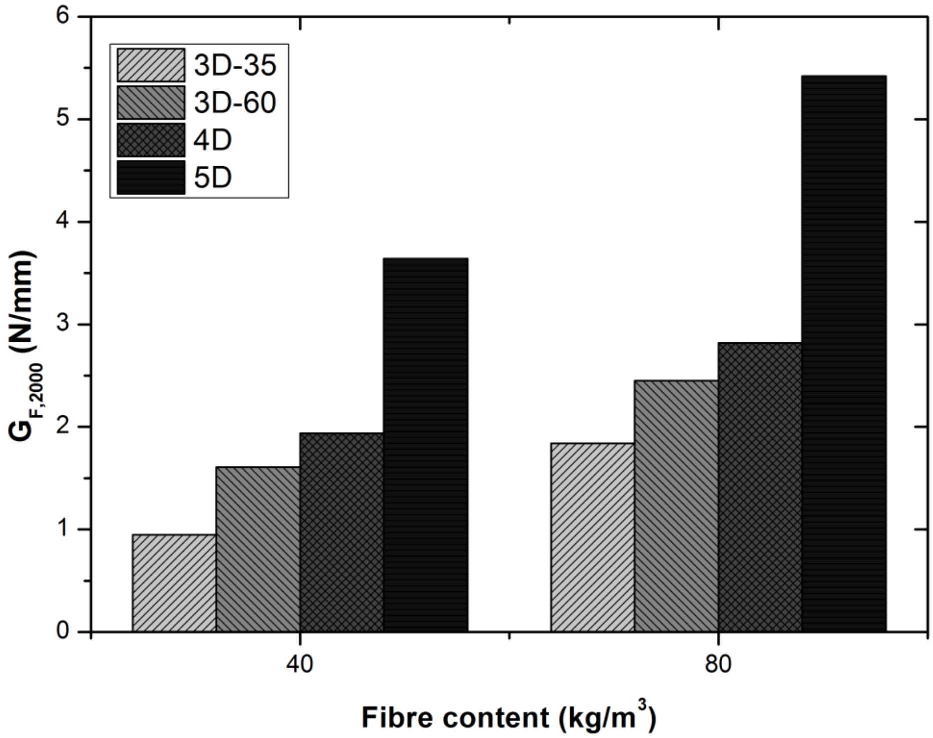

Figure 8.5 Comparison of fracture energy of SFR-SCC

The comparison of the fracture energy of SCC reinforced by different hooked end steel fibres is shown in Figure 8.5. As it is expected, the $G_{F,2000}$ of all SFRC-SCC series increases with the fibre dosage increases. The increment of the fracture energy is almost linearly proportional to the increment of the fibre content for all SFRC-SCC series. The percent increase in the $G_{F,2000}$ of 3D-35, 3D-60, 4D and 5D fibres is 94%, 52.17%, 45% and 50%, respectively when fibre dosage increases from 40 to 80 kg/m^3. The $G_{F,2000}$ of 5D fibres is higher than those of 3D-35, 3D-60 and 4D fibres by 283 %, 126% and 88% for fibre content 40 kg/m^3, while, the corresponding increase for 80 kg/m^3 is 195%, 121% and 92%, respectively. The lower values of $G_{F,2000}$ for both the 3D-35 and 3D-60 fibres may be a result of the fibre rupture during the pull-out. These results highlight that energy dissipated to bridge cracks of SFR-SCC is to a great extent influenced by the balanced combination of wire strength and anchorage design, especially at high fibre dosage. Fibres with multiple hook bends would provide a higher resistance to the pull-out whereas fibres of single hook bends will provide a moderate or limited resistance to crack propagation. Nevertheless, both types of hooked end fibres would contribute largely to preserve the structural stability and structural integrity of concrete elements. In practical structural applications, a combination of high anchorage strength and high tensile strength fibres may contribute more effectively to increase the durability and service life of a structural element than the use of single bends and relatively lower tensile strength fibres.

8.3.3 Analysis of fibre distribution and numbers at the cracked sections

To understand further the influence of the fibre content and fibre distribution on the stress-crack width response, the total number of fibres visible on the fractured surfaces was counted to investigate a further relationship for post-cracking behaviour. Therefore, the cross section of the cylinder is divided into four different locations (A, B, C, and D) as shown in Figure 8.6.

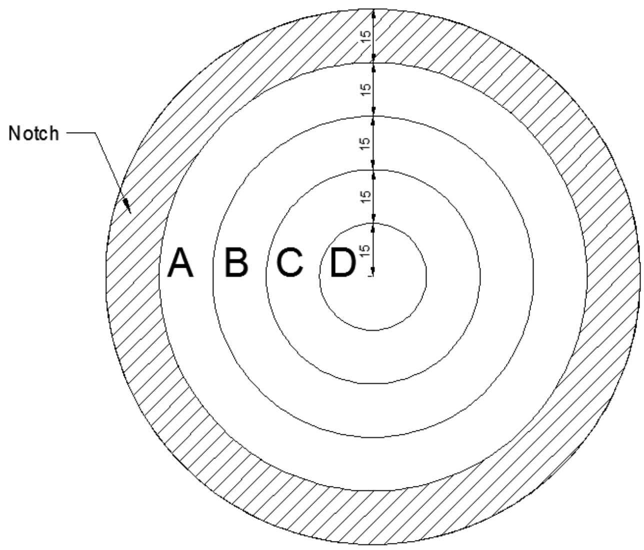

Figure 8.6 Cross-sectional surface shows analysis of the fibre distribution in the different domains

Table 8.3 presents the average results of the distribution and number of fibres counted in different locations for each specimen. It is noteworthy that the number of effective fibres (N_{eff}) is only counted when the hook is partially or completely straightened. Additionally, the ruptured fibres visible on cracked sections are also regarded as effective, since they offer resistance to cracking against fibre slippage up to their failure. From visual inspection of fractured surfaces, the fibre rupture is only observed for 3D-35 and 3D-60 fibres.

Table 8.3 Average number of fibres counted on different locations of fractured cross sections

Mix	Domain				N_{total}		N_{eff}	
	A	B	C	D	average	Cv (%)	average	Cv (%)
3D-35-40	32%	24%	31%	13%	46	21.5	42	9.2
3D-35-80	27%	38%	25%	10%	82	14.2	78	6.8
3D-60-40	29%	28%	29%	14%	34	21.6	26	11.8
3D-60-80	29%	27%	35%	9%	58	9.4	48	9.9
4D-60-40	31%	34%	21%	14%	28	8.7	16	18.9
4D-60-80	32%	30%	19%	19%	49	16.6	28	25.7
5D-60-40	25%	34%	23%	18%	24	18.7	8	18.7
5D-60-80	15%	38%	35%	12%	44	22.6	15	29.7

As it can be observed from Table 8.3, the highest density of fibres is almost distributed in the locations (A, B, C) and the lowest in the location (D) for all fibres series. It is clear that as the fibre content increases the total number of fibres (N_{total}) counted on the fractured surfaces is also increased. However, the number of effective fibres (N_{eff}) is decreased when fibre dosage increases, especially for the 4D and 5D fibres. This may occur due to the pulling out of a group of fibres simultaneously (group effect) hence reducing the efficiency of fibres. Moreover, the efficiency of the fibre also decreases with increasing the number of the hook bends which results in a lower number of N_{eff}. The 4D and 5D fibres have the lowest number of N_{eff} compared with 3D-60 and 3D-35 fibres.

This indicates that less energy is invested to deform the hook bends of 4D and 5D fibres during the pull-out. The main reason for this fact is the incompatibility between the medium concrete strength and high anchorage strengths of 4D and 5D fibres. Therefore, concrete with higher strength is needed to ensure more energy is absorbed by the hook bends of these fibres during pull-out.

8.3.4 Relationship between fibre distribution and post-cracking behaviour

To better understand the post-cracking behaviour of SFR-SCC, the correlation between the average numbers of fibres counted on the two fractured surfaces and post-cracking parameters was analysed. The average values of peak and post-peak parameters of all series are summarized in Table 8.2.

Figures 8.7-8.10 show the relationship between the maximum tensile stress (σ_{peak}) and number of fibres counted on the fracture surfaces for all specimens. It can be seen that an almost linear correlation can be traced between these two parameters, which is in agreement with other results reported previously [25, 35]. As can be seen from Figures 8.7-8.10 that the σ_{peak} is closely related to the number of counted fibres, particularly to the N_{eff}, with the exception of 5D fibres series. For this series (Figure 8.10), no clear trend can be identified between the σ_{peak} and N_{eff}, which provides a lower coefficient of determination (R^2) of 0.21. This discrepancy may be a result of variability in the deformation and straightening level of hook bends due to incompatibility between high anchorage strength of 5D fibres and relatively moderate concrete strength. A high variability of this implies a large scattering in the σ_{peak} as shown in Table 8.2. Generally, the scattering in the σ_{peak} of 4D and 5D fibres is always higher than the ones observed for both the 3D fibres (Table 8.2).

It is also interesting to note that despite the 3D-35 and 3D-60 fibres series have the greater number of N_{eff}, the highest values of σ_{peak} is observed for 4D and 5D fibres. For the fibre content of 40 kg/m^3, the average value of N_{eff} for 3D-35, 3D-60, 4D and 5D fibres are 42, 26, 16 and 8, and the corresponding values of σ_{peak} are 1.21, 2.15, 2.59 and 2.85 MPa, respectively. In the case of fibre content of 80 kg/m^3, the average number of N_{eff} for 3D-35, 3D-60, 4D and 5D fibres are 78, 48, 28 and 15, and the corresponding values of σ_{peak} are 2.56, 3.62, 4.56 and 6.87 MPa, respectively.

On the other hand, the post-peak parameter i.e. σ_{2000} also appears to be significantly influenced by the hook geometry of the fibre. It can be observed from Figures 8.3a and 8.4a that the residual strength increases dramatically with an increase in the number of bends at the fibre ends. The post-peak response of 5D fibres exhibits a significant increase in residual strength compared with those of other fibres. Such improvement occurs mainly due to high energy invested to deform and straighten the hook bends during debonding and pull-out process. This indicates that the anchorage strength is the most important parameter affecting the post-cracking response, regardless of the number of fibres that bridge the cracked surfaces.

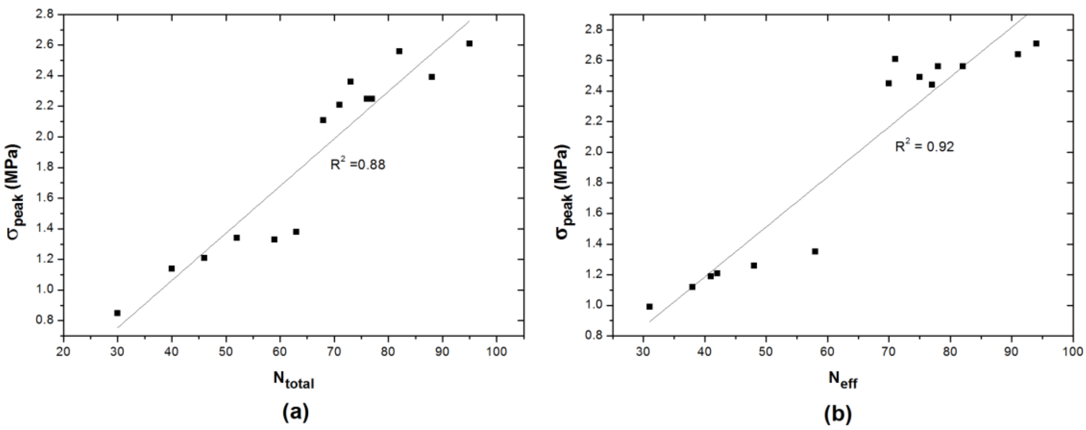

Figure 8.7 Relationship between the σ_{peak} and number of fibres in the fracture surfaces of 3D-35 fibres: (a) Total number (N_{total}) and (b) Effective fibres (N_{eff})

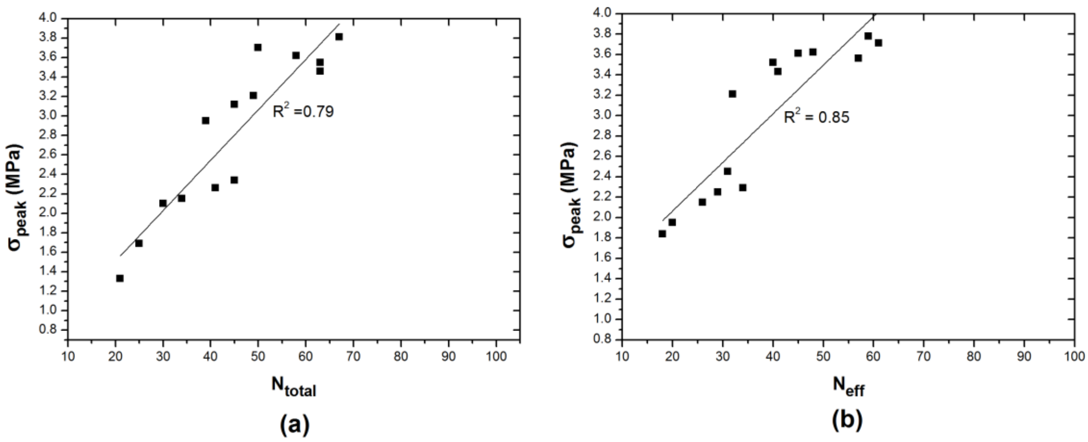

Figure 8.8 Relationship between the σ_{peak} and number of fibres in the fracture surfaces of 3D-60 fibres:(a) Total number (N_{total}) and (b) Effective fibres (N_{eff})

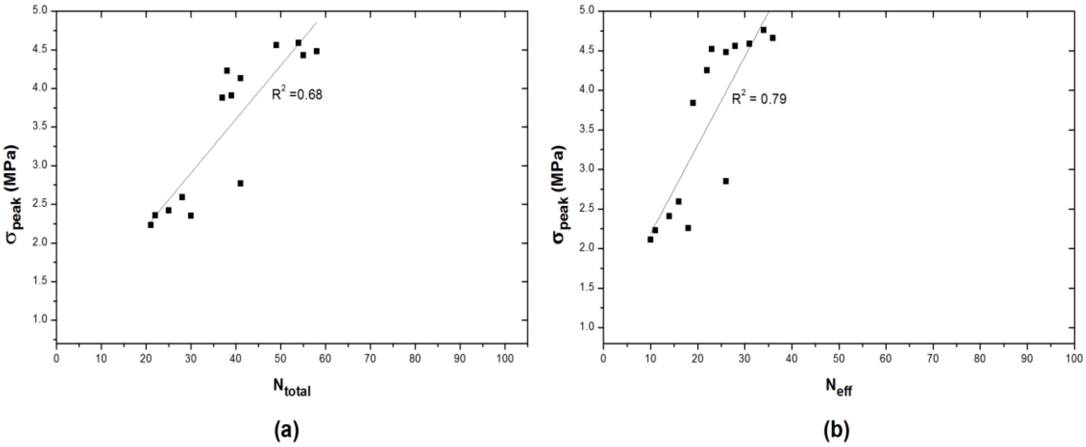

Figure 8.9 Relationship between the σ_{peak} and number of fibres in the fracture surfaces of 4D fibres: (a) Total number (N_{total}) and (b) Effective fibres (N_{eff})

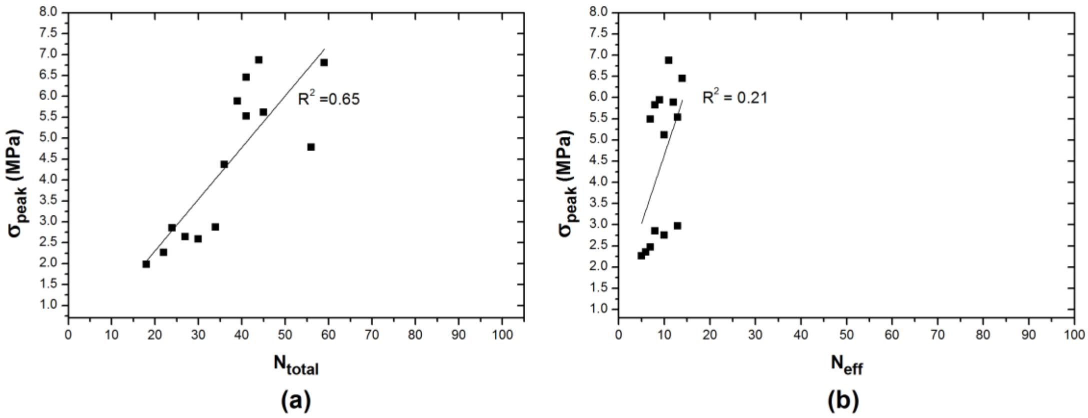

Figure 8.10 Relationship between the σ_{peak} and number of fibres in the fracture surfaces of 5D fibres: (a) Total number (N_{total}) and (b) Effective fibres (N_{eff})

8.4 Concluding remarks

In this chapter, the tensile behaviour of steel fibre reinforced self-compacting concrete (SFRC) was assessed by a uniaxial tensile test. Four types of hooked-end steel fibre with different geometries at the fibre dosage of 40 and 80 kg/m^3 were investigated and the following main conclusions were gathered:

1) For all specimens reinforced with hooked-end steel fibres, the stress-crack width response was almost linear up to the load at crack initiation and a smooth transition in the post-peak region was observed. The strain-hardening response was clearly evident in the case of SCC reinforced with 5D fibres.

2) The increase of the fibre dosage improved significantly the post-peak and fracture energy response for all fibres. However, the positive effect of the increase of fibre content is more distinct for the 5D series than those of 3D and 4D fibres.

3) The number of hook bends was the most influential factor on the post-cracking response. As the hook bends increased, the post-cracking response considerably increased, where 5D fibres specimens showed the highest values of peak and post-peak strength.

4) While increasing fibre dosage was necessary for improving the post-cracking response, increasing the number of fibres at the cracked sections did not necessarily lead to enhanced post-peak behaviour. Although, specimens reinforced with 3D fibres had a much high number of effective fibres, the peak and post-peak strength of 4D and 5D fibres were significantly higher.

5) The fibre rupture was observed only for specimens reinforced with the 3D fibres. For the 4D and 5D fibres, only a partial straightening of the hook occurred due to the imbalance between the moderate concrete strength and high anchorage strength of these fibres.

Chapter 9 Conclusions and Future Perspectives

9.1 Introduction

The development of steel fibre reinforced concrete (SFRC) marks an important milestone in enhancing the efficiency and quality of the construction materials, which are more likely to be used in a wide variety of structural applications in the near future. The success of any fibre reinforced cementitious composite depends upon the bond between the reinforcing fibre and the matrix. However, characteristics of the bonding of SFRC are yet to be understood. This research project provides a comprehensive and detailed understanding of the bonding mechanisms associated with the pull-out behaviour of steel fibres with different geometry and matrix strength.

The present research project has been carried out involving both experimental and analytical studies regarding the bond characteristics of SFRC. The experimental programme covers major aspects controlling the tensile behaviour of SFRC which was carried out at two different scales. At a production stage, various physical parameters, such as fibre characteristics (geometry, embedded length, diameter and tensile strength), fibre orientation and matrix quality, on the pull-out behaviour have been investigated. The influence of the elevated temperatures (20-800°) on the bonding mechanisms of SFRC was also assessed. At products in use, the tensile response of SFRC composite was evaluated by means of flexural and uniaxial tensile tests. These would enable a deeper understanding of the reinforcing mechanisms of the SFRC and all parameters that influence the overall composite behaviour. The assessment of the post-cracking response of SFRC has been limited to the self-compacting concrete matrix and exposure to normal temperature conditions.

With the gathered experimental results, analytical model was developed to predict the pull-out behaviour of hooked end fibres embedded in various matrix strengths. With wider applications of the present model, an important step toward a reliable predictive approach for possible better design and optimization of SFRC for structural applications has therefore been proposed.

9.2 Concluding remarks

This PhD project has contributed to the science of tensile behaviour of SFRC by improving the understanding of bonding mechanisms of steel fibres through investigating the material characteristics, reaction of physical parameters and thermal response of SFRC and its constituents. The conclusive statements of this research can be summarised as follows:

The **Chapter 2** of this thesis understood through a literature review the bonding mechanisms of SFRC and numerous related aspects, namely, experimental techniques to measure the shear bond strength, experimental and theoretical investigations on the pull-out behaviour of steel fibres. It is evident that a clear and comprehensive approach to characterize the bond mechanisms in SFRC is still missing. The existing analytical models could not provide a robust and detailed approach for predicting the pull-out response, especially to take into account the variation of fibre characteristics (e.g. fibre geometry and tensile strength) and matrix quality.

Little investigation on the post-cracking behaviour of SFRC subjected to high temperature could be found in the literature. Furthermore, in spite of many experimental investigations and recent advances in SFRC research, the information on bond mechanisms of steel fibres after exposure to the elevated temperatures was unavailable.

The **Chapter 4** aimed at understanding experimentally the pull-out behaviour of steel fibres with varying parameters, such as fibre characteristics (geometry, embedded length, diameter and tensile strength), fibre orientation as well as matrix strength. From these investigations the following conclusions can be drawn:

1) The experimental results of single pull-out tests clearly showed that the fibre geometry, the matrix quality and the fibre orientation were the most important parameters governing the pull-out behaviour of hooked end fibres. The quality of the matrix played a clear influence on interfacial properties between the steel fibre and the matrix. As the matrix strength increased, the maximum pull-out load and the bond strength increased significantly. However, the fibre rupture tended to occur when the matrix with very high strength was combined with fibre having high mechanical and anchorage but relatively low tensile strength. In such a scenario, the fibre tensile strength also played a great role as it determined either a fibre being pulled-out or its failure during the pull-out process.

2) The mechanical anchorage efficacy provided by the fibre strongly depended on its hook geometry. The number of bends at fibre ends had a direct influence on the pull-out behaviour. Due to the variation in the hook geometry, there was a significant difference between the pull-out behaviour of all three hooked fibres even though they had same diameter and embedded length. As the number of bends in the hook increased, the maximum pull-out load and pull-out work increased dramatically. To what extent the pull-out response could be improved depended principally on the quality of the matrix.

3) Bonding mechanisms controlling the pull-out behaviour of the inclined fibres were remarkably different from those of the aligned fibres. For the former in addition to the debonding and friction stages, further actions, such as fibre bending, matrix spalling and local frictional effect, were evidenced. The maximum pull-out load and pull-out work of the inclined fibres were higher than those of aligned fibres up to an inclination angle of 15°. However, a further increase in the inclination angle (i.e. 45° and above) not only decreased the pull-out load due to fibre bending and matrix spalling but also led to fibre rupture for all hooked end fibres.

The **Chapter 5** advances an analytical model to predict the pull-out behaviour of hooked end fibres embedded in various concrete matrices. The significant contributions of this chapter includes the analysis and modelling of the pull-out behaviour of hooked end fibres embedded in various matrix strengths, specifically:

4) A new formulation was developed to predict the pull-out behaviour of steel fibres with various hooked ends geometry and various matrix strengths. The model was established based on the concept of Alwan's frictional pulley along with two, three and four plastic hinges to simulate the mechanical anchorage effect provided by the hook. The mechanical contribution of the hook was a function of the cold work needed to straighten the fibre during the pull-out. The input parameters used in this model were directly related to geometrical and mechanical properties of each fibre. Model predictions were validated against experimental results for single fibre pull-out tests, and a good agreement was achieved.

The **Chapter 6** of this thesis investigated the bond characteristics of steel fibres after exposure to various elevated temperatures (20-800°C). The specific conclusions are:

5) The bonding mechanisms associated with the pull-out behaviour of straight and hooked end steel fibres were further investigated after exposure to elevated temperatures (20-800°C). The bond strength of straight fibres decreased gradually with increasing temperature. However, the bond strength of all hooked end fibres did not vary significantly throughout a range of 20–400°C temperature, but within the temperature range of 600–800°C, the pull-out strength decreased significantly for all concretes. The reduction in bond strength at elevated temperatures was found to be strongly related to the degradation in properties of the constituent materials, i.e. the fibres and concrete.

The last part of this project studied the tensile behaviour of SFRC by means of three-point bending tests **(Chapter 7)** and uniaxial tensile tests **(Chapter 8)**.

The post-cracking behaviour was assessed in terms of load-crack mouth opening displacement (CMOD) relation for bending tests and stress-crack width (σ verses w) relation for uniaxial tensile tests. Both tests are also accompanied by the qualitative and quantitative analysis of the fibre orientation and distribution in the tested specimens and their relation to the post cracking response. Major findings are:

6) The fibre geometry and fibre content significantly affected the post-cracking response of SFRC. The strain-hardening behaviour accompanied by multiple cracking was clearly observed for concrete reinforced with 5DH fibres in both bending and tensile tests. The factors which affect the pull-out behaviour of single fibre also influenced the post-cracking response of SFRC. In addition, other factors such as fibre distribution and fibre orientation also influenced the post-cracking behaviour.

9.3 Future perspectives

This section provides a list of recommendations for extension of the study based on the knowledge established through the completion of this PhD research. The gaps concerning the characterization and design of SFRC are identified, which should further add value to the research field.

1) The influence of the fibre orientation on the pull-out behaviour is yet to be investigated. Although the pull-out response of both straight and hooked end fibres embedded in ultra-high performance matrix (UHPC) under various inclination angles was experimentally investigated in Chapter 6, the bonding mechanisms of hooked end fibres are expected to change depending upon the strength of matrix. Moreover, the experimental results in Chapter 4 show some differences in terms of pull-out strength and failure mode when fibres are pull-out from different matrix strengths. It would therefore be appropriate for a further investigation to focus on the pull-out behaviour of inclined fibres embedded in low-high strength combinations.

2) In this study, an analytical model to predict the pull-out behaviour of hooked end fibres embedded in a various matrix strength has been employed. The proposed model provides a comprehensive and straightforward approach, which may contribute to the continuous growth of using these hooked end fibres in structural applications that have been observed in the recent years. Further research should be carried out to enlarge the scope of application of the current model for different pull-out conditions. In this context, the analytical models to predict the pull-out behaviour of inclined hooked end steel fibres as well as the high temperatures effect.

3) An insight into the influence of temperature on bonding mechanisms under elevated temperatures needs to be enlarged. Although the bond characteristics of straight and hooked end fibres after exposure to high temperatures have been extensively investigated in this research, the studies on pull-out behaviour of steel fibres under elevated temperatures has not yet been reported. The bond mechanisms governing the pull-out behaviour of hooked end fibres under elevated temperatures may differ from those verified in the residual conditions. For that purpose, the pull-out behaviour of hooked end fibres under elevated temperatures should be carefully evaluated.

4) In order to gain more in-depth understanding of the versatile reinforcement mechanisms, further investigations on SFRC composite under elevated temperatures in both bending and tension tests with large-scale elements are needed.

5) In this research the experimental programme covers the major aspects governing the tensile response of SFRC. However, there are some limitations, such as the incapability of conserving all design parameters and elucidating the internal failure mechanisms at nano/micro scales. More experiments are needed to investigate nano/micro-scale characterisation, especially X-ray computed tomography tests. These tests can be used to

observe and quantify the porosity in SFRC and study the fundamental failure mechanisms.

6) Numerical analysis is needed to investigate the bond stress-slip relationship as well as to obtain insights into the local fibre/matrix interactions and to provide supporting information for the analytical modelling.

7) Experimental investigations on the size effects on structural strength of SFRC are still very limited. Further experiments to provide more test data is necessary for the validations and improvements of current models.

References

[1] D. Yoo, N. Banthia, J. Yang, Y. Yoon, Size effect in normal- and high-strength amorphous metallic and steel fiber reinforced concrete beams, Construction and Building Materials. 121 (2016) 676-685.

[2] D. Yoo, N. Banthia, Mechanical and structural behaviors of ultra-high-performance fiber-reinforced concrete subjected to impact and blast, Construction and Building Materials. 149 (2017) 416-431.

[3] X.X. Zhang, A.M. Abd Elazim, G. Ruiz, R.C. Yu, Fracture behaviour of steel fibre-reinforced concrete at a wide range of loading rates, Int. J. Impact Eng. 71 (2014) 89-96.

[4] S. Abdallah, M. Fan, Anchorage mechanisms of novel geometrical hooked-end steel fibres, Mater. Struct. 50 (2017) 139.

[5] S. Abdallah, M. Fan, X. Zhou, Effect of Hooked-End Steel Fibres Geometry on Pull-Out Behaviour of Ultra-High Performance Concrete, World Academy of Science, Engineering and Technology, International Journal of Civil, Environmental, Structural, Construction and Architectural Engineering. 10 (2016) 1530-1535.

[6] S.J. Foster, The application of steel-fibres as concrete reinforcement in Australia: from material to structure, Mater. Struct. 42 (2009) 1209-1220.

[7] N. Buratti, B. Ferracuti, M. Savoia, Concrete crack reduction in tunnel linings by steel fibre-reinforced concretes, Construction and Building Materials. 44 (2013) 249-259.

[8] J. Granju, S. Ullah Balouch, Corrosion of steel fibre reinforced concrete from the cracks, Cement and Concrete Research. 35 (2005) 572-577.

[9] S. Abdallah, M. Fan, K.A. Cashell, Bond-slip behaviour of steel fibres in concrete after exposure to elevated temperatures, Constr. Build. Mater. 140 (2017) 542-551.

[10] N. Banthia, A study of some factors affecting the fiber–matrix bond in steel fiber reinforced concrete, Canadian Journal of Civil Engineering. 17 (1990) 610-620.

[11] T. Abu-Lebdeh, S. Hamoush, W. Heard, B. Zornig, Effect of matrix strength on pullout behavior of steel fiber reinforced very-high strength concrete composites, Constr. Build. Mater. 25 (2011) 39-46.

[12] E. Zīle, O. Zīle, Effect of the fiber geometry on the pullout response of mechanically deformed steel fibers, Cem. Concr. Res. 44 (2013) 18-24.

[13] F. Laranjeira, C. Molins, A. Aguado, Predicting the pullout response of inclined hooked steel fibers, Cem. Concr. Res. 40 (2010) 1471-1487.

[14] J. Won, J. Lee, S. Lee, Predicting pull-out behaviour based on the bond mechanism of arch-type steel fibre in cementitious composite, Composite Structures. 134 (2015) 633-644.

[15] S. Abdallah, M. Fan, D.W.A. Rees, Analysis and modelling of mechanical anchorage of 4D/5D hooked end steel fibres, Mater Des. 112 (2016) 539-552.

[16] Y. Ding, F. Zhang, F. Torgal, Y. Zhang, Shear behaviour of steel fibre reinforced self-consolidating concrete beams based on the modified compression field theory, Composite Structures. 94 (2012) 2440-2449.

[17] S. Lee, J. Won, Flexural behavior of precast reinforced concrete composite members reinforced with structural nano-synthetic and steel fibers, Composite Structures. 118 (2014) 571-579.

[18] A.A. Abdul-Razzak, A.A.M. Ali, Influence of cracked concrete models on the nonlinear analysis of High Strength Steel Fibre Reinforced Concrete corbels, Composite Structures. 93 (2011) 2277-2287.

[19] D. Yoo, S. Kang, Y. Yoon, Enhancing the flexural performance of ultra-high-performance concrete using long steel fibers, Composite Structures. 147 (2016) 220-230.

[20] H. Ju, K.S. Kim, D.H. Lee, J. Hwang, S. Choi, Y. Oh, Torsional responses of steel fiber-reinforced concrete members, Composite Structures. 129 (2015) 143-156.

[21] B. Bendtsen, J.G. Sanjayan, Assessment of shear capacity methods of steel fiber reinforced concrete beams using full scale prestressed bridge beams, Mater. Struct. 48 (2015) 3473-3483.

[22] J.P. Romualdi, M. Ramey, S.C. Sanday, Prevention and Control of Cracking by Use of Short Random Fibers, Special Publication. 20 (1968) 179-204.

[23] R. Swamy, Fibre reinforcement of cement and concrete, Matériaux et Construction. 8 (1975) 235-254.

[24] M. Eik, J. Puttonen, H. Herrmann, An orthotropic material model for steel fibre reinforced concrete based on the orientation distribution of fibres, Composite Structures. 121 (2015) 324-336.

[25] R.B. Jewell, K.C. Mahboub, T.L. Robl, A.C. Bathke, Interfacial bond between reinforcing fibers and calcium sulfoaluminate cements: fiber pullout characteristics, ACI Mater. J. 112 (2015) 39.

[26] A.E. Naaman, H. Najm, Bond-slip mechanisms of steel fibers in concrete, ACI Mater. J. 88 (1991).

[27] S. Abdallah, M. Fan, X. Zhou, S. Geyt, Anchorage Effects of Various Steel Fibre Architectures for Concrete Reinforcement, International Journal of Concrete Structures and Materials. (2016) 1-11.

[28] J. Feng, W. Sun, X. Wang, X. Shi, Mechanical analyses of hooked fiber pullout performance in ultra-high-performance concrete, Constr. Build. Mater. 69 (2014) 403-410.

[29] Y. Lee, S. Kang, J. Kim, Pullout behavior of inclined steel fiber in an ultra-high strength cementitious matrix, Constr. Build. Mater. 24 (2010) 2030-2041.

[30] J. Won, J. Lee, S. Lee, Flexural behaviour of arch-type steel fibre reinforced cementitious composites, Composite Structures. 134 (2015) 565-571.

[31] J.G. Sanjayan, A. Nazari, H. Pouraliakbar, FEA modelling of fracture toughness of steel fibre-reinforced geopolymer composites, Mater Des. 76 (2015) 215-222.

[32] V.M. Cunha, Steel fibre reinforced self-compacting concrete (from micromechanics to composite behavior), (2010).

[33] K. Wille, A.E. Naaman, Pullout behavior of high-strength steel fibers embedded in ultra-high-performance concrete, ACI Mater. J. 109 (2012).

[34] J. Won, B. Hong, S. Lee, S.J. Choi, Bonding properties of amorphous micro-steel fibre-reinforced cementitious composites, Composite Structures. 102 (2013) 101-109.

[35] J. Won, J. Lee, S. Lee, Bonding behaviour of arch-type steel fibres in a cementitious composite, Composite Structures. 133 (2015) 117-123.

[36] J. Won, J. Lee, S. Lee, Predicting pull-out behaviour based on the bond mechanism of arch-type steel fibre in cementitious composite, Composite Structures. 134 (2015) 633-644.

[37] S. Abdallah, M. Fan, D.W.A. Rees, Effect of elevated temperature on pull-out behaviour of 4DH/5DH hooked end steel fibres, Composite Structures. 165 (2017) 180-191.

[38] N. Banthia, J. Trottier, Concrete reinforced with deformed steel fibers, part I: bond-slip mechanisms, ACI Mater. J. 91 (1994).

[39] A.E. Naaman, Fiber to matrix bond mechanisms in FRC composites, (2012) 598 - 610.

[40] G. Nammur Jr, A.E. Naaman, Bond stress model for fiber reinforced concrete based on bond stress-slip relationship, ACI Mater. J. 86 (1989).

[41] A.E. Naaman, H. Najm, Bond-slip mechanisms of steel fibers in concrete, ACI Mater. J. 88 (1991) 135–145.

[42] F. Laranjeira de Oliveira, Design-oriented constitutive model for steel fiber reinforced concrete, Unpublished Doctoral dissertation.Universitat Politècnica de Catalunya, Spain. (2010).

[43] I. Markovic, High-Performance Hybrid-Fibre Concrete: Development and Utilisation, IOS Press, 2006.

[44] A. Bentur, S. Wu, N. Banthia, R. Baggott, W. Hansen, A. Katz, C. Leung, V. Li, B. Mobasher, A. Naaman, Fiber-matrix interfaces, (1995) 139-182.

[45] Y. Chan, V.C. Li, Effects of transition zone densification on fiber/cement paste bond strength improvement, Adv. Cem. Based Mater. 5 (1997) 8-17.

[46] R. Gray, C. Johnston, The influence of fibre-matrix interfacial bond strength on the mechanical properties of steel fibre reinforced mortars, International Journal of Cement Composites and Lightweight Concrete. 9 (1987) 43-55.

[47] W. Ren, Z. Yang, R. Sharma, C. Zhang, P.J. Withers, Two-dimensional X-ray CT image based meso-scale fracture modelling of concrete, Engineering Fracture Mechanics. 133 (2015) 24-39.

[48] A. Qsymah, R. Sharma, Z. Yang, L. Margetts, P. Mummery, Micro X-ray computed tomography image-based two-scale homogenisation of ultra high performance fibre reinforced concrete, Constr. Build. Mater. 130 (2017) 230-240.

[49] S. Wei, J.A. Mandel, S. Said, Study of the interface strength in steel fiber-reinforced cement-based composites, 83 (1986) 597-605.

[50] A. Bentur, S. Mindess, Fibre reinforced cementitious composites, 1990,.

[51] A. Bentur, S. Mindess, Fibre Reinforced Cementitious Composites, CRC Press, 2006.

[52] V.C. Li, H. Stang, Interface property characterization and strengthening mechanisms in fiber reinforced cement based composites, Adv. Cem. Based Mater. 6 (1997) 1-20.

[53] M. Valcuende, C. Parra, Bond behaviour of reinforcement in self-compacting concretes, Constr. Build. Mater. 23 (2009) 162-170.

[54] K. Wille, A.E. Naaman, Effect of ultra-high-performance concrete on pullout behavior of high-strength brass-coated straight steel fibers, ACI Mater. J. 110 (2013).

[55] N. Banthia, A study of some factors affecting the fiber-matrix bond in steel fiber reinforced concrete, Canadian Journal of Civil Engineering. 17 (1990) 610-620.

[56] T. Ng, T. Htut, S. Foster, Fracture of steel fibre reinforced concrete—the Unified Variable Engagement Model, UNICIV Report R-460, School of Civil and Environmental Engineering, The University of New South Wales, Sydney. (2012).

[57] R. Breitenbücher, G. Meschke, F. Song, Y. Zhan, Experimental, analytical and numerical analysis of the pullout behaviour of steel fibres considering different fibre types, inclinations and concrete strengths, Structural Concrete. 15 (2014) 126-135.

[58] K. Holschemacher, T. Mueller, Y. Ribakov, Effect of steel fibres on mechanical properties of high-strength concrete, Mater Des. 31 (2010) 2604-2615.

[59] M. Alberti, A. Enfedaque, J. Galvez, M. Canovas, I. Osorio, Polyolefin fiber-reinforced concrete enhanced with steel-hooked fibers in low proportions, Mater Des. 60 (2014) 57-65.

[60] A.A. Shah, Y. Ribakov, Recent trends in steel fibered high-strength concrete, Mater Des. 32 (2011) 4122-4151.

[61] P. Robins, S. Austin, P. Jones, Pull-out behaviour of hooked steel fibres, Mater. Struct. 35 (2002) 434-442.

[62] P. Soroushian, C. Lee, Distribution and orientation of fibers in steel fiber reinforced concrete, ACI Mater. J. 87 (1990).

[63] C. Sorensen, E. Berge, E.B. Nikolaisen, Investigation of fiber distribution in concrete batches discharged from ready-mix truck, International Journal of Concrete Structures and Materials. 8 (2014) 279-287.

[64] D. Yoo, N. Banthia, S. Kang, Y. Yoon, Effect of fiber orientation on the rate-dependent flexural behavior of ultra-high-performance fiber-reinforced concrete, Composite Structures. 157 (2016) 62-70.

[65] L.F.M. Duque, B. Graybeal, Fiber orientation distribution and tensile mechanical response in UHPFRC, Mater. Struct. 50 (2017) 55.

[66] T. Soetens, A. Van Gysel, S. Matthys, L. Taerwe, A semi-analytical model to predict the pull-out behaviour of inclined hooked-end steel fibres, Constr. Build. Mater. 43 (2013) 253-265.

[67] A. Beglarigale, H. Yazıcı, Pull-out behavior of steel fiber embedded in flowable RPC and ordinary mortar, Constr. Build. Mater. 75 (2015) 255-265.

[68] W. Zheng, H. Li, Y. Wang, Compressive behaviour of hybrid fiber-reinforced reactive powder concrete after high temperature, Mater Des. 41 (2012) 403-409.

[69] D.A.S. Rambo, F. de Andrade Silva, R.D. Toledo Filho, Mechanical behavior of hybrid steel-fiber self-consolidating concrete: materials and structural aspects, Mater Des. 54 (2014) 32-42.

[70] F. Isla, G. Ruano, B. Luccioni, Analysis of steel fibers pull-out. Experimental study, Constr. Build. Mater. 100 (2015) 183-193.

[71] A. Kaïkea, D. Achoura, F. Duplan, L. Rizzuti, Effect of mineral admixtures and steel fiber volume contents on the behavior of high performance fiber reinforced concrete, Mater Des. 63 (2014) 493-499.

[72] A. Van Gysel, Studie van het uittrekgedrag van staalvezels ingebed in een cementgebonden matrix met toepassing op staalvezelbeton onderworpen aan buiging, status: published. (2000).

[73] Y. Chan, S. Chu, Effect of silica fume on steel fiber bond characteristics in reactive powder concrete, Cem. Concr. Res. 34 (2004) 1167-1172.

[74] P. Guerrero, A.E. Naaman, Effect of mortar fineness and adhesive agents on pullout response of steel fibers, Materials Journal. 97 (2000) 12-20.

[75] N. Banthia, J. Trottier, Deformed steel fiber—cementitious matrix bond under impact, Cem. Concr. Res. 21 (1991) 158-168.

[76] R. Gray, Experimental techniques for measuring fibre/matrix interfacial bond shear strength, Int J Adhes Adhes. 3 (1983) 197-202.

[77] K. Wille, A. Naaman, Bond stress-slip behavior of steel fibers embedded in ultra high performance concrete, (2010) 99-111.

[78] Z. Li, B. Mobasher, S.P. Shah, Characterization of Interfacial Properties in Fiber-Reinforced Cementitious Composites, J Am Ceram Soc. 74 (1991) 2156-2164.

[79] M. Tuyan, H. Yazıcı, Pull-out behavior of single steel fiber from SIFCON matrix, Constr. Build. Mater. 35 (2012) 571-577.

[80] L. Den Boer, Concrete technology and pull-out testing of steel fibre reinforced normal gravel concrete, (1973) 97-106.

[81] G. Tattersall, C. Urbanowicz, Bond strength in steel-fibre-reinforced concrete, Magazine of Concrete Research. 26 (1974) 105-113.

[82] P. Stroeven, Y. De Haan, C. Bouter, S. Shah, Pull-out tests of steel fibres, Testing and Test Methods of Fiber Cement Composites. (1978) 345-353.

[83] D.J. Kim, S. El-Tawil, A.E. Naaman, Loading rate effect on pullout behavior of deformed steel fibers, ACI Mater. J. 105 (2008).

[84] A.E. Naaman, F. Moavenzadeh, F.J. McGarry, Probabilistic analysis of fiber-reinforced concrete, J. Eng. Mech. 100 (1974).

[85] A. Burakiewicz, Testing of fibre bond strength in cement matrix, (1978) 355-365.

[86] R.J. Gray, Fibre/matrix interfacial bond shear strength and its influence on the mechanical properties of steel fibre reinforced cementitious matrices, (1982).

[87] R. Gray, C. Johnston, The measurement of fibre-matrix interfacial bond strength in steel fibre-reinforced cementitious composites, (1978) 317-328.

[88] D. Pinchin, D. Tabor, Inelastic behaviour in steel wire pull-out from Portland cement mortar, J. Mater. Sci. 13 (1978) 1261-1266.

[89] B. Hughes, J. Dougill, Fibre bond strengths in cement and concrete, Magazine of Concrete Research. 27 (1975) 161-166.

[90] M. Maage, Fibre bond and friction in cement and concrete, (1978) 329-336.

[91] A. Naaman, S. Shah, Bond studies on oriented and aligned steel fibres, (1975) 171-178.

[92] A.E. Naaman, S. Shar, Pull-out mechanism in steel fibre-reinforced concrete, Journal of the Structural Division. 102 (1976).

[93] U.N. Gokoz, A.E. Naaman, Effect of strain-rate on the pull-out behaviour of fibres in mortar, International Journal of Cement Composites and Lightweight Concrete. 3 (1981) 187-202.

[94] P. Mangat, M. Motamedi-Azari, B.S. Ramat, Steel fibre-cement matrix interfacial bond characteristics under flexure, International Journal of Cement Composites and Lightweight Concrete. 6 (1984) 29-37.

[95] Y.M. Abbas, M.I. Khan, Fiber–Matrix Interactions in Fiber-Reinforced Concrete: A Review, Arabian Journal for Science and Engineering. 41 (2016) 1183-1198.

[96] P. Bartos, Review paper: bond in fibre reinforced cements and concretes, International Journal of Cement composites and Lightweight concrete. 3 (1981) 159-177.

[97] A.E. Naaman, H. Najm, Bond-slip mechanisms of steel fibers in concrete, ACI Mater. J. 88 (1991).

[98] J.M. Alwan, A.E. Naaman, P. Guerrero, Effect of mechanical clamping on the pull-out response of hooked steel fibers embedded in cementitious matrices, Concrete Science and Engineering. 1 (1999) 15-25.

[99] H. Cox, The elasticity and strength of paper and other fibrous materials, British journal of applied physics. 3 (1952) 72.

[100] L. Greszczuk, Theoretical studies of the mechanics of the fiber-matrix interface in composites, in: Anonymous Interfaces in Composites, ASTM International, 1969.

[101] P. Lawrence, Some theoretical considerations of fibre pull-out from an elastic matrix, J. Mater. Sci. 7 (1972) 1-6.

[102] V.S. Gopalaratnam, S.P. Shah, Tensile failure of steel fiber-reinforced mortar, J. Eng. Mech. 113 (1987) 635-652.

[103] V. Gopalaratnam, J. Cheng, On the Modelling of Inelastic Interfaces in Fibrous Composites. Cement Based Composites: Bonding in Cementitious Composites, 114 (1988) 225-231.

[104] G. Nammur, A.E. Naaman, S.K. Clark, Analytical Prediction of the Pull-out Behavior of Steel Fibres in Cementitious Matrices. Cement Based Composites: Bonding in Cemenitious Composites, 114 (1988) 217-224.

[105] H. Stang, Z. Li, S. Shah, Pullout problem: stress versus fracture mechanical approach, J. Eng. Mech. 116 (1990) 2136-2150.

[106] A. Takaku, R. Arridge, The effect of interfacial radial and shear stress on fibre pull-out in composite materials, J. Phys. D. 6 (1973) 2038.

[107] C. Hsueh, Elastic load transfer from partially embedded axially loaded fibre to matrix, J. Mater. Sci. Lett. 7 (1988) 497-500.

[108] C. Hsueh, Interfacial debonding and fiber pull-out stresses of fiber-reinforced composites, Materials Science and Engineering: A. 123 (1990) 1-11.

[109] C. Hsueh, Interfacial debonding and fiber pull-out stresses of fiber-reinforced composites II: Non-constant interfacial bond strength, Materials Science and Engineering: A. 125 (1990) 67-73.

[110] A.E. Naaman, G.G. Namur, J.M. Alwan, H.S. Najm, Fiber pullout and bond slip. II: Experimental validation, J. Struct. Eng. 117 (1991) 2791-2800.

[111] G. Chanvillard, Modeling the pullout of wire-drawn steel fibers, Cem. Concr. Res. 29 (1999) 1027-1037.

[112] C. Sujivorakul, A. Waas, A. Naaman, Pullout response of a smooth fiber with an end anchorage, J. Eng. Mech. 126 (2000) 986-993.

[113] P. Ghoddousi, R. Ahmadi, M. Sharifi, Fiber pullout model for aligned hooked-end steel fiber, Canadian Journal of Civil Engineering. 37 (2010) 1179-1188.

[114] A.E. Naaman, G.G. Namur, J.M. Alwan, H.S. Najm, Fiber pullout and bond slip. I: Analytical study, J. Struct. Eng. 117 (1991) 2769-2790.

[115] L. Vandewalle, RILEM TC 162-TDF: Test and design methods for steel fibre reinforced concrete, Mater. Struct. 33 (2000) 3-6.

[116] S.H.P. Cavalaro, R. López, J.M. Torrents, A. Aguado, Improved assessment of fibre content and orientation with inductive method in SFRC, Mater. Struct. 48 (2015) 1859-1873.

[117] W. Zheng, B. Luo, Y. Wang, Stress–strain relationship of steel-fibre reinforced reactive powder concrete at elevated temperatures, Mater. Struct. 48 (2015) 2299-2314.

[118] RILEM Technical Committee TC208-HFC, SC2, V. Li, G. van Zijl, F.H. Wittmann, Durability of Strain-Hardening Fibre-Reinforced Cement-Based Composites (SHCC): State of the Art Report, Springer, 2010.

[119] D. Wang, C. Shi, Z. Wu, J. Xiao, Z. Huang, Z. Fang, A review on ultra high performance concrete: Part II. Hydration, microstructure and properties, Constr. Build. Mater. 96 (2015) 368-377.

[120] B. En, 197-1 (2000) Cement: composition, specifications and conformity criteria for common cements, British Standards Institution, London. (2000).

[121] D. joo Kim, Strain Rate Effect on High Performance Fiber Reinforced Cementitious Composites using Slip Hardening High Strength Deformed Steel Fibers, ProQuest, 2009.

[122] B. EN, 12350-8: 2010 Testing fresh concrete, Self-compacting concrete.Slump-flow test.

[123] R. Deeb, A. Ghanbari, B.L. Karihaloo, Development of self-compacting high and ultra high performance concretes with and without steel fibres, Cement and concrete composites. 34 (2012) 185-190.

[124] C. Shi, Z. Wu, J. Xiao, D. Wang, Z. Huang, Z. Fang, A review on ultra high performance concrete: Part I. Raw materials and mixture design, Constr. Build. Mater. 101, Part 1 (2015) 741-751.

[125] S.F. Lee, S. Jacobsen, Study of interfacial microstructure, fracture energy, compressive energy and debonding load of steel fiber-reinforced mortar, Mater. Struct. 44 (2011) 1451-1465.

[126] Q. Zeng, K. Li, T. Fen-chong, P. Dangla, Pore structure characterization of cement pastes blended with high-volume fly-ash, Cem. Concr. Res. 42 (2012) 194-204.

[127] Z. Wu, C. Shi, K.H. Khayat, Influence of silica fume content on microstructure development and bond to steel fiber in ultra-high strength cement-based materials (UHSC), Cement and Concrete Composites. 71 (2016) 97-109.

[128] T. Nguyen, A. Toumi, A. Turatsinze, Mechanical properties of steel fibre reinforced and rubberised cement-based mortars, Mater Des. 31 (2010) 641-647.

[129] A. Prakash, S. Srinivasan, A.R.M. Rao, Numerical investigation on steel fibre reinforced cementitious composite panels subjected to high velocity impact loading, Mater Des. 83 (2015) 164-175.

[130] C. Sujivorakul, Development of High Performance Fiber Reinforced Cement Composites using Twisted Polygonal Steel Fibers, University of Michigan., 2002.

[131] D.W.A. Rees, CHAPTER 5 - ELASTIC-PERFECT PLASTICITY, in: D.W.A. Rees (Ed.), Basic Engineering Plasticity, Butterworth-Heinemann, Oxford, 2006, pp. 127-160.

[132] B. Xu, J.W. Ju, H. Shi, Progressive micromechanical modeling for pullout energy of hooked-end steel fiber in cement-based composites, Int J Damage Mech. (2010) 1056789510385260.

[133] O. Arioz, Effects of elevated temperatures on properties of concrete, Fire Saf. J. 42 (2007) 516-522.

[134] T. Pothisiri, P. Panedpojaman, Modeling of bonding between steel rebar and concrete at elevated temperatures, Constr. Build. Mater. 27 (2012) 130-140.

[135] P. Pliya, A. Beaucour, A. Noumowé., Contribution of cocktail of polypropylene and steel fibres in improving the behaviour of high strength concrete subjected to high temperature, Constr. Build. Mater. 25 (2011) 1926-1934.

[136] W. Khaliq, V. Kodur, Thermal and mechanical properties of fiber reinforced high performance self-consolidating concrete at elevated temperatures, Cem. Concr. Res. 41 (2011) 1112-1122.

[137] C.S. Poon, Z.H. Shui, L. Lam, Compressive behavior of fiber reinforced high-performance concrete subjected to elevated temperatures, Cem. Concr. Res. 34 (2004) 2215-2222.

[138] V. Kodur, Properties of concrete at elevated temperatures, ISRN Civil Engineering. 2014 (2014).

[139] A. Lau, M. Anson, Effect of high temperatures on high performance steel fibre reinforced concrete, Cem. Concr. Res. 36 (2006) 1698-1707.

[140] G.A. Khoury, Effect of fire on concrete and concrete structures, Progress in Structural Engineering and Materials. 2 (2000) 429-447.

[141] S.L. Suhaendi, T. Horiguchi, Effect of short fibers on residual permeability and mechanical properties of hybrid fibre reinforced high strength concrete after heat exposition, Cem. Concr. Res. 36 (2006) 1672-1678.

[142] L.T. Phan, High-strength concrete at high temperature-an overview, Proceedings of 6th International Symposiumon Utilization of High Strength/High Performance Concrete, Leipzig, Germany. (2002) 501-518.

[143] B. Chen, J. Liu, Residual strength of hybrid-fiber-reinforced high-strength concrete after exposure to high temperatures, Cem. Concr. Res. 34 (2004) 1065-1069.

[144] G.M. Chen, Y.H. He, H. Yang, J.F. Chen, Y.C. Guo, Compressive behavior of steel fiber reinforced recycled aggregate concrete after exposure to elevated temperatures, Constr. Build. Mater. 71 (2014) 1-15.

[145] R.H. Haddad, L.G. Shannis, Post-fire behavior of bond between high strength pozzolanic concrete and reinforcing steel, Constr. Build. Mater. 18 (2004) 425-435.

[146] Y. Tai, H. Pan, Y. Kung, Mechanical properties of steel fiber reinforced reactive powder concrete following exposure to high temperature reaching 800 °C, Nucl. Eng. Des. 241 (2011) 2416-2424.

[147] K.K. Sideris, P. Manita, E. Chaniotakis, Performance of thermally damaged fibre reinforced concretes, Constr. Build. Mater. 23 (2009) 1232-1239.

[148] W. Khaliq, Performance Characterization of High Performance Concretes Under Fire Conditions, , 2012.

[149] A. Elghazouli, K. Cashell, B. Izzuddin, Experimental evaluation of the mechanical properties of steel reinforcement at elevated temperature, Fire Saf. J. 44 (2009) 909-919.

[150] M. Barburski, S.V. Lomov, Influence of oxidation on steel fiber yarn and knitted fabric properties, Journal of Industrial Textiles. 45 (2016) 1516-1529.

[151] M. Ezziane, L. Molez, R. Jauberthie, D. Rangeard, Heat exposure tests on various types of fibre mortar, European journal of environmental and civil engineering. 15 (2011) 715-726.

[152] P. Sukontasukkul, W. Pomchiengpin, S. Songpiriyakij, Post-crack (or post-peak) flexural response and toughness of fiber reinforced concrete after exposure to high temperature, Constr. Build. Mater. 24 (2010) 1967-1974.

[153] A. Vesel, M. Mozetic, A. Drenik, N. Hauptman, M. Balat-Pichelin, High temperature oxidation of stainless steel AISI316L in air plasma, Appl. Surf. Sci. 255 (2008) 1759-1765.

[154] H.A. El-Mal, A. Sherbini, H. Sallam, Mode II Fracture Toughness of Hybrid FRCs, International Journal of Concrete Structures and Materials. 9 (2015) 475-486.

[155] H. Li, G. Liu, Tensile Properties of Hybrid Fiber-Reinforced Reactive Powder Concrete After Exposure to Elevated Temperatures, International Journal of Concrete Structures and Materials. (2016) 1-9.

[156] M.S. Islam, S. Alam, Principal component and multiple regression analysis for steel fiber reinforced concrete (SFRC) beams, International Journal of Concrete Structures and Materials. 7 (2013) 303-317.

[157] P.R. Tadepalli, H.B. Dhonde, Y. Mo, T.T. Hsu, Shear Strength of Prestressed Steel Fiber Concrete I-Beams, International Journal of Concrete Structures and Materials. 9 (2015) 267-281.

[158] G. Srikar, G. Anand, S.S. Prakash, A Study on Residual Compression Behavior of Structural Fiber Reinforced Concrete Exposed to Moderate Temperature Using Digital Image Correlation, International Journal of Concrete Structures and Materials. (2016) 1-11.

[159] M. Pająk, T. Ponikiewski, Flexural behavior of self-compacting concrete reinforced with different types of steel fibers, Constr. Build. Mater. 47 (2013) 397-408.

[160] A. Abrishambaf, J.A.O. Barros, V.M.C.F. Cunha, Relation between fibre distribution and post-cracking behaviour in steel fibre reinforced self-compacting concrete panels, Cem. Concr. Res. 51 (2013) 57-66.

[161] İ Şanal, N. Özyurt Zihnioğlu, To what extent does the fiber orientation affect mechanical performance? Constr. Build. Mater. 44 (2013) 671-681.

[162] L. Ferrara, P. Bamonte, A. Caverzan, A. Musa, I. Sanal, A comprehensive methodology to test the performance of Steel Fibre Reinforced Self-Compacting Concrete (SFR-SCC), Constr. Build. Mater. 37 (2012) 406-424.

[163] A.G. Kooiman, Modelling steel fibre reinforced concrete for structural design, (2000).

[164] L. Ferrara, A. Meda, Relationships between fibre distribution, workability and the mechanical properties of SFRC applied to precast roof elements, Mater. Struct. 39 (2006) 411-420.

[165] N. Ozyurt, T.O. Mason, S.P. Shah, Correlation of fiber dispersion, rheology and mechanical performance of FRCs, Cement and Concrete Composites. 29 (2007) 70-79.

[166] T. Rilem, 50-FMC, 1985, Determination of the Fracture Energy of Mortar and Concrete by Means of Three-point Bend Tests on Notched Beams. 285-290.

[167] M. Wecharatana, S. Shah, Fracture Toughness of Fiber Reinforced Concrete. (1983).

[168] V.S. Gopalaratnam, R. Gettu, On the characterization of flexural toughness in fiber reinforced concretes, Cement and concrete composites. 17 (1995) 239-254.

[169] Y. Ding, Investigations into the relationship between deflection and crack mouth opening displacement of SFRC beam, Constr. Build. Mater. 25 (2011) 2432-2440.

[170] G.H. Mahmud, Z. Yang, A.M.T. Hassan, Experimental and numerical studies of size effects of Ultra High Performance Steel Fibre Reinforced Concrete (UHPFRC) beams, Construction and Building Materials. 48 (2013) 1027-1034.

[171] B. EN, 14651: 2005 A1: 2007, Test method for metallic fibre concrete.Measuring the flexural tensile strength (limit of proportionality (LOP), residual). (2007) 1-20.

[172] C. Astm, 1018, Standard test method for flexural toughness and first crack strength of fibre reinforced concrete(Using beam with third-point loading). American Society of Testing and Materials, Philadelphia, Annual Book of Standard, 4. 02(1994) 509-516,.

[173] D. CNR, 204/2006 (2006) Guidelines for the design, construction and production control of fibre reinforced concrete structures, National Research Council of Italy. 59.

[174] P. JSCE-SF4 III, Method of Tests for Steel Fiber Reinforced Concrete, Concrete Library of JSCE, The Japan Society of Civil Engineers. (1984).

[175] T. RILEM, 162 TDF: Design of Steelfibre Reinforced Concrete–Method, Recommendations, Material and Structures. (2001).

[176] G. Giaccio, J.M. Tobes, R. Zerbino, Use of small beams to obtain design parameters of fibre reinforced concrete, Cement and Concrete Composites. 30 (2008) 297-306.

[177] M.H.A. Beygi, M.T. Kazemi, I.M. Nikbin, J.V. Amiri, The effect of water to cement ratio on fracture parameters and brittleness of self-compacting concrete, Mater Des. 50 (2013) 267-276.

[178] F. Bencardino, Mechanical Parameters and Post-Cracking Behaviour of HPFRC according to Three-Point and Four-Point Bending Test, Advances in Civil Engineering. 2013 (2013).

[179] A. Abrishambaf, J.A.O. Barros, V.M.C.F. Cunha, C. Frazão, Time dependent behaviour of fibre pull-out in self-compacting concrete, Cement and Concrete Composites. 77 (2017) 14-28.

[180] M. Alberti, A. Enfedaque, J. Gálvez, Fibre reinforced concrete with a combination of polyolefin and steel-hooked fibres, Composite Structures. 171 (2017) 317-325.

[181] M. di Prisco, M. Colombo, D. Dozio, Fibre-reinforced concrete in fib Model Code 2010: principles, models and test validation, Structural Concrete. 14 (2013) 342-361.

[182] K. Wille, S. El-Tawil, A.E. Naaman, Properties of strain hardening ultra high performance fiber reinforced concrete (UHP-FRC) under direct tensile loading, Cement and Concrete Composites. 48 (2014) 53-66.

[183] F. Bencardino, L. Rizzuti, G. Spadea, R.N. Swamy, Experimental evaluation of fiber reinforced concrete fracture properties, Composites Part B: Engineering. 41 (2010) 17-24.

[184] B.E. Barragán, Failure and Toughness of Steel Fiber Reinforced Concrete Under Tension and Shear, Universitat Politècnica de Catalunya, 2002.